

AUTOMATIC CHANGE DETECTION IN MULTIPLE PIGMENTED SKIN LESIONS

Konstantin Korotkov

Dipòsit legal: Gi. 1344-2014
<http://hdl.handle.net/10803/260162>

ADVERTIMENT. L'accés als continguts d'aquesta tesi doctoral i la seva utilització ha de respectar els drets de la persona autora. Pot ser utilitzada per a consulta o estudi personal, així com en activitats o materials d'investigació i docència en els termes establerts a l'art. 32 del Text Refós de la Llei de Propietat Intel·lectual (RDL 1/1996). Per altres utilitzacions es requereix l'autorització prèvia i expressa de la persona autora. En qualsevol cas, en la utilització dels seus continguts caldrà indicar de forma clara el nom i cognoms de la persona autora i el títol de la tesi doctoral. No s'autoritza la seva reproducció o altres formes d'explotació efectuades amb finalitats de lucre ni la seva comunicació pública des d'un lloc aliè al servei TDX. Tampoc s'autoritza la presentació del seu contingut en una finestra o marc aliè a TDX (framing). Aquesta reserva de drets afecta tant als continguts de la tesi com als seus resums i índexs.

ADVERTENCIA. El acceso a los contenidos de esta tesis doctoral y su utilización debe respetar los derechos de la persona autora. Puede ser utilizada para consulta o estudio personal, así como en actividades o materiales de investigación y docencia en los términos establecidos en el art. 32 del Texto Refundido de la Ley de Propiedad Intelectual (RDL 1/1996). Para otros usos se requiere la autorización previa y expresa de la persona autora. En cualquier caso, en la utilización de sus contenidos se deberá indicar de forma clara el nombre y apellidos de la persona autora y el título de la tesis doctoral. No se autoriza su reproducción u otras formas de explotación efectuadas con fines lucrativos ni su comunicación pública desde un sitio ajeno al servicio TDR. Tampoco se autoriza la presentación de su contenido en una ventana o marco ajeno a TDR (framing). Esta reserva de derechos afecta tanto al contenido de la tesis como a sus resúmenes e índices.

WARNING. Access to the contents of this doctoral thesis and its use must respect the rights of the author. It can be used for reference or private study, as well as research and learning activities or materials in the terms established by the 32nd article of the Spanish Consolidated Copyright Act (RDL 1/1996). Express and previous authorization of the author is required for any other uses. In any case, when using its content, full name of the author and title of the thesis must be clearly indicated. Reproduction or other forms of for profit use or public communication from outside TDX service is not allowed. Presentation of its content in a window or frame external to TDX (framing) is not authorized either. These rights affect both the content of the thesis and its abstracts and indexes.



Universitat de Girona

PhD Thesis

Automatic Change Detection in Multiple Pigmented Skin Lesions

Konstantin Korotkov

2014



Universitat de Girona

PhD Thesis

Automatic Change Detection in Multiple Pigmented Skin Lesions

Konstantin Korotkov

2014

DOCTORAL PROGRAM IN TECHNOLOGY

Supervised by: Dr. Rafael García

Work submitted to the University of Girona in partial fulfillment of the requirements
for the degree of Doctor of Philosophy

Посвящается моим родителям
Dedicated to my parents

Acknowledgements

I believe that courage and inspiration are the essential ingredients that make up and sustain any endeavor. I am lucky that during my doctoral studies I have always had a source of both, and for that, I am sincerely grateful to my supervisor, Rafael García. Without his brilliant ideas and continuous support, this work would simply not be possible. Nor would it be possible without my family that has always been there for me despite the overwhelming distances between us. Their love and encouragement helped me immensely in the completion of this thesis. My most loving thanks to my parents, Natalya and Evgeniy, brother Kirill, grandma Elizaveta, aunt Anna and uncle Alexander, cousins, Nikolay and Kseniya, my great grandmother Galina and granduncle Alexander.

My special thanks go to my friends many of whom are fellow PhD students and know first-hand what it takes to be one. They were there to help me out whenever I needed it the most: Kenneth, Victor, Isaac, Guillaume, Mojdeh, Habib, Sharad, Chrissy, Chee Sing, Shihav, Sonia, Jan, and Andrey.

Also, I would like to thank my colleagues: Nuno, Tudor and László, for their time and invaluable suggestions; Josep, Ricard P. and Ricard C., for taking the trouble to help me with all my technical problems; and Joseta, Mireia, and Montse, for keeping my back in the ruthless world of paperwork. My gratitude, as well, to the anonymous reviewers and the members of the defense panel for evaluating my work. Besides, this thesis largely owes its completion to the AGAUR FI-DGR 2011 grant provided by the Autonomous Government of Catalonia. I am grateful and honored to be among its holders.

Last but never least, I wish to thank my fiancée, and soon to be wife, Amanda, for standing beside me throughout my PhD. Her unwavering faith in me, even at the times when I could not share it, her patience and love encouraged me not to give up and accomplish what I had undertaken.

Publications

This thesis resulted in the publication of a comprehensive review article:

K. Korotkov and R. García, “Computerized analysis of pigmented skin lesions: a review,” *Artificial Intelligence in Medicine*, 2012, 56, 69–90.

Also, an article titled “Design, Construction, and Testing of a New Total Body Skin Scanning System” is currently under review in the *IEEE Transactions of Medical Imaging* journal.

Abbreviations

ANN	Artificial Neural Networks
CAD	Computer-Aided Diagnosis
CBIR	Content-Based Image Retrieval
CCD	Charge-Coupled Device
CDS	Clinical Diagnosis Support
CIELUV	Commission Internationale de l'Éclairage 1976 ($L^* u^* v^*$) color space
DA	Discriminant Analysis
DOF	Depth of Field
DTEA	Dermatologist-like Tumour Extraction Algorithm
ELM	Epiluminiscence Microscopy
GVF	Gradient Vector Flow
HSV	Hue Saturation Intensity (color space)
JPEG	Joint Photographic Experts Group
KL-PLS	Kernel Logistic Partial Least Squares
KLT	Karhunen-Loève Transform
kNN	k -Nearest Neighbors

ABBREVIATIONS

LED	Light-Emitting Diode
MSER	Maximally Stable Extremal Regions
NCC	Normalized Cross-Correlation
PCA	Principal Component Analysis
PDE	Partial Differential Equations
PSL	Pigmented Skin Lesion
RANSAC	RAndom SAmples Consensus
RGB	Red Green Blue (color space)
ROI	Region of Interest
SIFT	Scale-Invariant Feature Transform
SRM	Statistical Region Merging
SVM	Support Vector Machines
TBSE	Total Body Skin Examination
TBSI	Total Body Skin Imaging
UV	Ultraviolet radiation
WBP	Whole Body Photography

List of Figures

1.1	Anatomy of the skin	2
1.2	Clinical and dermoscopic images of benign PSLs	4
1.3	Clinical and dermoscopic images of malignant melanomas	6
1.4	Standardized poses for TBSI	9
1.5	Samples of commercially available dermoscopes	10
1.6	Two dermoscopy images of a PSL acquired with a difference of one year	15
2.1	Literature categorization tree	18
3.1	Exterior view of the scanner: the acquisition compartment	47
3.2	Exterior view of the scanner: the equipment compartment	48
3.3	The camera setup and patient poses for image acquisition	52
3.4	Schematic views of the turntable steps	53
3.5	Schematic representation of the coordinate systems in the scanner . . .	59
3.6	Marker encoding using the colors of the surrounding squares	61
3.7	The abacus encoding scheme for 4 colors	62
3.8	Images of the calibration pattern	63
3.9	Neighbor corners selection in the pattern	66
3.10	Sample images demonstrating imaging subsystem limitations	68
3.11	The limits of the patient area in the acquisition chamber	68
4.1	The pipeline for intra-exploration mole mapping	72
4.2	Image projection of a lesion's normal vector	79
4.3	Schematics of possible scenarios during mole set creation	81
4.4	Failed homography computation using SIFT features	82
4.5	Single representation of two lesions	83
4.6	Best camera/view selection during mole set merging	86
4.7	Mole comparison scenarios	88
4.8	The lesion matching condition during the mole set merging procedure .	89

LIST OF FIGURES

4.9	Mole match propagation: possible bridge exception scenarios	90
4.10	The pipeline for detecting new and evolving lesions	92
4.11	An example of non-coinciding views of the same mole in 2 explorations .	93
4.12	Scenarios for the view selection in the target exploration	95
5.1	Skin (foreground) detection	104
5.2	Image preprocessing for mole detection	106
5.3	Mole detection using MSER	108
5.4	SIFT feature matches in stereo images	110
5.5	Mole correspondences in stereo pairs	112
5.6	Evaluation of PSL stereo triangulation	114
5.7	Mole sets computed at three different turntable positions	115
5.8	Overlapping mole sets	116
5.9	Mole matching at different turntable positions	118
5.10	Unsuccessful matching of moles at remote turntable positions	119
5.11	Mole set match propagation	120
5.12	Examples of outliers in the mole map	121
5.13	A complete mole map of a reference patient	122
5.14	Clinical and dermoscopy images of relevant lesions of a patient	125
5.15	Inter-exploration lesion matching	127
5.16	Change detection in PSLs	129
A.1	Sample image of binarization using different intensity thresholds	138
A.2	Example of a MSER detection with different parameters	139
A.3	Point correspondence and epipolar geometry	141
A.4	Image scale-space representation	144
A.5	The scale-space pyramid used in SIFT	145
A.6	Extrema detection in the difference-of-Gaussian images	146
A.7	Creation of a SIFT keypoint descriptor	149
A.8	Sample SIFT feature detection	151
A.9	Triangulation of a 3D point using its projections in stereo images	153
A.10	Line parameterization	154

List of Tables

1.1	Methods for the diagnosis of melanoma clinically and by dermoscopy. . .	12
1.2	Confusing acronyms of methods for melanoma diagnosis	13
2.1	PSL image preprocessing operations	20
2.2	Feature extraction for pattern analysis	27
2.3	Dermoscopic features of PSLs	28
2.4	Clinical features of PSLs	30
2.5	Classification methods in computerized analysis of PSL images	36
2.6	Proprietary CAD software and dermoscopy instruments	38
3.1	The intrinsic parameters of the cameras	57
4.1	Summary of the algorithm parameters	100

LIST OF TABLES

List of Algorithms

1	Primary steps for visual marker identification	64
2	Image foreground (skin) detection	74
3	Image preprocessing for mole detection	75
4	Mole matching in a stereo pair	77
5	Resolving a bridge exception during mole match propagation	91
6	PSL change detection	98
7	The RANSAC robust estimation algorithm.	151
8	Adaptive algorithm for determining the number of RANSAC samples . .	152

LIST OF ALGORITHMS

Contents

Abbreviations	ix
List of Figures	xi
List of Tables	xiii
List of Algorithms	xv
Abstract	xxv
1 Introduction	1
1.1 The human skin	1
1.2 Pigmented skin lesions	3
1.3 Malignant melanoma	5
1.4 Melanoma screening	7
1.4.1 Imaging techniques	7
1.4.1.1 Clinical photography	8
1.4.1.2 Dermoscopy	9
1.4.1.3 Baseline images	10
1.4.2 Melanoma diagnosis methods	11
1.4.3 Automated diagnosis of melanoma	12
1.4.3.1 Clinical impact	13
1.5 Research motivation	14
1.6 Thesis outline	16
2 Computerized analysis of PSLs: a literature review	17
2.1 Single lesion analysis	19
2.1.1 Image preprocessing	20
2.1.2 Lesion border detection	21
2.1.2.1 PSL border detection methodology	22
2.1.2.2 Comparison of segmentation algorithms	24
2.1.3 Feature extraction	25
2.1.4 Registration and change detection	32

CONTENTS

2.1.4.1	Change detection	32
2.1.4.2	Registration	33
2.1.5	Lesion classification	34
2.1.6	CAD systems	37
2.1.7	3D lesion analysis	40
2.2	Multiple lesion analysis	40
2.2.1	Lesion localization	41
2.2.2	Lesion registration	41
2.3	Conclusion	42
3	A total body skin scanner	45
3.1	Hardware design	46
3.1.1	The imaging subsystem	49
3.1.2	The lighting subsystem	50
3.2	The scanning procedure	51
3.3	Camera calibration	53
3.3.1	The intrinsic calibration	53
3.3.2	The extrinsic calibration	58
3.3.2.1	The calibration board	59
3.3.2.2	Visual marker recognition	63
3.4	Prototype restrictions	67
3.5	Conclusions	69
4	Automatic PSL change detection	71
4.1	Intra-exploration mole mapping	71
4.1.1	Mole detection	72
4.1.1.1	Foreground (skin) detection	72
4.1.1.2	Image preprocessing	73
4.1.2	Stereo-pair processing	75
4.1.2.1	Mole matching	76
4.1.2.2	Mole triangulation	78
4.1.3	Mole set creation	79
4.1.3.1	Multiple representations of one lesion	80
4.1.3.2	Single representation of multiple lesions	82
4.1.4	Mole set merging	83
4.1.4.1	Matching moles across mole sets	84

4.1.4.2	Mole match propagation	89
4.2	Inter-exploration operations	91
4.2.1	Mole matching	92
4.2.2	Change detection	97
4.3	Conclusion	98
5	Results and discussion	103
5.1	Intra-exploration operations	103
5.1.1	Skin detection	103
5.1.2	Image preprocessing	105
5.1.3	Mole detection	107
5.1.4	Mole matching in stereo pairs	109
5.1.5	PSL triangulation and mole set creation	113
5.1.6	Mole set merging	117
5.2	Mole map validation	121
5.2.1	The ground truth problem	121
5.2.2	Preliminary evaluation	123
5.3	Inter-exploration operations	126
5.3.1	Lesion matching	126
5.3.2	Change detection	128
6	Conclusions	131
6.1	Summary of the thesis	132
6.2	Contributions	133
6.3	Limitations	134
6.4	Further work	134
A	Methodology	137
A.1	Maximally Stable Extremal Regions	137
A.2	Epipolar geometry	140
A.3	Scale-Invariant Feature Transform	142
A.4	The RANSAC algorithm	150
A.5	Triangulation	153
	References	157

CONTENTS

Resum

El melanoma maligne és el més rar i mortal de tots els càncers de pell, causant tres vegades més morts que el conjunt de totes les altres malalties malignes de la pell. Afortunadament, en les primeres etapes, és completament curable, fent de les exploracions de pell a nivell de cos complert (TBSE, de l'anglès Total Body Skin Examination) un procés fonamental per a molts pacients. Durant el TBSE, els dermatòlegs busquen els signes típics de melanoma en les lesions pigmentades de la pell (PSL, Pigmented Skin Lesions), així com PSLs sotmesos als ràpids canvis característics del càncer. Conjuntament amb la fotografia de referència clínica i dermatoscòpica, el càlcul de TBSE pot ser molt tediós i lent, especialment per a pacients amb un gran nombre de lesions. A més a més, establir correspondències correctes entre el cos i les imatges, i entre les diferents imatges, per a cadascuna de les lesions, pot ésser d'extrema dificultat.

Malgrat els avenços en les tècniques d'escaneig cutani, les eines per a realitzar TBSEs de forma automàtica no han rebut massa atenció. Aquest fet es posa de relleu en la nostra revisió de la literatura, que cobreix l'àrea de l'anàlisi per computador d'imatges de PSL. En aquesta revisió, es resumeixen diverses aproximacions per a la implementació del diagnòstic assistit per ordinador, comentant-ne els seus components principals. En particular, es proposa una classificació ampliada de descriptors de característiques PSL, associant-los amb mètodes específics pel diagnòstic de melanoma, dividint-los entre imatge clínica i dermatoscòpica.

Amb l'objectiu de l'automatització de TBSEs, hem dissenyat i construït un escàner corporal de cobertura total per adquirir imatges de la superfície de la pell utilitzant llum amb polarització creuada. Equipat amb 21 càmeres d'alta resolució de baix cost i una plataforma giratòria, aquest escàner adquireix automàticament un conjunt d'imatges amb solapament, que cobreix el 85–90% de la superfície de la pell del pacient. La calibració extrínseca del sistema es du a terme utilitzant una sola imatge de cada càmera i un patró de calibratge amb un codi de colors dissenyat específicament. A més, hem desenvolupat un algoritme pel mapeig automàtic de les PSLs i l'estimació dels canvis entre exploracions. Els mapes produïts relacionen les imatges de les lesions individuals amb la seva ubicació en el cos del pacient, resolent el problema de correspondència del cos a la imatge i d'imatge a imatge en TBSEs. Actualment, l'escàner es limita a pacients amb escàs pèl corporal. Per a un examen complet de la pell, on el cuir cabellut, els palmells de les mans, les plantes dels peus i les parts interiors dels braços han de ser fotografiats manualment.

Els tests inicials de l'escàner mostren que aquest pot ésser utilitzat satisfactòriament

pel mapeig automàtic i el control de canvis temporal de múltiples lesions: els PSLs importants per a realitzar-ne el seguiment han estat mapejats successivament en les diverses exploracions. D'altra banda, durant la comparació d'imatges, totes les lesions amb canvis artificials introduïts han estat correctament identificades com “evolucionades”. Per tal de desenvolupar estudis clínics més amplis, amb diferents tipus de pell, l'escàner s'ha instal·lat a la Unitat de Melanoma de l'Hospital Clínic de Barcelona.

Resumen

El melanoma maligno es el más raro y mortal de todos los cánceres de piel, causando tres veces más muertes que el conjunto de todas las enfermedades malignas de la piel. Afortunadamente, en las etapas tempranas, es completamente curable, haciendo que el examen de piel de cuerpo completo (del inglés Total Body Skin Examination, TBSE) sea un procedimiento fundamental para muchos pacientes. Durante el TBSE, los dermatólogos buscan los signos típicos de melanoma en las lesiones pigmentadas de la piel (Pigmented Skin Lesions, PSLs), así como PSLs sometidas a los rápidos cambios característicos del cáncer. Junto a la fotografía de referencia clínica y dermatoscópica, un TBSE puede ser muy tedioso y lento, especialmente para los pacientes con gran número de lesiones. Además, establecer correspondencias correctas entre las lesiones en el cuerpo y las imágenes, o en diferentes imágenes, puede ser extremadamente difícil.

A pesar de los avances en las técnicas del escaneo corporal, las herramientas para realizar TBSEs de forma automática no han recibido la debida atención. Este hecho queda patente en nuestra revisión bibliográfica que cubre el análisis de imágenes por computador de PSLs. En esta revisión, se resumen varias estrategias para la implementación del diagnóstico asistido por ordenador, comentando sus componentes principales. En concreto, se propone una clasificación ampliada de descriptores de características PSL, asociándolos con métodos específicos para el diagnóstico del melanoma, y dividiéndolos entre imagen clínica y dermatoscópica.

Con el objetivo de la automatización de TBSEs, hemos diseñado y construido un escáner corporal de cobertura total para adquirir imágenes de la superficie de la piel utilizando luz con polarización cruzada. Equipado con 21 cámaras de alta resolución de bajo coste y una plataforma giratoria, este escáner adquiere automáticamente un conjunto de imágenes con solapamiento, que cubre el 85–90% de la superficie de la piel del paciente. La calibración extrínseca del sistema se lleva a cabo utilizando una sola imagen de cada cámara y un patrón de calibración con un código de colores diseñado específicamente. Además, hemos desarrollado un algoritmo por mapeo automático de las PSLs y la estimación de los cambios entre exploraciones. Los mapas producidos relacionan las imágenes de las lesiones individuales con su ubicación en el cuerpo del paciente, resolviendo el problema de correspondencia cuerpo-imagen e imagen-imagen de las lesiones en TBSEs. Actualmente, el escáner se limita a pacientes con escaso vello corporal. Asimismo, para un examen completo de la piel, el cuero cabelludo, las palmas de las manos, las plantas de los pies y las partes interiores de los brazos deben ser fotografiadas manualmente.

Las pruebas iniciales del escáner muestran que este puede ser utilizado satisfactoriamente para el mapeo automático y el control de cambios temporal de múltiples lesiones: los PSLs importantes para realizar el seguimiento eran mapeados sucesivamente en varias exploraciones. Por otra parte, durante la comparación de imágenes, todas las lesiones en las que se han introducido cambios artificiales, han sido correctamente identificadas como “evolucionadas”. Para desarrollar estudios clínicos más amplios con diferentes tipos de piel, el escáner se ha instalado en la Unidad de Melanoma del Hospital Clínic de Barcelona.

Abstract

Malignant melanoma is the rarest and deadliest of skin cancers causing three times more deaths than all other skin-related malignancies combined. Fortunately, in its early stages, it is completely curable, making a total body skin examination (TBSE) a fundamental procedure for many patients. During TBSE, dermatologists look for pigmented skin lesions (PSLs) exhibiting typical melanoma signs as well as PSLs undergoing the rapid changes characteristic of cancer. Accompanied by clinical and dermoscopic baseline photography, a TBSE can be very tedious and time-consuming, especially for patients with numerous lesions. In addition, establishing correct body-to-image and image-to-image lesion correspondences can be extremely difficult.

Despite the advances in body scanning techniques, automated assistance tools for TBSEs have not received due attention. This fact is emphasized in our literature review covering the area of computerized analysis of PSL images. In this review, we summarize various approaches for implementing PSL computer-aided diagnosis systems and discuss their standard workflow components. In particular, we propose an extended categorization of PSL feature descriptors, associating them with specific methods for diagnosing melanoma, and separating clinical and dermoscopic images.

Aiming at the automation of TBSEs, we have designed and built a total body scanner to acquire skin surface images using cross-polarized light. Equipped with 21 low-cost high-resolution cameras and a turntable, this scanner automatically acquires a set of overlapping images, covering 85–90% of the patient’s skin surface. A one-shot extrinsic calibration of all the cameras is carried out using a specifically designed color-coded calibration pattern. Furthermore, we have developed an algorithm for the automated mapping of PSLs and their change estimation between explorations. The maps produced relate images of individual lesions with their locations on the patient’s body, solving the body-to-image and image-to-image correspondence problem in TBSEs. Currently, the scanner is limited to patients with sparse body hair and, for a complete skin examination, the scalp, palms, soles and inner arms should be photographed manually.

The initial tests of the scanner showed that it can be successfully applied for automated mapping and temporal monitoring of multiple lesions: PSLs relevant for follow-up were repeatedly mapped in several explorations. Moreover, during the baseline image comparison, all lesions with artificially induced changes were correctly identified as “evolved”. In order to perform a wider clinical trial with a diverse skin image set, the scanner has been installed in the Melanoma Unit at the Clinic Hospital of Barcelona.

Moles are blemishes—not “beauty spots”.

Stanford Cade, “*Malignant Melanoma*” [2]

Chapter 1

Introduction

The skin is the largest organ in the human body and an excellent protection from the aggressions of the environment. It keeps us safe from infections, water loss and ultraviolet radiation (UV). However, if care is not taken, after years of faithful service, the protector itself can turn into a treacherous and merciless foe: the skin can become a source of a deadly cancer. Fortunately, this does not happen without warning: the skin usually exhibits signs which can help detect this dangerous metamorphosis. These signs may differ according to the type of malignancy and can sometimes be hard to perceive. Thus, one of the key indicators of malignant melanoma—the deadliest skin cancer—are *melanocytic nevi*, also known as moles or pigmented skin lesions (PSLs). The occurrence of nevi, their appearance and especially their evolution can indicate a developing or progressing malignancy.

To understand the nature of malignant tumors of the skin better and see how computer vision can help in their treatment, it is essential to know more about the clinical aspects of this problem. In this chapter, we offer a brief introduction into the main dermatological concepts related to melanoma of the skin.

1.1 The human skin

The skin consists of two principal layers: the epidermis and the dermis (see Fig. 1.1). The dermis is made of collagen (a type of protein) and elastic fibers. It contains two sub-layers: the papillary dermis (thin layer) and the reticular dermis (thick layer). While the former serves as a “glue” that holds the epidermis and the dermis together, the latter contains blood and lymph vessels, nerve endings, sweat glands and hair follicles. It provides energy and nutrition to the epidermis and plays an important role

1. INTRODUCTION

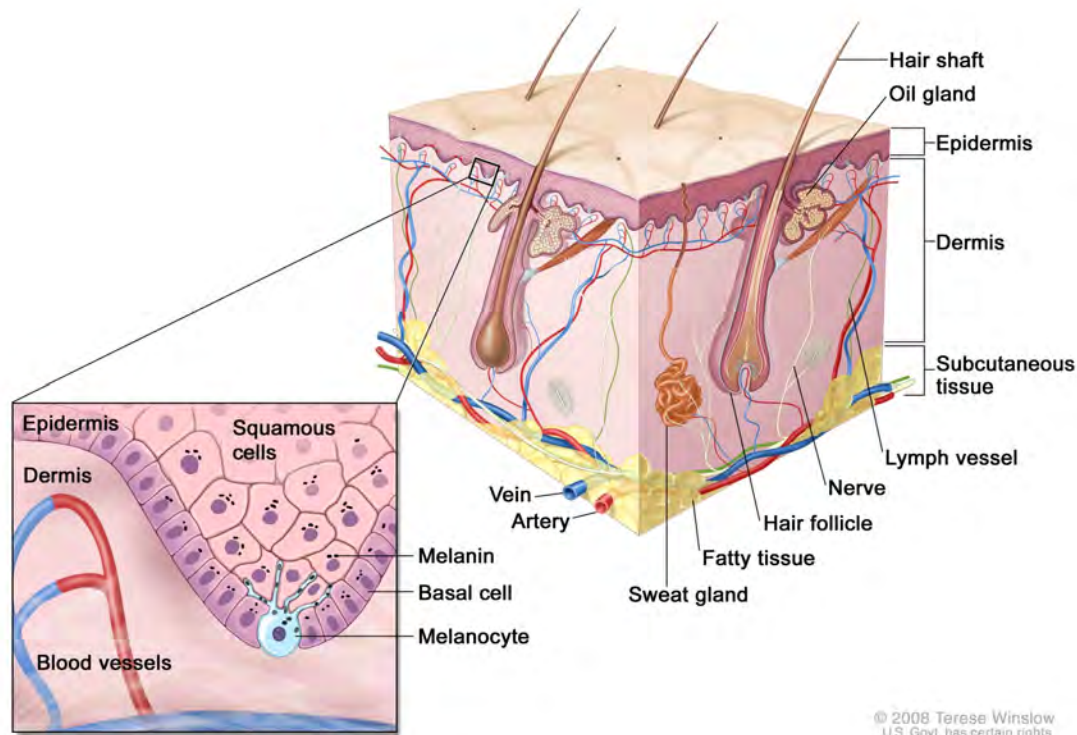


Figure 1.1: Anatomy of the skin showing the epidermis, the dermis, and subcutaneous (hypodermic) tissue. Illustration used with permission, copyright 2008 by Terese Winslow.

in thermoregulation, healing and the sense of touch [1].

The other layer, the epidermis, is a stratified squamous epithelium, a layered scale-like tissue, which fulfills the protective functions of the skin. On simple morphological grounds, the epidermis can be divided into four distinct layers from the bottom to the top: stratum basale, stratum spinosum, stratum granulosum and stratum corneum [3].

There are four types of cells in the epidermis: keratinocytes, melanocytes, Langerhans' cells and Merkel cells. Keratinocytes represent the majority (95%) of cells in the epidermis and are the driving force for continuous renewal of the skin [3]. Their abilities to divide and differentiate allow them to travel for approximately 30 days from the basal layer (stratum basale) to the horny layer (stratum corneum). During this time, the keratinocytes produced by division in the basal layer (here called *basal cells*) move through the next layers transforming their morphology and biochemistry (differentiation). As a result of this movement and transformation, the flattened cells without nuclei, filled with keratin, come to form the outermost layer of the epidermis and are called *corneocytes*. Finally, at the end of the differentiation program, the corneocytes

lose their cohesion and separate from the surface in the so-called desquamation process. This is how our skin is constantly being renewed.

Merkel cells are probably derived from keratinocytes, but they act as mechanosensory receptors in response to touch forming close connections with sensory nerve endings [3]. In turn, Langerhans' cells are dendritic cells¹ that detect foreign bodies (antigens) that have penetrated the epidermis and deliver them to the local lymph nodes.

In this project, the type of skin cells that most interest us are melanocytes. These are dendritic cells found in the basal layer of the epidermis [3]. Unlike Langerhans' cells, melanocytes produce packages of melanin pigment and use their dendrites to distribute them to surrounding keratinocytes (see Fig. 1.1). Besides protecting the subcutaneous² tissue from being damaged by UV radiation, melanin also contributes to the color of the skin (as well as that of the hair and eyes). Whenever the levels of UV radiation increase, melanocytes start producing more melanin, hence our tanning reaction to sun exposure.

Nevertheless, it is not the aesthetic results of melanocyte activity that draw our attention, but their malignant transformation potential. Although cancer can develop in almost any cell in the body, certain cells are more cancer-prone than others and the skin is no exception. Most skin cancers develop from non-pigmented basal and squamous keratinocytes. Their transformation results in basal cell carcinoma and squamous cell carcinoma, respectively [1, 4]. However, melanocytes that undergo a malignant transformation produce a less common but far more deadly and aggressive cancer: malignant melanoma. The epidemiology and treatment of this cancer, as well as some skin lesions known as its precursors, are described in the following sections.

1.2 Pigmented skin lesions

When melanocytes grow in clusters alongside normal cells, pigmented skin lesions or melanocytic nevi appear on the surface of the skin [1] and are considered to be a normal part of the skin. The most common benign PSLs are:

- *Freckle* or *ephelis* – a pale-brown, macular lesion, usually less than 3 mm in

¹Dendritic cells have branched projections, the dendrites, that give them the name and a tree-like appearance. Normally, cells of this kind are involved in processing and carrying antigen material to cells in the immune system.

²Subcutaneous – being, living, occurring, or administered under the skin (from sub- + Latin *cutis* skin). Definition by Merriam-Webster dictionary.

1. INTRODUCTION

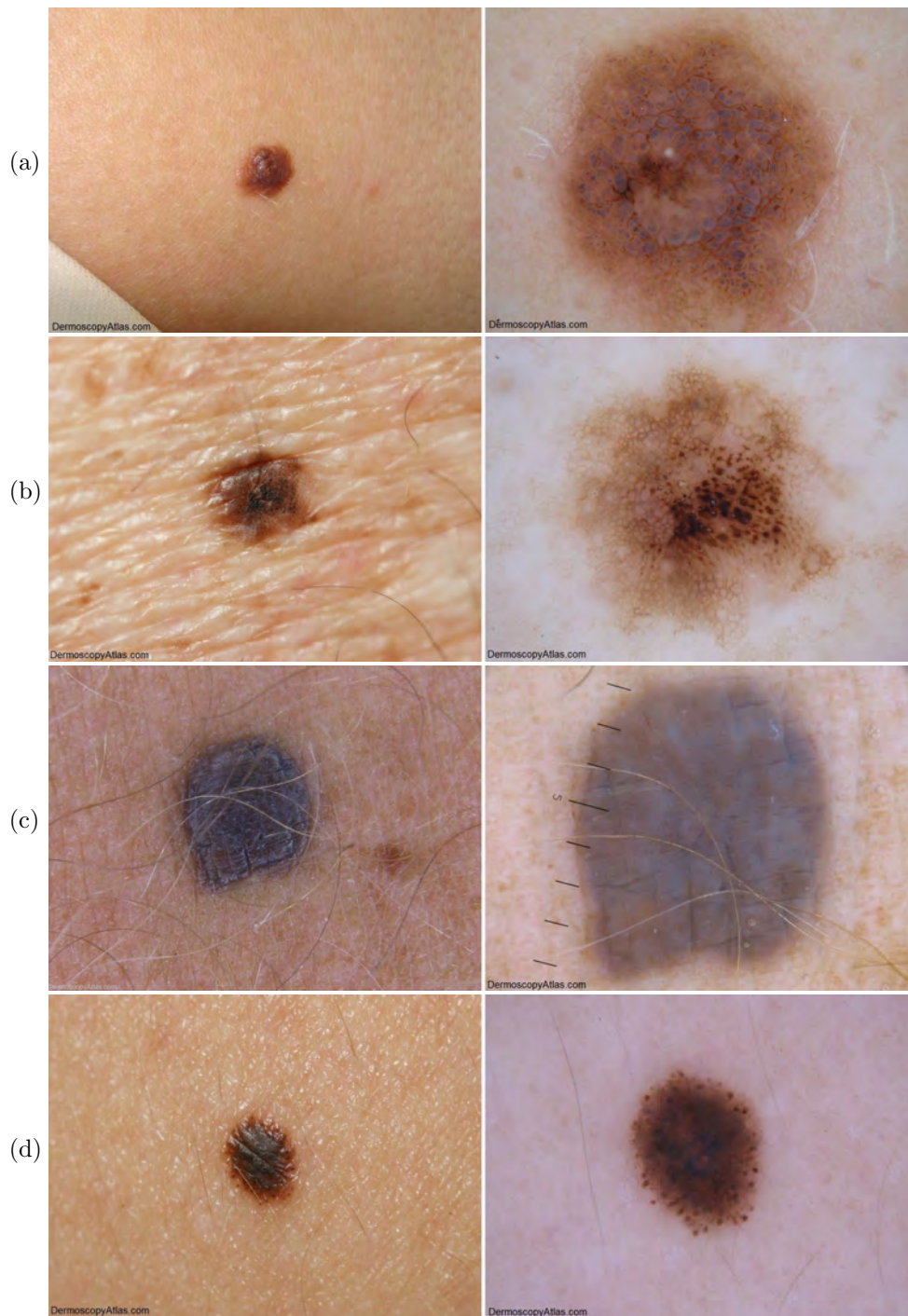


Figure 1.2: Clinical (right column) and dermoscopic (left column) images of benign pigmented skin lesions: (a) congenital nevus; (b) dysplastic nevus; (c) blue nevus; (d) Spitz nevus. Images submitted to www.dermoscopyatlas.com by Dr. Ian McColl (a), Dr. Cliff Rosendahl (b,d) and Dr. Greg Canning (c). Used with permission.

diameter with a poorly defined lateral margin, which appears and darkens on light-exposed skin sites during periods of ultraviolet exposure [5].

- *Common nevus* – a typical flat melanocytic nevus or mole.
- *Congenital nevus* (Fig. 1.2a) – a mole that appears at birth, also known as “birth-mark”.
- *Atypical or dysplastic nevus* (Fig. 1.2b) – a common nevus with inconsistent coloration, irregular or notched edges, blurry borders, scale-like texture and a diameter of over 5 mm [1]. Atypical mole syndrome, also known as “Familial Atypical Multiple Mole Melanoma” (FAMMM) or dysplastic nevus syndrome, describes individuals with large quantities of atypical nevi and possibly inherited melanomas. The relative risk of developing a melanoma in such individuals is around 6 to 10 times that of people with very few nevi [5].
- *Blue nevus* (Fig. 1.2c) – a melanocytic nevus comprised of aberrant collections of benign pigment-producing melanocytes, located in the dermis rather than at the dermoepidermal junction [5]. The optical effects of light reflecting off melanin deep in the dermis provides its blue or blue-black appearance.
- *Pigmented Spitz nevus* (Fig. 1.2d) – an uncommon benign nevus, usually seen in children, difficult to distinguish from melanoma [5].

Among these benign lesions, congenital and acquired dysplastic nevi are the known precursors to malignant melanoma [6].

1.3 Malignant melanoma

In 1821, Dr. William Norris, a general practitioner in Stourbridge, England, described the autopsy of a patient with what he thought was a fungoid disease: “...*thousands upon thousands of coal black spots, of circular shapes and various sizes, were to be seen closely dotting the shining mucous, serous, and fibrous membranes of most of the vital organs; I should think the most dazzling sight ever beheld by morbid anatomist.*” [7]. This somewhat exalted description is one of the first documented clinical observations of a metastasized malignant melanoma. Later, in 1857, Dr. Norris would state a number of principles concerning the epidemiology, pathology and treatment of the disease, which constitute the basic knowledge we have about melanoma to date [8].

1. INTRODUCTION

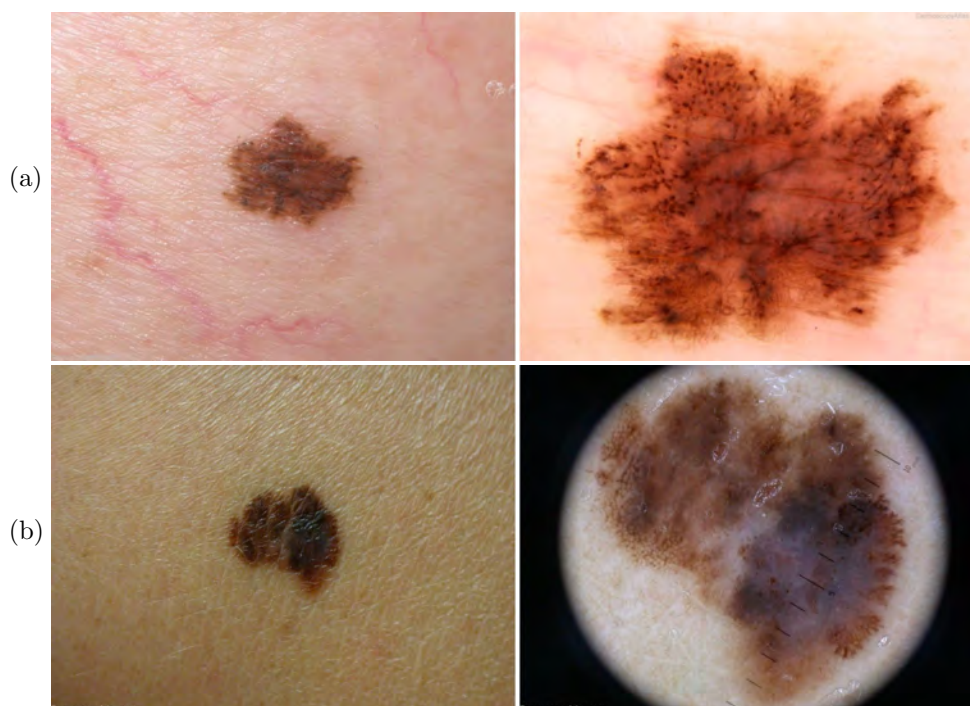


Figure 1.3: Clinical (right column) and dermoscopic (left column) images of: a) in-situ melanoma (stage 0); b) invasive melanoma (Breslow thickness 0.8 mm, stage I/II); Images submitted to www.dermoscopyatlas.com by Dr. Alan Cameron (a), Dr. Jean-Yves Gourhant (b). Used with permission.

Malignant melanoma (see Fig. 1.3) is characterized by the most rapidly increasing incidence and causes the majority (75%) of deaths related to skin cancer [4, 9]. White-skinned peoples are the most susceptible to developing this type of cutaneous malignancy and there is conclusive data showing that the dominant cause is intermittent sun exposure. Furthermore, sun-beds are also positively associated with melanoma [5].

The highest phenotypic risk factor of this cancer is the presence of increased numbers of melanocytic nevi (especially in the case of atypical mole syndrome) followed by fair skin type, high density of freckles, eye and hair color. In addition, family history is a very important factor in the risk-estimation of melanoma occurrence [5].

In its advanced stages (with signs of metastases), melanoma is incurable, and the treatment, being solely palliative, includes surgery, immunotherapy, chemotherapy, and/or radiation therapy [10]. Among other factors, the stage of melanoma is measured by its depth of invasion. In this respect, the most valuable prognostic factor is Breslow's depth or thickness [11]. This means of measuring the vertical growth of melanoma was proposed by Dr. Alexander Breslow in 1970. In general, the deeper the

measurement (depth of invasion), the higher the chances for metastasis and the worse the prognosis.

Fortunately, early-stage melanoma (see Fig.1.3a) is highly curable [9]. In fact, the results of Breslow’s experiments showed that lesions less than 0.76 mm thick do not produce metastases [11]. This highlights the critical importance of timely diagnosis and treatment of melanoma for patient survival [12].

Friedman et al. [6], the authors of the ABCD criteria for early melanoma detection, emphasized in their paper that “*by performing periodic complete cutaneous examinations, by teaching patients the technique of routine self-examination of the skin, and by proper use of diagnostic aids (particularly skin biopsy), physicians can improve the chances for early diagnosis and prompt eradication of malignant melanoma*”. Thus, the importance of regular screening procedures for patients with a high risk of developing melanoma is beyond doubt.

1.4 Melanoma screening

The prevailing strategy for skin screening procedures is total body skin examination (TBSE) [13]. TBSE consists of meticulously analyzing every pigmented lesion on the patient’s body and determining those which exhibit signs of a developing melanoma. This can be a very tedious and time-consuming process (up to several hours), especially for patients with atypical mole syndrome. To facilitate the recognition of melanoma during the examination, dermatologists apply specific diagnostic rules and criteria as well as using various imaging techniques. Furthermore, the application of artificial intelligence to melanoma diagnosis allows the creation of systems for computer-aided diagnosis.

1.4.1 Imaging techniques

Dermatologists use a number of non-invasive imaging techniques to help them diagnose skin lesions. Besides traditional photography, which has been used for a long time in dermatology [14], there are a number of imaging modalities that allow the visualization of different skin lesion structures. These modalities include dermoscopy, confocal laser scanning microscopy, optical coherence tomography, high frequency ultrasound, positron emission tomography, magnetic resonance imaging and various spectroscopic imaging techniques, among others. For more information on all the imaging modalities for melanoma diagnosis, the interested reader can refer to the available reviews: [12, 15–22].

1. INTRODUCTION

We have focused our research on the two imaging techniques most commonly used in dermatological practice: clinical photography and dermoscopy.

1.4.1.1 Clinical photography

Dermatological photographs (digital or not) showing a single or multiple skin lesions on the surface of the skin are referred to as *clinical* or *macroscopic* images. These images reproduce what a clinician sees with the naked eye [23]. The left column in Figs. 1.2 and 1.3 demonstrate such macroscopic images. Clinical imaging is used to document PSLs, mapping their location on the human body and tracking their changes over time as sensitive signs of early melanoma [24].

Apart from taking photographs of single lesions or separate groups of lesions, physicians may recur to total body photography, also known as total body skin imaging (TBSI) and whole body photography (WBP) [13]. This is a method of photographic documentation of a person's entire cutaneous surface through a series of body sector images.

During a TBSI procedure the patient should assume a set of standardized body poses (see Fig. 1.4). The lighting conditions must be appropriate to allow the best contrast between PSLs and the skin. In addition, the setup of a TBSI system should be easily reproducible for successive acquisitions. The body parts that must be photographed are: the face, the neck, the area behind the ears, the scalp (in bald individuals), the anterior and posterior torso, and the extremities (including palms and soles).

Advantages of total body skin imaging include [24]:

- potential aid for change identification in lesions not suspected at the time of initial evaluation. The study conducted by Feit et al. [25] showed that TBSI helped detect new and subtly changing melanomas which did not satisfy classical clinical features of melanoma;
- efficient evaluation of large numbers of lesions;
- lack of reliance on expert interpretation of dermoscopic images.

Ideally, whole body photography should be systematically combined with other techniques, including dermoscopy, for improved diagnostic efficiency and accuracy [24]. The study conducted in [26] showed that monitoring by total body photography and sequential dermoscopy detects thinner melanomas.

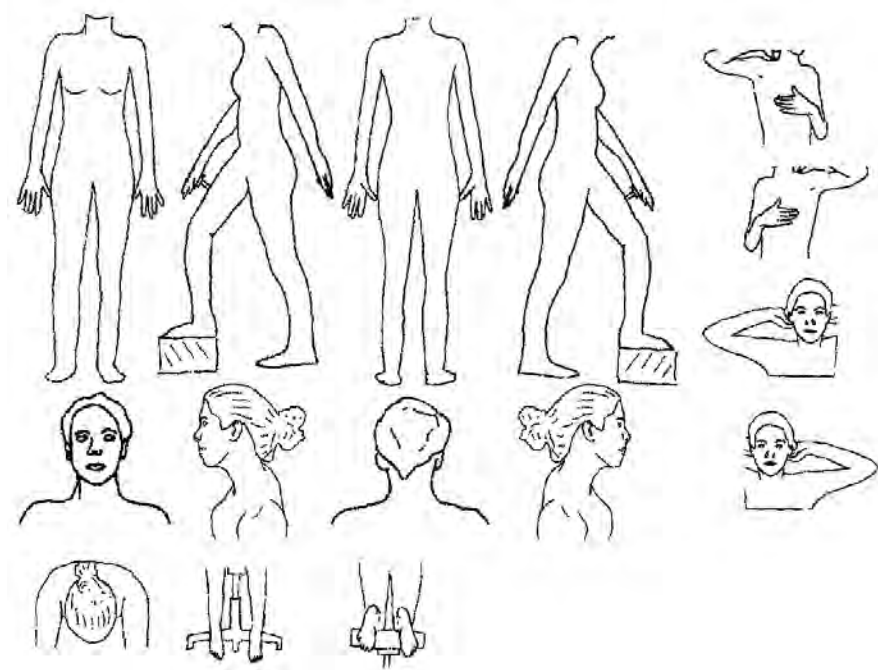


Figure 1.4: Standardized poses for TBSI proposed by Halpern in [13]

The survey conducted in [27] showed that although there was an increase in the use of TBSI during the last decade, it was only moderate when compared to that of dermoscopy. Dermatologists specified that using TBSI reduces patient anxiety, helps early melanoma detection and leads to fewer biopsies. However, logistical and financial constraints were named as obstacles to its wide application in clinical practice [27].

1.4.1.2 Dermoscopy

Originally, the term “dermoscopy” referred to a non-invasive imaging technique for PSLs that allows visualization of their subsurface structures by means of a hand-held incident light magnifying device (microscope) and an immersion fluid (with a refracting index that makes the horny layer of the skin more transparent to light and eliminates reflections) [28–30]. Contact between the skin and the glass plate of the microscope is essential in this case. This technique is also known as dermatoscopy, in vivo cutaneous surface microscopy, magnified oil immersion diascopy and most commonly, epiluminis- cence microscopy (ELM). Sample images are shown in the right column of Figs. 1.2 and 1.3. As can be seen in the images, dermoscopy allows visualization of a variety of different structures such as globules, streaks or pigment networks. It also greatly improves color contrast within the borders of the lesion.

1. INTRODUCTION



(a) Dermlite® II Fluid



(b) Dermlite® II Pro HR

Figure 1.5: Samples of commercially available dermoscopes produced by Dermlite®: (a) immersion fluid dermoscope using non-polarized light; (b) cross-polarized light dermoscope. Both devices can be attached to a digital camera.

A significant modification in how dermoscopy was conducted came with the substitution of non-polarized light for cross-polarized light. In devices of this type, the use of immersion fluid or direct skin contact are not needed, and the images acquired by polarized and non-polarized light dermoscopes are almost identical. However, the “almost” part is responsible for the subtle differences in lesion visualization, such as melanin brightness or color appearance [30, 31]. In order to differentiate between these two types of dermoscopy, polarized light dermoscopy is sometimes referred to as “videomicroscopy” [30, 32] or XLM (for cross-polarised epiluminescence) [33]. Nevertheless, in general, the term “dermoscope” refers to devices using both types of light sources. Fig. 1.5 shows modern dermoscopes based on non-polarized and cross-polarized light technique.

Another imaging modality related to dermoscopy is the transillumination technique. In dermatology, this is a technique of visualizing a lesion by directing light onto the skin in such a way that the back-scattered light illuminates the lesion from within. The device used for this is patented and called Nevoscope [34–36], but has not been widely adopted in clinical practice.

1.4.1.3 Baseline images

Baseline cutaneous photography [37] is an important concept in dermatology. The term “baseline” refers to the date of the patient’s previous cutaneous image, i.e. the newly acquired images are compared to the baseline image during a follow-up examination

so that the evolution and/or appearance of new lesions can be detected. Baseline images can be either clinical or dermoscopic, and do not in fact have to be limited to photography: images acquired by any other means may have a baseline reference.

1.4.2 Melanoma diagnosis methods

During screening procedures, clinicians and dermatologists use certain criteria to determine whether a given lesion is a melanoma. Performing the procedure without a dermoscope or with the help of clinical baseline images, the ABCDE criteria [38] and the Glasgow 7-point checklist [39] can be used.

The latter contains 7 criteria: 3 major (changes in size, shape and color) and 4 minor (diameter ≥ 7 mm, inflammation, crusting or bleeding and sensory change), but has not been widely adopted [38]. The so-called ABCD criteria, proposed in 1985 by Friedman *et al.* [6], have been extensively applied in clinical practice, mostly due to simplicity of use [17, 38]. This mnemonic defines the diagnosis of a lesion based on its asymmetry (A), irregularity of the border (B), color variegation (C) and the diameter (D), that is generally greater than 6 mm for suspicious lesions. Later, in 2004, Abbasi *et al.* [38] proposed expanding the ABCD criteria to ABCDE by incorporating the E for “evolving” of the lesion over time, which reflects the results of the studies similar to the one performed in [40, 41], and includes changes in features such as size, shape, surface texture, color, etc.

In order to differentiate between melanoma and benign melanocytic tumors using dermoscopic images, new diagnostic methods were created and existing clinical criteria were adapted. These methods are summarized in Table 1.1. Note the identical names of the criteria for different imaging modalities: ABCD rule of dermoscopy and 7-point checklist [42]. It is important to clearly differentiate between them to avoid any confusion since they attempt to provide lesion diagnosis based on different types of information.

To this end, Table 1.2 shows differences between methods of melanoma diagnosis which share practically identical names but refer to different image modalities. As the table illustrates, the modified meaning of the letters in the ABCD rule of dermoscopy is: B for border sharpness and D for Differential structures. Importantly, besides these changes, all the criteria in this method have a fairly different interpretation from their clinical counterparts. Moreover, the “items” on the 7-point checklist differ completely from those on the Glasgow 7-point checklist. Although the first three points on both lists are awarded a higher score, they are all adapted specifically according to the

1. INTRODUCTION

Table 1.1: Methods for the diagnosis of melanoma clinically and by dermoscopy.

Clinical image / Naked-eye inspection	Dermoscopic image*
ABCD criteria	ABCD rule [†]
ABCDE criteria	ABCD-E criteria
—	ABC-point list [A(A)BCDE]
Glasgow 7-point checklist	7-point checklist [†]
—	7 features for melanoma
—	3-point checklist
—	Pattern analysis [†]
—	Menzies' method [†]

* The list of diagnostic methods by dermoscopy was taken from [42]. References to respective papers can be found therein.

[†] These methods were evaluated in the study during the virtual consensus net meeting on dermoscopy (CNMD) [43].

structures visible in the dermoscopic images (see Table 1.2). More information on the performance comparison of the ABCD rule of dermoscopy and the 7-point checklist and implications for computer-aided diagnosis can be found in [44].

Nevertheless, it is important to note that these methods for diagnosing melanoma from both clinical and dermoscopic images are used to determine only whether suspicious lesions *could be* melanoma. The actual diagnosis is carried out by a pathologist after such suspicious lesions are excised (biopsied). A diagram of the lifecycle of a suspicious lesion can be found in [45].

1.4.3 Automated diagnosis of melanoma

Systems for the automated diagnosis of melanoma, computer-aided diagnosis (CAD) or clinical diagnosis support (CDS) systems, are intended to reproduce the decision of the dermatologist when observing images of PSLs. They were primarily developed to respond to a desired increase in specificity and sensitivity in melanoma recognition when compared to that of dermatologists, and a reduction in morbidity related to lesion excisions. Although such systems are being developed for various imaging modalities (see [46, 47]), in our research we considered automated melanoma recognition systems based only on clinical photography, dermoscopy and spectrophotometry.

Most of these automated systems are based on the aforementioned melanoma diagnostic methods. In general, image processing techniques are used to locate and delineate the lesion(s), extract image parameters describing the dermatological features of the lesion(s), and, based on these parameters, perform the diagnosis. The generic steps of

Table 1.2: Confusing acronyms that have different meanings in clinical (CI) vs. dermoscopic images (DI). Variation of criteria names is highlighted in bold. Note that even with the identical names of the criteria their meaning is different for CI and DI.

ABCD [†] criteria (CI)	ABCD rule of dermoscopy (DI)
(A) Asymmetry: overall shape of the lesion	(A) Asymmetry: contour, colors and structures
(B) Border irregularity: ill-defined and irregular borders	(B) Border sharpness : abrupt cut-off of pigment pattern
(C) Color variegation: colors are non-uniform	(C) Color variegation: presence of 6 defined colors
(D) Diameter: ≥ 6 mm	(D) Differential structures : presence of 5 differential structures
Glasgow 7-point checklist (CI)	7-point checklist (DI)
(1) Changes in size	(1) Atypical pigment network
(2) Changes in shape	(2) Blue-whitish veil
(3) Changes in color	(3) Atypical vascular pattern
(4) Diameter ≥ 7 mm	(4) Irregular streaks
(5) Inflammation	(5) Irregular dots/globules
(6) Crusting or bleeding	(6) Irregular blotches
(7) Sensory change	(7) Regression structures

[†] ABCDE (CI) and ABCD-E (DI) exploit the corresponding ABCD criteria and include “evolving” and “enlargement and other morphological changes”, respectively.

a CAD system for melanoma identification are highlighted in Fig. 2.1.

1.4.3.1 Clinical impact

Studies have shown that the performance of automated systems for melanoma diagnosis is sufficient under experimental conditions [48]. However, the practical value of automated dermoscopic image analysis systems is still unclear. Although most patients would accept using computerized analysis for melanoma screening, currently it cannot be recommended as a sole determinant of the malignancy of a lesion due to its tendency to over-diagnose benign melanocytic and non-melanocytic skin lesions [48]. In addition, according to Day and Barbour [45], there are two main shortcomings in the general approach to developing a CAD system for melanoma identification:

1. A CAD system is expected to reproduce the decision of pathologists (a binary result like “melanoma/non-melanoma lesion”) with only the input used by dermatologists: clinical or dermoscopic images;
2. Histopathological data are not available for all lesions, only for those considered suspicious by dermatologists.

1. INTRODUCTION

The former is a methodological problem. It reflects the fact that a CAD system is intended to diagnose a lesion without sufficient information for diagnosis or any interaction with the dermatologist. This was highlighted by Dreiseitl *et al.* in their study into the acceptance of CDS systems by dermatologists [49], i.e. that the currently available CDS systems are designed to work “in parallel with and not in support of” physicians, and because of this, only a few systems are found in routine clinical use. Thus, an ideal CAD or CDS system for melanoma identification should reproduce the decision of dermatologists (i.e. define the level of “suspiciousness” of a lesion) [45] and provide dermatologists with comprehensive information regarding the grounds for this decision [49].

1.5 Research motivation

Over the last 30 years, more people have had skin cancer than all other cancers combined [50]. Accounting for less than 5% of these cases, melanoma causes the majority of related deaths [10]. It is essential to take measures preventing the development of this malignancy, but early detection of melanoma is vital.

Total body skin examination plays a primordial role in monitoring and detecting a developing melanoma. However, non-automated screening of patients with large numbers of lesions (e.g., more than 50) can be very tedious and time-consuming. Expert physicians have to examine every suspicious lesion for the typical signs of melanoma, and use baseline images to detect those that had evolved. Thus, besides the difficulty of identifying suspicious lesions, this procedure can also suffer from issues related to establishing correct body-to-image or image-to-image lesion correspondences. For example, Fig. 1.6 shows two dermoscopic images of the same mole acquired with a difference of one year. The report states that during this period there were no significant changes in the lesion’s structure. But because of the difference in the orientation of the dermoscope at the moment of image acquisition, the recognition of the PSL is not easy.

Moreover, without proper baseline photographs, it is difficult to determine if a PSL which exhibits ambiguous dermoscopic signs is:

- (a) an old lesion that has evolved since the last examination;
- (b) an old lesion that has NOT changed, but was not noticed previously;
- (c) a completely new lesion;

Nevertheless, the automation of TBSI procedures, which could eliminate all the described issues, has not received much attention. Only less than 4% of the publications

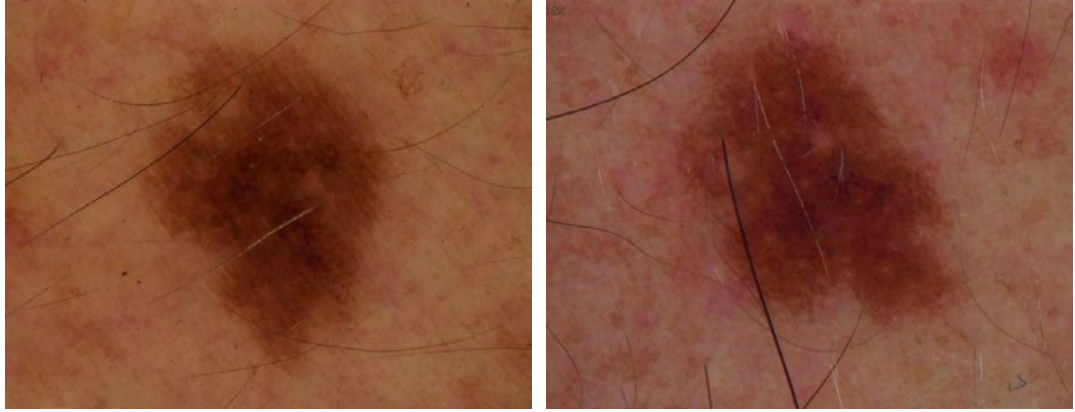


Figure 1.6: Two dermoscopy images of a PSL acquired with a difference of one year using the same imaging device (MoleMax[™]). No morphological change was reported. Images courtesy of Dr. J. Malvey.

reviewed in this work (see Chapter 2) addressed the computerized analysis of multiple skin lesions. It is possible that such a low percentage may be the consequence of the specific nature of the problem. TBSI requires finding a trade-off between image resolution and body coverage per image, where the resolution is governed by the needs of change detection.

In spite of the fact that this trade-off is relatively easy to achieve with modern cameras, and despite the development of total body photographic systems (e.g. [51,52]), their automation stays mostly at the level of accessing and storing images. This lack of attention and absence of research on completely automated systems for TBSI at present seem unjustified considering the importance of this process in detecting early-stage melanoma.

Therefore, this work attempts to fill the gap in research on computerized analysis of multiple pigmented skin lesions, and open new perspectives for its application in dermatological clinical practice. With the objective of facilitating the TBSE procedures for patients and physicians, we designed and built a total body scanner allowing for acquisition of skin surface images using cross-polarized light. It is capable of capturing a set of 504 photographic images under controlled lighting conditions covering approximately 85-90% of the body's surface. For this scanner, we developed a framework of algorithms for automated detection of pigmented skin lesions, their mapping in three-dimensional space and consequent change detection between screening sessions. Applied to the acquired images, these algorithms produce a precise map which links images of individual PSLs with their real locations on the patient's body, thus, solving the body-to-image and image-to-image correspondence problems during TBSE.

1.6 Thesis outline

This thesis describes the research work that resulted in the development and validation of the algorithms for change detection in multiple nevi using the total body skin scanner. Prior to designing the algorithms, we exhaustively studied the literature that exists in the field of computerized analysis of pigmented skin lesions. **Chapter 2** reports the findings of this literature review.

Chapter 3 contains a description of the hardware design of the total body skin scanner including the screening (image acquisition) and the extrinsic calibration (pattern design and related image processing methodology) procedures.

Chapter 4 presents the software developed for PSL mapping and change detection. The description is divided into two sections distinguishing the pipelines for intra- and inter-exploration (examination) image processing.

Chapter 5 reports the results of testing all the algorithms on real datasets acquired in laboratory and clinical settings, while **Chapter 6** concludes this thesis.

Additional information on the techniques used in the implementation of the PSL mapping and change detection pipelines can be found in the **Appendix**.

The measures science gives us in abundance are to be used not timidly but bravely to combat this pigmented foe, who claims the fairest and the youngest and the old with equal impartiality.

Stanford Cade, “*Malignant Melanoma*” [2]

Chapter 2

Computerized analysis of PSLs: a literature review

In 1992, Stoecker and Moss summarized in their editorial the potential benefits of applying digital imaging to dermatology [53]. These benefits were viewed according to the technology available at the time, including of course the capabilities of computer vision techniques, and the results of the earlier research in the area (e.g. [34, 54]). Among others, these included objective non-invasive documentation of skin lesions, systems for their diagnostic assistance by malignancy scoring, identifying changes, and teleradiagnosis. This was the first time a journal had dedicated an entire special issue to methods for computerized analysis of images in dermatology specifically applied to skin cancer. Almost two decades later, the 2011 publication of the second special issue, *Advances in skin cancer image analysis* [55], allowed us to clearly see the changes that have taken place in this field. More importantly, we are able to see how close we are to making certain benefits real rather than potential, and which ones have turned out to be even more beneficial than initially predicted.

Such an overview can also reveal various problems in the way of achieving one of the main goals—the creation of reliable automated means of assistance in melanoma diagnosis. Apart from the known methodological [45] and the dataset [56] problems, there exists what we call a bibliography problem. While the research history of computerized analysis of PSLs is vast and spread across hundreds of publications, comprehensive literature reviews are scarce. Yet without adequate material facilitating the assessment of previous work, especially for those new to the field, researchers have to repeatedly carry out the same work of article look-up, leaving less time for their analysis.

For this reason, we have attempted to create an extensive literature review estab-

2. COMPUTERIZED ANALYSIS OF PSLs: A LITERATURE REVIEW

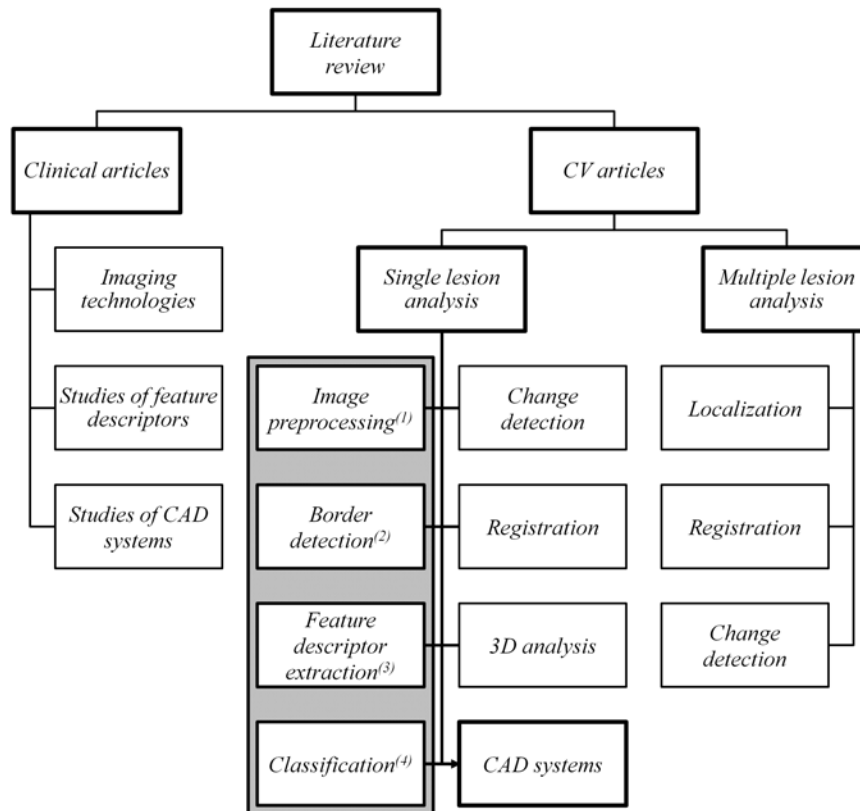


Figure 2.1: Literature categorization tree. The rectangles in the highlighted area correspond to generic steps of the CAD systems for melanoma identification.

lishing both a broad and a more detailed perspective on PSL computerized analysis aimed at melanoma detection. We classified the available literature into several categories based on the nature of the analyzed information. In particular, it was subdivided according to the following two criteria (see Fig. 2.1):

1. The nature of the publication: clinical or computer vision articles.

Clinical articles (published in medical research journals) contain relevant information about dermatological disorders, report results from clinical studies on available CAD systems and algorithms, or review imaging technologies. Clinical articles usually contain from no to a medium amount of technical detail on the studied algorithms, and also present statistical data. The target audience is physicians.

Computer vision articles (published in computer vision or technical journals and in conference proceedings) describe and review research results regarding the de-

velopment of dermatological CAD systems. They contain a fair amount of technical detail on the algorithms. The target audience is computer vision researchers.

2. Number of analyzed lesions: single or multiple lesion analysis. This criterion created a highly uneven distribution of computer vision papers, since less than 4% of all the reviewed papers are dedicated to multiple lesion analysis. This is an important finding which clearly shows the main focus area in the field: the analysis of dermoscopic/clinical images of single PSLs.

The detailed subdivision of the literature was based on the typical workflow steps of CAD systems for melanoma recognition from single lesion images. Fig. 2.1 shows these steps in the highlighted area, numbered according to their position in the workflow. Other boxes in the figure represent literature/steps which usually do not form part of CAD systems, although this is not always the case. Some systems [57, 58] actually conduct lesion registration and change detection as a part of their workflow or as an additional function. The category “CAD systems” contains articles describing architecture of automated melanoma diagnosis systems including all steps of the workflow, whereas articles from other categories concentrate only on specific steps, but in more detail. Note that the workflow is defined only for the systems used in *single lesion analysis*.

The literature referenced in this work (with publication dates from 1984 to 2013) is directly related to the computerized analysis of PSLs, and its distribution shows where efforts have been concentrated in recent decades. Counting more than 400 publications in total (this only includes papers found relevant for our review, not all of which are referenced herein), the distribution of clinical to computer vision articles is approximately 24% to 76%, respectively. The reviewed clinical articles concern only single PSL analysis, with the majority dedicated to CAD system studies (over 60%). In turn, publications on “Multiple lesion analysis” are found only among the computer vision articles. In the latter category, most papers on “Single lesion analysis” concentrate on “Border detection” (28%) and “Feature extraction” (29%), 19% on “CAD systems” and 16% on “Classification” categories. The rest of the papers were attributed to other categories.

2.1 Single lesion analysis

This section reviews computerized analysis methods applied to images depicting a single PSL. Each subsection below represents a category of the literature classification and

2. COMPUTERIZED ANALYSIS OF PSLs: A LITERATURE REVIEW

Table 2.1: PSL image preprocessing operations

Operation	References
Artifact rejection	
Hair	[59–77]
Air bubbles	[60, 68, 78]
Specular reflections	[68, 79]
Ruler markings	[64, 68, 78]
Interlaced video misalignment	[79]
Various artifacts:	
Median filter	[57, 80–85]
Wiener filter	[86]
Image enhancement	
Color correction/calibration	[87–91]
Illumination correction	[69, 78, 92–95]
Contrast enhancement	[96–99]
Edge enhancement by KLT	[80, 82]

provides references to relevant publications and reviews.

2.1.1 Image preprocessing

After a clinical or dermoscopic image is acquired, it may not have the optimal quality for subsequent analysis. The preprocessing step serves to compensate for the imperfections of image acquisition and eliminate artifacts, such as hairs or ruler markings. Good performance of the methods at this stage not only ensures correct behavior of the algorithms in the following stages of analysis, but also relaxes the constraints on the image acquisition process.

Table 2.1 contains references to studies which have implemented the most common preprocessing operations on PSL images. These can be roughly subdivided into artifact rejection and image enhancement operations. Table 2.1 does not include color transformation techniques, which are commonly used in dermatological image processing. Celebi *et al.* in [56] briefly summarize these techniques together with methods of artifact removal and contrast enhancement.

Among the most common and necessary artifact rejection operations is hair removal. The main reason for developing such algorithms is the fact that hair present on the skin may occlude parts of the lesion, making correct segmentation and texture analysis impossible. To avoid this problem and the need to shave the lesion area at the time of acquisition, hairs are removed by software.

A typical hair-removal algorithm comprises two steps: hair detection and hair repair (restoration or “inpainting”). The latter consists in filling the image space occupied by hair with proper intensity/color values. Its output greatly affects the quality of the lesion’s border and texture. And since this information is indispensable for correct diagnosis from dermoscopic images, it is important to ensure the best hair repair output.

The first widely adopted method of hair removal in dermoscopic images, DullRazor[®], was proposed in 1997 [59]. In 2011, Kiani and Sharafat [71] improved it to remove light-colored hairs. While some of the approaches use generalized methods of supervised learning to detect and remove hairs [61, 72], others use more specific algorithms. Recently, Abbas *et al.* [73] reviewed the existing methods and proposed a broad classification into three groups based on their hair repair algorithm type: linear interpolation techniques [59, 60, 63, 70], inpainting by nonlinear partial differential equations (PDE) based diffusion algorithms [62, 66, 67, 78] and exemplar-based methods [64, 65, 68]. Their own hair repair method [73] used fast marching image inpainting, and was later improved in [100].

Median filtering is widely used to suppress spurious noise, such as small pores on the skin, shines and reflections [57, 81, 85], thin hairs or small air bubbles (minimizing or completely removing them [80, 84]). Other artifacts in dermatological images also include ruler markings, specular reflections and even video field misalignment caused by interlaced cameras (see Table 2.1).

Of image enhancement operations, perhaps the most important one, from the point of view of lesion diagnosis, is color correction or calibration. This operation consists in recovering real colors of a photographed lesion, thus allowing for a more reliable use of color information in manual and automatic diagnosis. Recent studies place special emphasis on color correction in images with a joint photographic experts group (JPEG) format (as opposed to raw image files) obtained using low-cost digital cameras [90, 91]. Other operations in this category are illumination correction, and contrast and edge enhancement. In order to perform the latter operation, Karhunen-Loève transform (KLT), also known as Hotelling Transform or principal component analysis (PCA), is widely used.

2.1.2 Lesion border detection

An accurately detected border of a skin lesion is crucial for its automated diagnosis. Therefore, border detection (segmentation) is one of the most active areas in the computerized analysis of PSLs. A lot of effort has been made to improve lesion segmentation

2. COMPUTERIZED ANALYSIS OF PSLs: A LITERATURE REVIEW

algorithms and come up with adequate measures of their performance.

The problem of lesion border detection is not as trivial as it may seem. Firstly, since dermatologists do not usually delineate lesion borders for diagnosis [45] there exists a ground truth problem. Segmentation algorithms are intended to reproduce the way human observers, who are generally not very good at discriminating between subtle variations in contrast or blur [101], perceive the boundaries of a lesion. But because of high inter- and intra-observer variability in PSL boundary perception among dermatologists [101–103] the ground truth often lacks definiteness and has to be obtained as a fusion of several manual segmentations. Secondly, the morphological structure of a lesion itself (depigmentation, low lesion-to-skin gradient, multiple lesion regions, etc.) can act as a confusion factor for both manual and automatic segmentation. These problems have led to the development of a wide variety of PSL segmentation methods which span all categories of segmentation algorithms [56].

These algorithms can be classified in many ways regarding, for instance, their level of automation (automatic vs. semi-automatic), their number of parameters or the required methods of postprocessing [56]. However, the purpose of this subsection is not to review all these methods, but to provide information regarding available reviews and comparisons and to emphasize the role of certain approaches to the problem.

2.1.2.1 PSL border detection methodology

Morphological differences in the appearance of PSLs in clinical and dermoscopic images directly influence the choice of method for border detection. Moreover, various conditions, such as type of lesion, location, color conditions or angle of view, add to the diverse difficulties in segmenting using the same imaging modality [56, 60, 104]. Therefore, the available methods aim to provide robustness in difficult segmentation cases adapting to specific conditions of the image type (e.g. [105]).

Clinical images One of the earliest works on skin lesion border detection was published in 1989 and used the concept of *spherical coordinates* for color space representation [106]. Since then, it has been widely adopted in the literature for lesion feature extraction and color segmentation. Comparisons of different color spaces applied to segmentation were carried out in [107, 108] and in [96].

In 1990, Golston *et al.* estimated the role of several determinants of the lesion border, namely color, luminance, texture and 3D information [109]. While 3D information was mostly absent, color and luminance appeared to be the major factors for most of the images. Thus, the authors discussed an overall algorithm that would take into account

several border determinants based on their level of confidence, and proposed a radial search method based on luminance information. Similarly, in support of multifactorial descriptiveness of the lesion border, Dhawan and Sicsu proposed combining grey-level intensity and textural information [110]. Further works concentrated on improving existing techniques [111] and applying a multitude of different approaches, including edge detection [104, 112], active contours [62], PDE [62, 67], gradient vector flow [113] and many others.

Dermoscopic images Following the trend initiated by clinical images, multiple segmentation algorithms and their combinations were investigated for dermoscopic images. Fleming *et al.* [60] discussed several implementations of segmentation algorithms. Though agreeing that one of the most efficient border determinants is color, they proposed an approach incorporating spatial and chromatic information to produce better segmentations. After implementing and testing various algorithms, the final method combined principal component transform, stabilized inverse diffusion equations and thresholding in the green channel.

Later thresholding approaches became more sophisticated in comparison with the relatively simple methods of single color channel thresholding proposed earlier [60, 114]. Iterative thresholding [115], type-2 fuzzy logic based thresholding [116], fusion of thresholds [117–119], hybrid [120], local entropy [121] and color histogram thresholding [122] have been proposed recently. Many other approaches have been applied to the segmentation of dermoscopic images. Among them are various algorithms using and combining different categories of techniques, such as clustering [123–126], soft computing (neural networks [115, 127, 128] and evolution strategy [129]), supervised learning [61, 72, 130, 131], active contours [33, 132], and dynamic programming [74], to name but a few.

Without doubt, all these (and other approaches not mentioned here) have their advantages and drawbacks. However, it should be noted that most of the algorithms are tested on various fairly small datasets, not many of which include special “difficult” cases. Consequently, the performance assessment for these algorithms is not trivial, especially based only on the results reported by the authors. In this respect, the comparison studies allow these algorithms to be assessed in a more uniform framework, clearly defining their strengths and weaknesses.

2. COMPUTERIZED ANALYSIS OF PSLs: A LITERATURE REVIEW

2.1.2.2 Comparison of segmentation algorithms

In 1996, Hance *et al.* published a comparison of 6 methods of PSL segmentation [133]. It included techniques such as fuzzy c-means, center split, multiresolution, split and merge, PCT/median cut and adaptive thresholding. The latter two methods proved to be more robust than the others based on the exclusive-OR evaluation metric proposed therein. Melli *et al.* [134] compared the performance of color clustering techniques with the mean-shift algorithm obtaining the best score. In another comparison of segmentation methods implemented by Silveira *et al.* [135], an adaptive snake algorithm was the best among gradient vector flow (GVF), level set, adaptive thresholding, expectation-maximization level set and fuzzy-based split-and-merge algorithm (which had the best performance among fully automated methods).

Statistical region merging (SRM) was introduced and compared in [136, 137] to optimized histogram thresholding, orientation-sensitive fuzzy c-means [123], gradient vector flow snakes [138], dermatologist-like tumour extraction algorithm (DTEA) [103] and JSEG algorithm [139]. Overall results from this comparison on 90 dermoscopic images determined the superiority of the SRM, followed by DTEA and JSEG. However, Zhou *et al.* [140] reported that on a considerably larger dataset of 2300 dermoscopic images SRM, JSEG and a clustering-based method incorporating a dermoscopic spatial prior [105] were outperformed by a spatially-smoothed exemplar-based classifier algorithm. According to the latest comparison to date (end of 2013) [141], GVF snakes outperformed automatic thresholding, k-means, mean-shift, region growing, and watershed algorithms.

However, these studies still do not provide unified results for all the tested algorithms. Firstly, because of the differences in the *datasets* employed including different ground-truth definitions, and secondly, due to different *evaluation metrics*. In fact, the two highlighted factors are essentially the basis for performance comparison between segmentation algorithms.

Almost all standard metrics for evaluation of PSL segmentation algorithms, such as sensitivity, specificity, precision, border error and others [56, 133, 142, 143], are based on the concepts of true (false) positives (negatives). Recently, Garnavi *et al.* [143] proposed a weighted performance index which uses specific weighting for these metrics and unites them under one value for easier comparison with other methods. Alternative metrics used by different authors include pixel misclassification probability [102], Ham-moude and Hausdorff distances (not the most relevant metrics from a clinical point of view) [135] and normalized probabilistic rand index [142]. The reviews of these metrics

can be found in [56, 142, 143]. In addition to this, [56] provides an excellent summary of 18 algorithms with their characteristics and reported evaluation.

Equally important in this work [56] is the outline of requirements for a systematic PSL border detection study, which, if a public dermoscopy dataset is provided, can favor a rapid development of more reliable automated diagnosis systems. Therefore, such a dataset, with a standardized ground-truth definition, will allow researchers to immediately report performance results for their methods, and thereby boost overall progress in the field. The first public database containing 200 dermoscopy images was published on-line in 2013 by Mendonça *et al.* [144]. It contains medically annotated (clinical and histological diagnosis, medical segmentation and the assessment of several dermoscopic criteria) images of 80 common nevi, 80 atypical nevi, and 40 melanomas.

2.1.3 Feature extraction

To correctly diagnose a PSL (or classify it as “suspicious”), clinicians rely on the so-called features of the lesion. These features depend on the method of diagnosis in use. For example, asymmetry of a lesion is a feature of the ABCD-rule, and pigmented network is a feature in pattern analysis (see Section 1.4.2 for details). In computerized PSL analysis, in order to classify a lesion most automated systems aim to extract such features from the images and represent them in a way that can be understood by a computer, i.e. using image processing features. In this review, for clarity we use the term “features” to denote clinical and dermoscopic lesion features, and the term “feature descriptors” for image processing features.

Many works can be found on PSL feature extraction in the literature. However, only a few of them review or summarize the feature descriptors used in CAD systems. In particular, in 1997, Umbaugh *et al.* [145] described a computer program for automatic extraction and analysis of PSL features. They classified the proposed feature descriptors into binary object features, histogram, color, and spectral features. Binary object features included area, perimeter, and aspect ratios, among others. Histogram features comprised statistical measures of grey level distribution as well as features of co-occurrence matrices. Metrics obtained from color transforms, normalized colors and color differences were used to represent color features. Finally, spectral features represented metrics derived from the Fourier transform of the images.

Research carried out by Zagrouba and Barhoumi [146], besides reviewing CAD system development, provides a brief look at the feature selection algorithms. Feature selection is an important procedure to be carried out prior to lesion classification. It

2. COMPUTERIZED ANALYSIS OF PSLs: A LITERATURE REVIEW

aims to reduce the number of extracted feature descriptors in order to lower the computational cost of classification. However, this reduction is not trivial because eliminating redundancy among feature descriptors may adversely affect their discriminatory power. The development of feature selection procedures for various sets of extracted feature descriptors can be found in [83, 147–150].

Finally, a very good overview of CAD systems and feature descriptors was published in 2009 by Maglogiannis and Doukas [151]. In their work, they provided information regarding methods of PSL diagnosis and a list of typical feature descriptors used in the literature. They also compared the performance of several classifiers on a dataset of dermoscopic images using several feature selection algorithms on one feature set (see Section 2.1.5 for more details). The results obtained showed that the performance of the classifiers was greatly dependent on the selected feature descriptors. This fact emphasizes the importance of feature descriptors in the computerized analysis of PSL.

In this work, we propose an extended categorization of feature descriptors (see Tables 2.2–2.4), associating them with specific methods of diagnosis, separating clinical and dermoscopic images and discriminating references according to our literature classification. Such a categorization can help the reader: (1) to gain perspective regarding the existing approaches in PSL feature description, (2) to clarify differences in the representation of clinical and dermoscopic features, and, most importantly, (3) to obtain a complete source of references on the descriptors of interest.

For the purpose of conciseness and generalization, rather than look at individual descriptors we attempted to cluster them into groups with other related descriptors. Of course, taking this approach meant determining how each group of descriptors uniquely corresponded to the feature it aimed to describe. In other words, while most authors specified in their publications that a descriptor was mimicking a certain feature, others would use it to describe a different feature or not associate it with any feature in particular. A clear example of such a group is the one labelled “Lesion’s area & perimeter” (see Tables 2.3 and 2.4). We attributed this group to the “Border irregularity/sharpness” feature in line with most publications, and not to the “Asymmetry” feature, as some authors have done [93, 187]. Nevertheless, attributing this group is not such a straightforward task, since, as a geometry or shape parameter, it could well be used to describe both features. An identical majority reasoning was applied to the other groups of feature descriptors. Descriptors for which we could not define a specific clinical attribution were listed separately. All explanations on the groups can be found in the tables.

Table 2.2: Feature extraction for pattern analysis [42].

Pattern analysis		References
Global patterns	Reticular	[152–154] [155] ^a [156] ^b
	Globular	[152–154, 157] [155] [156]
	Cobblestone	[153, 157] [155]
	Homogeneous	[152–154, 157] [155] [156]
	Starburst	[155]
	Parallel	[153, 157][155]
	Multicomponent	[154]
	Non-specific	—
Local features	Pigment network	[60, 72, 158–165] [166–168] ^c [58] ^b
	Dots/globules	[60, 61, 169] [58]
	Streaks	[170, 171] [166, 172] ^c
	Blue-whitish veil	[173–176] [172, 177, 178] ^c
	Regression structures	[61, 179, 180] [172, 177, 178] [181] ^b
	Hypopigmentation	[61] [181]
	Blotches	[182–184] [185] ^d
	Vascular structures	[186]

^a Computer vision article from the "Classification" category

^b Computer vision article from the "CAD systems" category

^c Feature extraction following the 7-Point checklist for dermoscopy

^d Clinical article from the "Studies of lesion features" category

Among the diagnosis methods considered were the ABCD-rule and pattern analysis for dermoscopic images, and the ABCDE criteria for clinical images. Table 2.2 contains references to articles aimed at computing descriptors for pattern analysis features [42]. The majority of the papers referenced in this table belong to the "Feature extraction" category. Among these, a number were dedicated to feature extraction following the 7-point checklist method for melanoma diagnosis from dermoscopic images [166–168, 172, 177, 178]. A preliminary study on detection of some dermoscopic structures (blue-whitish veil, atypical pigmented network and irregular pigmentation) can be found in [44].

Descriptors of features used in the ABCD-rule of dermoscopy and the ABCDE clinical criteria are summarized in Tables 2.3 and 2.4. This separate representation helps to highlight differences and similarities in the computerized description of these features. As illustrated by these two tables, the largest groups of feature descriptors are present in both types of images (clinical and dermoscopy) and define the similarities. The differences, on the other hand, can be seen in smaller groups or even individual descriptors. For example, dermoscopic interest points [250], size functions [247–249], scale-invariant

2. COMPUTERIZED ANALYSIS OF PSLs: A LITERATURE REVIEW

Table 2.3: Dermoscopic features of pigmented skin lesions according to ABCD rule of dermoscopy [42, 243] and their descriptors

Dermoscopic features	Feature descriptors	Clinical references			Computer vision references		
		Features ^a	CAD systems ^a	Features ^b	Lesion classification	CAD systems ^b	
Asymmetry Review: [209]	Lesion's centroid & moments of inertia ^c	[185, 188–191]	[114, 192–197]	[174, 198]	[199–203]	[82, 83, 204–208]	
	Symmetry maps	—	—	[210]	—	[63]	
	Fourier descriptors	—	—	[211]	—	—	
	Global point signatures (GPS)	—	—	[212]	—	—	
	Other symmetry descriptors	[191, 213]	[214, 215]	[216]	[187]	[86, 217, 218]	
Border sharpness	Lesion's area & perimeter ^d	[185, 188, 189]	[192, 195–197]	[174]	[187, 199–203]	[82, 83, 86, 204, 206–208, 217]	
	Convex hull descriptors ^e	—	—	—	—	[83, 86]	
	Bounding box descriptors ^e	—	—	—	[202, 203]	[83, 204, 206]	
	Fractal geometry ^f	—	[196]	[219]	[199, 200]	[82, 86]	
	Gradient-based descriptors	[190]	[114, 214]	[216, 220, 221]	[187, 201]	[57, 86, 204–207, 217, 218]	
	Multi-scale roughness descriptors	—	—	[222]	—	—	
	RGB statistical descriptors ^g	—	[193–197, 214, 215]	[176, 216, 223, 224]	[187, 199–203, 225, 226]	[83, 86, 207, 208, 217]	
Color variegation	Alternative color space descriptors ^h	[190]	[192, 196, 214]	[216, 223, 224]	[187, 200–203, 225, 226]	[83, 204, 206–208, 217, 227, 228]	
	Munsell color space descriptors	—	—	—	—	[229]	
	Generalized color moments	—	—	[224]	—	—	
	Relative color statistical descriptors ⁱ	—	[214]	[174, 230]	[187]	[206, 217, 218]	
	Color quantization ^j	[188, 189, 209, 231]	[192, 196, 214]	[216, 224, 230, 232, 233]	[187, 200, 202, 234]	[82, 205, 206, 217, 228, 229]	
	Multidim. receptive fields histograms	—	—	—	[234]	—	
Other	Wavelet-based descriptors	—	—	[235]	[202, 226, 236–241]	[58, 81]	
	Gabor filter descriptors	—	[195]	—	[199, 225, 242]	[228]	
	Intensity distribution descriptors	—	[193, 194, 214]	[216]	[187]	[204, 217, 218]	
	Haralick descriptors ^k	—	[193, 194, 214]	[163, 174, 216]	[187, 201, 203]	[83, 207, 217, 218, 227–229]	

Table 2.3: Dermoscopic features of pigmented skin lesions. (*continued*)

Dermoscopic features	Feature descriptors	Clinical references		Computer vision references		
		Features ^a	CAD systems ^a	Features ^b	Lesion classification	CAD systems ^b
	Local binary pattern (LBP)	—	—	[244]	[245]	—
	Various texture descriptors	—	—	[244]	[246]	[228]
	Size functions	—	[247]	—	[248, 249]	—
	SIFT and color SIFT	—	—	—	[226]	—
	Dermoscopic interest points	—	—	[250]	—	—
	Bag-of-features framework	—	—	—	[226, 228, 242]	—

^a Clinical papers describing studies of PSL feature descriptors and CAD systems, respectively

^b Computer vision papers describing PSL feature extraction and design of CAD systems, respectively

^c This group includes all measures based on computing principal and/or symmetry axes, and centroid of the lesion. *Asymmetry index/percentage* [151], *aspect ratio (lengthening)*, *radial distance distribution* are among other descriptors in the group.

^d These descriptors define the relation between the area and perimeter of an object, and thus, describe its symmetrical and border characteristics. In particular, it includes a descriptor known as *compactness index/ratio or roundness* ($I = P^2 / 4\pi A$ or $I = 4\pi P^2 / A$), as well as *circularity*, *thinness ratio* or *regularity* ($I = 4\pi A / P^2$). In essence, these ratios represent one descriptor.

^e There are various descriptors based on the convex hull (CH) and bounding box (BB) of a lesion. In particular, *extent* is the ratio of the area of the lesion to the area of its CH (same as *solidity*) or BB (same as *rectangularity*), whereas *convexity* is the ratio of the perimeter of the CH to the perimeter of the lesion, and *elongation* is the ratio between the height and the width of the BB.

^f *Fractal geometry* group includes Fourier (fractal) dimension [251] and lacunarity [86].

^g *RGB descriptors* encompass statistical information from the RGB channels in the form of such values as min/max, average, variance, entropy, energy, kurtosis, range and others.

^h *Alternative color space descriptors* include parameters (statistical or not) derived from non-RGB color spaces (except for normalised RGB) - HSV/HSI (hue, saturation, value/intensity), spherical coordinates [106], CIELUV and others.

ⁱ This group comprises descriptors based on *relative color*, such as statistics on *relative difference*, *ratio* and *chromaticity* [174] of separate color channels, mostly in RGB color space.

^j *Color quantization* descriptors refer to features obtained after reduction of the quantity of colors in the image. This reduction or quantization can be done using color prototypes, histograms or clustering. Typical descriptors include *number of colors* and *percent melanoma color*.

^k Descriptors based on *co-occurrence matrices*. These contain *entropy*, *inertia*, *correlation*, *inverse difference* and other statistical parameters.

2. COMPUTERIZED ANALYSIS OF PSLs: A LITERATURE REVIEW

Table 2.4: Clinical features of pigmented skin lesions according to ABCDE criteria [38, 42] and their descriptors

Clinical features	Feature descriptors	Clinical references			
		CAD systems ^a	Feature extraction	Lesion classification	CAD systems ^b
Asymmetry	Lesion's centroid & moments of inertia ^c	[252]	[253–256]	[257–261]	[80, 92, 93, 146, 148, 262–267]
	Symmetry distance (SD)	—	[268, 269]	—	—
Border irregularity	Lesion's area & perimeter ^d	[54, 252, 270–274]	[254–256, 268, 275–277]	[257–261]	[80, 92, 93, 146, 148, 262–267, 278]
	Convex hull ^e	[272, 273]	—	—	[92, 93, 148, 266]
	Bounding box ^e	[270]	—	—	[92, 93]
	Fractal geometry ^f	[252]	[251, 279–282]	—	[80, 146]
	Gradient-based descriptors	[54, 271]	—	—	[80, 92, 93, 146]
	Irregularity index	—	[283, 284]	—	—
	Sigma-ratio	—	[285]	—	—
	Best-fit ellipse	—	[256]	—	[266]
	Fourier feature	—	[255]	—	—
	Polygonal approximation	—	[276]	—	—
	Conditional entropy	—	[286]	—	—
	Hidden Markov models	—	[287]	—	—
	Wavelet transform	—	[288]	—	—
	Centroid distance diagram	—	[289]	—	—
Color variegation	RGB statistical descriptors ^g	[54, 252, 271]	[149, 255, 256, 277, 290]	[257–260, 291]	[92, 262, 264, 265, 267]
	Alternative color space descriptors ^h	[270, 292]	[255, 290, 293]	[257, 258, 260, 261]	[262, 264, 265, 267, 278]
	Own channel representation	—	—	—	[93]
	Relative color statistical descriptors ⁱ	—	[149, 255, 290, 293, 294]	[257, 258]	[262, 265, 267]
	Color quantization ^j	—	[149, 290, 294–296]	[259]	[92, 278]
	Color homogeneity, photometry-geometry correlation	—	—	—	[80, 146]
	Parametric maps	—	[297]	—	—
	Semi-major axis of the best-fit ellipse	—	[256]	—	—
	—	—	—	—	—
	—	—	—	—	—

Table 2.4: Clinical features of pigmented skin lesions (*continued*)

Other features	Intensity distribution descriptors	[252, 272–274, 298]	—	[263, 266]
	Skin pattern analysis	—	[256, 299–303]	—
	Haralick descriptors ^k	[270]	[304]	[92, 278]
	Various texture descriptors	—	[305]	—
	Wavelet-based descriptors	—	—	[306]
	Independent component analysis based descriptor	—	—	[291]
	Tensor decomposition	—	[307]	—

^a Clinical papers describing studies of PSL feature descriptors and CAD systems, respectively

^b Computer vision papers describing PSL feature extraction and design of CAD systems, respectively

^c This group includes all measures based on computing principal and/or symmetry axes, and centroid of the lesion. *Asymmetry index/percentage* [151], *aspect ratio (lengthening)*, *radial distance distribution* are among other descriptors in the group.

^d These descriptors define the relation between the area and perimeter of an object, and thus, describe its symmetrical and border characteristics. In particular, it includes a descriptor known as *compactness index/ratio* or *roundness* ($I = P^2 / 4\pi A$ or $I = 4\pi P^2 / A$), as well as *circularity*, *thinness ratio* or *regularity* ($I = 4\pi A / P^2$). In essence, these ratios represent one descriptor.

^e There are various descriptors based on the convex hull (CH) and bounding box (BB) of a lesion. In particular, *extent* is the ratio of the area of the lesion to the area of its CH (same as *solidity*) or BB (same as *rectangularity*), whereas *convexity* is the ratio of the perimeter of the CH to the perimeter of the lesion, and *elongation* is the ratio between the height and the width of the BB.

^f *Fractal geometry* group includes Fourier (fractal) dimension [251] and lacunarity [86].

^g *RGB descriptors* encompass statistical information from the RGB channels in the form of such values as min/max, average, variance, entropy, energy, kurtosis, range and others.

^h *Alternative color space descriptors* include parameters (statistical or not) derived from non-RGB color spaces (except for normalised RGB) - HSV/HSI (hue, saturation, value/intensity), spherical coordinates [106], CIELUV and others.

ⁱ This group comprises descriptors based on *relative color*, such as statistics on *relative difference*, *ratio* and *chromaticity* [174] of separate color channels, mostly in RGB color space.

^j *Color quantization* descriptors refer to features obtained after reduction of the quantity of colors in the image. This reduction or quantization can be done using color prototypes, histograms or clustering. Typical descriptors include *number of colors* and *percent melanoma color*.

^k Descriptors based on *co-occurrence matrices*. These contain *entropy*, *inertia*, *correlation*, *inverse difference* and other statistical parameters.

2. COMPUTERIZED ANALYSIS OF PSLs: A LITERATURE REVIEW

feature transform (SIFT) descriptors and the bag-of-features framework¹ are used only on dermoscopic images, while a series of articles on skin pattern analysis [256, 299–302] and various approaches in describing border irregularity are only used for clinical images. At the same time, a group of textural feature descriptors (Haralick parameters) is rather large in dermoscopic image analysis and fairly small when used on clinical images. This is explained by the fact that dermoscopy images provide more detailed textural information than macroscopic clinical images [229], enabling a more complex analysis.

Overall, Tables 2.3–2.2 provide an overview of approaches for extracting features from PSL images, and an indication of the distribution of research efforts in relation to specific literature categories. However, it must be noted that these tables do not contain a complete list of publications in all categories, but only those that appeared in the scope of our survey and provided sufficient information on the proposed feature descriptors.

2.1.4 Registration and change detection

In most cases, methods in PSL change detection are dependent on image registration. Therefore, we will first explain the motivation behind change detection and then introduce several methods used to register PSL images.

2.1.4.1 Change detection

According to the last letter of the ABCDE mnemonic for melanoma detection, a lesion’s evolution over time is very important in detecting melanoma in its early stages. In other words, as was mentioned in Section 1.4.2, changes in lesion size and colour are among the most frequent symptoms in signalling the developing of melanoma. Furthermore, the study conducted by Menzies *et al.* [41] demonstrates that change of a lesion alone (short-term and without exhibiting classic surface microscopic features) can be a reliable sign of a developing melanoma. Hence, *detection of a lesion’s change is as important as correctly identifying its surface microscopic patterns, and can be a sufficient ground to excise it.*

Many commercial CAD systems (see Table 2.6) offer the function “automatic follow-up examination”, but this is usually limited to a side-by-side or alternating display of images (blink comparison) taken at different moments in time. This only facilitates a visual assessment of changes, without providing any quantitative information that might

¹Various schemes for feature sampling are tested and discussed in [308] and [309].

be useful for lesion diagnosis and discovering new patterns of color and morphology evolving in skin cancer lesions.

Furthermore, not much attention has been paid to developing automated systems for assessing changes in PSLs. Popa and Aiordachioaie [310] attempted to use genetic algorithms to determine changes in lesion borders from two clinical images taken at different moments in time and from different angles. A method of lesion classification based on its evolution was presented in [57]. The basic idea of this CAD system was to employ discretized histograms of oriented gradients to describe lesion evolution, and use them as an input to hidden Markov models. Another CAD system [58] assesses lesion changes by segmenting its two images, registering them by means of PCA and stochastic gradient descent, and obtaining a difference map. A different approach implementing feature-based change detection as opposed to difference maps was presented by the researches from the same team in [311]. However, the solutions overcoming its application difficulties outlined in the paper have not been proposed yet.

2.1.4.2 Registration

The methods of automatic and manual² lesion change detection are dependent on correctly aligning (registering) two images of a lesion taken at two different moments in time. In addition to the image registration methods used in work on change detection, there are some papers which we attributed specifically to the “Registration” category. In particular, Maglogiannis [312] used the Log-Polar representation of the Fourier spectrum of the images, and Pavlopoulos [313] proposed a two-step hybrid method, in which the scaling and rotation parameters are estimated using cross-correlation of a triple invariant image descriptors algorithm, and the translation parameters are estimated by non-parametric statistical similarity measures and a hill-climbing optimization.

Anagnostopoulos *et al.* [314] used a modification of the SIFT [315] algorithm bundled with RANSAC [316] to compute a homography model between two images. SIFT features were also used by Furusho and Iyatomi in [317], but the match outliers were filtered using a method based on Tukey’s biweight function. Correct point correspondences were also used for color calibration by means of a cumulative brightness transfer function.

²Side-by-side or blink comparison.

2. COMPUTERIZED ANALYSIS OF PSLs: A LITERATURE REVIEW

2.1.5 Lesion classification

Lesion classification is the final step in the typical workflow for the computerized analysis of images depicting a single PSL. Depending on the system, the output of lesion classification can be binary (malignant/benign or suspicious/non-suspicious for malignancy), ternary (melanoma/dysplastic nevus/common nevus) or n -ary, which identifies several skin pathologies. These outputs represent classes (types) of PSLs that a system is trained to recognize. To accomplish the task of classification, the existing systems apply various classification methods to feature descriptors extracted during the previous step. The performance of these methods depends both on the extracted descriptors and on the chosen classifier. Therefore, the comparison of classification approaches gives optimal results when performed on the same dataset and using the same set of descriptors.

The article by Maglogiannis and Doukas [151] summarized classification results reported by the authors of several CAD systems and performed a unified comparison of 11 classifiers on a set of feature descriptors (applying different feature selection procedures) using a dataset of 3,639 dermoscopic images. The 11 chosen classifiers represented the most common classifier groups used in the PSL computerized analysis, including artificial neural networks (ANN), regression analysis and decision trees among others. The comparison was conducted in three sub-experiments, which defined the number of output classes. The first two experiments assumed *melanoma/common nevus* and *dysplastic/common nevus* classes, whereas the third experiment united all three classes. As a result of these experiments, support vector machines (SVM) showed the best overall performance. Nevertheless, the authors concluded that it was the selected feature descriptors and the learning procedure that were critical for the performance of the classifiers.

Many other articles from the “Classification” and “CAD systems” categories compare two or more classifiers. In particular, the performance comparisons between ANN and SVM has been reported in several papers: [81, 234, 239, 240, 260, 289, 318]; overall, the performance of SVM was marginally better. Discriminant analysis (DA) was compared to ANN in [264, 277] and to ANN and SVM in [260, 289], demonstrating equal or marginally worse performance. Bayesian classifier was evaluated against SVM in [242] and against ANN and k -nearest neighbors (k NN) in [85]. It was shown to be inferior to the ANN but outperformed the k NN algorithm. Despite all these comparisons, it is still difficult to establish an absolute hierarchy in the performance of classifiers for PSLs. The reason for this, besides the marginal differences in the numerical evalua-

tion results, lies in the structure of the comparisons themselves: different feature and image sets, different classifier parameters and different learning procedures. Nonetheless, Dreiseitl *et al.* [318] took a relative approach to evaluation and concluded their comparison by ranking the classifiers as performing *well* (k NN), *very well* (ANN, SVM and logistic regression), or *not well suited* (decision trees paradigm—due to continuous input variables).

Table 2.5 contains references from three literature categories which use, develop and/or test classification methods in diagnosing PSL from dermoscopic and clinical images. The papers in the “Classification” category tend to dwell more on details specific to the proposed approach of lesion classification. The two other categories contain references to studies that use one or more classification methods to analyze, propose or improve complete CAD systems. Therefore, these papers generally provide less detail on implementation, but still contain comparative performance results.

In Table 2.5 we included papers that classify lesions from images acquired using either modality. The reason for this being that the classification step in PSL CAD systems depends not on the information available in the image, but on the interpretation of this information, i.e. the extracted feature descriptors. However, one may argue that as these descriptors encode information specific to image types, they are thus distinct for the two modalities. But even considering this distinction, it is almost impossible to clearly separate feature descriptors into two classes according to these image modalities, simply because of the similarity of the feature descriptor groups (see Tables 2.3 and 2.4).

Classification methods were grouped according to their corresponding category without taking into account specific implementation characteristics. For example, such groups as ANN and discriminant analysis include various methods that can be considered “a type” of these larger groups of methods. Also, as several publications compare algorithms, they can be found in one or more rows of the table. As for the popularity of techniques used for lesion classification, an obvious preference is given to artificial neural networks, followed by SVM, discriminant analysis, k NN and decision trees. Other approaches, such as kernel logistic partial least square regression (KL-PLS) and hidden Markov models, are also explored and adapted to the problem.

The table also shows that supervised machine learning algorithms are largely preferred to unsupervised approaches. Above all, this is related to the nature of the classification problem, and to the high diversity of clinical and dermoscopic features that can point to the malignant or benign nature of a lesion. Thus, there are many sample lesions whose corresponding biopsy-established diagnosis partially or completely contradicts the observed clinical and dermoscopic features [41, 340]. In this case, the

2. COMPUTERIZED ANALYSIS OF PSLs: A LITERATURE REVIEW

Table 2.5: Classification methods used in computerized analysis of clinical and dermoscopic PSL images

Lesion classification methods and tools	References according to the categories		
	Classification	CAD systems	Studies of CAD systems
ANN	[199, 234, 235, 238–240, 257–261, 277, 289, 318–321]	[80–82, 85, 181, 217, 264, 265]	[192, 195, 197, 273, 274, 322–332]
SVM	[155, 226, 234, 239, 240, 242, 245, 246, 249, 260, 289, 306, 318]	[81, 83, 207, 228, 229]	[215, 247]
Decision trees	[44, 174, 200, 225, 258, 304, 318]	[92, 93, 262, 333]	[193, 194]
kNN	[200, 234, 244, 261, 318]	[85, 93, 206, 228, 229]	[194, 334]
Discriminant analysis	[200, 260, 277, 282, 289]	[264]	[32, 54, 271, 272, 334–340]
Regression analysis	[187, 289, 318]	[333]	[45, 292, 341, 342]
Multiple classifiers	[200, 203, 208]	[85, 229]	[196]
Bayesian classifiers	[242]	[85, 267]	—
Fuzzy logic	[237, 294]	[86]	—
Attributional calculus	[202, 239, 241]	—	—
ADWAT ¹	[236, 237]	—	—
K-means/PDDP ²	[201]	—	—
KL-PLS	—	[343]	—
Minimum distance classifier	—	[204]	—
Hidden Markov models	—	[57]	—
AdaBoost meta-classifier	[44, 225, 344]	[92, 228]	—

¹ ADWAT – adaptive wavelet transform based tree-structured classification, a method designed for classifying epi-illumination PSL images

² PDDP – principal direction divisive partitioning

training/testing paradigm for the development of classification algorithms is widely used to teach a classifier to recognize such unusual manifestations of malignant tumours. However, exploring unsupervised learning methodologies also seems promising in understanding the relationship between observed features and PSL malignancy [201].

2.1.6 CAD systems

This subsection contains an overview of the literature dedicated to developing and studying computer-aided diagnosis systems for PSLs. Among the first papers to summarize progress in this area were [345] and [346], both published in 1995. Later publications include [146, 217] and [151] and are targeted at computer vision researchers. However, most of the papers that compare the performance of CAD systems are clinical study papers (“Studies of CAD systems” category). These papers often provide comparative tables with different characteristics of the systems such as the size of the dataset and its distribution (e.g. malignant melanomas versus dysplastic nevi), image type, classification method(s), and performance metrics (e.g. sensitivity, specificity and others). Though these tables do not allow for absolute comparison between CAD systems, they do help to analyze and quantify different aspects of existing approaches. Such comparative tables can be found in [23, 46, 47, 342, 347–349].

Nowadays, a number of systems are commercially available for computer-aided diagnosis of PSLs. The literature is abundant with references to studies researching and developing these systems, which are mainly based on dermoscopy. Table 2.6 lists some of the proprietary CAD systems we encountered during our literature survey. It includes systems based on dermoscopy as well as several spectrophotometric systems (other imaging modalities were not included). Most of these CAD systems are complete setups consisting of acquisition devices (dermoscopes) and analysis software. Some diagnosis systems serve as additional modules to acquisition systems, such as DANAOS or MoleAnalyser expert systems (see Table 2.6).

One of the most cited CAD systems used for melanoma detection is DB-Mips[®] (Dell’Eva-Burroni Melanoma Image Processing Software). It is also known as DBDermoMips, DDA-Mips, DEM-Mips, DM-Mips and DB-DM-Mips, depending on the period of development. According to Vestergaard and Menzies who surveyed automated diagnostic instruments for cutaneous melanoma [47], it is difficult to draw overall conclusions regarding the performance of this system due to the use of different classifiers in differently structured studies. In particular, they refer to two earlier studies involving expert dermatologists: [323] and [326]. In the former [323], the classifier’s accuracy was higher

2. COMPUTERIZED ANALYSIS OF PSLs: A LITERATURE REVIEW

Table 2.6: Proprietary CAD system software and digital dermoscopy analysis instruments

Software/Instrument	Modality	Developer	References
DANAOS expert system ¹	Dermoscopy	Visioned AG (Bielefeld, Germany)	[195, 197, 328, 330, 350]
DB-Mips®	Dermoscopy	Biomips Engineering SRL (Sienna, Italy)	[32, 323, 325–327, 329, 334–336, 338–340, 351, 352]
DermoGenius System®	Dermoscopy	DermoScan GmbH (Regensburg, Germany)	[353]
MEDS ²	Dermoscopy	ITC-irst (Trento, Italy)	[196, 200]
MelaFind®	Multispectral dermoscopy	MELA Sciences, Inc. (Irvington, NY, USA)	[354, 355]
MoleAnalyzer expert system ³	Dermoscopy	FotoFinder Systems GmbH (Bad Birnbach, Germany)	[350, 356]
MoleMate™	Siascopy ⁴	Biocompatibles (Farnham, Surrey, UK)	[297, 357, 358]
MoleMax™	Dermoscopy	Derma Medical Systems (Vienna, Austria)	[318, 331]
SolarScan®	Dermoscopy	Polartechnics Ltd (Sydney, Australia)	[41, 359]
SpectroShade®	Spectrophotometry	MHT (Verona, Italy)	[274, 298]

¹ Software developed during the European multi-center diagnostic and neural analysis of skin cancer (DANAOS) trial. Used in microDERM®.

² MEDS – melanoma diagnosis system

³ MoleAnalyzer was initially developed in the University of Tuebingen (Germany). Used in the FotoFinder dermoscope.

⁴ Siascopy™ is based on the spectrophotometric intracutaneous analysis (SIA) technique.

than that of experienced clinicians using only the epiluminescence technique. However, in the latter case [326], the specificity of the system was significantly lower. Importantly, the same classifier, ANN, was used in both settings. The authors of the survey suggest that these results reflected dramatic differences in the proportion of dysplastic nevi in the benign sets.

Proprietary systems based on spectrophotometry include MoleMate™, SpectroShade® and MelaFind®. The latter uses multispectral dermoscopy to acquire images in 10 different spectral bands, from blue (430 nm) to near infrared (950 nm) [355]. Siascopy (MoleMate™ system) analyzes information regarding the levels of haemoglobin, melanin and collagen within the skin by interpreting the wavelength combinations of the received light [357]. For more references see Table 2.6.

Overviews and comparisons of the technical characteristics of digital dermoscopy analysis (DDA) instruments can also be found in the literature. DB-Mips, MoleMax II, Videocap, Dermogenius, microDerm and SolarScan are summarized in [340, 360], and Dermogenius Ultra, FotoFinder and microDerm are compared in [350]. According to the latter, the reviewed computer-aided diagnostic systems provide little to no added benefit for experienced dermatologists/dermoscopists. A description of other systems together with their performance evaluation can be found in [47].

It is also worth mentioning CAD systems that attempt to diagnose a PSL based on its visual similarity to images of lesions with known histopathology. Systems that use this approach are called content-based image retrieval (CBIR) systems. The primary goal of CBIR is to search a database to find images closest in appearance to a query image. Various metrics establishing similarities between extracted lesion feature descriptors are used for this purpose: Bhattacharyya, Euclidean or Mahalanobis distances, among others. The choice of the metric depends on the nature of the feature descriptors. Thus, Rahman and Bhattacharya [229] and Ballerini *et al.* [227] use Bhattacharyya and Euclidean distances for color and texture features, respectively, whereas Celebi and Aslandogan [148] use the Manhattan distance for descriptors based on the shape information of the lesion. The commonly-used measure for evaluating content-based retrieval systems is the precision-recall graph [229]. At the present time, results for systems of both clinical [148, 278] and dermoscopic [227, 229, 263, 361] image retrieval leave room for improvement

2. COMPUTERIZED ANALYSIS OF PSLs: A LITERATURE REVIEW

2.1.7 3D lesion analysis

The first attempts to reconstruct 3D images of PSLs were made with the introduction of the ‘Nevoscope’ device in 1984 [34]. The principle of this reconstruction was based on obtaining images of a transilluminated lesion at three different angles (90° , 180° and 45°) and applying a limited-view computed tomography (CT) reconstruction algorithm [34, 35, 362]. As the result of several consecutive reconstructions of a lesion, its changes in thickness, size, color and structure could be evaluated.

Similar to 2D analysis of PSLs, features extracted from the 3D lesion representation are used for computer-aided diagnosis. McDonagh *et al.* [363] apply dense reconstruction from a stereo-pair image to obtain 3D shape moment invariant features. In order to automatically distinguish between non-melanoma lesions, they feed these features into a Bayesian classifier along with relative color brightness, relative variability, and peak and pit density features.

The latest approach to PSL characterization from 3D information is via photometric stereo. The features for lesion classification from photometric 3D include skin tilt and slant patterns [364] and statistical moments of enhanced principal curvatures of skin surfaces [365, 366]. In [366], the performance of an ensemble classifier comprising discriminant analysis, artificial neural network and a C4.5 decision tree is tested on enhanced 3D curvature patterns and a set of 2D features: color variegation and border irregularity. According to the obtained results, 3D curvature patterns did not outperform traditional 2D features, but definitely demonstrated their effectiveness in melanoma diagnosis; moreover, an ensemble classifier proved to be more efficient than single classifiers in this task.

2.2 Multiple lesion analysis

As we mentioned in Section 1.5, the literature on the analysis of multiple PSLs is scarce. Some publications do exist on the steps essential for assessing change in images of multiple lesions: localization and registration. However, practically the only article in which lesion localization and registration algorithms are applied together to automatically estimate dimensional changes in PSLs is the one by Voigt and Claßen [367]. It was published in 1995 and the authors introduced the technique for lesion tracking/change detection as “topodermatography”. It used simple image thresholding for PSL localization and the structure elements of the acquisition framework for registration. No further work on improving the algorithm or implementing it in clinical practice has

been reported.

2.2.1 Lesion localization

In 1989, Perednia *et al.* [368] used a Laplacian-of-Gaussian filter to detect the borders of multiple lesions. They later proposed the concept of “brightness pits”, according to which multiple levels of brightness pits are detected in the image and a number of their parameters are extracted [369]. Based on these parameters, DA and k NN algorithms learn to discriminate pits belonging to skin lesions and localize them in the images. In [370] and [371], the authors combined multiresolution hierarchical segmentation, region growing and neural networks. The latter served to analyze nodes of the pyramid generated by the segmentation step and find the most appropriate representation of PSLs.

Taeg *et al.* [372] applied an SVM algorithm to classify PSL candidates, obtained through difference of Gaussians filtering after a hair removal procedure on the detected skin regions. The recognition of moles from candidates was also performed in [373], where a modified mean shift filtering algorithm is applied to the images followed by region growing, which pre-selects possible candidates. Subsequently, these candidates are fed to the rule-based classifier for definite identification. Finally, during work conducted on face recognition by skin detail analysis in [374], PSLs were detected by normalized cross-correlation matching; a Laplacian-of-Gaussian filter mask was used as a template.

2.2.2 Lesion registration

Several registration approaches have been proposed in the literature. Among them, the 3-point geometrical transformation algorithm based on correct identification of initial matches was proposed by Perednia and White in [375]. The same authors developed a method for automatic derivation of initial PSL matches by means of Gabriel graph representation of lesions in an image [376]. A similar initialization step is a requirement for the baseline algorithm [377], which exploits geometrical properties of the lesions with respect to the baselines derived from the two initial matches.

McGregor performs the registration of multiple lesion images in [378] by first creating lesion maps. This is done by using a centre-surround differential operator to form clusters and later thinning them via a “centring” mask at different image scales. These maps are then registered by detecting the 4 pairs of matching lesions that provide the best “global matching metric”. The registration step requires initial lesion matches, which are obtained by minimizing the distance and angular error of local

2. COMPUTERIZED ANALYSIS OF PSLs: A LITERATURE REVIEW

neighbourhoods.

Huang and Bergstresser treated the problem of PSL registration as a bipartite graph matching problem [379]. The authors used Voronoi cells to measure similarities between PSLs, and preserved their topology. Another approach using graph matching was proposed by Mirzaalian *et al.* in [380]. In this study, the authors incorporated proximity regularization, angular agreement between lesion pairs and normalized spatial coordinates into the extended hyper-graph matching algorithm. Coordinate normalization was performed using the human back template, which offers performance advantages over other methods, as well as challenges such as defining anatomical landmarks for template creation. Later, in [381] the same authors formulated the PSL registration/matching problem as the relaxed labeling of the corresponding association graph in a high order Markov random field optimization framework. They also added a new entropy term to the objective function encouraging the cost function towards solutions with low uncertainty.

2.3 Conclusion

Two decades ago, before digital imaging largely substituted film photography in medicine, researchers envisioned the potential benefits of its application in dermatology [53]. Many of these benefits became a reality: objective non-invasive documentation of skin lesions, digital dermatological image archives, telediagnosis, quantitative description of clinical features of cutaneous lesions and even their 3-dimensional reconstruction. And although automatic PSL diagnosis systems are not yet perfect, their most valuable functionality has already been achieved: the description of lesion characteristics.

We presented an overview of research in the computerized analysis of dermatological images. We based it on specific aspects resulting from the fusion of the two different disciplines: dermatology and computer vision. In particular, the following points were emphasized:

- The difference between dermoscopic and clinical image acquisition of individual PSLs, which lies in how the structural information of a photographed lesion is visualized. It is essential to take this into account when applying pre-processing, border detection or feature extraction algorithms to the images of skin lesions. Moreover, frequent discrepancies in terminology found in the literature relate precisely to this fundamental difference between the two modes of acquisition. As a consequence, clinical diagnosis methods have at times been incorrectly attributed to image types in the computer vision literature.

-
- Clearly separating publications that analyze images of individual and multiple pigmented skin lesions. There is a large discrepancy in the number of articles published on each subject. This may be related to the fact that total body skin imaging is not widely adopted. Opinion is still divided regarding the trade-off between its usefulness for melanoma detection versus logistic constraints and financial considerations related to its application [13]. Consequently, the demand for automated solutions to total body screening is not as high as that for individual lesion analysis.
 - The analysis of images depicting individual PSLs generally focuses on developing computer-aided diagnosis systems aimed at automatically detecting melanoma from clinical and dermoscopic images. Overall, these systems follow the same workflow: image preprocessing, detection of lesion borders, extraction of clinical feature descriptors of a lesion and, finally, classification. Various approaches have been proposed for implementing all of the steps in this workflow; however, the steps of border detection and feature extraction have the largest number of publications dedicated to them.
 - Scarcity of reported material on automating change detection both in individual and multiple PSL images. Despite the fact that rapid change in lesion morphology and size is probably the only sign of an early-stage melanoma, to the best of our knowledge cases where fully automated change assessment is implemented have not yet been proposed.

Furthermore, we classified publications related to the computerized analysis of dermatological images into several categories. In the scope of this classification, we reviewed the categories that comprise the workflow of typical CAD systems and provided summary tables for those references in which the methods of preprocessing, feature extraction and classification of PSL images are implemented.

Another important contribution of this review is the extended categorization of existing clinical and dermoscopic feature descriptors. We clustered these into groups of related descriptors associated with the specific diagnosis methods, separating clinical and dermoscopic images, and discriminating references according to the literature classification. Since feature descriptors are critical for PSL classification, such a categorization is useful for a number of reasons: providing an overview of existing methods in PSL feature extraction, demonstrating the difference between clinical and dermoscopic feature descriptors, and aggregating a list of corresponding relevant references.

2. COMPUTERIZED ANALYSIS OF PSLS: A LITERATURE REVIEW

Computer-aided diagnosis systems for pigmented skin lesions have demonstrated good performance in the experimental setting and have a high level of acceptance among patients. However, at present, such systems cannot yet be used to provide the best diagnostic results or replace the clinicians' skill or histopathology. Nonetheless, these systems are now used for educating general practitioners, giving advanced training to expert clinicians and providing second opinions during screening procedures [46, 48]. In other words, "clinical diagnosis support system" might be a more correct term to refer to CAD systems for skin cancer at the current stage of their development.

Finally, an important step to improve output quality in these systems and unite the efforts of different research groups working in this area is to provide a publicly available benchmark dataset for the algorithms being developed. Each PSL image in this dataset should be accompanied by the ground truth definition of the lesion's border and its diagnosis with additional dermoscopy reports [42] from several dermatologists. Such a dataset has been anticipated for a very long time, and only recently, a relatively small database satisfying these characteristics was made available for public use [144].

Although it is the lot of man but once to die, the victim of malignant melanoma need not die by inches from the Black Death.

Stanford Cade, “*Malignant Melanoma*” [2]

Chapter 3

A total body skin scanner

Knowing a PSL’s previous state allows predicting its malignancy using one of the most reliable signs of a developing melanoma: changes in color, shape and/or size [382]. These changes are also referred to as “evolving” in some of the melanoma detection algorithms [38].

In order to recognize changing lesions during total body skin examination, physicians need a baseline for each lesion. This baseline can be provided by total body photography consisting of periodically acquiring photographs of patients in standardized poses (please, refer to Section 1.4 for more details). The images acquired are used to detect changes in moles via simple visual comparison as described in [25].

Despite a variety of body scanning techniques and devices used in the medical, textile or cosmetics industries [383], the level of automation of WBP systems for melanoma detection remains low both in terms of image acquisition and processing. One of the reasons is that the majority of these systems are designed to recover 3D information of the body shape rather than considering its textural information. It mainly concerns devices using laser, white light or time of flight technologies. On the other hand, scanners based on photogrammetry¹ need to provide high-resolution images for a comprehensive analysis together with a sufficient image overlap for 3D reconstruction, which poses a certain engineering trade-off. Consequently, some scanners using multiple cameras (e.g., [52]) offer automated image acquisition, but do not report any means to analyze and compare images automatically.

Taking this trade-off into account, we designed and built a new total body scanning system capable of automatically acquiring high-resolution images of 85–90% of the

¹Photogrammetry based scanners infer 3D information about objects from their photographic images, acquired using one or several cameras. Computer vision and image processing techniques are used to this end [384].

3. A TOTAL BODY SKIN SCANNER

cutaneous surface and creating a precise map of all visible moles. In contrast with traditional photogrammetry-based systems, our scanner does not rely on dense skin texture reconstruction, but rather focuses on detecting and mapping individual moles. Such an approach allows solving the lesion-to-image correspondence problem by having a direct link between a mole's location on the patient's body and its images (at least two). At the same time, the controlled environment of the scanner offers a solution to the problem of automatic lesion matching across two different scans, or explorations. In this way, moles that appear and disappear can be detected, as well as the evolution of all the lesions can be tracked across explorations, enabling their automatic change detection.

Further along in this chapter, we describe the design, the calibration procedure and the operational sequence of the total body skin scanner developed. We also discuss the limitations of the system imposed by the components employed (the turntable, the cameras and the dimensions of the booth), and provide suggestions for future improvements.

3.1 Hardware design

The dimensions of the proposed scanning system illustrated in Figs. 3.1 and 3.2 are $1400 \times 990 \times 2200$ mm. The doors are positioned at the front and the side of the scanner's cabin allowing for easy access as well as ensuring free exit in case of an emergency stop. The operator's control panel is located to the right of the front door and consists of a 19-inch touchscreen, an emergency stop button, operation light-emitting diodes (LEDs) and a safety key. The touchscreen enables the operator to control the image acquisition process directly. The three LEDs indicate the power state of the system, whether the turntable is in motion or the emergency stop has been activated.

The interior of the scanner is divided into two areas: the acquisition and the equipment compartments. The former is the patient area accessible via the doors, while the latter can be reached by removing the rear composite wall boarding.

1. **The acquisition compartment** (Fig. 3.1) is a light-tight chamber exposed to a camera rig, a fluorescent lighting system and a turntable on the floor level. A backrest column, padded with soft material, is attached to the turntable and the roof frame. It adds rigidity to the structure, provides support to the patient and, at the same time, establishes a reference point for his/her positioning in the chamber. A sliding horizontal bar installed on the backrest column serves



Figure 3.1: Exterior view of the scanner (3D model): the acquisition compartment. The two doors allow for easy entrance and exit regardless of the position of the backrest column. The control panel is located next to the front door and consists of a touchscreen, emergency stop button and operation LEDs. The interior of the acquisition chamber is shown in the image on the right (the side door removed). The camera rig is covered by black paneling and located in the middle of the cabin. On the side of the rig, there are the two sections of the lighting system as well as the four intake fans. The backrest column, padded with soft blue material, is attached to the turntable at the bottom and to the roof frame at the top.

as a hand support. During the exploration, the turntable rotates making several stops, so that the patient is exposed to the cameras from different angles. These stops are hereafter called *turntable positions* or *steps*, and the proposed prototype uses 12 steps per pose of the patient (see Section 3.2).

The chamber is ventilated using 6 fans: four for air supply and two for exhaust. The supply fans, with a diameter of 80 mm, are located symmetrically on the sides of the lighting system. They force external air, drawn through the ventilation openings in the rear wall of the scanner, into the acquisition compartment. The two 120 mm exhaust fans take the air out through the ceiling of the compartment. Because of the lighting system, the air in the closed acquisition chamber can heat up rapidly (the working temperature of the fluorescent lamps is 35°C). Hence, in order to prevent possible excessive heat in the chamber and reduce electricity

3. A TOTAL BODY SKIN SCANNER



Figure 3.2: Exterior view of the scanner (3D model): the equipment compartment. At the bottom and the top of the side paneling there are ventilation openings for air intake and exhaust. The interior of the equipment compartment can be seen in the image on the right (the two parts of the composite paneling are removed). There are three shelves holding the equipment cabinet, the PC, and the stereo speakers. Behind the shelves are the camera rig, the lighting system and the intake fans facing the interior of the acquisition chamber.

consumption, turning the lights off between explorations is recommended.

2. **The equipment compartment** (Fig. 3.2) contains a personal computer (PC) and a cabinet with a variable frequency drive (VFD), a transformer and switch controllers. The PC controls the acquisition process, stores image data and manages all input/output requests. The switch controllers and the VFD allow direct software communication between the PC and the lighting system and turntable. The cameras are connected to the computer via USB interface: several external USB controllers are used for the purpose.

To communicate with the patient while the doors of the cabin are closed, the operator can use a microphone installed on the control panel. The sound will be amplified by the speakers located in the equipment compartment (the speakers can be optionally used for music playback during the scanning procedure). Moreover, the interior of the acquisition compartment can be monitored from the outside using the live video stream

transmitted from a USB camera inside the chamber. This is useful for controlling the scanning procedure (change of pose), as well as for a rapid response to emergency situations.

3.1.1 The imaging subsystem

The imaging subsystem of the scanner uses 21 identical commercial digital cameras equipped with 12 mega-pixel charge-coupled device (CCD) sensors (4000×3000 pixels) and lenses with a focal length of 7.4–44.4 mm (35 mm film equivalent: 35–210 mm) capable of $6\times$ optical zooming. These cameras support a portable application programming interface that provides a detailed software control over most of the acquisition parameters. Moreover, their price-quality ratio gives them an advantage over industrial cameras with similar specifications.

The cameras are installed on two parallel columns in portrait orientation: 11 on the left and 10 on the right (when looking through the cameras' viewfinders), as illustrated in Figs. 3.1 and 3.3a. Both columns are rotated 5° around their vertical axes, so that all cameras are directed "inwards". The vertical spacing between any two adjacent cameras installed on the same column equals 165 mm, while that between those installed on the opposing columns is two times less, 82.5 mm. The baseline, or the horizontal spacing between the cameras on the two columns, is 100 mm. With this arrangement and a $3\times$ zoom factor, we achieve a trade-off between image overlap and resolution/magnification when the cameras are focused at a distance of approximately 400–450 mm. Moreover, the cameras' view angles are suitable for both matching the detected feature points in inter-column stereo pairs and extracting their 3D positions.

Before calibrating the cameras, they must be initialized with predefined parameters (F-number, ISO value, exposure time, etc.) and their focus points must be locked at a fixed distance. We set the aperture to its minimum (F8.0) in order to maximize the depth of field (DOF), while the exposure time and the ISO value were set to $1/30$ of a second and 200 respectively, resulting in well-lit images and an acceptable tolerance to the patient's motion.² The cameras' function of automatic focusing by contrast detection is not used because the skin's texture is too uniform for an accurate enough estimation of the focus distance. Moreover, the time needed for each camera to focus automatically is variable. This does not satisfy the requirement of simultaneous image acquisition by all the cameras (see Section 4.1.2.1 for details).

²During the exploration, the patient will need to hold the same pose and avoid abrupt movements while the camera sensors collect light. Since it is nearly impossible for the patient to remain completely motionless, the scanning system should have a tolerance to slight, unwanted movements.

3. A TOTAL BODY SKIN SCANNER

Therefore, in order to fix the focus point, we make use of the calibration board, described further in Section 3.3, whose colored squares have well-defined edges. The board is placed in the scanner, attached to the backrest column. Then, the turntable is rotated 90° so that the pattern appears facing the cameras at a distance of approximately 400 mm (395 mm from the pattern to the camera case and 5–15 mm to the sensor). Each camera takes a single shot using the auto-focusing function, thus, acquiring an image of the calibration pattern. The estimated focus points are retained and used throughout the exploration(s), while the images serve to compute the extrinsic parameters of the rig with respect to the center of the turntable.

3.1.2 The lighting subsystem

The acquisition compartment is illuminated by a lighting system consisting of 16 double-capped fluorescent lamps divided into two sections. Each section is a combination of four 39-Watt and four 54-Watt lamps with a luminous efficiency³ of 86 lm/W, which emit high color temperature light (6500K, “cool daylight”). The total nominal luminous flux⁴ of the fluorescent lamps in the two sections equals $\Phi_V = 63,984$ lm for the total wattage $\Phi_E = 744$ W.

The lighting system’s lamps and all the cameras are equipped with linear polarizers and circular analyzers, respectively. The mutual angle between their polarizing axes is 90° , making the acquisition process similar to that of cross-polarized dermoscopy [30]. Using cross-polarized light allows eliminating any reflections on the skin’s surface, however, at the expense of light energy losses during both emission and capture. We compensate this loss by using a longer exposure time (1/30 s) and a higher ISO sensitivity value (200) on all cameras.

The resulting illuminance⁵ at the point lying on the plane of the calibration board, and equidistant (350 mm) from the two lighting sections, was measured to be approximately 5000 lx.⁶ Similar values with minor fluctuations were reported at all heights in the acquisition chamber along the same vertical line. However, when the measurement point was moved along the horizontal dimension of the calibration plane closer to the

³Luminous efficiency/efficacy of a light source determines how well it converts input (electrical) energy into the energy of visible light (measured in lumens per watt (lm/W)).

⁴Luminous flux/power is a photometric measure of the total amount of light emitted by a light source (measured in lumens(lm)). In other words, it is the radiance power of the source across the whole electromagnetic spectrum weighted by the average spectral sensitivity of the human eye at a given wavelength.

⁵Illuminance is the amount of luminous flux from a light source falling on a given surface, measured in lux (lx=lm/m²).

⁶The measurements were taken with a hand-held analogue illuminometer Kyoritsu Model 5200.

center of light ray concentration of the lighting system sections, the obtained illuminance values reached as much as 7000 lx. These levels of illuminance are adequate to uniformly light the skin surface of the patient at the focusing distance of the camera rig and account for light losses during the image's capture. For comparison, the recommended level of illuminance for the performance of visual tasks of low contrast or very small size over a prolonged period (inspection tasks, very difficult assembly or jewelry manufacturing) is 2000–5000 lx [385].

According to [386], fluorescent light sources with similar characteristics belong to the Risk Group 0 (RG0, “exempt from risk”) of photo-biological hazard. Moreover, the effects of short-term exposure to ultraviolet radiation emitted by a fluorescent light source are thought to be negligible. Similarly, there is no evidence that blue light from artificial lighting belonging to RG0 would have an impact on the retina greater than that of sunlight. Therefore, as the sole precaution during the exploration, the patient is advised to either avoid looking directly at the light source or have his/her eyes closed.

3.2 The scanning procedure

Once the focus points are fixed and the cameras calibrated (see Section 3.3), the image acquisition procedure can be started. In order to photograph a minimum of 85% of the skin's surface, the patient needs to assume two poses:

- Pose 1: face the backrest column with the hands down at the sides (Fig. 3.3b). Used to scan the posterior region of the body, the shoulders, the arms and the back of the hands.
- Pose 2: back to the column, grasping the horizontal bar behind with both hands (Fig. 3.3c). Exposes the anterior region of the body, the face and the sides of the trunk to the cameras .

To begin, the patient assumes pose 1. The turntable rotates 180 degrees counter-clockwise making stops for the cameras to acquire images at the following 11 angles or positions: 15°, 30°, 45°, 60°, 80°, 100°, 120°, 135°, 150°, 165° and 180° (see Fig. 3.4). In total, there are 12 positions at which the images are acquired, starting with step 0, when the turntable is in the initial state. Note that in the range of the first and the last 4 positions, the turntable makes 15-degree rotations each step, while at the four middle positions it rotates 20°. This is done to increase the overlap between the images acquired when the body (shoulders) is closer to the cameras, and hence, the

3. A TOTAL BODY SKIN SCANNER

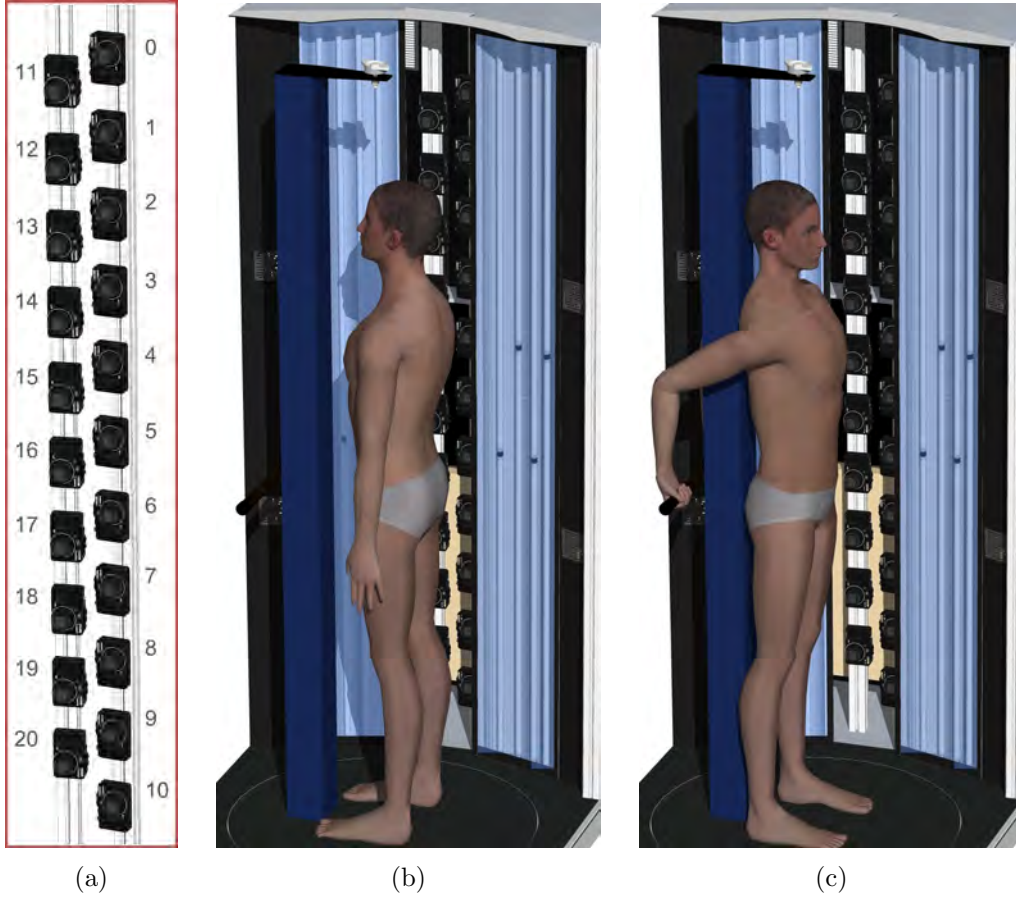


Figure 3.3: (a) The setup of the cameras on the columns and their indexes. (b) Pose 1 for image acquisition: the patient faces the backrest column with the arms on the sides. (c) Pose 2: the patient stands with his/her back to the column, holding the horizontal bar behind with both hands. The interior of the acquisition compartment shown in (b) and (c) demonstrates the camera rig (with the cover removed), the lighting system, and the turntable with the backrest column.

relative displacement is bigger. And at the same time, we reduce data redundancy when imaging the trunk which appears farther from the cameras at steps 5-8.

After the turntable reaches 180° , the patient is asked to assume pose 2. Once the pose has changed, the operator resumes the procedure and the turntable rotates 180° clockwise making stops at the same positions for image acquisition.⁷ In total, the 21 cameras capture one image at 24 turntable positions resulting in 504 high-resolution images covering most of the skin's surface. Only the inner side of the arms, the palms, the soles and the upper part of the scalp are not covered during the exploration. In

⁷In order to differentiate between the turntable's positions when the patient is in two different poses, we number them from 0 to 23. The first twelve are for pose 1, and the remaining are for pose 2.

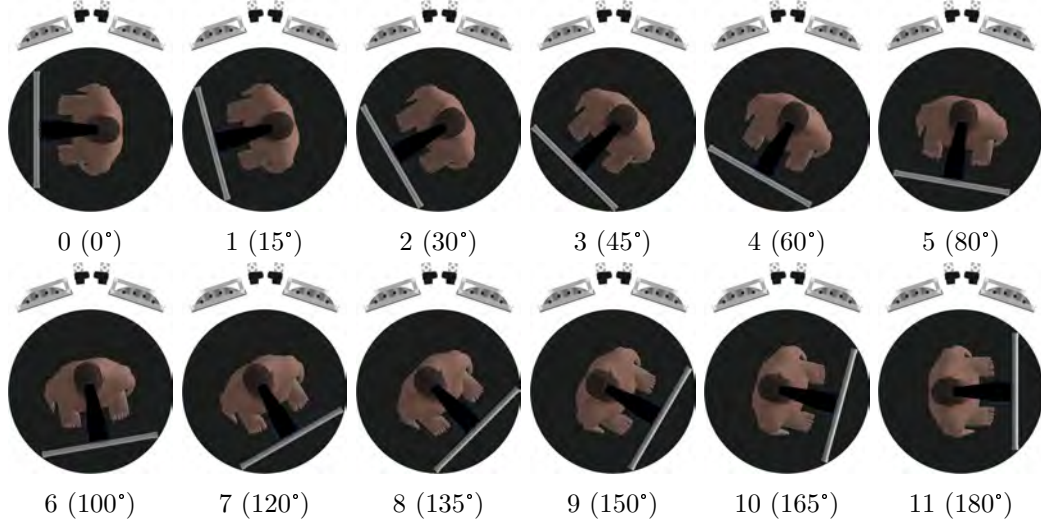


Figure 3.4: Schematic top views of the acquisition compartment with the turntable at different angles/steps. The patient assumed pose 1 facing the backrest column. After step 12, the patient changes his/her pose and the turntable rotates clockwise to complete the exploration.

order to complete the TBSE, these areas should be photographed separately by the operator or the physician.

At the end of the acquisition procedure, all the images are copied from the cameras' memory modules to the PC and the scanner's database is updated with the dataset information using the details of the patient and the operator. The whole procedure takes approximately 6 minutes, greatly improving the time needed for manual image acquisition. A non-automated complete skin examination, with or without dermoscopy, takes less than 3 minutes on average [387]. However, added manual image acquisition for lesion change tracking, which requires around 1 minute per mole, it will take at least 30 minutes more for a patient with 30–40 lesions.

3.3 Camera calibration

Besides the specific lighting conditions and positioning of the patient, the controlled environment of the scanner relies heavily on the camera's measurements. For this reason, the cameras in the scanner must be calibrated, both intrinsically and extrinsically.

3.3.1 The intrinsic calibration

The intrinsic calibration procedure is applied to determine the internal parameters of a camera, which include the focal length, the principal point, and an estimation of

3. A TOTAL BODY SKIN SCANNER

the lens distortion. These parameters need to be estimated not only to obtain the exact characteristics of a camera, but also to make use of the epipolar geometry (see Appendix A.2) when one or two cameras are installed in a stereo rig. In brief, the focal length is the distance between the focal point of the lens and the image plane (the sensor of the camera). The projection of the focal point onto the image plane along the optical axis⁸ defines the principal point. Finally, there are several types of lens distortion, such as radial, tangential and “thin prism”, which can be approximated by means of different models. These models are normally represented using a system of parametric equations, which reduce the description of distortion to several parameters. Detailed information on the intrinsic camera parameters and a variety of methods for their estimation can be found in [388, 389].

Despite the fact that all the cameras employed in the scanner are of the same model, the intrinsic calibration we obtain for one cannot be applied to all. This is due to distinctions in the acquired parameters which are normally the result of lens imperfections or differences in the mechanical components. These distinctions lead to considerable inaccuracies in the epipolar geometry of the camera rig, which is an important part of the lesion mapping pipeline (see Section 4).

Therefore, each camera had to be calibrated individually. For that purpose, we used a black-and-white calibration checkerboard containing 19×27 squares of 9.5×9.5 mm and the Camera Calibration Toolbox for Matlab[®] [390]. According to the pinhole camera model [388], the projection of a point $\mathbf{Q} = (X, Y, Z)^T$, given in the camera’s reference frame, to the image plane is:

$$\mathbf{q} = \begin{bmatrix} f \frac{X}{Z} + p_x \\ f \frac{Y}{Z} + p_y \end{bmatrix}, \quad (3.1)$$

where f is the focal length of the camera, and $(p_x, p_y)^T$ are the coordinates of the principal point (all expressed in metrics).

The goal of the camera calibration procedure is to find the transformation matrix \mathbf{K} , so that:

$$\begin{bmatrix} \mathbf{q} \\ 1 \end{bmatrix} = \mathbf{K}[\mathbf{I}|\mathbf{0}] \begin{bmatrix} \mathbf{Q} \\ 1 \end{bmatrix}. \quad (3.2)$$

In this equation, \mathbf{I} is a 3×3 identity matrix, $\mathbf{0}$ is a 3×1 vector of zeros, and the resulting point \mathbf{q} is expressed in homogeneous coordinates. The matrix \mathbf{K} is called the

⁸The optical axis is the line passing through the center(s) of curvature of the lens or an optical system. This axis normally coincides with the symmetry axis of the lens(es).

intrinsic camera calibration matrix and has the following form:

$$\mathbf{K} = \begin{bmatrix} f & 0 & p_x \\ 0 & f & p_y \\ 0 & 0 & 1 \end{bmatrix}. \quad (3.3)$$

Eq. 3.2 assumes that point \mathbf{Q} is expressed in the coordinate system of the camera. When the point(s) in space \mathbf{Q} are expressed in terms of a different coordinate system (the world coordinate frame), Eq. 3.2 is generalized to include the camera's orientation and position with respect to that system:

$$\begin{bmatrix} \mathbf{q} \\ 1 \end{bmatrix} = \mathbf{K}[\mathbf{R}|\mathbf{t}] \begin{bmatrix} \mathbf{Q} \\ 1 \end{bmatrix}. \quad (3.4)$$

\mathbf{R} is the rotation matrix and \mathbf{t} is the translation vector, which together represent the *extrinsic parameters* of the camera.

When we work with CCD cameras, it is convenient to establish direct metric-to-pixel correspondences. Thus, to obtain a point on the image plane expressed in pixel units, we can modify \mathbf{K} in the following way:

$$\mathbf{K}' = \begin{bmatrix} m_x & 0 & 0 \\ 0 & m_y & 0 \\ 0 & 0 & 1 \end{bmatrix} \cdot \mathbf{K} = \begin{bmatrix} \alpha_x & 0 & x_0 \\ 0 & \alpha_y & y_0 \\ 0 & 0 & 1 \end{bmatrix}. \quad (3.5)$$

In this representation, m_x and m_y are the pixel dimensions in the horizontal and vertical directions respectively, $\alpha_x = fm_x$ and $\alpha_y = fm_y$ represent the focal length of the camera in pixel units, and (x_0, y_0) are the coordinates of the principal point, also in pixels. A more generic version of the calibration matrix \mathbf{K}' includes a skew parameter for non-rectangular pixels $K'_{1,2} = s$, however, it is seldom used, and is normally equal to zero.

However, the simplest pinhole model described above does not provide a description of the lens distortion, and hence, cannot be accurately applied to real cameras. In order to add distortion to the pinhole model, we need to start at the very beginning as lens distortion occurs during the initial projection of the world point to the image plane. Assuming a normalized projection of point \mathbf{Q} onto the image plane ($f = 1$), and that the origin of the camera coordinates coincides with the principal point ($p_x = p_y = 0$),

3. A TOTAL BODY SKIN SCANNER

we obtain

$$q_n = \begin{bmatrix} q_{n_x} \\ q_{n_y} \end{bmatrix} = \begin{bmatrix} \frac{X}{Z} \\ \frac{Y}{Z} \end{bmatrix}. \quad (3.6)$$

Having a distortion model, we can apply it directly to the normalized image coordinates and obtain the distorted point \mathbf{q}_d . The distortion model implemented in [390] combines the radial and tangential components in the following way:

$$\mathbf{q}_d = d_r \mathbf{q}_n + d_t = (1 + k_1 r^2 + k_2 r^4) \begin{bmatrix} q_{n_x} \\ q_{n_y} \end{bmatrix} + \begin{bmatrix} 2k_3 \cdot q_{n_x} q_{n_y} + k_4 (r^2 + 2q_{n_x}^2) \\ 2k_4 \cdot q_{n_x} q_{n_y} + k_3 (r^2 + 2q_{n_y}^2) \end{bmatrix}, \quad (3.7)$$

where $r^2 = q_{n_x}^2 + q_{n_y}^2$, and $\{k_1, k_2\}$ and $\{k_3, k_4\}$ are the coefficients for the radial and the tangential components, respectively.

Now, in order to obtain the normalized distorted point \mathbf{q}_d in pixel units, it has to be denormalized and transformed accordingly using the calibration matrix K' :

$$\mathbf{q}_p = K' \mathbf{q}_d. \quad (3.8)$$

Once the point correspondences $\mathbf{Q} \mapsto \mathbf{q}_p$ are known, the calibration using the toolbox is performed in two steps [390]: the initialization and the nonlinear optimization. The initialization provides a closed-form solution to compute the calibration parameters based on the vanishing points and using the pinhole model without lens distortion. During the nonlinear optimization step, the total reprojection error is iteratively minimized (in the least-squares sense) over all the calibration parameters by means of the gradient descent algorithm. As the toolbox also computes the extrinsic parameters of the cameras with respect to the calibration plane, there will be $8 + 6n$ parameters to estimate: 8 intrinsic ($\alpha_x, \alpha_y, (p_x; p_y), \{k_1, k_2, k_3, k_4\}$) and $6n$ extrinsic (3 angles of rotation and 3 displacements, where n is the number of pattern images).

Table 3.1 shows the parameters obtained after calibrating all the cameras in the rig. As can be seen, there is a considerable discrepancy between the estimated locations of the principal points for different cameras. In a perfect camera assembly, we would expect the principal point to be in the geometrical center of the sensor at the pixel (1500;2000). However, its mean location for the 21 calibrated cameras is at (1495.60;1972.28), with a standard deviation of 94.6 and 30.96 pixels for the horizontal and the vertical coordinates, respectively. The error, or the uncertainty, of the estimated principal points for all the cameras has a mean value of 2.92 pixels for the horizontal and 3.15 for the vertical coordinate. This is a solid result, especially considering the high image resolution of 3000×4000 pixels.

Table 3.1: The intrinsic parameters of the cameras obtained using the calibration procedure.

Cam idx	Focal length		Principal point		Distortion coefficients			
	(px mm) ^a		coordinates ± error ^b (px)		k ₁	k ₂	k ₃	k ₄
0	5555.02	10.55	(1406.19; 1939.35) ± (3.90; 3.79)		-0.1304	0.2376	-0.0014	-0.0031
1	5547.02	10.54	(1390.51; 1989.97) ± (2.73; 2.58)		-0.1307	0.2490	-0.0016	-0.0021
2	5596.66	10.63	(1404.67; 1985.88) ± (2.37; 2.73)		-0.1299	0.2828	0.0004	-0.0018
3	5583.10	10.61	(1411.74; 1941.18) ± (1.92; 2.53)		-0.1380	0.2947	-0.0011	-0.0008
4	5641.88	10.72	(1400.05; 1890.25) ± (3.03; 3.07)		-0.1365	0.2670	-0.0034	-0.0034
5	5630.09	10.70	(1446.42; 1919.77) ± (3.31; 3.66)		-0.1291	0.2427	-0.0020	-0.0035
6	5578.98	10.60	(1430.84; 1975.38) ± (3.25; 3.57)		-0.1479	0.2990	-0.0016	-0.0032
7	5570.47	10.58	(1436.63; 1999.69) ± (2.66; 2.77)		-0.1325	0.2513	-0.0007	-0.0030
8	5590.63	10.62	(1372.32; 2010.65) ± (2.79; 2.96)		-0.1369	0.2578	-0.0013	-0.0041
9	5538.98	10.52	(1381.82; 1965.06) ± (2.59; 2.73)		-0.1357	0.2420	-0.0007	-0.0032
10	5564.53	10.57	(1429.60; 1995.10) ± (2.82; 3.32)		-0.1359	0.2542	0.0008	-0.0005
11	5601.63	10.64	(1574.84; 1961.87) ± (2.91; 3.07)		-0.1217	0.2100	-0.0019	0.0020
12	5576.81	10.60	(1618.69; 2014.28) ± (3.35; 3.40)		-0.1323	0.2650	-0.0015	0.0011
13	5555.40	10.56	(1630.74; 1981.58) ± (2.69; 3.45)		-0.1356	0.2838	-0.0027	0.0021
14	5573.02	10.59	(1553.92; 1982.88) ± (3.02; 3.29)		-0.1394	0.2651	-0.0021	0.0025
15	5601.23	10.64	(1596.72; 1955.19) ± (3.24; 3.49)		-0.1390	0.2699	-0.0030	0.0027
16	5657.06	10.75	(1594.05; 1963.53) ± (3.84; 4.41)		-0.1430	0.2642	-0.0034	0.0015
17	5526.78	10.50	(1589.61; 1983.77) ± (2.82; 3.06)		-0.1382	0.2556	-0.0031	0.0013
18	5569.80	10.58	(1577.99; 1990.11) ± (3.19; 3.33)		-0.1406	0.2834	-0.0022	0.0020
19	5588.61	10.62	(1575.91; 2009.22) ± (2.44; 2.75)		-0.1340	0.2513	-0.0020	-0.0002
20	5529.09	10.51	(1584.31; 1963.20) ± (2.38; 2.26)		-0.1453	0.2912	-0.0013	0.0021
Avg	5579.85	10.60	(1495.60; 1972.28) ± (2.92; 3.15)			—		

^a The focal length of the camera is expressed in units of camera pixels $((\alpha_x + \alpha_y)/2)$, and in millimeters (f). The latter is estimated using the pixel size of $m_x = m_y \approx 1.9 \cdot 10^{-3}$ mm derived from the manufacturer's data sheet.

^b The numerical error of the principal point estimation is approximately three times the standard deviation [390].

The value corresponding to the focal length of the cameras is expressed in pixel units: the average of α_x and α_y in Eq. 3.5. We converted this value into millimeters, using the pixel size approximated at $m_x = m_y \approx 1.9 \cdot 10^{-3}$ according to the manufacturer's specifications. While the focal length indicated in the image EXIF⁹ data corresponds to 11 mm, the average value of the estimated focal distance is 10.6 mm. The results obtained for the distortion coefficients clearly show that the radial component has a much higher weight and causes a significant image deformation.

⁹EXIF (Exchangeable Image File Format) is a standard for data exchange between imaging devices and software. The type of information stored in a file may vary with the camera model and normally includes data such as the time stamp, camera settings, color information, etc.

3. A TOTAL BODY SKIN SCANNER

3.3.2 The extrinsic calibration

The mapping algorithms developed for the scanner rely on information about the position and orientation of the cameras with respect to some global reference frame. The scanner's reference frame has its origin at the center of the turntable with the X -axis oriented upwards, and the Z -axis directed towards the camera rig (see Fig. 3.5). In order to obtain this information, one must either take very precise physical measurements (which is extremely difficult, especially for the orientation), or perform the extrinsic calibration with an object of known geometry. Due to possible changes in the placement of the cameras and the tediousness of taking physical measurements, calibration appears to be the optimal solution. Hence, we designed a calibration pattern to be used specifically in this scanning system. It satisfies all of the following requirements, allowing for an automatic one-shot extrinsic self-calibration of the scanner's cameras:

- compactness for easy mounting and dismounting;
- being visible to all cameras;
- containing distinguishable visual markers.

Visual markers are needed to establish point correspondences between the calibration plane and the image planes (camera sensors). Once the point correspondences are known, the orientations \mathbf{R}_n and positions \mathbf{t}_n of the cameras in three-dimensional space with respect to a given origin of coordinates can be easily recovered. For this reason, we once again make use of the functionality of the Camera Calibration Toolbox:

1. Estimate the planar transformation—homography¹⁰—between the real pattern and its image using the normalized direct linear transformation algorithm [388]. The homography obtained is then additionally refined by iteratively minimizing the reprojection error in the least-squares sense. Note, the resulting homography matrix contains only the physical part of the transformation, i.e. the rotation and the translation, because the image points are normalized prior to homography estimation.
2. Extract the rotation and the translation components from the homography matrix. The image plane and the camera plane are physically related by some

¹⁰In computer vision, planar homography can be defined as a projective mapping (a 3×3 matrix) between points belonging to two different planes. Normally, it relates a planar surface in space with the image plane of a camera observing that surface. Consequently, the homography matrix incorporates two transformations: the physical rotation and translation of the plane, as well as camera projection parameters (intrinsics).

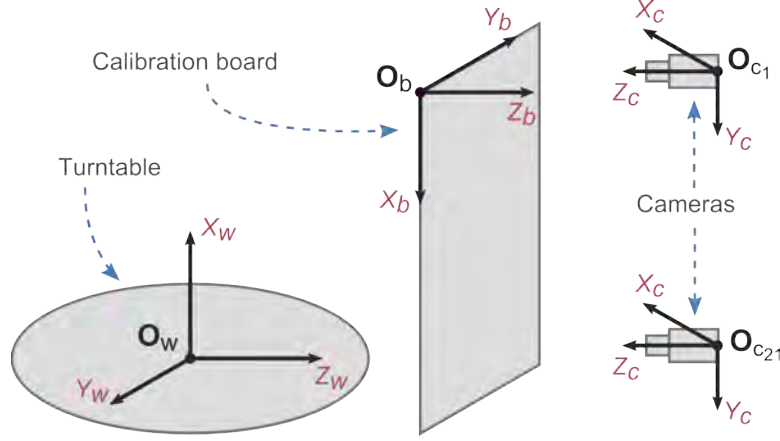


Figure 3.5: Schematic representation of the coordinate systems used in the scanner. The origin of the world coordinate system \mathbf{O}_w is in the center of the turntable. \mathbf{O}_b and $\mathbf{O}_{c1}..\mathbf{O}_{c21}$ are the coordinate origins of the calibration board and the cameras, respectively.

rotation \mathbf{R} and some translation \mathbf{t} . Hence, we can rewrite Eq. 3.4 to represent the homography between the point on the plane ($Z = 0$) and a normalized image plane point:

$$\begin{bmatrix} \mathbf{q}_n \\ 1 \end{bmatrix} = [\mathbf{R}|\mathbf{t}] \begin{bmatrix} \mathbf{Q} \\ 1 \end{bmatrix} = \begin{bmatrix} \mathbf{r}_1 & \mathbf{r}_2 & \mathbf{r}_3 & \mathbf{t} \end{bmatrix} \begin{bmatrix} X \\ Y \\ 0 \\ 1 \end{bmatrix} = \begin{bmatrix} \mathbf{r}_1 & \mathbf{r}_2 & \mathbf{t} \end{bmatrix} \begin{bmatrix} X \\ Y \\ 1 \end{bmatrix}. \quad (3.9)$$

Therefore,

$$\begin{bmatrix} q_{n_x} \\ q_{n_y} \\ 1 \end{bmatrix} = s\mathbf{H} \begin{bmatrix} X \\ Y \\ 1 \end{bmatrix}, \quad (3.10)$$

where \mathbf{H} is the homography matrix defined up to a scale factor s due to universal scale ambiguity (s is decoupled from \mathbf{H}). From this last equation, we can directly deduce the translation vector \mathbf{t} and the rotation components \mathbf{r}_1 and \mathbf{r}_2 which must be normalized previously. Finally, the third rotation vector can be found using the orthogonality property: $\mathbf{r}_3 = \mathbf{r}_1 \times \mathbf{r}_2$.

3.3.2.1 The calibration board

The calibration pattern is based on a colored checkerboard with squares of 10×10 mm. In this pattern, vertices common to at least four adjacent squares represent

3. A TOTAL BODY SKIN SCANNER

marker points, which are also referred to as *corners*. Each corner can be made unique and distinguishable by means of the colors of the squares and additional symbolic information. In order to minimize the number of distinct colors used in this encoding and to maximize the number of codes they provide, the colors are distributed in the pattern according to what we define as the *abacus encoding scheme*. The name suggests an analogy with abacus beads alternately slid along adjacent wires in order to create a number or, in this case, a pattern.

The idea of the scheme is the following: given n ($n \in \mathbb{Z}, n > 0$) uniquely colored squares and one distinguishable separator square, we can build a pattern $\mathbf{X} = [\mathbf{x}_1 \cdots \mathbf{x}_k \cdots \mathbf{x}_{n+1}]^T$, where $\mathbf{x}_1 \dots \mathbf{x}_{n+1}$ are row-vectors with $(2n + 1)$ elements, while k is the position of the middle row. This pattern will contain an $n \times 2n$ matrix \mathbf{C} of uniquely encoded internal corners (markers). In order to build \mathbf{X} and obtain \mathbf{C} , we need to perform the following steps:

- (1) Using the given squares, create a row-vector $\mathbf{y} = \langle y_1, y_2, \dots, y_{6n+1} \rangle$, where colored squares and separators are alternated, so that there are exactly $2n - 1$ squares between any two repeating colors. Start with the separator square.
- (2) Superimpose a window \mathbf{w} of $2n + 1$ elements on vector \mathbf{y} at position $p_k = 2n + 1$, so that:

$$\mathbf{w}_{p_k} = \langle y_{p_k}, y_{p_k+1}, \dots, y_{p_k+2n+1} \rangle. \quad (3.11)$$

- (3) Determine the index of the middle row (\mathbf{x}_k) of pattern \mathbf{X} and assign the selected window \mathbf{w}_{p_k} to it:

$$k = \lceil (n + 1)/2 \rceil, \quad (3.12)$$

$$\mathbf{x}_k = \mathbf{w}_{p_k}, \quad (3.13)$$

where $\lceil \cdot \rceil$ is the ceiling operator returning the smallest integer that is greater than or equal to the enclosed value.

- (4) The rest of the rows in \mathbf{X} are assigned by sliding window \mathbf{w} left or right along \mathbf{y} :

$$\mathbf{x}_i = \mathbf{w}_{p_i} = \langle y_{p_i}, y_{p_i+1}, \dots, y_{p_i+2n+1} \rangle, \quad (3.14)$$

where

$$p_i = \begin{cases} p_k + m, & \text{if } m \in 2\mathbb{Z} + 1 \\ p_k - m, & \text{if } m \in 2\mathbb{Z} \end{cases} \quad \text{and } m = |k - i|. \quad (3.15)$$

- (5) Matrix \mathbf{C} is formed by the internal corners of pattern \mathbf{X} . Each corner is uniquely

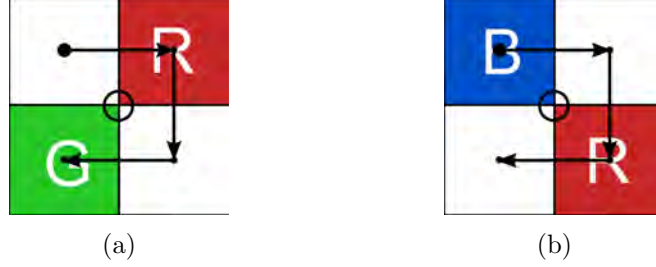


Figure 3.6: Marker encoding using the colors of the surrounding squares. The colors are listed clockwise starting from the top left. The markers depicted have the codes (a) *white – red – white – green* and (b) *blue – white – red – white*.

encoded by the colors of its 4 surrounding squares read clockwise starting from the top left (see Fig. 3.6).

To illustrate the scheme, suppose that we have $n = 4$ squares colored in red, green, blue and cyan, and a separator square of white (in Fig. 3.7, the squares are marked with the initial letters of these colors). We combine them into a sequence \mathbf{y} according to step (1), a part of which can be seen in Fig. 3.7.a. Then, we select a window \mathbf{w} wide enough to include all four squares enclosed by the separators, in total $2 * 4 + 1 = 9$ squares (see Fig. 3.7.b). This window is assigned to the middle row \mathbf{x}_k of the desired pattern (Fig. 3.7.c), where $k = 3$.

Next, by moving the window a given number of squares to the left or to the right from its original position (Fig. 3.7.b), we can obtain the rest of the rows of the pattern. More specifically, according to step (4), in order to obtain rows \mathbf{x}_2 and \mathbf{x}_4 , we need to move the window $m = 1$ squares to the right (Fig. 3.7.d). And by moving the window $m = 2$ squares to the left (Fig. 3.7.e), we get rows \mathbf{x}_1 and \mathbf{x}_5 . Fig. 3.7.c shows the complete pattern \mathbf{X} as the result of our operations with the sequence of squares \mathbf{y} . It contains exactly 32 ($\mathbf{C}_{4 \times 8}$) unique corners highlighted with circles in the figure. The uniqueness of each element in \mathbf{C} is guaranteed by the four surrounding squares in the pattern (see step (5) of the scheme). For example, $\mathbf{C}_{1,1}$ is identified as *white – cyan – white – red* and $\mathbf{C}_{1,2}$ (row 1, column 2) has the code *cyan – white – green – white*.

Similarly, on our calibration board, we use a pattern \mathbf{X} created with $n = 6$ colors, each having a unique number: red (1), green (2), blue (3), cyan (4), magenta (5) and yellow (6). The separator square is also white (0). The colors' numbers are used by the computer to encode and store the marker's color description. Thus, the corner from the previous example with the code *cyan-white-green-white* is represented as 4020.

The pattern is of 7×13 squares and contains $n \cdot 2n = 72$ unique markers. However, this number of visual markers is not enough for a one-shot calibration of all the cameras

3. A TOTAL BODY SKIN SCANNER

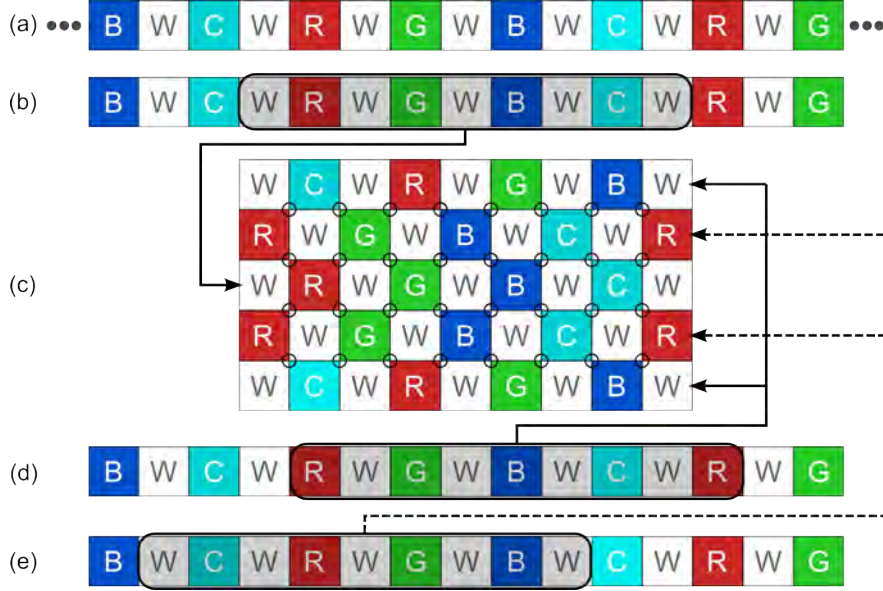
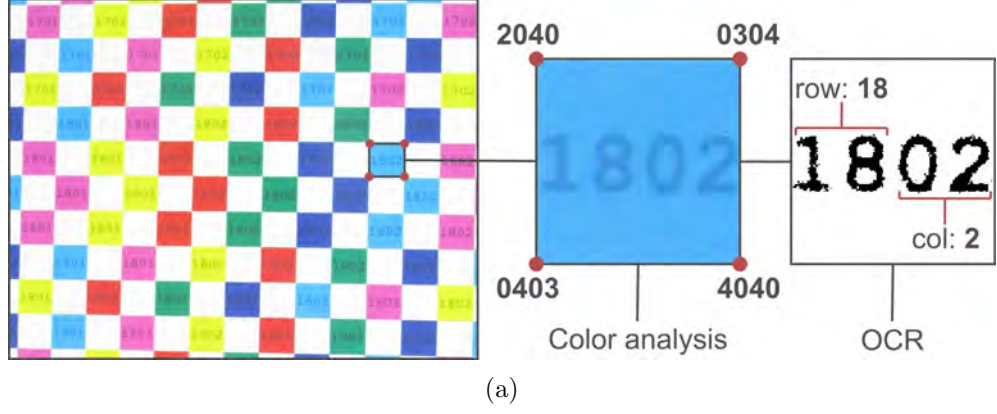


Figure 3.7: The abacus encoding scheme for $n = 4$ colors. (a) Part of the vector $\mathbf{y} = \langle y_1, y_2, \dots, y_{25} \rangle$. (b) Window \mathbf{w} of $2 * 4 + 1 = 9$ squares superimposed on \mathbf{y} at position 9. (c) Final pattern built by combining different parts of vector \mathbf{y} , obtained in (b), (d) and (e). The circles denote the matrix of markers (corners) $\mathbf{C}_{4 \times 8}$. (d) Window \mathbf{w} slid one square to the right with respect to (b). (e) Window \mathbf{w} slid two squares to the left.

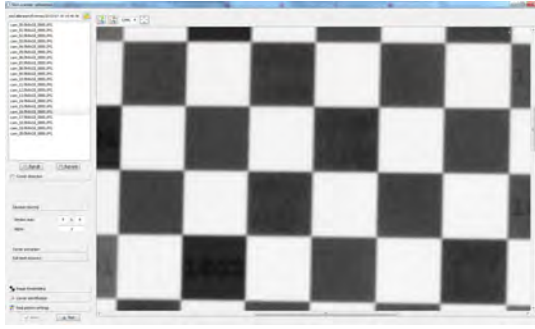
because the pattern would appear in the field of view of only a few of them. Therefore, we replicated it and tiled the copies along the vertical and horizontal dimensions, creating a continuous periodic pattern \mathbf{X}' . It consists of 33×2 sub-patterns \mathbf{X} , so that $\mathbf{X}'_{i,j} = \mathbf{X}$ for $i, j \in \mathbb{N}_{>0}$, and measures 1980×250 mm. An image of this pattern acquired by one of the cameras is shown in Fig. 3.8.

Vertically, the tiling was done so that the last row of the upper sub-pattern $\mathbf{X}'_{i,j}$ is at the same time the first row of the sub-pattern $\mathbf{X}'_{i+1,j}$ directly below it. In the same way, for the patterns tiled horizontally, the last column of sub-pattern $\mathbf{X}'_{i,j}$ to the left is the first column of $\mathbf{X}'_{i,j+1}$ to the right. Each colored square in the pattern \mathbf{X}' bears a number identifying the row i and the column j of its corresponding sub-pattern $\mathbf{X}'_{i,j}$. This ensures the uniqueness of the markers in the whole pattern. The numbers are written inside the squares, and their colors have the same hue, but a lower intensity as compared to the background. In this way, the numbers are easily readable and the color integrity of the squares is sufficient.

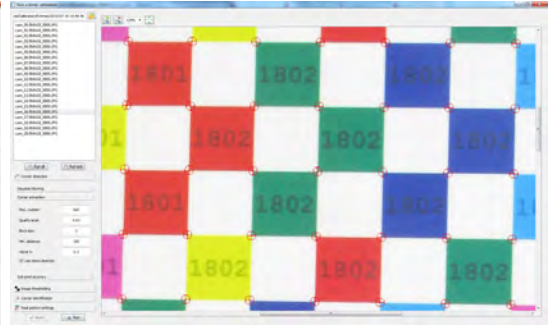
Overall, using this calibration pattern, all that is needed is to recognize one number and the colors of two diagonal squares in order to identify all the markers visible in the image. This makes it a very robust system for automatic camera calibration.



(a)



(b)



(c)

Figure 3.8: Images of the calibration pattern. (a) Part of the real calibration pattern mounted in the scanner and photographed by camera 16. The image contains fragments of sub-patterns $\mathbf{X}'_{17,1}$, $\mathbf{X}'_{18,1}$, $\mathbf{X}'_{19,1}$, $\mathbf{X}'_{17,2}$, $\mathbf{X}'_{18,2}$, and $\mathbf{X}'_{19,2}$. The highlighted corners of the cyan square are identified clockwise as *green – cyan – white – white* (2040), *white – blue – white – cyan* (0304), *cyan – white – cyan – white* (4040), and *white – cyan – white – blue* (0403). Next, the cyan square is binarized and analyzed with the Tesseract OCR engine. The first two digits denote the sub-pattern’s row (18), while the second two are the column (2). (b-c) Software interface for the extrinsic camera calibration. The two images demonstrate a part of the pattern shown in (a) in gray-scale and with corners detected, respectively.

3.3.2.2 Visual marker recognition

The main steps for visual marker identification are given in Algorithm 1. Since each marker is represented by a point common to some adjacent squares of the pattern, the procedure starts by detecting the corners in the image. For each corner detected, we assign its four immediate neighbors: the corners located to its north, south, east and west (see Fig. 3.9). Following that, the attributes of one of the corners in the image—the colors of its surrounding squares and the number of the sub-pattern it belongs to—need to be identified. The attributes of the rest of the corners in the image can be deduced recursively knowing the pattern structure and the corners’ neighborhood information. In this way we can obtain the correspondences between the real pattern’s

3. A TOTAL BODY SKIN SCANNER

Algorithm 1: Primary steps for visual marker identification

Data: Image of the calibration pattern I
Result: List of point correspondences \mathbf{pp}

```

1 /* Corner detection */
2 /* 1. Transform I to gray scale */
3  $G \leftarrow \text{colorToGrayscale}(I)$ ;
4 /* 2. Smooth G */
5  $G \leftarrow \text{applyGaussianFilter}(G)$ ;
6 /* 3. Find corners in the binary image */
7  $\mathbf{cc} \leftarrow \text{detectCorners}(G)$ ;
8 /* Corner identification */
9 /* 4. Assign neighbors (north, south, east and west) to each corner */
10  $\mathbf{nn} \leftarrow \text{findNeighbors}(\mathbf{cc})$ ;
11 /* 5. Recognize initial corner */
12  $\mathbf{pp}_i \leftarrow \text{identifyInitialCorner}(\mathbf{cc}, \mathbf{nn})$ ;
13 /* 6. Identify the rest of the corners recursively */
14  $\mathbf{pp} \leftarrow \text{identifyCorners}(\mathbf{pp}_i, \mathbf{nn})$ 

```

markers and their coordinates in the images.

The steps outlined in Algorithm 1 are applied to all 21 images acquired during the calibration phase (see Section 3.1.1). The description of each step in the algorithm is provided below:

1. **Color-to-gray-scale image conversion.** The main task of the gray-scale image conversion is to increase the contrast between the white and the colored squares in the gray-level image. To do this we retain the lowest color intensity value for each pixel:

$$G_{x,y} = \min(I_{x,y,1}, I_{x,y,2}, I_{x,y,3}), \quad (3.16)$$

where x, y are pixel coordinates, and I and G are the color and gray-scale images, respectively. The white squares have higher intensities than the surrounding colored squares in all channels, so the contrast between the resulting “white” and “gray” areas will be significant. See Fig. 3.8b for an example of the gray-scale conversion.

2. **Smoothing the gray-scale image.** After the conversion, the gray-scale image is not going to be uniform. This is due to the image noise and the fact that the numbers indicating the sub-pattern have lower intensities than that of their respective squares. For these reasons, the corner detection may produce unwanted artifact corners inside the squares. In order to smooth the non-uniform areas, the

image is convolved with a Gaussian filter.¹¹ For the chosen lens magnification factor and the distance between the calibration board and the cameras, the size of the filter was set to 9×9 pixels with $\sigma = 3$.

3. **The corner detection** is performed by means of the Harris corner detector [391]. The minimum distance between the corners found was set to 100 pixels (based on the calibration images) and only the most stable ones in this vicinity were retained. The sensitivity parameter of the detector was set to $k = 0.2$.
4. **Neighbor assignment.** Each marker in the real pattern has a maximum of 4 immediate orthogonal neighbors: those lying to the north, south, east and west of the marker of interest (see Fig. 3.9a). Most of the markers have a full 4-connected neighborhood, except for those located at the extreme corners of the calibration pattern (2 neighbors) and those on the borders (3 neighbors).

In order to establish a link between the pattern corners detected in the images and the real markers in the pattern, we need to determine their neighborhoods. For that, we select the 4 points closest to each corner of interest and assess the angles between the vectors formed by the neighbor-pairs and the axes in the image (Fig. 3.9). The angle between the neighbor-pair vector and the vertical axis (\vec{x}) conditions the north and the south neighbors, while the east and the west neighbors are determined by the angle with the horizontal axis (\vec{y}). Ideally, the vectors should coincide with the axes, but because the pattern is not strictly fronto-parallel to the cameras, the angle will be defined within a certain range t_α , which was empirically set to 17° .

Following the example in Fig. 3.9a, point E is assigned as the eastern neighbor of C if the angle between the vector \vec{CE} and the \vec{y} -axis is less than t_α . Similarly, point N is the northern neighbor of C if vector \vec{CN} and the \vec{x} -axis form an angle less than $180^\circ - t_\alpha$ (compensated for the opposite directions of the vectors). The other neighbors are assigned in the same way.

5. **Corner attribute identification.** In order to identify the attributes of a corner of interest, i.e. the colors of the squares and the sub-pattern number, the regions of interest (ROIs) corresponding to the diagonally opposite squares have to be extracted. For that we rely on the neighborhood information obtained in the previous step and extract the ROI containing the pattern square north-west of

¹¹In 2-D, a circularly symmetric Gaussian filter has the form: $G(x, y) = \frac{1}{2\pi\sigma^2} e^{-\frac{x^2+y^2}{2\sigma^2}}$, where σ is the standard deviation of the Gaussian distribution.

3. A TOTAL BODY SKIN SCANNER

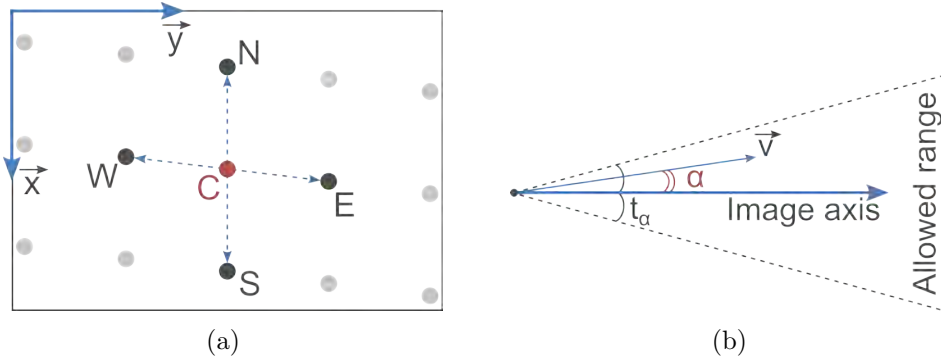


Figure 3.9: Neighbor corners selection. (a) A schematic representation of an image depicting the calibration board. The points are the corners of the pattern: C is the corner of interest, N, S, E and W are the closest neighbors of C . The vectors \vec{x} and \vec{y} are the axes of the image. (b) The definition of the angle α which determines the side of the neighbor (north, south, east or west). \vec{v} is one of the vectors $\vec{CN}, \vec{CS}, \vec{CE}$ or \vec{CW} . Image axis can be either \vec{x} or \vec{y} . If α is less than the threshold angle t_α , then the corner is either the eastern (for image axis \vec{y}) or the southern (for \vec{x}) neighbor. While if α is less than $180^\circ - t_\alpha$, the neighbor lies to the west (for \vec{y}) or the north (for \vec{x}).

the corner of interest. We identify the color of the square by simply taking the median value of the pixels in each channel and compare them against explicitly defined RGB ranges.¹² If the square color is white, we extract and analyze the north-east and the south-west squares, otherwise, we continue with the south-eastern ROI.

After identifying the colors of the two non-white diagonally opposite squares adjacent to the corner of interest, its sub-pattern number must be determined. Therefore, we binarize both colored square ROIs and apply the Tesseract optical character recognition [392] to read the printed digits. The corner will be assigned to the sub-pattern with the largest identification number, which is especially important when the marker is on the border between two sub-patterns.

Prior to the ROI binarization, the color images of the squares are transformed to a gray-level representation. If the color is red, green or blue, the respective RGB plane is used as the gray-scale image. If the color is yellow, magenta or cyan, we use the color-constituting plane with the smallest mean intensity value, e.g., for the yellow color, we choose between the red and the green channel. The binarized images of the sub-pattern numbers are obtained by globally thresholding the gray-scale image using the Otsu method [393]. Despite its simplicity, the performance of this method is sufficient for the Tesseract engine to correctly recognize the

¹²This solution lacks generality and strongly depends on the lighting conditions but is easy to tune and works very well in the controlled environment of the scanner.

digits.

6. **Recursive corner identification.** Having identified one pattern corner in the image, and knowing the neighborhood information of the markers in the calibration board, it is fairly easy to identify the other corners. This can be done by recursively finding the correspondences between the markers' neighbors in the image and those in the real pattern. This procedure is very fast as well as reliable: once all parameters are set, failure is possible only if the first corner is identified incorrectly due to damage of the pattern surface or a drastic change in the illumination conditions.

3.4 Prototype restrictions

The scanning system described is intended for use in a clinical setting with the aim of performing total body imaging and detecting new and/or evolving skin lesions. In this respect, there are several restrictions defining the eligibility of the patients for scanning. Firstly, the absence or scarcity of body hair. This requirement is essential, since the automatic assessment of lesion change cannot be performed correctly in the presence of hair, as can be appreciated in Fig. 3.10a. Moreover, because of body hair, the algorithms presented in Chapter 4 may fail to establish correspondences between lesion images that were acquired during consecutive explorations.

Secondly, although the scanner cabin can freely accommodate patients with a height and weight of up to 199 cm and 200 kg respectively, there is a restriction on the subject's body constitution. This is due to the dimensions of the turntable and its distance from the cameras, which can be defined as follows: all body regions of the patient must be within the volume created by (1) the plane tangent to the backrest column, and (2) the larger arc of the turntable formed by the intersection with that plane. This volume is shown in Fig. 3.11a, and its 2D schematics in Fig. 3.11b. The blue delineation in the latter figure is the profile of the described volume.

An additional constraint is imposed by the necessity of fixing the focusing points of the cameras. Consequently, a 400–450 mm distance to the calibration board was chosen so that the elements of the trunk, including the shoulders when the turntable rotates, are in focus in all the images acquired. However, the depth of field (DOF) resulting from the adopted configuration may not perform equally well for all patients at every turntable position even if they satisfy the previous requirement. Depending on the constitution of the subject, some body areas, if too far or too close to the camera

3. A TOTAL BODY SKIN SCANNER



Figure 3.10: Examples demonstrating limitations of the imaging subsystem. (a) Body hair (pectoral area) obstructing the view of the skin lesions. The detection and change assessment of PSL may fail for patients with dense body hair. (b) Blurring in images of body regions that are outside the camera's depth of field. The image, captured by camera 19 at turntable position 21 (pose 2), depicts the legs of a patient above the knees. The left thigh, which is closer to the camera, is in focus, while the right one in the background is blurred. The body hair on this image is not dense, however, it can pose a problem for inter-exploration PSL matching (for details, see Sections 4.2.1, 5.3.1, and 6.3)

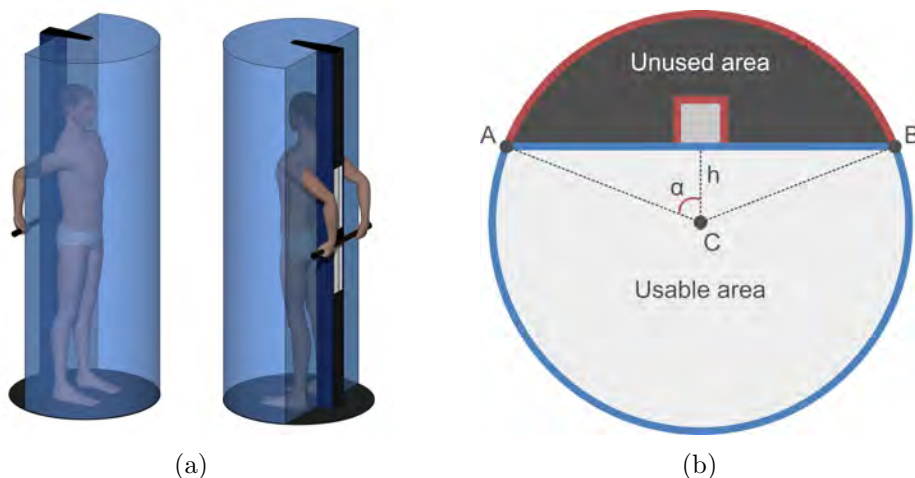


Figure 3.11: The volume defining limits of the patient area in the acquisition chamber. (a) A 3D representation of the volume depicting the turntable, the backrest column and a patient in pose 2 inside the volume. (b) A 2D schematics (top view) of the turntable with the volume profile delineated. The radius AC of the turntable is equal to 400 mm, the distance from its center to the column is 145 mm, and the length of the chord AB is 372.79 mm. The angle forming the larger arc AB is $360^\circ - 2\alpha = 222.5^\circ$, where $\alpha = 68.75^\circ$.

rig, may appear blurry in the images. For example, the shins of a patient of asthenic habitus in pose 2 (with the back to the column) will be outside the DOF at turntable steps 5–6. Similarly, an individual with wide shoulders/hips, or a large abdominal

region, may be too close to the cameras, exceeding the lower limit of the DOF.

The example shown in Fig. 3.10b demonstrates a scenario of passing the higher limit of the depth of field, where the right thigh is much farther from the camera than the left one. As can be seen, besides the expected difference in resolution and level of detail, the farther thigh is out of focus. It must be noted though, that the imaging system has not been extensively tested on patients with various body constitutions. Therefore, the final configuration of the camera parameters and the focusing distance may be subject to change in the future.

3.5 Conclusions

The total body skin scanner described in this chapter serves to perform a complete exploration of the patient's skin surface. Equipped with a rig of high-resolution digital cameras, polarized lighting system and a mechanically driven turntable, the scanner provides a controlled environment for an optimal total body image acquisition. The scanning procedure is automated and requires a minimal involvement of the operator: necessary patient data input/retrieval and monitoring for pose changes and emergency situations. The output of an automated skin examination procedure is a set of overlapping images (more than 500) covering the entire visible body surface of the patient.

In order to utilize the controlled environment of the acquisition chamber, the cameras must be calibrated both intrinsically and extrinsically. The intrinsic calibration was performed on each camera separately, using a black-and-white calibration board. For the purpose of performing a one-shot extrinsic calibration of the camera rig, we designed a special pattern bearing unique visual markers. We also developed a software to automatically recognize the markers in the pattern images and, thus, obtain a set of corresponding points necessary for the estimation of the cameras' positions and orientations.

One of the main hardware trade-offs that we had to accept in this skin scanner lies in the configuration of the imaging subsystem, i.e. the number of cameras, their orientations and locations, and their parameter settings. The system must be able to capture images with high resolution with at least a 50–70% overlap between adjacent cameras and a large depth of field, so that body regions at different distances from the cameras are in focus. In addition, the number of cameras had to be minimized in order to decrease the final cost and complexity of the imaging subsystem. Thus, the camera set-up, described in Section 3.1.1 reaches a satisfactory trade-off between all the desired requirements and provides an image resolution in the range of 9–22 pixels per

3. A TOTAL BODY SKIN SCANNER

millimeter (px/mm), with an average of 14 px/mm.¹³ Nevertheless, this setup must be extensively tested in a real clinical setting on patients with different body constitutions, hence, the established camera parameters and the focusing distance may be modified to achieve a better overall performance.

In addition, there are ways to improve the image quality with respect to focusing and image resolution, sacrificing, however, the cost of the scanner. One of them is using either an external, active auto-focusing system based on ultrasonic sound waves or cameras equipped with such a system. In this way, it will be possible to dynamically define the focus point for each camera. Such a set-up can be used as far as the cameras are able to capture images simultaneously after establishing the focusing distance.

Overall, given the characteristics of the equipment employed, the proposed scanner set-up provides an optimal balance between the image resolution, the depth of field and the number of cameras employed. Moreover, the mutual orientation of the two camera columns allows for reliable interest point matching in stereo images, which, in turn, forms the algorithmic basis for the PSL mapping proposed in the following chapter.

¹³This range was estimated using the PSL data of two patients of different heights and weights. Overall, the image resolution is conditioned by the distances between the cameras and the body region in the field of view, and will vary depending on the patient's constitution.

Chapter 4

Automatic PSL change detection

The total body skin scanner presented acquires 504 high-definition skin surface images in one exploration. This is a large amount of raw data and cannot be used “as is” to detect changes in PSLs. In the first place, the data need to be processed so as to segregate images of lesions which are going to be compared with the baseline. Moreover, it is clear that many lesions will appear in more than one image, hence, it is essential that the system identifies these lesions and keeps track of all their views. Finally, all the PSLs detected during one exploration must be matched to those obtained in a successive scan. Therefore, a set of image and data processing operations allowing for such data segregation and organization, which we call *mole mapping*, must be applied.

Mole mapping means detecting PSLs in the images and establishing their *intra-* and *inter-exploration correspondences*. While the former defines correspondences between PSLs on the patient’s body and their images acquired during one exploration, the latter links lesions between two successive scans. In other words, upon completing an exploration, the scanner will have a set of images from different angles assigned to each lesion detected. And after scanning the same patient again, it will automatically determine correspondences between lesions identified in the two explorations.

4.1 Intra-exploration mole mapping

The pipeline for obtaining intra-exploration correspondences, or a mole map, consists of the three main stages shown in Fig. 4.1. The first stage provides 2D information about the lesions in the images, i.e. locations and dimensions. Then, this information is passed to the next stage where groups of moles (mole sets) are acquired at each position of the turntable. In the final stage, these sets are combined into one map.

4. AUTOMATIC PSL CHANGE DETECTION

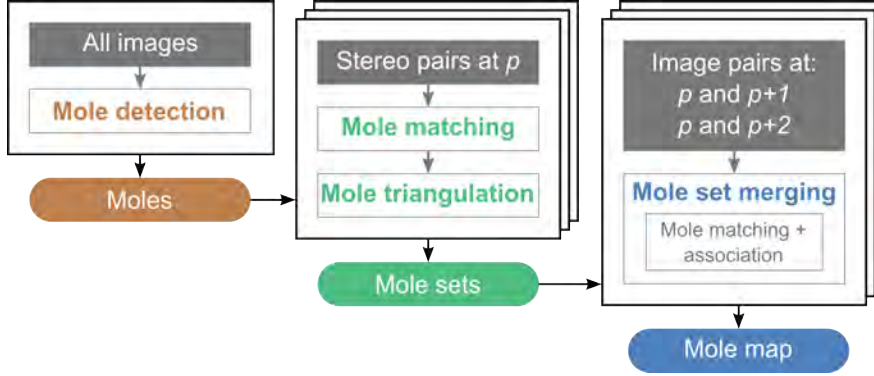


Figure 4.1: The pipeline for creating a mole map. At first, PSLs are detected in the acquired images as blobs using the MSER detector. Then, these blobs are matched and triangulated in stereo pairs at every turntable position $p \in P$, where $P = [0, 23]$, resulting in 24 sets of mole representations, with associated 3D coordinates and 2D images. The stereo mole matching is carried out by computing homographies (using SIFT features) between the lesions’ ROIs and assessing their locations in the common reference frame. Finally, all the mole sets are merged into a mole map by matching overlapping moles between sets p and $p + 1$, as well as p and $p + 2$, and associating all indirect matches.

4.1.1 Mole detection

We detect moles by means of the maximally stable extremal regions (MSER) detector [394]. The interested reader can find details of this algorithm in Appendix A.1. In brief, given a grayscale image, MSER is able to find salient blobs of various dimensions and shapes. Several parameters regulating the stability and size of the resulting blobs can be used to tweak the algorithm in order to obtain the desired output. Because PSLs are normally darker spots of variable shapes and sizes on a lighter skin, we can successfully use this detector to determine their precise locations.

However, depending on the saturation of the background (lighter or darker skin), lesions with the same real intensity will appear differently.¹ Therefore, it is essential that prior to the detection phase, the input image is preprocessed in such a way that all distinctions related to skin color are attenuated as much as possible. In concrete, we want the algorithm to detect well-distinguished lesions that look darker than the surrounding skin, no matter its color.

4.1.1.1 Foreground (skin) detection

Before enhancing the images, we need to define image areas that correspond to the patient’s skin (image foreground). This information is crucial, because: (1) the ranges

¹Moreover, based solely on the color characteristics of the PSLs, an untrained observer can hardly distinguish a light-colored nevus from a dark freckle. However, we can ignore this distinction for the moment as in our study we are interested in the detection of changes in PSLs in general.

of skin intensities are required for correct contrast stretching, and (2) MSER blobs and SIFT features detected in the image background (scanner walls or the backrest column) should not be taken into account. In order to separate the foreground, we explicitly define the skin region in the HSV (Hue-Saturation-Value) color space, as can be seen in Algorithm 2. Apart from the fact that it is the simplest of the existing skin detection techniques [395], due to the controlled environment of the scanner’s acquisition chamber, it yields excellent results.

The algorithm starts with the conversion of the input RGB image to an HSV color space:

$$\begin{aligned} H &= \arccos \frac{0.5((R - G) + (R - B))}{\sqrt{(R - G)^2 + (R - B)(G - B)}}, \\ S &= 1 - 3 \frac{\min(R, G, B)}{R + G + B}, \\ V &= \frac{1}{3}(R + G + B). \end{aligned}$$

The hue channel of the HSV space is invariant to illumination changes (assuming white light) [395], hence, it is robust against uneven illumination at different body orientations with respect to the cameras. After this conversion, the H and V channels are smoothed using a Gaussian function to attenuate high contrast pixels on the skin’s surface, i.e. hairs and darker moles. Moreover, we have empirically defined a range of numerical hue values corresponding to different skin types. Thresholding the hue image using these values helps create an initial skin mask which serves as the refinement for the thresholded “value” channel.

By means of a multiplication factor of 3, the “value” channel—or the luminance—is artificially saturated. Due to the black color of the scanner’s interior (background), the luminance of the well-lit patient’s skin (foreground) becomes significantly higher and, after its range is normalized, allows for easy thresholding. But prior to that, the new luminance channel is convolved with the hue mask to get rid of any foreground artifacts (hair, clothing if any, etc.). Finally, the obtained mask is smoothed using a median filter. The filter sizes we used in the experiments were 7×7 pixels for the median and 11×11 pixels with $\sigma = 3$ for the Gaussian.

4.1.1.2 Image preprocessing

Now, when areas in the images that correspond to the patient’s skin surface are known, it is possible to prepare the images for the blob detection stage. We use a sequence of simple operations for this purpose. Namely, given a color image I_{rgb} resized by a

4. AUTOMATIC PSL CHANGE DETECTION

Algorithm 2: Image foreground (skin) detection

```

Data: Image  $I_{rgb}$  of size  $1000 \times 750 \times 3$ 
Result: Binary foreground mask  $M_F$  of size  $1000 \times 750$ 

1   $T_h^{low} = 0.01, T_h^{high} = 0.25, T_v = 0.4;$                                 /* Thresholds */
2  /* RGB to HSV conversion */
3   $I_{hsv} \leftarrow RGBtoHSV(I_{rgb}); I_h \leftarrow I_{hsv}(:, :, 1); I_v \leftarrow I_{hsv}(:, :, 3);$ 
4  /* Gaussian smoothing */
5   $I_h \leftarrow I_h \otimes g; I_v \leftarrow I_v \otimes g;$ 
6  /* Hue thresholding */
7  for all pixels  $p$  in  $I_h$  do
8      if  $I_h(p) > T_h^{low}$  AND  $I_h(p) < T_h^{high}$  then
9           $M_T(p) \leftarrow 1;$                                 /* Temporary skin mask */
10         else
11              $M_T(p) \leftarrow 0$ 
12         end
13 end
14 /* Intensity (value) gain and contrast stretching */
15  $I_v \leftarrow stretchContrast(3 \cdot I_v);$ 
16 /* Hue-based masking */
17  $I_v \leftarrow I_v \circ M_T;$ 
18 /* Intensity thresholding */
19 for all pixels  $p$  in  $I_v$  do
20     if  $I_v(p) > T_v$  then
21          $M_F(p) \leftarrow 1;$                                 /* Final foreground mask */
22     else
23          $M_F(p) \leftarrow 0$ 
24     end
25 end
26 /* Foreground mask filtering with median filter */
27  $M_F \leftarrow M_F \otimes f$ 

```

factor of $\alpha = 0.25$, the gray-scale image I_g is obtained by finding the minimum intensity value of each pixel across the 3 channels of I_{rgb} : $I_g(x, y) = \min(I_{rgb}(x, y, c))$, where (x, y) are pixel coordinates and $c \in [1, 2, 3]$ are color channel indices. Next, we improve the contrast of I_g by stretching the range of skin intensities (obtained using the skin mask) to the full range of normalized values $[0, 1]$. Finally, we compute image I_{gp} by subtracting I_g from its complement: $I_{gp}(x, y) = 1 - 2 \cdot I_g(x, y)$. Running a 5×5 median filter on the resulting I_{gp} helps reduce unwanted image noise. See Algorithm 3 for the pseudo-code description of the algorithm.

This preprocessing procedure allows emphasizing pigmented lesions which normally have lower intensity values than the surrounding skin, by practically eliminating higher intensities in the background. At the same time, undesirable artifacts, such as hair,

Algorithm 3: Image preprocessing for mole detection

Data: RGB image I_{rgb} of size $4000 \times 3000 \times 3$

Result: Processed grayscale image I_{gp} of size 1000×750

```
1  $I_{rgb} \leftarrow \text{resize}(I_{rgb}, 0.25);$ 
2 /* Obtain grayscale image  $I_g$  */
3 for  $i \leftarrow 1$  to 1000 do
4   for  $j \leftarrow 1$  to 750 do
5      $I_g(i, j) \leftarrow \min([I_{rgb}(i, j, 1), I_{rgb}(i, j, 2), I_{rgb}(i, j, 3)]);$ 
6   end
7 end
8 /* Stretch image contrast using the skin intensity values */
9  $I_g \leftarrow \text{stretchContrast}(I_g, \text{skinMask});$ 
10 /* Subtract  $I_g$  from its complement */
11  $I_{gp} \leftarrow 1 - 2 \cdot I_g;$ 
12 /* Filter the result */
13  $I_{gp} \leftarrow I_{gp} \otimes f;$ 
```

acne and pores, are attenuated and cannot be represented as stable extremal regions as PSLs after the preprocessing.

Running the MSER detector on the image I_{gp} yields stable mole regions (blobs) which are approximated by ellipses with their respective dimensions (major and minor axes) and locations (center coordinates). Additionally, we filter these blobs based on their size and aspect ratio. It is rather safe to assume that PSLs with the largest axis less than $T_a = 15$ pixels are not going to be useful for a change analysis. Furthermore, the natural shape of a PSL is an ellipse with a small value of flattening. Highly flattened shapes, such as blobs produced by hair or skin folds, can be discarded by thresholding their compression factor: the ratio between the minor and the major semi-axes. The minimum value allowed was empirically set to $T_{ar} = 0.2$.

4.1.2 Stereo-pair processing

Depending on the location, each camera in the scanner has 2 or 4 immediate neighbor cameras, whose arrangement makes a significant vertical or horizontal overlap of their images possible. We distinguish between vertical and diagonal camera neighbors as: (a) adjacent cameras on the same column and (b) those belonging to different columns, respectively. These cameras can be combined into *stereo pairs*, 39 in total.

The stereo image pairs acquired by these cameras can be used for matching and subsequent triangulation of the moles detected (MSER blobs). However, stereo pairs can be combined only using images obtained at the same turntable position $p \in P$,

4. AUTOMATIC PSL CHANGE DETECTION

where $P = [0, 23]$. This condition is based on the fact that the pose of the patient may not be exactly the same at two turntable positions due to breathing and/or involuntary movements. This effectively means that the epipolar geometry is not applicable in this case, and the triangulation error can be too big if the stereo-images are not acquired simultaneously.

4.1.2.1 Mole matching

In order to match mole blobs in a stereo pair, we make use of epipolar geometry computed from the extrinsic and intrinsic calibration of the cameras (see Appendix A.2 for details). Given a mole (a MSER blob) in one image, its match candidates in another image are sought along the corresponding epipolar line. Candidate moles are chosen so that their distances from the epipolar line do not exceed the threshold T_e , which was empirically set at 60 pixels. This tolerance is acceptable taking into account the size of the images (4000×3000 pixels) and that in some views the skin surfaces may appear highly slanted.

In addition, the match candidates detected undergo a filtering procedure that eliminates obvious erroneous correspondences. This procedure is based on the known information about the cameras' mutual arrangement. In other words, by comparing the row-coordinates of the target mole and its match candidates, we can expect a certain pattern. Namely, for the vertical camera neighbors, the coordinate difference should be greater than $\frac{1}{3}$ of the image's height (~ 1300 px), while for the diagonal neighbors it must not exceed 2000 pixels.

Next, the mole candidates acquired are compared visually. This is done by computing a homography transformation $H_{3 \times 3}$ between image patches (ROIs) taken around the corresponding MSER blob centers.² For this purpose, we use SIFT [315] to detect and describe salient keypoints in both ROIs and then find their correspondences. The foreground (skin) masks are used to discard any keypoints detected in the background. Next, the obtained SIFT correspondences are fed into the random sample consensus (RANSAC) algorithm [316] for inlier detection based on fitting a projective homography model (see Appendices A.3 and A.4 for more information on these algorithms). The homography, if computed and valid, serves to transform one of the ROIs into the reference frame of the other. And by estimating how close the two mole blobs are to each other in the common reference frame, it is possible to determine whether they represent the same real lesion. Therefore, in order for two mole representations to match,

²Since the camera-to-body distances are similar for most patients, we empirically fixed the ROI size to 400×400 pixels.

Algorithm 4: Mole matching in a stereo pair

Data: Images I_1, I_2 ; lists of detected MSER blobs in each image m_1, m_2 ;
threshold T_H
Result: Matrix M containing index pairs of matching MSER blobs

```
1 /* Get epipolar match candidates */
2  $cM \leftarrow getEpipolarMatches(m1, m2)$ ;
3 for all candidates  $c$  in  $cM$  do
4   /* Extract image ROIs around the blobs */
5    $R_1 \leftarrow extractROI(I_1, m_1)$ ;  $R_2 \leftarrow extractROI(I_2, m_2)$ ;
6   /* Extract skin mask ROIs around the blobs */
7    $B_1 \leftarrow extractSkinMask(I_1, m_1)$ ;  $B_2 \leftarrow extractSkinMask(I_2, m_2)$ ;
8   /* Compute homography transformation */
9    $H \leftarrow computeHomography(R_1, R_2, B_1, B_2)$ ;
10  if  $H$  is NOT empty AND  $exp(abs(ln(abs(H(3,1)) + abs(H(3,2))))) > T_H$  then
11    /* Warp the MSER ellipse of mole2 to the ref. frame of mole 1 */
12     $m_2 \leftarrow warp(m_2, H)$ ;
13    /* Compute the distance between the two ellipses */
14     $d \leftarrow euclideanDistance(m_1.location, m_2.location)$ ;
15    if  $d < m_1.majorAxis$  AND  $d < m_2.majorAxis$  then
16      | Append  $m_1(cM(c, 1))$  and  $m_2(cM(c, 2))$  to  $M$ 
17    end
18  end
19 end
```

the following condition has to be satisfied:

- *The distance between the centers of the moles' ellipses must be smaller than both their major axes.*

See Algorithm 4 for the pseudo-code of the matching procedure.

If the homography can be computed, i.e. there are enough SIFT feature matches, its validity is verified by satisfying the condition

$$e^{|ln(|H_{3,1}| + |H_{3,2}|)|} < T_H, \quad (4.1)$$

where $T_H = 800$ is the accepted threshold. The absolute sum of the elements $H_{3,1}$ and $H_{3,2}$ of the normalized homography can give an idea of how misshaped the image will be after the transformation: the larger the value, the more the induced deformation. An excessively misshaped image means that the transformation homography was computed using wrong SIFT feature matches and, thus, should be discarded. By using logarithmic and exponential functions, we can amplify the resulting value so that the threshold can reliably cut off incorrect transformations.

4. AUTOMATIC PSL CHANGE DETECTION

4.1.2.2 Mole triangulation

Once the matching MSER blobs in a stereo pair have been found, we can now acquire their locations in 3D space, i.e perform the triangulation. Knowing the intrinsic and extrinsic parameters of the stereo rig, the reconstruction by triangulation is unambiguous and straightforward. The “mid-point method” [396, 397] used for this purpose is very simple. Although its accuracy is considered to be poor [397], it can well be applied to obtain the 3D locations of PSLs. Firstly, because the final triangulation output is not expected to be, nor can be, precise due to the unavoidable motion of the subject during the exploration. And secondly, due to the linear implementation, the algorithm is very fast, which is an important advantage when processing many points (lesions). The interested reader can find a detailed explanation of the algorithm in Appendix A.5.

During the triangulation, we also compute normals to the local surfaces of the lesions. To do this, a ring of 180 points is placed around the center of the mole ellipse in one ROI. The diameter of the ring is equal to the major axis of the mole’s MSER ellipse. Knowing the homography transformation between the two regions of interest, the coordinates of each point in the ring can be computed in the other ROI. Then, by triangulating these points, a three-dimensional ring surrounding the detected lesion is obtained. The normal of the plane fit to the 3D point ring is the normal to the mole’s surface.

Using the normal to the lesion surface, we can compute two important metrics. One is the resolution of the image at the mole site, which shows how many pixels of the mole ROI constitute 1 millimeter on the skin’s surface (px/mm). In order to compute this, we need to know the distance from the camera to the PSL and its estimated diameter in millimeters. While the former is straightforward, the latter can be obtained using the relationship from the pinhole camera model [388]:

$$\frac{d}{D} = \frac{f}{L}. \quad (4.2)$$

In this relationship, f is the focal length of the camera, L is the distance between the mole and the camera, and D and d are the diameter of the mole and its projection (in mm), respectively. Consequently, the local resolution of the image at the lesion site is

$$\gamma = \frac{d'}{D}, \quad (4.3)$$

where d' is the diameter of the lesion’s blob in pixels.

The second metric η is a relative quantitative measure which will serve to define

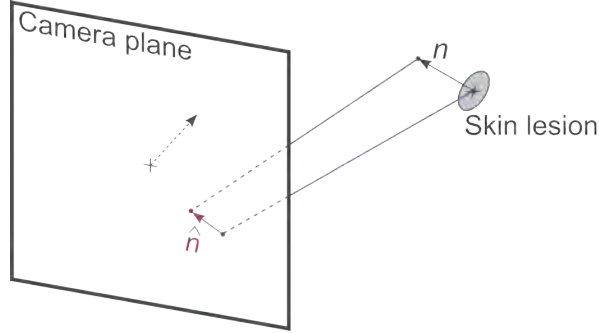


Figure 4.2: The projection, \hat{n} , of a lesion's normal unit vector, n , to the image plane. It is used to compute the η -metric for best mole view selection.

the best view of a mole among the available images (at least two). In this metric, we seek to maximize the pixel-per-millimeter resolution and, at the same time, minimize the skew of the mole's projection on the image plane. In other words, a camera with the smallest η will be both close to the lesion and as perpendicular to its normal as possible. The definition of the metric is

$$\eta = \frac{|\hat{n}^2|}{\gamma}, \quad (4.4)$$

where \hat{n} is the image projection of the unit vector normal to the surface of the lesion (see Fig. 4.2). The less perpendicular the mole's normal is to the camera plane, the larger the length of the projected vector. In addition, we raise the numerator to the second power to prioritize the orientation of the mole over the image resolution.

Overall, the result of the stereo-pair processing performed at each turntable position is a set of 3D points corresponding to the centers of the real PSLs. Each 3D point has a local surface normal and is connected to the two ROIs of the stereo pair with known px/mm resolutions and η -metrics. At this stage, the points representing the same real lesion, but obtained using different stereo pairs, are not yet identified. This identification is done at the next stage of the mole mapping pipeline—the mole set creation.

4.1.3 Mole set creation

Once the detected PSLs are matched and triangulated across all stereo pairs, they can be grouped into *mole sets*. A mole set is a totality of all detected lesions linked

4. AUTOMATIC PSL CHANGE DETECTION

with their 2-D views (ROIs containing MSER ellipses) and triangulations³ at a given turntable position. Throughout the text, the elements of mole sets are referred to as *mole representations* or *virtual moles*.

In order to create a mole set, the ellipses and triangulations of every PSL obtained using various stereo pairs have to be linked together. For example, if MSER ellipse number 15 in image 5 (m_{15}^5) is matched to ellipse number 19 in image 6 (m_{19}^6), which, in turn, is linked to m_{20}^{16} , it means that ellipses m_{15}^5 and m_{20}^{16} must be connected as well. Using recursive tracing, it is easy to recover all such indirect connections of the triangulations via the lesion’s direct stereo match information. In this particular example, when searching for all 2D views of a mole represented by m_{15}^5 , we will first explore its stereo matches (m_{19}^6), then the matches of the matches (m_{20}^{16}), and so on, until the total number of connected ellipses has been covered. In this way, we will get a set of MSER ellipses (here, it will include only m_{15}^5 , m_{20}^{16} , and m_{19}^6) and their corresponding triangulations representing one real PSL on the patient’s body.

The schematic in Fig. 4.3a demonstrates an ideal input for the tracing algorithm: the MSER ellipses successfully matched and triangulated across the AB, AC, AD, BD and CD stereo pairs. Had connections AB and AC not been established previously, the recursive search would still show that the ellipses in images A, B, C and D represent the same real PSL.

However, in certain cases, the tracing may not produce the desired results: it can either create false connections or skip the true ones. Consequently, it is possible that one lesion has multiple representations, and vice versa—several real PSLs can be represented as one mole.

4.1.3.1 Multiple representations of one lesion

It is possible that during stereo matching, an image pair depicting the same PSL is not registered correctly due to an insufficient number of SIFT feature matches for homography computation. Effectively, this will lead to a break in the recursive search, and two or more groups of stereo triangulations may not be merged, creating several representations of one real mole (see Fig. 4.3b for the schematic of such a scenario). The problem during SIFT feature matching can be a result of the peculiarity of the skin area around the lesion (e.g. lesions on skin folds or in areas with a non-uniform

³A real mole can have more than one triangulation because it appears in more than one stereo pair at the same turntable position. Although not coinciding completely due to image noise, their positions are very close normally, hence, their average is a good approximation of the real mole’s location in 3D space.

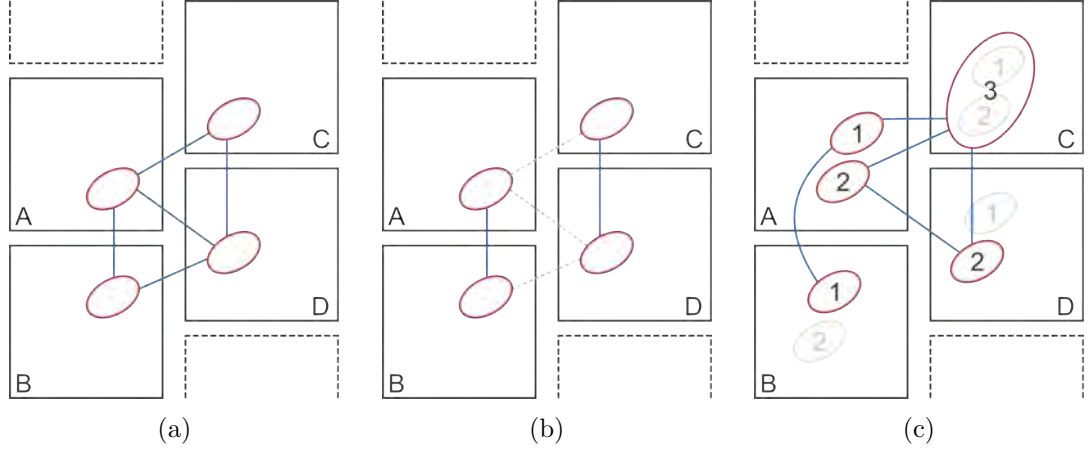


Figure 4.3: Schematics of possible scenarios during mole set creation. Squares A–D denote images acquired by the cameras of the rig with their layout preserved. The ellipses represent MSER blobs after mole detection. (a) Ideal scenario. The ellipses in images A–D represent the same real PSL, all stereo-pair matches have been computed correctly. (b) Multiple representations of a single lesion. The MSER ellipses could not be matched in the image pairs AC, AD and BD. Simple recursive tracing will yield two moles instead of one. (c) Single representation of multiple lesions. Ellipse C.3 is the “bridge”: moles 1 and 2 have been detected as one blob by MSER. Lesion 2 in image B and lesion 1 in D have not been detected by MSER. Because the bridge blob was matched to A.1 on one side, and A.2 and D.2 on the other, real lesions 1 and 2 will be represented as one after the recursive tracing.

surface profile, such as the ears or the nose) combined with the specific orientation of the patient with respect to the cameras. These combinations may cause the appearance of skin patches to differ in a stereo pair to such an extent that only one or two SIFT features can be matched correctly. An example of a homography computation failure is shown in Fig. 4.4.

In order to overcome such situations, we rely on the precision of the intrinsic and extrinsic camera calibration. Specifically, given that the triangulations obtained using stereo-images have sufficient precision (see Section 5.1.5), it is possible to define a distance threshold below which two mole points in 3D are considered as representing the same real PSL. Based on our experiments, we set the threshold’s value at $T_d = 4$ mm. In addition, this thresholding is safeguarded by a condition which prevents the algorithm from erroneously merging two triangulations representing distinct lesions located close to each other. It checks whether any two MSER ellipses linked to these triangulations have been detected together in at least one image. If this condition is not satisfied, it is safe to assume that there was a mismatch, and that the two mole representations should be merged.

4. AUTOMATIC PSL CHANGE DETECTION

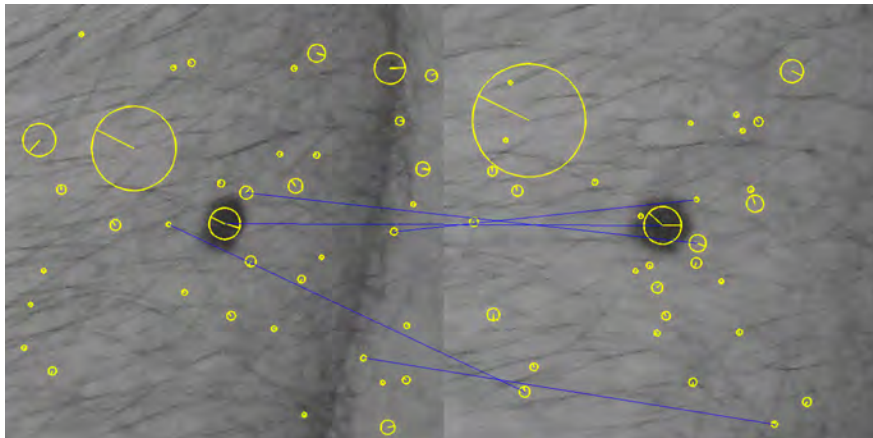


Figure 4.4: Failed homography computation using SIFT features. Blue lines connect SIFT points satisfying the homography model estimated by RANSAC. Points without a match are outliers for this model. The images are acquired by cameras 4 (on the left) and 15 (on the right) at turntable position 9. The lesion is located in the central part of the lumbar area next to the vertebral column (paravertebral region). The convexity formed by the spinal muscles, together with the orientation of the patient with respect to the cameras, causes a substantial difference in the appearance of the skin patch in the two images.

4.1.3.2 Single representation of multiple lesions

As a side effect of using MSER for PSL detection, sometimes two lesions located close to each other (3–5 mm) may be detected in an image as one blob. The factors that play a major role in correct/incorrect detection are the angle of view of the camera, the size of the lesions and the relative skin-lesion contrast. The more slanted the view and/or the smaller and lighter the moles, the more probable it is that these moles will appear as one larger blob. Such blobs, which include two or more smaller lesions, are further referred to as “bridge blobs” or “bridge moles”. An example of a detected bridge blob is shown in Fig. 4.5.

The output of the recursive tracing algorithm, given the presence of a bridge blob, can be predicted looking at the schematic diagram shown in Fig. 4.3c. Image A contains two MSER ellipses representing two real PSLs. The rest of the images contain only one mole each: mole 1 is detected in B, mole 2 in D, and C.3 replaces both moles at once. Since, the stereo-pair matching showed that the bridge ellipse C.3 is the same as A.1, A.2 and D.2, the tracing will yield that all ellipses represent a single real PSL.

Fortunately, it is very easy to detect a “bridge” scenario. If after the tracing procedure the group of MSER ellipses representing a real mole contains more than one ellipse per image (this is how we know the number of real PSLs), it means that there is at least one bridge in this group. However, depending on the situation, the available



Figure 4.5: Two small PSLs located on the left cheek of a patient. Images acquired by cameras 11(a) and 1(b) at turntable position 20. Due to the small size of the lesions, their proximity to each other and the low contrast against the skin, the MSER detects them as a single lesion in image (b), and the algorithm later defines them as a bridge blob.

direct matches may not indicate which one of the ellipses it is (although the hypothetical example in Fig. 4.3c provides such information). Most of the time, they will have to be identified by visual comparison of the patches depicting non-bridge ellipses with the rest. For this purpose, we use the matching procedure described in Section 4.1.2.1 with the only difference that the match candidates are already available.

4.1.4 Mole set merging

When the mole sets are generated for every turntable position p , we can plot the 3D triangulations of each PSL representation (the elements of the mole sets) in the global reference frame.⁴ The sets of 3D points corresponding to the neighboring positions $p \pm 1$ and $p \pm 2$ will have considerable overlaps, i.e. the points representing the same real PSLs will be located very close to each other or even coincide. The task of the mole set merging is to identify and merge the virtual moles which belong to different sets but represent the same real lesions. In this way, a single complete set of virtual moles—a mole map—can be created.⁵ Two such maps acquired at different moments in time can be registered and used in an automatic change assessment of individual lesions.

The main difficulty of this task is that with two mole sets, reliable ways of comparing their elements are scarce. In the case of treating both sets simply as two clouds of 3D points and performing non-rigid registration, there is a high risk that a misalignment

⁴See Section 3.3.2 for coordinate system definitions.

⁵It must be noted that the mole map will actually contain two sets of virtual moles for the two poses (turntable positions $[0, 11]$ and $[12, 23]$). The respective mole sets must be merged separately.

4. AUTOMATIC PSL CHANGE DETECTION

will occur. The most probable scenario for that happening is the following:

- *Two lesions are located next to each other on the patient's body. One of them was detected and triangulated only in the first mole set, while the other mole was detected only in the second set. Using only a distance constraint with respect to the rest of the moles, it is impossible to distinguish between the two lesions while merging the sets, so they are very likely to be registered incorrectly.*

Thus, we can use the geometrical constraint only when coupled with some additional information such as the moles' appearance. But the parameters of the moles' MSER ellipses (dimensions and orientation) are not sufficient in the case of resembling lesions or when there is a drastic change in the viewing angle. Therefore, besides the visual information of the lesion itself, the topological information around the mole (neighboring lesions and the skin) must be taken into account as well.

4.1.4.1 Matching moles across mole sets

In order to carry out the comparison of two virtual moles belonging to different mole sets, taking into account both the geometrical and visual constraints, we can apply the principle of the mole matching procedure described in Section 4.1.2.1. However, a number of important adjustments and modifications need to be made:

1. **Match candidate selection.** The candidate pairs are selected based on their distance from each other in 3D space: moles within the radius of $r_c = 30$ mm are chosen for visual comparison. This distance is enough to account for slight pose shifts of the patient during the turntable rotation. Using this approach, every mole will have to be compared with each of its neighbors,⁶ making it a rather computationally expensive procedure.

One way to reduce the number of comparisons per two mole sets is to prune the candidate pairs after a successful match. We can discard the pairs that include one of the moles just compared, if the following condition is satisfied:

- *The distance computed in an image between the matched lesion from one mole set, m_1 , and a candidate from the same set, m_c , must exceed, up to a factor, the size of the major axis of the matched lesion from the other set, m_2 . Of course, to compute this distance, m_1 and m_c must have their corresponding MSER blobs detected in the same image.*

⁶Due to the possible presence of bridge moles (see Section 4.1.3.2) in one of the sets, an exhaustive comparison is preferred.

To put it in an example, suppose that mole 8 (m_8) at position p matches mole 10 (m_{10}) at $p + 1$, and there are two more candidate pairs including m_8 and m_{10} : ($m_8 \leftrightarrow m_{12}$) and ($m_7 \leftrightarrow m_{10}$). These candidate pairs will be discarded if the following holds true:

$$d(m_8, m_7) < k \cdot \mathcal{A}(m_{10}) \quad \text{and} \quad d(m_{10}, m_{12}) < k \cdot \mathcal{A}(m_8). \quad (4.5)$$

In these inequalities, d is the Euclidean distance between the locations of the two moles in an image, \mathcal{A} returns the size of the mole's major axis and $k \in \mathbb{R}_1^+$ is a multiplicative factor, which, based on our experiments, was assigned the value of 3.

2. **Camera/view selection.** When the candidate pair is known, we need to choose the optimal images for comparison. The larger the interval between the turntable positions, the greater the difference in the viewing angles and the more difficult it is to compute the homography. Hence, the views containing the candidate moles need to be chosen so as to minimize the viewing angle difference.

For this reason, we establish the preference system, where, for merging mole sets at positions $[0, 11]$, the preferred camera at position p should be on the left column, and at $p + 1$ on the right (vice-versa for positions $[12, 23]$). Fig. 4.6 shows such preferred image planes highlighted in red. If the available views do not satisfy the preference, the optimal camera is the one with the smallest corresponding η -metric (see Section 4.1.2.2).

3. **The ROIs of the lesions.** In order to account for distinct viewing angles at different turntable positions when detecting and matching SIFT features, the ROIs should have adequate dimensions. Otherwise, there is a risk of not obtaining enough correct matches to compute the homography, especially when matching moles at positions p and $p + 2$. Because of this, following a series of experiments with images of different body regions, we increased the original 400×400 ROI to 600×600 pixels.

In addition, to make use of the visual information from the lesion's neighbors in the mole set, the ROI is extracted so that its center coincides with the center of gravity of the lesion neighborhood. The neighborhood is defined in 3D as a sphere with the radius of $r_n = 20$ mm: any lesion lying within this sphere and having a projection in the selected view will be added to the neighborhood.

4. AUTOMATIC PSL CHANGE DETECTION

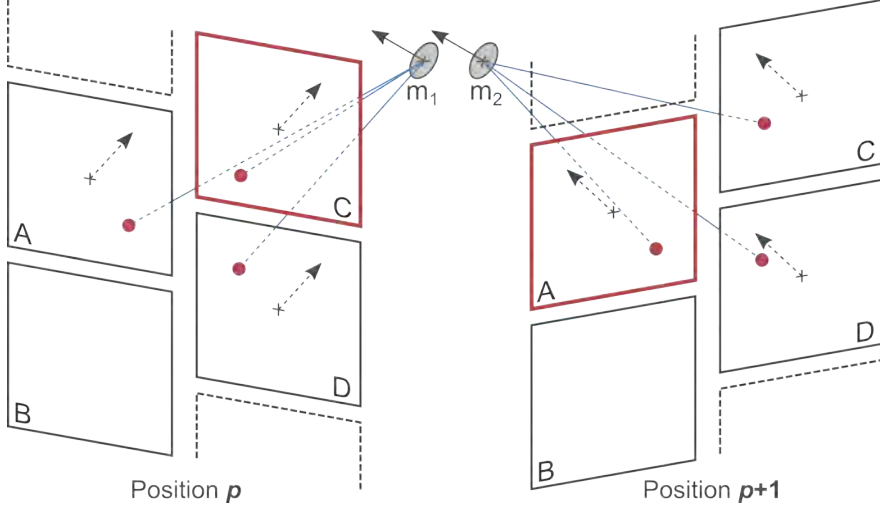


Figure 4.6: Best camera/view selection during mole set merging for the patient's pose 2 (turntable positions [12, 23]). Lesions m_1 and m_2 belong to the mole sets acquired at turntable positions p and $p + 1$, respectively. Squares A – D denote images acquired by the cameras of the rig with their layout preserved. Red dots are the projections of m_1 and m_2 on the images. The optimal views to compare the two moles are highlighted in red. The arrows denote the normals to the camera and the mole planes.

4. **ROI pre-warping.** In order to facilitate the computation of the homography, prior to extracting SIFT features from the ROI images, we use the known camera geometry at both positions and “pre-warp” the ROIs. In other words, we compute an approximate homography transformation between the two selected views using the plane of the mole in 3D [388]:

$$H_p = K_2(R - \mathbf{t}\mathbf{n}^T/d)K_1^{-1}, \quad (4.6)$$

where R and \mathbf{t} are the rotation matrix and the translation vector of camera 1 with respect to camera 2, \mathbf{n} is the vector normal to the mole's plane, d is the distance from the mole's plane to camera 1, and K_1 and K_2 are respective camera matrices. This transformation would be precise if not for patient's motion and image noise. Applying it to one of the ROIs results in having two views with roughly the same viewing angle, which facilitates SIFT feature matching and the computation of the final homography.

5. **Inverse homography and putative matches.** Depending on the skin patch being observed (non-planar surfaces, such as ears, the nose, etc.), it is possible that the homography cannot be computed even using a “pre-warped” image (see

Fig. 5.10 for an example). To deal with such cases, we make use of the inverse homographies. That is to say, given the left and right ROIs from different turntable positions, we first find two “pre-homographies” to warp the left ROI onto the right image, and vice versa. After that, we try to compute the homography transformations for the two pairs of ROIs using SIFT features.

When a valid homography cannot be obtained for one of the pairs, it is probable that the second pair will give a correct transformation. If this is not the case (this may happen for the aforementioned areas when merging nonconsecutive mole sets), the match is considered to be a *putative match*:

- *The moles may represent the same or different real PSLs, but because of the viewing angles neither statement can be confirmed.*

When the merging procedure of the two mole sets has finished, some of the resulting putative matches can be pruned by simply checking if one of the candidate moles was matched to any other mole. In a further stage of the mole match propagation (see the next subsection), all putative matches are completely filtered.

6. **Match condition.** When the homographies between the two selected views have been computed and the ROIs warped, it must be established whether the two virtual moles represent the same real PSL. In most cases (especially for consecutive mole sets) the matching ellipses will have their centers within each other’s boundaries. But due to the difference in the viewing angles and the skin patch topology, it is possible that while not satisfying the “centers-in-the-boundaries” condition, the two ellipses still represent the same real lesion. A straightforward workaround for such cases would be to increase the allowed distance between the centers of the ellipses. However, an opposite scenario is also possible—two virtual moles representing different lesions can be located very close to each other (Fig. 4.7d), making such thresholding inefficient. Thus, an alternative and more elaborate condition is needed.

To ensure that all the scenarios shown in Fig. 4.7 are correctly resolved, an alternative condition should provide a trade-off between the relative dimensions of the ellipses and the distance between their centers. Effectively, the two ellipses should be considered matching if (1) the distance between their centers is comparable with their minor axes and (2) their orientations are aligned.

The first requirement can be satisfied using the line connecting the centers of both ellipses and the points where this line intersects them. The distance along this

4. AUTOMATIC PSL CHANGE DETECTION

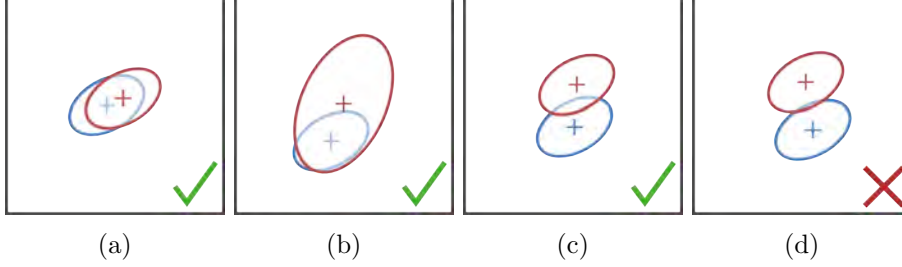


Figure 4.7: Various possible scenarios when comparing moles during the mole set merging. The blue and the red ellipses correspond to the original and the warped ROIs, respectively. In scenarios (a)–(c), both ellipses represent the same real lesion. Both moles in (a) satisfy the condition of the stereo-pair matching. The red ellipse in (b) is a bridge mole. The ellipses in scenario (c) do not satisfy the condition of the stereo-pair matching, but still represent the same real PSL. In scenario (d), the ellipses represent different lesions, but are close to each other because of the transformation inaccuracies.

line from the center of one ellipse to the intersection point on the other ellipse can give an idea of the degree of overlap between the two moles.⁷ The second requirement can be fulfilled by finding the angle between the major axes of the ellipses and incorporating it into the assessment of the distance criteria.

Fig. 4.8 demonstrates the condition graphically. The line connecting the centers C_1 and C_2 of ellipses e_1 and e_2 intersects them at points P_1 and P_2 , respectively. If we steadily move the two ellipses towards each other, distances $\overline{C_1P_2}$ and $\overline{C_2P_1}$ will decrease accordingly. The two moles match if one of these distances is smaller (up to a factor) than the semi-minor axis of the corresponding ellipse, i.e.

$$|\overline{C_1P_2}| < c \cdot \mathcal{B}(e_1) \cdot (1 - \sin(\alpha)) \quad \text{or} \quad |\overline{C_2P_1}| < c \cdot \mathcal{B}(e_2) \cdot (1 - \sin(\alpha)), \quad (4.7)$$

where \mathcal{B} returns the size of the moles' minor axis, α is the angle between the major axes of the two ellipses, and $c \in \mathbb{R}_0^1$ is the scale factor. If the orientations of the two ellipses coincide, there is no penalty on the distance threshold, whereas if they are perpendicular, the condition is unlikely to be satisfied. We set the multiplicative factor $c = \frac{2}{3}$ empirically as a trade-off between discarding all mismatches and recovering the likely matches.

⁷Another approach would be to compute the area of intersection of the two moles and compare it with some threshold value. The drawback is that it is unclear how to define this threshold, i.e. which ellipse should be used to compute the intersection area percentage corresponding to a pair of matching moles. The proposed method avoids this ambiguity and relies on the dimensions of the moles themselves.

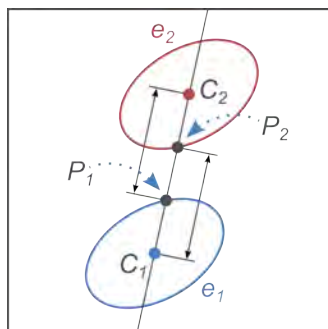


Figure 4.8: The lesion matching condition during the mole set merging procedure. C_1 and C_2 are the centers of ellipses e_1 and e_2 , respectively. Line $\overleftrightarrow{C_1C_2}$ intersects e_1 at point P_1 and e_2 at P_2 . The two moles match if Eq. 4.7 is satisfied.

4.1.4.2 Mole match propagation

Once the mole sets have been merged at all successive turntable positions ($p \pm 1, p \pm 2$), we need to run a recursive procedure to associate mole matches from nonsuccessive positions ($p \pm x$, where $x \in \mathbb{Z}_{>2}$). That is to say, two moles from mole sets A and B can match another mole from set C , but not match each other (indirect match). The objective of the association procedure is to make every mole match its counterparts from other sets directly examining all indirect matches recursively. In this way, for each mole of every set, there will be a group of lesions it matches in the rest of the sets.

The procedure is very similar to that described in Section 4.1.3, although the exceptions have to be resolved in a different manner. The main exception scenario also involves bridge moles, whose simplest case is shown in Fig. 4.9a. Two moles from set A as well as the mole in set C match the bridge mole in set B . As the result of the recursive match propagation procedure, all the moles in the three sets will be grouped to represent one real lesion.

Fortunately, it is easy to detect such exceptions, because in a group of virtual moles representing a real lesion, there should not be more than one lesion per set.⁸ If this condition is not satisfied, it indicates the presence of at least one bridge mole. However, determining which one(s) of the moles is/are the bridge(s) is not as straightforward. Ideally, it will be the lesion(s) directly matching two or more moles from the same mole set. But not all bridges in a group can be discovered in this way, as there may be several consecutive bridge moles, some of which are matched only to a single mole in

⁸In fact, it can happen that a bridge mole connects only single lesions in other mole sets. In this case, it is not possible to detect the exception, but the inconsistencies in the mole representation will not be present either.

4. AUTOMATIC PSL CHANGE DETECTION

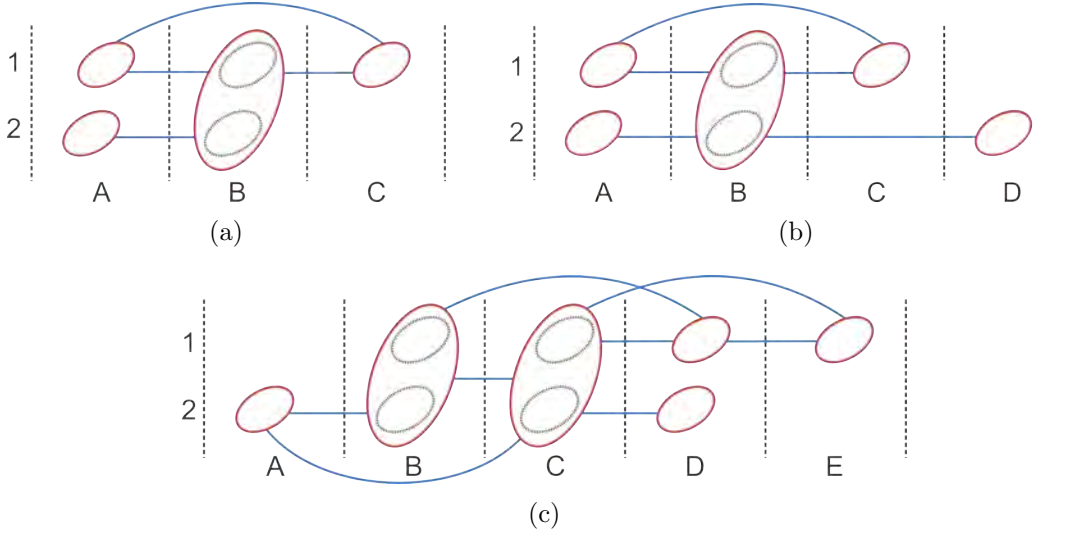


Figure 4.9: Some of the possible bridge exception scenarios during the mole match propagation. In each scenario, the ellipses represent virtual moles and the capital letters denote different mole sets. (a) The simplest case, resolvable by recursive tracing. (b)–(c) More complex scenarios that require visual comparison of lesions from nonconsecutive mole sets.

each set. An example of such a scenario can be created if we substitute mole *A.2* in Fig. 4.9c with a bridge mole, which, applying this logic, will not be detected as such. Nonetheless, such undetected bridges can be identified in later stages.

The main difficulty related with this scenario is the impossibility of assigning lesions that have direct matches only with bridges to any group representing a real PSL. Or rather, it is impossible to do this without a visual comparison of the lesions belonging to nonsuccessive mole sets, described in the previous section. For example, lesion 2 belonging to mole set *D* in Fig. 4.9b was matched only to the bridge mole at position *B*, and it is not clear whether it should match *A.1* or *A.2*. Similarly, in Fig. 4.9c, such a problematic lesion belongs to mole set *A*.

Thus, the generic steps for resolving the bridge exceptions during the mole set match propagation are listed in Algorithm 5. In order to split a group of virtual moles containing a bridge, we need to identify as many bridge moles as possible. Then, a recursive tracing is run on each lesion of the group cutting the search at the bridge(s). This effectively splits the given group into subgroups of connected lesions. At this point, these subgroups can still be merged further because lesions from nonconsecutive mole sets may be isolated by the bridge moles (see Figs. 4.9b–4.9c). The merging can be carried out only by direct visual comparison of the lesions described in detail in Section 4.1.4.1). Finally, after all comparisons have been done, the unidentified bridge

Algorithm 5: Resolving a bridge exception during mole match propagation

Data: A group of virtual moles with bridge moles, g

Result: A set of groups representing real lesions, G , the result of splitting g

```
1 /* Detect identifiable bridge lesions */
2  $b \leftarrow \text{identifyBridgeMoles}(g)$ ;
3 /* Trace the direct matches of every mole in the group, trimming the
   search at the bridges. Concatenate the obtained subgroups into a set.
   */
4 for all  $m$  in  $g$  do
5    $gTemp \leftarrow \text{traceMatches}(m, b)$ ;
6    $G \leftarrow \text{concatenate}(G, gTemp)$ ;
7 end
8 /* Search for indirect matches: compare the groups in  $G$  visually and
   merge the ones matching */
9  $mm \leftarrow \text{compareSubgroups}(G)$ ;
10  $G \leftarrow \text{mergeSubgroups}(G, mm)$ ;
11 /* Detect any unidentified bridge moles by checking for the repeating
   moles across the subgroups */
12  $b \leftarrow \text{identifyBridgeMoles}(G)$ 
```

moles can be detected by simply checking the subgroups for common lesions.

Once the matches have been propagated across all the turntable positions, the mole map is ready. In fact, the map has the same structure as a mole set, with the 3D locations and the local normals of the PSLs computed as the average of the corresponding values in the matching mole sets. Similarly, each virtual mole will have a number of corresponding 2D images from different viewpoints with a given η -metric and px/mm resolution, which will be employed in the change detection procedure.

4.2 Inter-exploration operations

Two explorations of the patient's skin surface performed several months apart can be used for automatic detection of changes that individual lesions undergo over time (see the general schema in Fig. 4.10). To do this, we only need to establish the correspondences between the lesions of the two mole maps, i.e. given a PSL in one map, we have to find which lesion it corresponds to on the other map. Once it has been done, the change detection using the image patches around the moles is straightforward.

4. AUTOMATIC PSL CHANGE DETECTION

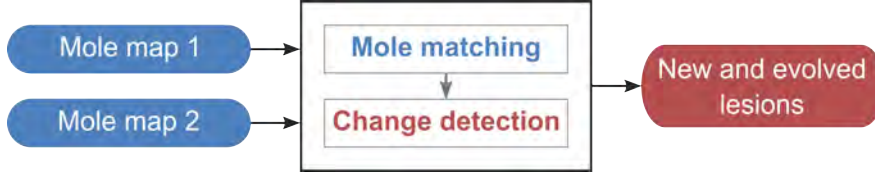


Figure 4.10: The pipeline for detecting new and evolving lesions given two mole maps acquired several months apart. The change detection is carried out on images of individual PSLs after the inter-exploration mole correspondences have been established.

4.2.1 Mole matching

Thanks to the controlled conditions in which skin explorations are performed, the process of finding correspondences is fairly simple in the vast majority of cases. A PSL photographed during a baseline scan by camera A at turntable position p is likely to be found in the image acquired by the same camera at the same position during a follow-up scan. Thus, a PSL match in another exploration can be determined using the same principle of visual comparison we employed for stereo matching and mole set merging (see Sections 4.1.2.1 and 4.1.4.1, respectively), with the only difference being that the candidate search can be limited to the image area containing the lesion because the viewing angles across explorations will coincide for most PSLs.

However, some lesions will not satisfy the assumption above. Due to slight differences in the orientation of the patient with respect to the cameras and/or specific locations of the PSLs on the body, the views in which the lesion appears in the two explorations may not coincide. For example, a lesion detected during scan 1 in the *right* part of image/view A at position p , in a subsequent exploration may appear in the *left* part of the same image A , but at position $p + 1$ (see Fig 4.11). A similar scenario is possible in the vertical dimension when, in the latest exploration, the mole appears at the same position p , but in the view directly above or below A .⁹ Thus, when matching lesions across explorations, all such exceptions must be taken into account.

The following steps are used to find a PSL in the target exploration, E_t , that matches a lesion in the reference scan, E_r , while accounting for both general and exception scenarios:

1. **Determine the optimal camera view** of this mole in E_r based on the η -metrics computed earlier (see Section 4.1.2.2 for details). In addition, we can

⁹This may happen if (1) the PSL is located on the arms or on the face, which are positioned differently as compared to the baseline exploration; or (2) the distance between the skin surface of the patient and the cameras is different (e.g. due to leaning to the side).

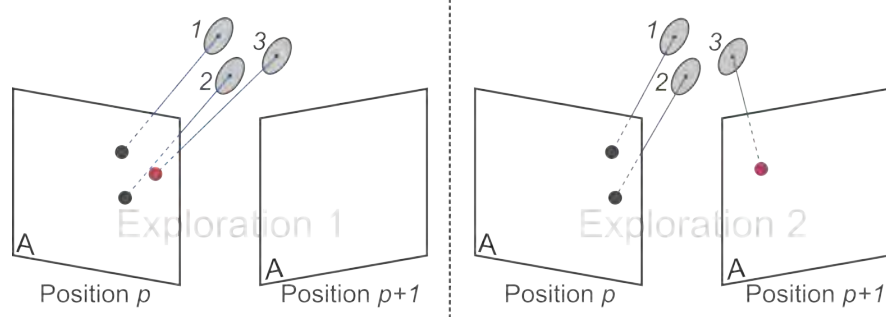


Figure 4.11: An example of non-coinciding views of the same mole in 2 explorations. The patient during the first scan was standing 1–2 cm closer to the backrest column than during the next exploration. As a result, mole 3 was photographed by camera *A* at a different turntable position.

constrain the selected view by ignoring lesions detected too close to the image borders. This will ensure a correct window selection for further change detection.

2. **Extract a ROI** around the reference mole in the image corresponding to the optimal view. For the best SIFT feature detection, the ROI must contain a sufficient area of the texture-rich surrounding skin. Moreover, the ROI should be wide enough to include the corresponding mole in the view of E_t , whose precise location is not yet known.¹⁰

Thus, in order to ensure the right ROI size for all PSLs, we need to take into account their distances to the selected camera plane. To do this, we establish the minimum and maximum possible widths of the ROI (in our experiments, we used 700 and 1500 pixels, respectively) which will correspond to the farthest and the nearest visible PSL from the selected view at a given turntable position. Using these corresponding extrema, we can introduce a simple hyperbola function to describe a continuous relation between the ROI width and the distance from the camera. The coefficients of this function can be obtained by solving the following system of equations for a and b :

$$\begin{cases} w_{\min} = \frac{a}{d_{\text{far}} + b}, \\ w_{\max} = \frac{a}{d_{\text{near}} + b}, \end{cases} \quad (4.8)$$

where d_{far} and d_{near} are the distances from the farthest and the nearest moles to the camera plane, while w_{\min} and w_{\max} are the corresponding desirable widths of

¹⁰ Assuming that this mole is likely to appear in the same image in both target (E_t) and reference (E_r) explorations, the mole's ROI in E_t is extracted from the same view.

4. AUTOMATIC PSL CHANGE DETECTION

the ROI.

3. **Compute the homography** between the two ROIs and check its validity using the condition described in Section 4.1.2.1. We can set the threshold to a higher value ($T_H = 2500$) because the two ROIs are going to have almost the same viewing angle.

However, an erroneously computed homography means that the contents of the two ROIs will differ significantly. This can happen because of (1) an abrupt movement by the patient during the image acquisition, (2) a slightly different arm positioning when assuming the pose, or (3) if the skin patch of the reference mole is altered in E_t (foreign marks on the skin, clothing, body hair, etc.). If the failure happened due to (1) or (3), it will not be possible to establish the lesion correspondence. However, if the homography could not be computed because of a slight shift in the patient's pose, selecting a different view will help. Hence, we can try the available views in order to compute a valid homography, and if none of the views produces one, we can assume that it is impossible to find the correspondence automatically. That said, a reference lesion will not be matched to a PSL in E_t only if the image acquisition protocol is not followed precisely.

4. After the homography has been computed successfully, **adjust the target image ROI**. Depending on the contents of the ROIs, after applying the computed transformation, the following scenarios are possible:
 - (a) The target mole ellipse in E_t is within the ROI and a smaller mole window¹¹ can be extracted.
 - (b) The target mole ellipse is outside or too close to one of the ROI borders, but is within the image boundaries and the mole window can be extracted (see Fig. 4.12a).
 - (c) The ellipse is outside or too close to one of the image borders (Figs. 4.12b–c) and the mole window cannot be extracted.

In the first scenario, we can proceed directly to subsequent steps in the algorithm, while in the last two, we need to select a different ROI in either the same or adjacent view acquired in E_t . Thus, in scenario (b), we will simply need to center the ROI on the ellipse projection and extract it from the same image

¹¹A mole window is a small ROI image big enough only to contain the entire PSL and is necessary for the change detection phase.

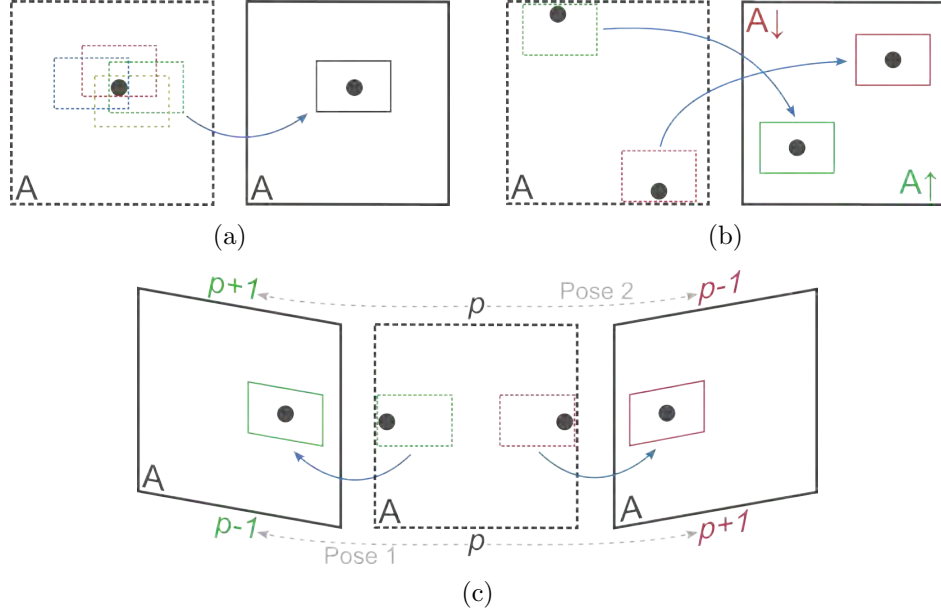


Figure 4.12: Scenarios for the view/image selection in the target exploration after applying the homography transformation. The larger squares denote views in E_t , while the smaller rectangles are image ROIs. The dots denote the locations of the target mole found using the homography transformation. The dashed views correspond to the initially selected views, and the dashed ROIs are the initial regions of interest. (a) The mole ellipse is outside or too close to at least one of the ROI borders (some possible ROIs shown in different colors) and there is enough space in the image. Solution: keep the same view/image and center the ROI on the ellipse’s location. (b) The mole ellipse is outside or too close to the top/bottom border of the image. Solution: use the view immediately above/below the initial view and determine the ellipse’s new approximate location using the 3D coordinates of the reference mole. $A\uparrow$ and $A\downarrow$ denote the views directly above and below A , respectively. (c) The mole ellipse is outside or too close to the left/right border of the image. Solution: use the same view at the following or previous turntable position. The position is determined based on the pose and the edge of the image closest to the ellipse. The approximate location of the ellipse in the new image is found similarly to (b).

(Fig. 4.12a). In turn, scenario (c) can be further subdivided depending on if the ellipse projection is close to the vertical (c.1) or horizontal (c.2) image borders.

The schematics of scenario (c.1) are shown in Fig. 4.12b. In the case of the ROI being close to the upper or the lower border of the image, we select the view just above or below the current camera, respectively. The location of the projection ellipse in the new image is estimated by computing an approximate homography transformation, the “pre-warping” homography described in Section 4.1.4.1. In this way, using the 3D coordinates of the reference mole in E_r , we can deduce the approximate location of the matching mole in E_t in the new image.

The scheme of scenario (c.2) is depicted in Fig. 4.12c. The procedure to select the new ROI follows the same logic as in (c.1) with the exception that in the

4. AUTOMATIC PSL CHANGE DETECTION

absence of horizontally adjacent views, we select the images acquired at other turntable positions. Concretely, depending on the pose of the patient (direction of the turntable rotation) and whether the lesion is closer to the left or the right border of the image, we select either the next or the previous turntable position, as shown in the figure.

After acquiring the new ROI in E_t , we register the reference and the target ROIs by once again computing the homography transformation using SIFT feature matching.

5. **Obtain the ellipse of the target mole.** This ellipse is needed to extract a target mole window of adequate size for the change detection as well as to determine the index of the matching mole in the map of E_t . If the ellipse was detected in the E_t mole mapping stage, it can be identified by means of a simple distance threshold. However, it can either form part of the mole map or not (the mole could not be matched with other lesions in the stereo pairs or at other turntable positions).

If it is a new lesion, or if this PSL was not detected during the mapping procedure, it must be segmented using MSER. For this purpose, we use the procedure described in Section 4.1.1.

6. **Extract mole windows** from the reference and the target ROIs using the mole ellipses. The side of the window is equal to

$$N = 2 \cdot l \cdot \max(\mathcal{A}(m_r), \mathcal{A}(m_t)), \quad (4.9)$$

where m_r and m_t are the ellipses of the moles in E_r and E_t , respectively, function \mathcal{A} returns the size of the mole's major axis and l is a scale coefficient (in our experiments, we used $l = 1.5$). However, at this stage, the size of the window around m_t is multiplied by 1.5 for the subsequent stage of image alignment by translation.

7. **Register mole windows by means of the weighted normalized cross-correlation (NCC).** This step is important for a more precise alignment of the two mole windows. The NCC [398] is performed on the normalized blue channels of the images, which provides the best skin-lesion contrast and, at the same time, eliminates weak artifacts such as hair or skin pores. In addition, the area of the lesion in the window containing m_r is weighted, so that significantly more

emphasis is put on the relevant pixels.

8. **Prepare the mole masks.** The binary masks specifying the PSL area in the mole windows can be obtained using the MSER segmentations computed earlier (see Section 4.1.1). These segmentations need only to be fit into the windows at the locations of the mole ellipses.

After all the steps of the algorithm have been performed, for each PSL there will be a pair of aligned images acquired in the two explorations. These images can be used for the assessment of changes the lesion has undergone before the follow-up screening.

4.2.2 Change detection

With the aligned mole images and masks extracted from the reference and the target explorations, the detection of changes in a lesion is straightforward. It is important to note that we do not intend to describe the changes precisely. Rather, the goal is to be able to indicate to the physician that certain PSLs are undergoing changes and are worth a closer examination. In addition, parameterizing the importance of the change should give a way of controlling noise tolerance in the system's output.

Algorithm 6 shows the basic steps needed to acquire the change mask of a lesion from two consecutive scans. At first, the images of the lesion are converted to the HSV representation, since it allows a more intuitive description of the changes in the appearance, clearly separating color and saturation. Then we compute a difference image using each channel individually (hue, saturation, value). This image shows how each pixel in one image is different from its corresponding pixel in the other image.

From the difference image we generate the gray-level change map by finding the maximum value of each pixel across all channels and applying a median filter to remove spurious noise. Now, this map can be binarized using the threshold provided, which, in our experiments, was set to $T_b = 0.1$. This parameter allows controlling how sensitive the system is going to be to the changes detected.

Finally, we combine the lesion masks from both images into one unified mask which defines the area where change is to be sought. In order to keep only the changes that occurred within the PSL and not in the surrounding skin, the binary change map obtained is merged with this unified lesion mask. Using the ratio of the total change area to the area of the mask, we can parameterize the importance of the lesion's evolution. For example, if we set this parameter to $T_c = 0.15$, the lesions with 15% of their area altered will be considered as undergoing important changes.

4. AUTOMATIC PSL CHANGE DETECTION

Algorithm 6: PSL change detection

Data: Mole images I_1 and I_2 , mole masks M_1 and M_2 , binary threshold τ

Result: Change mask C

```
1 /* Convert RGB images to HSV representation */
2  $H_1 \leftarrow RGBtoHSV(I_1)$ ;
3  $H_2 \leftarrow RGBtoHSV(I_2)$ ;
4 /* Compute the difference image (channel subtraction) */
5  $D \leftarrow |H_1 - H_2|$ ;
6 /* Find the biggest change for each pixel across all channels */
7  $C \leftarrow \max(D_H, D_S, D_V)$ ;
8 /* Apply median filter */
9  $C \leftarrow C \otimes f$ ;
10 /* Binarize the change mask */
11  $C \leftarrow \text{binarize}(C, \tau)$ ;
12 /* Obtain the unified mask */
13  $M \leftarrow M_1 \vee M_2$ ;
14 /* Combine the change mask with the unified lesion mask */
15  $C \leftarrow C \wedge M$ ;
```

4.3 Conclusion

This chapter described an approach to automatic detection of changes in multiple pigmented skin lesions using images acquired in the total body skin scanner. This approach consists of two main pipelines: the intra- and the inter-exploration operations. The former pipeline results in the creation of a map of distinguishable PSLs present on the patient's body. In the later, the maps of two consecutive explorations are registered, so that changes in individual lesions can be assessed.

Building the mole map consists of the following stages: (1) mole detection in individual images, (2) stereo-image processing, (3) creation of mole sets and (4) their merging into the final map. Prior to the detection of PSLs, all the images are preprocessed so as to distinguish the foreground (skin) areas, attenuate noise and highlight the lesions. After the PSLs have been detected in the images, they are matched to those photographed by the adjacent cameras (stereo pairs), and triangulated. The triangulations (3D locations) of the moles and their corresponding images at every position of the turntable form 24 mole sets. Finally, these mole sets are merged into a complete map covering the whole visible skin surface of the patient (maps acquired for pose 1 and 2 are stored separately).

The mole map registration is based on the assumption that most PSLs in both explorations can be found within the same view (camera and turntable position), if the

image acquisition protocol is followed carefully. Given the image region containing the lesion in the 1st exploration and the image area where we expect to find this lesion in the 2nd scan, we can compute a transformation between them. By assessing this transformation, we will verify whether the assumption holds, and if so, determine the exact location of the mole in the second image. After aligning the two image regions, it is easy to compute the difference image and estimate the amount of change the lesion has undergone between explorations.

The parameters required by the algorithms and their default values are summarized in Table 4.1. Some of the size parameters and thresholds (e.g. S_r , T_H or S_m) have different initializations in different parts of the pipelines. In order to keep the unique identification of the parameter values in use, they are marked with superscript indexes.

Both pipelines primarily rely on the narrow set of computer vision tools: MSER for mole detection and segmentation, epipolar geometry for triangulation, and SIFT features with RANSAC fitting for homography computation during lesion matching. Some points regarding the mole detection and matching procedures need to be stated:

- **Mole detection.** In this work, no clear distinction has been made between nevi and freckles. Freckles are normally lighter, but may vary in size, and, depending on the color of the surrounding skin, often manifest themselves as maximally stable regions during the detection. In addition, it may be difficult for an untrained person to distinguish a light brown nevus from a darker freckle. This fact adds an additional requirement to the mole detection procedure which, besides the detection of skin lesions, should differentiate between moles and freckles discarding the latter. A possible approach would be to use the mechanisms of a MSER detector for finding blobs to classify later into several categories (e.g. nevus, freckle, and other) by means of a supervised learning algorithm such as ANN or SVM. To the best of our knowledge, there have been no methods proposed to perform such a classification, which makes it a new perspective line of research.
- **Mole matching.** Given a mole's image, locating it on the body of a patient with a large number of PSLs poses a nontrivial problem for physicians during a TBSE procedure. It is also complicated by the fact that sometimes it is very hard to distinguish two moles visually without relying on the lesions surrounding them, especially if we consider evolving moles. Essentially, this is a comparison problem, when given two images, we need to determine if they depict the same lesion. Thus, the main challenge solved by our scanning system is carrying out this comparison automatically for all detected PSLs.

4. AUTOMATIC PSL CHANGE DETECTION

Table 4.1: Summary of the parameters used in the mapping and change detection pipelines.

Parameter		Nomenclature	Value
Skin detection			
1	Image resize factor	α	0.25
2	Hue threshold (low high)	T_h	0.01 0.25
3	Value threshold	T_v	0.4
4	Median filter size (px)	S_m^1	$[7 \times 7]$
5	Gaussian filter: size std. deviation (px)	S_g σ	$[11 \times 11]$ 3
Preprocessing			
6	Median filter size (px)	S_m^2	$[5 \times 5]$
MSER			
7	Relative stability score	Δ	40
8	Absolute stability score	v	0.999
9	Minimum blob area	A_{min}	$2.7 \cdot 10^{-4} \cdot A_{total}$
10	Maximum blob area	A_{max}	$0.01 \cdot A_{total}$
11	Max. size of the ellipse's large axis (px)	T_a	15
12	Min. allowed ratio of the ellipse	T_{ar}	0.2
Stereo matching			
13	Max. candidate-to-epipolar-line distance (px)	T_e	60
14	Homography threshold	T_H^1	800
15	ROI size (px)	S_r^1	$[400 \times 400]$
16	Peak threshold (SIFT)	ρ	0
17	Edge threshold (SIFT)	ε	5
18	Matching threshold (SIFT)	T_{sm}^1	1.4
19	RANSAC distance threshold	T_{rd}^1	0.05
Mole set computation			
20	Min. accepted PSL size (mm)	T_s	2
21	Min. distance between two different PSLs (mm)	T_d	4
Mole set matching			
22	Candidate neighborhood radius (mm)	r_c	30
23	Neighborhood radius for ROI selection (mm)	r_n	20
24	Multiplicative factor for candidate selection	k	3
25	ROI size (px)	S_r^2	$[600 \times 600]$
26	Multiplicative factor for the matching condition	c	2/3
Inter-exploration matching			
27	ROI size (px)	S_r^3	$[700 \times 1500]$
28	Matching threshold (SIFT)	T_{sm}^2	1.7
29	RANSAC distance threshold	T_{rd}^2	0.005
30	Homography threshold	T_H^2	2500
31	Multiplicative factor for smaller ROI selection	l	1.5
32	NCC weight	ω	6
Change detection			
33	Median filter size (px)	S_m^3	$[3 \times 3]$
34	Binarization threshold	T_b	0.1
35	Change threshold	T_c	0.15

In the same way as physicians constrain their search by knowing the region of the body depicted in an image, our system uses the known geometry of the cameras. However, our approach to determine the precise location of a mole is different. Unlike physicians, who normally refine their search using the moles' dermoscopic structures, the proposed system relies strongly on the visual information of the skin surrounding the mole. One of the drawbacks of such an approach is that it can be sensitive to the viewing angle of the cameras.

For instance, the appearance of a mole located on the medial border of the shoulder blade can vary in two images to an extent that it is impossible to find corresponding SIFT features. This may happen when comparing mole images acquired at the p^{th} and $(p + 2)^{th}$ turntable positions. In such cases, it is unclear whether two images depict the same lesion, so the result is considered to be a putative match until it can be resolved by the match association procedure.

A putative match cannot be resolved only when one of the moles does not have any matches in other mole sets. However, we discard such lesions, because, as experiments have shown, these are less stable and/or undersized moles/freckles which are not yet of interest for future change detection. But if, with time, these lesions enlarge or grow darker, they will be automatically detected during the exploration and compared with the baseline.

The experimental results of applying the proposed algorithms to real data are discussed in the next chapter.

4. AUTOMATIC PSL CHANGE DETECTION

...we must reinforce argument with results.

“The Booker T. Washington Papers: 1903–4” [399]

Chapter 5

Results and discussion

This chapter presents experimental results of the algorithms for the automatic PSL change detection in images acquired using the total body skin scanner described in Chapter 3. All input parameters for the algorithms were set empirically during the experiments. The results reported herein contain all necessary references to the description of the algorithms.

5.1 Intra-exploration operations

In each of the following subsections, we analyze and discuss the performance of individual stages of the mole mapping pipeline (intra-exploration operations).

5.1.1 Skin detection

Prior to the image processing and detection of PSLs on the patient’s body, we generate a “skin mask”: a binary image that defines the foreground area where the lesions are to be detected. This mask is essential for a correct estimation of the skin’s intensity ranges during the preprocessing stage. It is also useful for discarding MSER blobs detected on background elements such as the backrest column. This algorithm was described in Section 4.1.1.1, and the results of its application to the scanner’s image data are shown in Fig. 5.1.

As illustrated in the figure, the approach, although simple, allows for correct detection of skin of different types without producing many artifacts. Figs. 5.1a and b demonstrate a successful detection even in the presence of a tanned skin and clothing. A slight inconsistency in the masks can be seen in shaded underlit areas, for example, in Figs. 5.1c or 5.1e. In the former, it is the area of the chin, while in the latter, it is the

5. RESULTS AND DISCUSSION

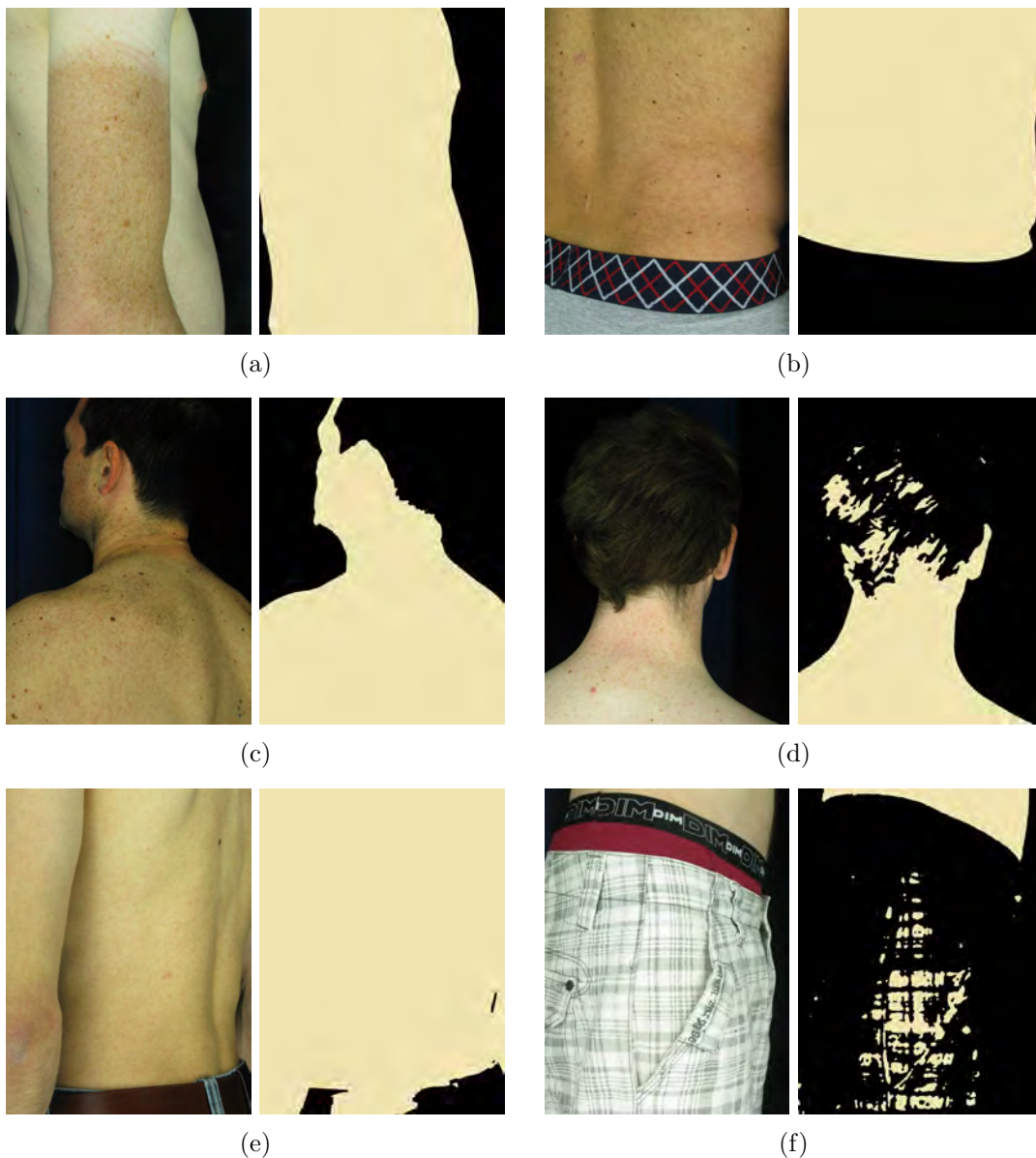


Figure 5.1: Foreground detection in images of different skin types. Images (a) and (b) demonstrate successful skin detection in the presence of a tan and clothing. (c)–(f) contain false negative and false positive pixels. In concrete, the dimly lit areas located in the chin area of (c) and between the right arm and torso in (e) produce incorrectly labeled “skin” pixels. On the other hand, the false positive pixels originating from the patient’s fair hair and clothes (the belt and shorts) are shown in (d) and (e)–(f), respectively. In all these cases, the hue of the positively labeled areas appears within the pre-determined “skin range”.

shaded stripe between the right arm and torso (on the right). In order to avoid very dark lesions being labeled as non-skin areas, we use Gaussian filtering prior to the hue

thresholding. Among our test images, there were no natural lesions mislabeled even without the filtering. However, we decided to apply additional smoothing because of erroneous masking results produced for some artificial lesions that were drawn with a black marker. Yet, this approach should be validated using more images of different patients to make sure that the masking operation does not produce incorrect labeling for any type of PSL.

Because the masking method is based on the hue information from the images, the false positive areas may include head hair. This is not the case for dark-haired patients, whereas directly lit fair hair is likely to produce some artifacts (Fig. 5.1d). Another source of false positives is undergarment worn by the patient during the exploration. As shown in Figs. 5.1e and f, the color of the clothing under direct illumination may fall into the predefined skin hue range and affect the final mask. It must be noted though, that in the clinical setting, the patient will be required to wear dark underwear, or alternatively, offered special clothing with a well-defined “non-skin” color (blue or green).

Overall, this simple method performs satisfactorily, providing a mask that, in most cases, reliably outlines the foreground for further operations.

5.1.2 Image preprocessing

In order to prepare image data for the MSER blob detection, we perform a preprocessing operation that emphasizes PSLs and attenuates the background (see Section 4.1.1.2 for description). Ideally, the intensity values corresponding to the lesions and the background in the output image should be on opposite ends of the intensity scale. While this is possible for relatively dark well-defined PSLs, pigmented lesions that are less salient will have intensities closer to the middle of the bandwidth. Consequently, using the MSER terminology, these lesions appear in images as less stable blobs, and the change in illumination or angle of view will largely affect the detection outcome.

Fig. 5.2 shows the preprocessing results for images of two different skin types. In order to develop an algorithm that robustly emphasizes PSLs on both fair and dark skin (upper and lower rows of the image, respectively), we employed a minimum-value gray level conversion scheme¹ along with the contrast stretching using the foreground mask. In addition, the image obtained was subtracted from its complement to improve the contrast between the lesions and the background skin. The effect of this operation can be seen by comparing images (b) and (c), and (f) and (g) in Fig. 5.2.

¹When converting an RGB image to gray scale, each pixel is assigned the smallest intensity value among all color channels.

5. RESULTS AND DISCUSSION

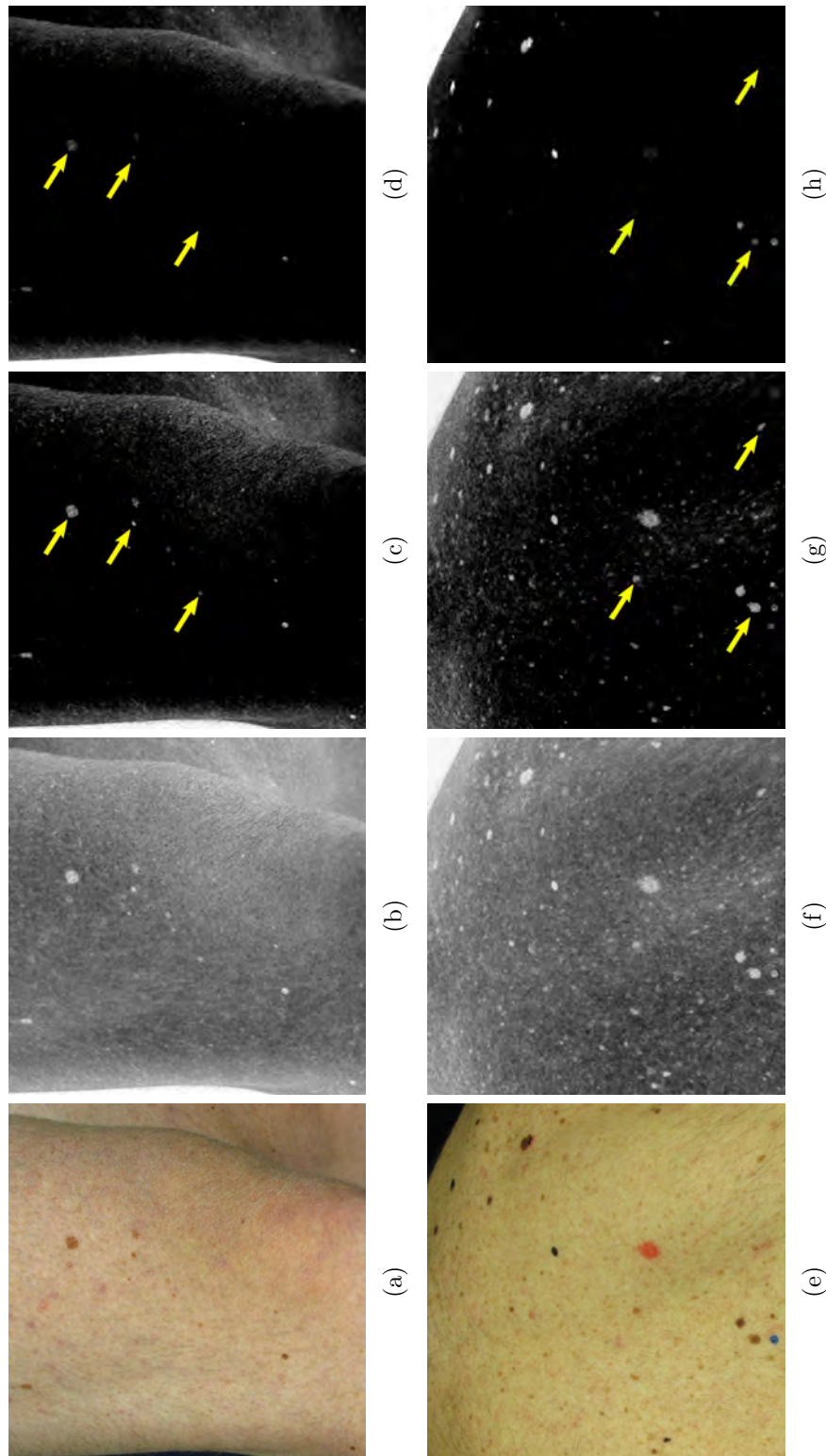


Figure 5.2: Results of preprocessing in images of different skin types. Upper row (a)-(d): right thigh slightly above the knee of subject 1. Lower row (e)-(h): the upper back area of subject 2 with some artificial lesions drawn in black, red and blue. The 2nd column of images, (b) and (f), shows the complement (inversion) of the gray scale input. The contrast in the images is further improved by complement subtraction: (c) and (g), respectively. The results of the same method but with a luma-based gray level conversion are shown in (d) and (h). Notice that darker moles have a better contrast, while most of the smaller, less salient lesions are attenuated or not present (highlighted by the arrows).

Images (d) and (h) demonstrate the output of this algorithm using a luma-based gray level conversion:² $Y' = 0.299R' + 0.587G' + 0.114B'$, with R' , G' and B' being gamma-corrected color channels. The darker (more stable) lesions have a slightly better contrast compared with those in (f) and (g), but some brighter PSLs are faint or even invisible (see the yellow arrows). Thus, the preprocessing method proposed results in an image where pigmented lesions of different brightness (and type) have a chance of being detected by MSER regardless of the patient's skin type. And since in this work no distinction between nevi and freckles was assumed, we are interested in retaining as many PSLs as possible. This will allow gathering enough experimental data during clinical trials of the scanner and creating additional PSL filters/classifiers if needed.

Consequently, the preprocessing scheme employed provides the MSER algorithm with an input adapted for the detection of both dark and light PSLs in different types of skin.

5.1.3 Mole detection

Once the input image is enhanced for the best performance of the MSER algorithm, we can apply the detector directly using a set of predefined parameters. These parameters (see Appendix A.1) were chosen empirically after numerous trials on images of various skin types acquired by cameras in different orientations and turntable positions:

1. Relative stability score of the blobs: $\Delta = 40$.
2. Absolute stability score: $v = 0.99$.
3. The maximum and minimum allowed for the blob's areas are defined using the fraction of the total area of the input image: $A_{min} = 2.7 \cdot 10^{-4} \cdot A_{total}$ and $A_{max} = 10^{-2} \cdot A_{total}$, respectively. Note that the image is resized prior to the detection, so that $A_{total} = 1000 \times 750 = 75 \cdot 10^4$ px. In addition, we filter the blobs detected according to the major semi-axis length ($T_a = 15$ pixels) and the aspect ratio ($T_{ar} = 0.2$).

The results of the detection of PSLs located on the back and arms of two patients can be seen in Fig. 5.3. The blue ellipses highlighting the lesions are fit into the maximally stable extremal blobs that those lesions represent in the processed images.

² Luma (Y') is formed as a weighted sum of $R'G'B'$, approximating the lightness response of vision [400]. The ITU-R Recommendation BT.601 standardizes the channel weighting coefficients for use in standard-definition television (SDTV). In our experiments, this method showed slightly better results than color channel averaging.

5. RESULTS AND DISCUSSION

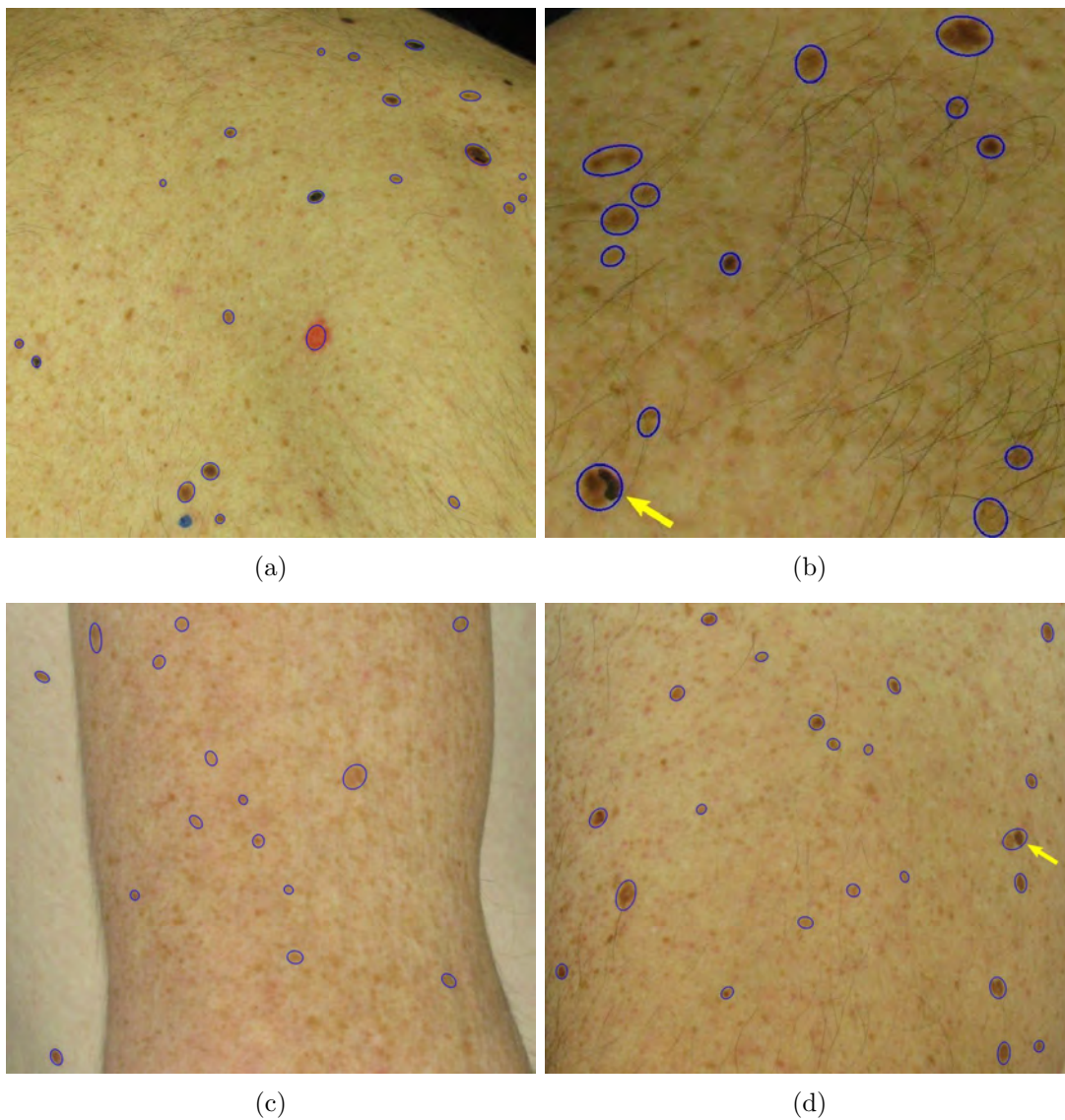


Figure 5.3: The output of mole detection using the MSER algorithm with the following parameters: $\Delta = 40$ and $v = 0.99$ (see Appendix A.1 for details). Area A of the regions detected is in the range $2.7 \cdot 10^{-4} < A < 10^{-2}$ of the total image area. (a)–(b) Mole constellations on the upper and lower back, respectively. The yellow arrow points to an artificially modified lesion. Regardless of color discrepancies between the original and the drawn mole parts, the lesion is detected as one region. (c)–(d) PSLs on the upper arm of two different patients. Note that in both cases many lesions detected are freckles, and not nevi. The arrow in (d) highlights two lesions detected as one (single representation of multiple lesions).

Fig. 5.3a contains the detection results for the image we looked at earlier in Fig. 5.2g. It can be seen that the blue and black artificial nevi at the bottom and the top of the image respectively, have not been detected by MSER. The former was discarded in the

skin masking stage because bright blue is outside the defined skin color range. The latter mole is located in the dimly-lit area, so the contrast between the lesion and the skin does not meet the limitations imposed by the MSER parameters. This could be improved by using an illumination correction algorithm or an adaptive procedure for local contrast enhancement. However, the drawback with these approaches would be an unnecessary amplification of other skin details such as hairs, pores or spots. Besides, the goal is not to detect *all* PSLs in one image, but rather concentrate on those in the best lit central area of the image. This is because we want to have the best view possible of each lesion (good lighting conditions, minimum body curvature, best angle of view) in order to assess the changes correctly. At the same time, multiple cameras and a sufficient number of turntable steps give a certain freedom to discarding less suitable lesion images.

In Fig. 5.3b, all the PSLs have been detected correctly, including a mole with an artificial change indicated by an arrow. The lesions detected in Figs. 5.3c and d are mostly freckles. Because the arms appear closer to the cameras during the image acquisition, the resolution in that area is better and it is easier for the algorithm to distinguish even the smallest PSL. One future improvement of this system will include a dynamic threshold definition for the minimum/maximum lesion size depending on the turntable's position at which the images were acquired.

An example of a single representation of two lesions, as discussed in Section 4.1.3.2, can be appreciated in Fig. 5.3d. Despite the fact that one of the two PSLs is a light freckle, in images acquired at different positions, or by a neighboring camera, they can be detected as a single lesion, causing a special situation during mole set creation or merging. These cases can be recognized and corrected by means of the heuristics described in the previous chapter.

In conclusion, the MSER algorithm is a powerful tool for the detection and coarse segmentation of multiple PSLs. Since its output is largely dependent on the intensity information of the input image, we can modify it to direct the method towards the result we want to obtain. Additionally, its output can be further improved by controlling the size limitations of the lesions detected as well as by applying machine learning to identify their types.

5.1.4 Mole matching in stereo pairs

In order to identify a skin lesion in a stereo pair, one must carry out a comparison of the moles' visual properties, such as size and shape. Human observers normally rely

5. RESULTS AND DISCUSSION

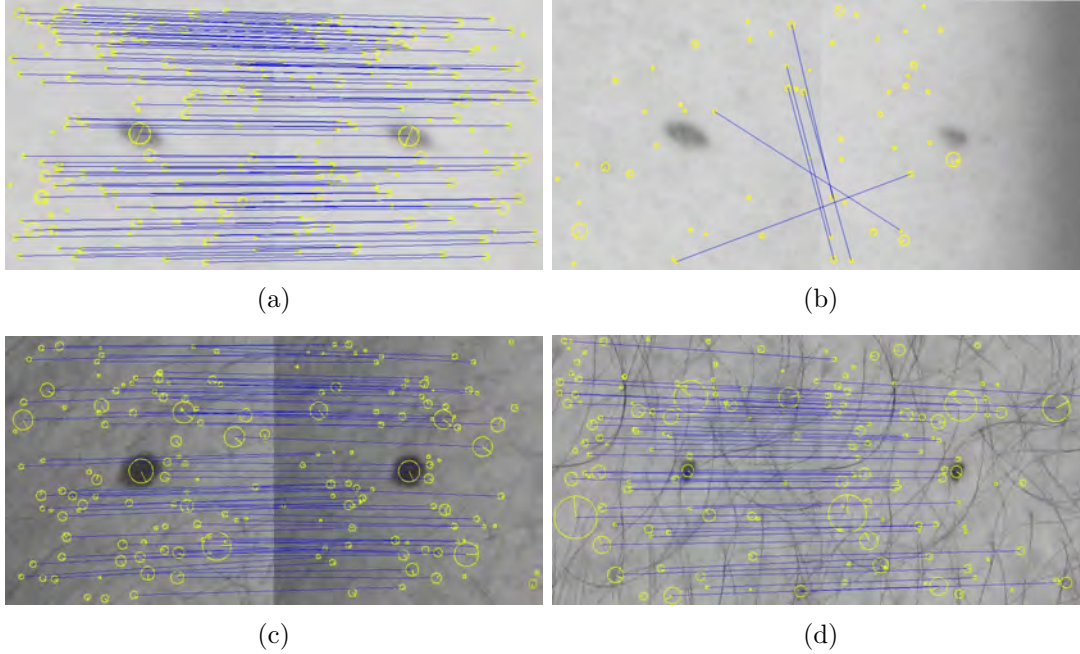


Figure 5.4: SIFT feature matches in stereo images. Blue lines connect SIFT points satisfying the homography model estimated by RANSAC. Points without a match are outliers for this model. (a) A PSL located in the lumbar region of patient 1, captured by cameras 4 and 14 (diagonal stereo pair). (b) The same lesion compared to its neighbor located 5 cm above (left image). (c) A mole in the lumbar region of patient 2 viewed by cameras 5 and 15. (d) A small PSL found on the right calf of patient 2, photographed by cameras 8 and 9 (vertical stereo pair). The results of the PSL matching in (a), (c) and (d) are positive, while the lesions in (b) are different. Note that hair on the skin does not impede correct feature matching.

on this information when the lesion to be matched has unique properties, at least in its neighborhood. But, because moles may have a very similar appearance, we tend more to analyze their spatial information, such as location and surrounding lesions.

Unfortunately, when it comes to carrying out such a comparison automatically, these options become insufficient. Thus, at least two counter-examples can be given:

- When relying on the surrounding moles of a lesion of interest, no decisive conclusions can be drawn in their absence.
- If two very similar moles are found close to each other, they can be easily mismatched: it is enough that one of them is detected only in the first image, and the other only in the second.

Taking this into account, the mechanism of automatic lesion comparison should use information of a different kind. Creating a reliable and distinctive descriptor for

PSLs is a very challenging task because of their similarities independently of their location on the body. Fortunately, some additional information can be extracted from a seemingly uniform background—the skin itself. We have noticed that the images’ resolution allows an efficient description of this information by means of the scale-invariant feature transform (SIFT, see Appendix A.3). Features detected and described in one image can be matched with their counterparts in the other image of a stereo pair. Having enough matches, as shown in Figs. 5.4a, c and d, we can deduce a sufficiently precise transformation (homography) between the two images. And when both are in the same coordinate frame, it is easy to determine whether they depict the same real PSL based only on the locations and dimensions of the corresponding MSER ellipses (Section 4.1.2.1). In the case of there not being enough correct SIFT matches to compute the homography, as demonstrated in Fig. 5.4b, it is clear that these images show different moles located far from each other.

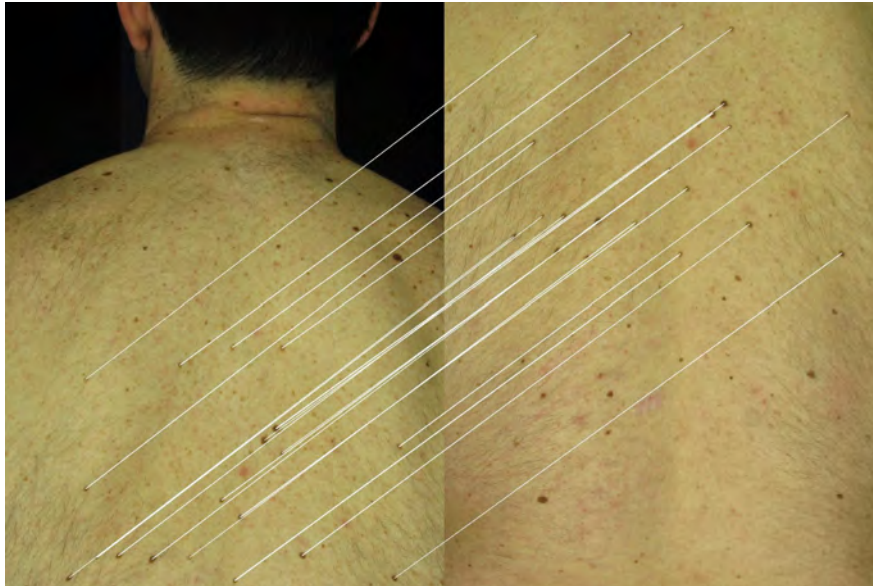
The SIFT features detected in stereo images showing the same lesion will be matched correctly in the vast majority of cases. Exceptionally, when the skin surface is highly slanted with respect to both or one of the cameras, there may be not enough matches to compute the homography (see Fig. 4.4 in Section 4.1.3). However, in these cases, a successful matching is not important, because more suitable views for lesion change assessment can be found at other turntable positions.

It must also be noted that body hair will not pose a problem for SIFT feature detection and matching in stereo images acquired simultaneously (Fig. 5.4c and d). However, this is not always true for images acquired in different explorations. For example, if the hair orientation is altered during undressing, the gradient information in the current and baseline images will be radically different (see Section 5.3.1). This will cause the keypoints to have different locations, orientations and descriptors, failing to produce enough matches for proper homography estimation. Because of this, we will exclude all patients with body hair from the scanner’s initial clinical validation (see Section 5.2).

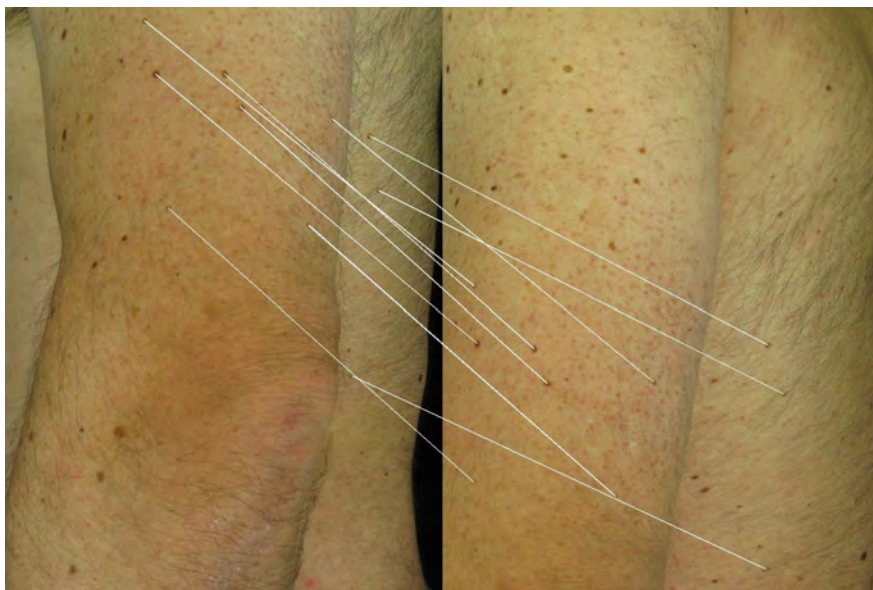
Fig. 5.5 shows mole matches in the images acquired by two camera pairs: vertical (cameras 13 and 14) and diagonal (4 and 14). As can be seen, the direction of the match lines is not uniformly defined due to the skin surface being at different distances from the cameras. Nevertheless, the matching lesions lie along epipolar lines, and the visual comparison is performed regardless of the distance to the cameras.

Overall, the stereo-matching procedure reliably establishes lesion correspondences in images acquired by neighboring cameras at the same turntable position. Failure is possible only when one of the lesion views is too slanted due to the position of the

5. RESULTS AND DISCUSSION



(a)



(b)

Figure 5.5: Mole correspondences in stereo pairs. (a) A vertical pair: images acquired by cameras 13 (left) and 14 (right) at turntable position 6. (b) A diagonal pair: cameras 4 and 14 at position 10.

patient with respect to the cameras and/or skin surface topography. However, such views can be ignored, because it can be safely assumed that the images acquired at other turntable positions will have a better view of the lesion.

5.1.5 PSL triangulation and mole set creation

Although the goal of the mole mapping is not to produce an accurate estimation of the moles' locations, but how well the system performs on average. The results of mole triangulation can be evaluated with respect to repeatability (precision) and accuracy. While the precision defines the consistency of the scanning system in estimating a 3D point's location with different stereo pairs, the accuracy indicates how close these estimations are to a real point. In order to determine these measures, we conducted two experiments: (1) using 4384 visible markers in the calibration pattern and (2) 579 PSLs detected in four explorations of two different patients. The first experiment included the ground truth for the 3D points of the calibration board, which provided a basis for the accuracy computation. For the PSL data of real patients, it is very difficult to acquire such a ground truth, especially when taking into account the involuntary movements during image acquisition.

In both experiments, we computed a number of unsigned distances between 3D points and determined their means and standard deviations; for the accuracy, the distances between the estimated and real points, and for the precision, those between triangulations produced by different stereo pairs for the same points/moles. Fig. 5.6 shows the probability density distributions describing the values obtained.³ The diagrams clearly demonstrate the difference in precision between the "synthetic" markers in the pattern and the real mole points (the red lines). The standard deviation is three times larger in the second experiment, with a mean precision 1.09 and 2.73 millimeters, respectively. This is explained by the fact that the calibration markers are well defined "corners" in space, so the detection noise has a much lower impact on the triangulation precision. In contrast, real lesions are three-dimensional surfaces of different sizes projected onto the 2D planes of the sensors. The coordinates of their projections' centroids are dependent on the orientation of the lesions with respect to the cameras and the accuracy of the blob detector. This inevitably leads to discrepancies in the 3D points estimated.

The blue line in Fig. 5.6b confirms that it is practically impossible to obtain accurate locations of the nevi on the patient's body due to the use of a turntable. Nevertheless, the precision shown by the algorithm in this experiment has the mean value of 5.55 mm with a standard deviation of 3.9 mm. Together with the accuracy measured at $\mu = 3.24$ mm with $\sigma = 0.82$, which was obtained on the "synthetic" data points (Fig. 5.6a), this estimation is sufficient to approximately determine a PSL's location on the body.

³Because the values are unsigned, the resulting Gaussians are not zero-centered.

5. RESULTS AND DISCUSSION

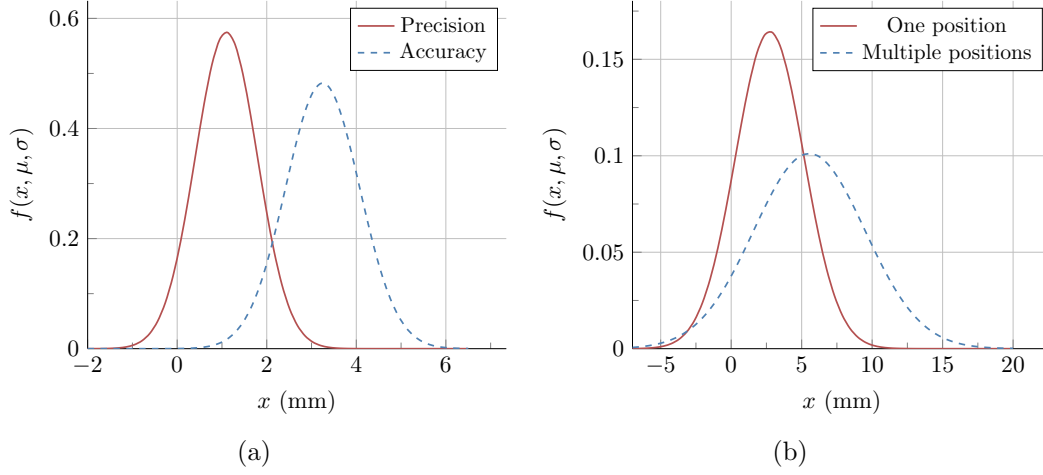


Figure 5.6: Evaluation of PSL stereo triangulation. (a) Normal probability distributions of the accuracy and precision across all cameras of the scanner. The precision ($\mu = 1.09$, $\sigma = 0.7$) is defined by the pairwise distances between all estimated coordinates of a point produced by different stereo pairs. The difference between the estimated and actual location of a 3D point describes the accuracy ($\mu = 3.24$, $\sigma = 0.8$). The mean and standard deviation values for both distributions were obtained using 4384 points in the fixed calibration pattern.

(b) PSL triangulation precision within the same turntable position ($\mu = 2.73$, $\sigma = 2.4$) and across different positions ($\mu = 5.55$, $\sigma = 3.9$). The latter distribution is less dense and has a larger mean value because the repeatability across different positions depends on the turntable's rotation noise and patient's movements. These functions were computed for a total of 579 PSLs mapped in 4 explorations (2 patients).

When all the PSLs detected are triangulated at every turntable position, they are unified into mole sets: groups of mole representations that have a unique 3D location linked with several 2D images. Mole sets are created by recursively tracing known stereo matches and performing visual comparisons in special situations (Section 4.1.3). The three-dimensional component, i.e. the PSL triangulations, of three non-overlapping mole sets is shown in Fig. 5.7. This is the result of scanning a patient with multiple nevi, lentigines and freckles. The mole blobs detected by MSER were not size-filtered, so that many small lesions could be triangulated and matched in stereo images. Due to the density of the lesions, the point cloud outlines the contours of the back, both arms and head of the patient.

The turntable stop angles were set up in a way that provides a sufficient overlap between neighboring mole sets. Examples of three consecutive sets are shown in Fig. 5.8a. The area zoom-in reveals the discrepancy between triangulations made at different stops (positions), which is consistent among individual moles of the sets. Moreover, the orientations of the normals to the local planes of the PSLs are also estimated consistently. Fig. 5.8b shows a portion of mole representations from all sets computed

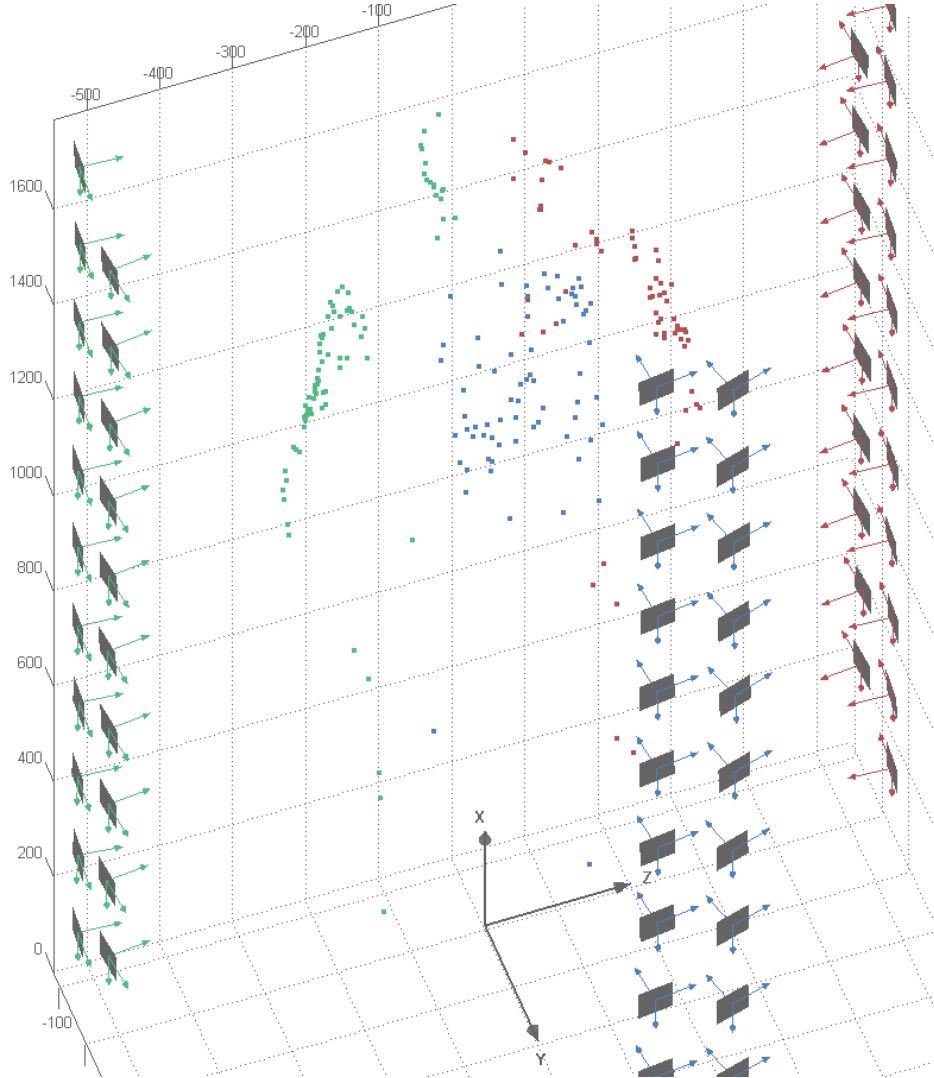


Figure 5.7: Mole sets (triangulated points) computed at three different turntable positions: 0, 5 and 11 (shown in red, blue and green, respectively). The larger coordinate system denotes the scanner’s global reference frame—the center of the turntable. The smaller systems mark the locations of the cameras relative to the turntable’s motion at each of the three positions (see Fig. 3.5 for the exact axes notation). Although the three point sets neither overlap nor cover the whole body surface, the resulting lesion cloud transmits the aspect of the human body with well distinguished arms, back and cheeks.

for the first pose (see Section 3.2). It can be seen that there are plenty of redundant mole representations for the patient’s back. This leaves room for the optimization of the turntable step configuration; however, as more experimental data is needed at this point, we decided to maintain the current configuration until more patients of different complexions are scanned.

5. RESULTS AND DISCUSSION

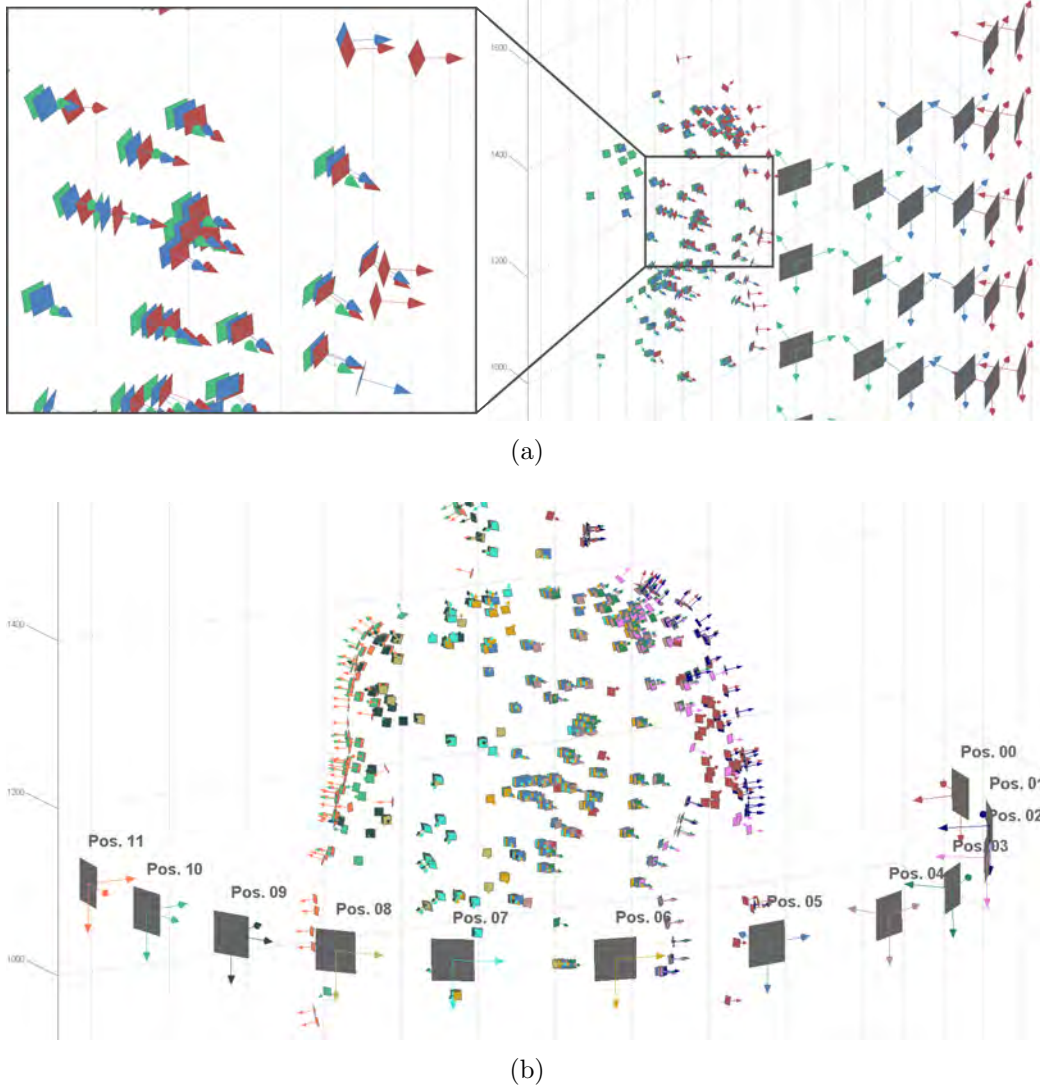


Figure 5.8: A 3D component of overlapping mole sets. (a) Mole sets computed at turntable positions 3 (red), 4 (blue), and 5 (green). The smaller arrows denote normals to the local planes of the moles, which are marked by square patches of the same color. The zoom-in of the selected area demonstrates the proximity of the lesions triangulated at different positions, as well as the similarity of their normals. (b) All mole sets (0–11) computed for pose 1. Each camera coordinate frame in the semicircle represents the whole rig at the given turntable position.

We can conclude that the triangulation step of the mapping pipeline produces a very good positional estimation of individual PSLs detected in stereo images. Given that the image acquisition procedure follows the established protocols (no abrupt movements or untimely pose changes), the discrepancies in 3D locations estimated at different turntable positions are minimal. During the mole set creation stage, the lesion

representations (images and triangulations) obtained with the stereo pairs at every turntable step are linked together. Essentially, these sets contain information about PSLs visible to the cameras from a certain point of view (stop angle).

5.1.6 Mole set merging

In order to create a complete map of the PSLs on a patient’s body, the sets of mole representations obtained at every turntable position must be merged together. The merging is to be carried out separately for the two poses: turntable steps [0,11] and [12,23]. For the moment, we have not considered merging the two resulting parts of a full map, however, this will be addressed in future work (Section 6.4).

The mole set merging procedure uses the same principle of homography-based visual comparison of individual lesions applied in stereo-pair matching (see Section 4.1.4). Due to the fact that the images to be compared are not acquired simultaneously and the patient is not absolutely still, we cannot rely on the epipolar geometry for the match candidate selection. Instead, the Euclidean distance between moles’ triangulations is used for the purpose. Images depicting moles are selected so that the difference in the viewing angles is minimized, and the ROIs are transformed according to the known camera geometry prior to extracting and matching the SIFT points.

Fig. 5.9 shows an example of a successful matching of mole representations at consecutive turntable positions. The lesion highlighted in Figs. 5.9a–c was photographed by cameras installed on both columns, and has a different appearance in each image. The view in Fig. 5.9c has the lowest η -metric because the lesion is most fronto-parallel to camera 14 at position 5. In order to compare any two of the mole’s ROIs, one of them is transformed using the fixed camera geometry to obtain roughly the same point of view of the lesion as in the other ROI. Thus, Fig. 5.9d shows SIFT matches between the transformed image (a) on the right and the original image (b) on the left. The lesion was photographed at positions 3 and 4 respectively, making it a “ $p \pm 1$ ” matching case. Likewise, in Fig. 5.9e, the “ $p \pm 2$ ” candidates are matched, with image (a) transformed accordingly (on the right).

Nevertheless, the visual comparison based on SIFT feature matches may fail in certain cases. When the difference between the viewing angles of two images is too sharp and the skin surface around a lesion is not planar, the SIFT points detected will have dissimilar descriptors. Consequently, the result of SIFT-feature matching will contain too many outliers, causing the homography estimation by RANSAC to be unable to converge to a solution. An example of such a failure is shown in Fig. 5.10,

5. RESULTS AND DISCUSSION

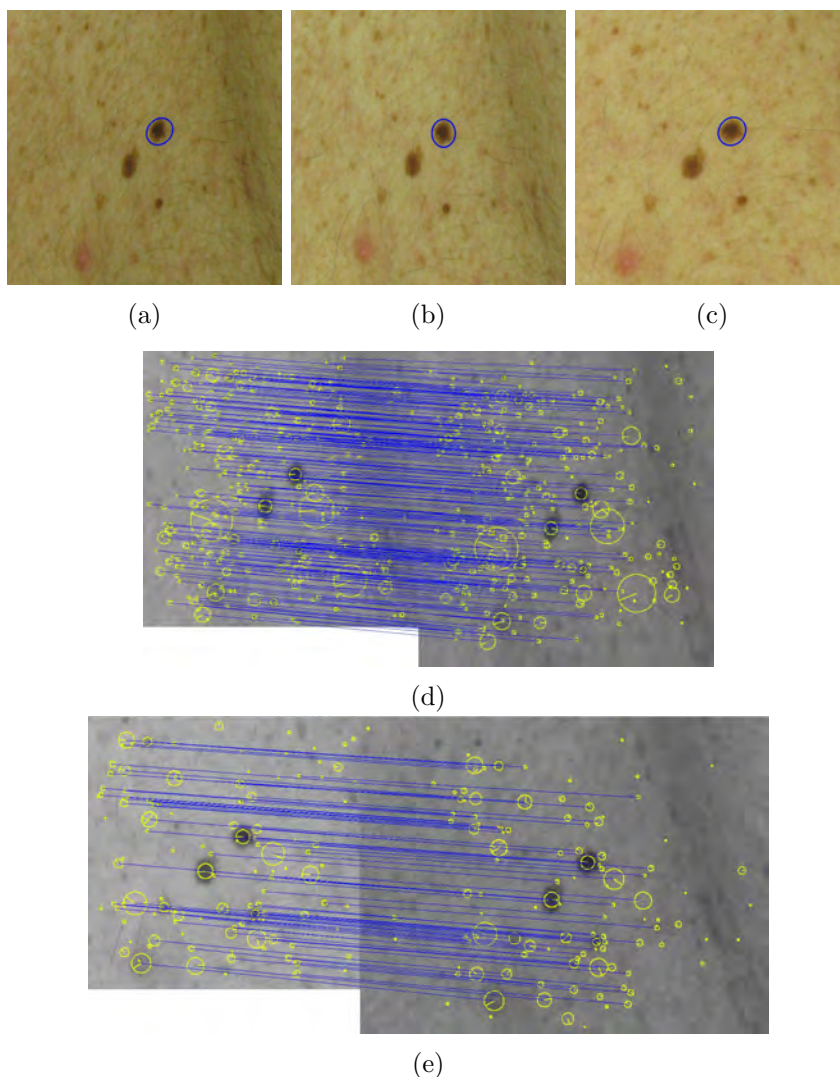


Figure 5.9: Successful mole matching at different turntable positions. (a)–(c) Images of the same lesion captured by cameras 3, 13, and 14 at positions 3, 4, and 5, respectively. These images were selected by the algorithm based on the mutual proximity of the views (Section 4.1.4.1). Note the distinctions in the appearance of the lesion due to different angles of view of the images. (d) The corresponding SIFT features detected in images (b) on the left and (a) on the right. The latter was “pre-warped” to appear as if captured from the same angle as (b). (e) The same thing happens but between (c) and (a).

where visual comparison is attempted on lesion images acquired at turntable positions 5 and 7. Despite the prior transformation of the ROI in (a), most of the SIFT point matches selected by RANSAC are outliers, and the candidates are labeled as a putative match (see Section 4.1.4.1).

Normally, putative matches can be resolved if the candidates match mole repre-

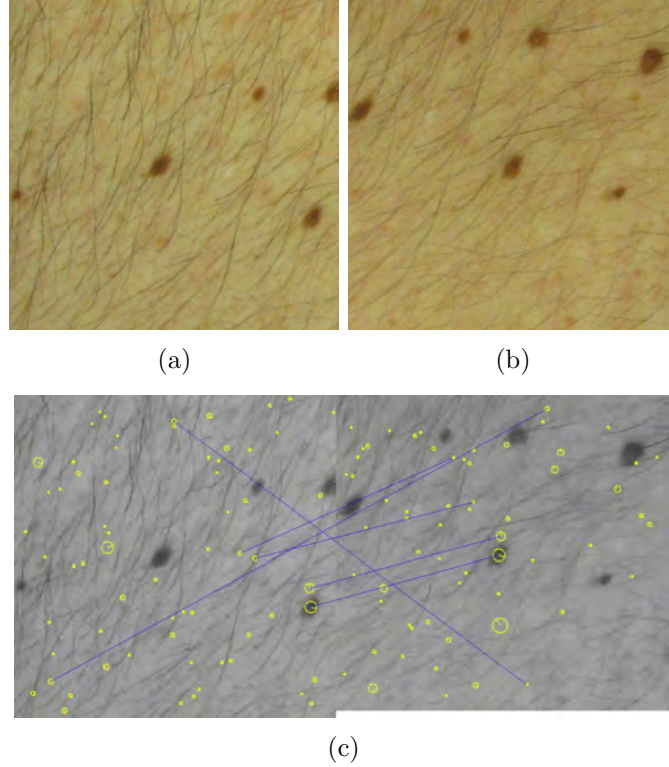


Figure 5.10: Unsuccessful matching of moles at remote turntable positions. (a)–(b) Images acquired at positions 5 and 7 by cameras 3 and 14 respectively, the lesions do not match. (c) The difference in the angles of view (even taking into account the initial warping) together with the specific relief of the skin surface around the PSL cause most SIFT features to have very dissimilar descriptors.

sentations at other positions. Otherwise, these lesions are considered unimportant for documentation because the absence of matches at neighboring positions suggests that they are either too small or not salient enough. Unfortunately, the true quantification of the failure rate during mole set matching is impossible without a generalization over numerous scans of patients of different constitutions and PSL counts. This quantification will be done as a part of a clinical validation of the scanner in the Melanoma Unit of the Hospital Clínic de Barcelona (see Section 5.2).

Once the virtual moles are matched at all positions $p \pm 1$ and $p \pm 2$, the propagation procedure automatically relates lesions matching indirectly at positions $p \pm x$. Fig. 5.11 demonstrates lesion correspondences and their propagation graphically. The points and arrows represent lesion triangulations with their normals, and the colors denote the mole sets these lesions belong to: red (1), blue (2), green (3), and brown (4). Fig. 5.11b shows these mole sets after $p \pm 1$ and $p \pm 2$ matching has been carried out, leaving the red and brown mole sets unmatched. Running the propagation procedure

5. RESULTS AND DISCUSSION

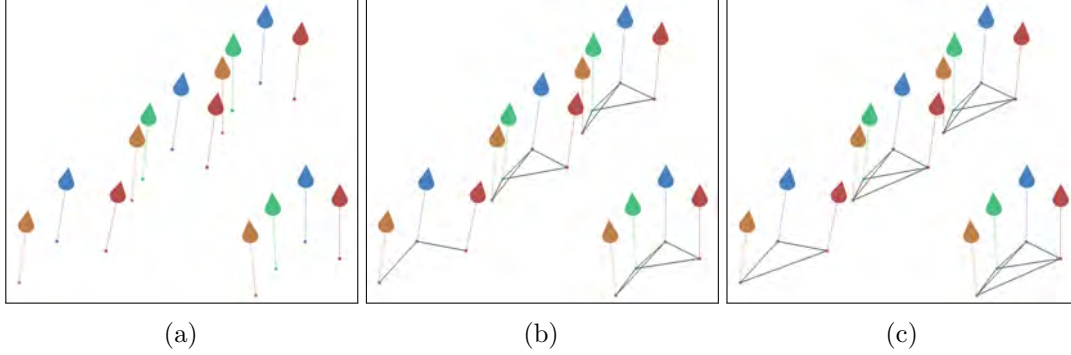


Figure 5.11: Mole set match propagation. (a) Lesion representations belonging to four different mole sets: 1 (red), 2 (blue), 3 (green), and 4 (brown). The points are the mole's 3D locations and the arrows represent normals to their surfaces. (b) Correspondences after the $p \pm 1$ and $p \pm 2$ matching procedure. (c) The result of match propagation.

completes the matching and relates virtual moles connected indirectly (Fig. 5.11c).

An important shortcoming of our approach to mole set merging is its inability to find corresponding PSLs when they do not belong to successive mole sets. For example, if a lesion is represented in mole sets 3, 4 and 7, it is impossible to connect virtual moles at the 4th and 7th turntable positions. As a result, the map will contain an undesirable artifact created by two representations of one lesion. These artifacts can be produced by smaller/less salient PSLs detected unevenly across the turntable steps. This problem, together with the MSER blob filtering and turntable step adjustment, will be addressed in future work

In conclusion, the proposed configuration of the scanner, which uses a turntable to obtain a 360° view of the patient's skin surface, creates the need for mole set merging. A drawback of this operation is that it requires multiple visual comparisons of PSLs over various turntable steps leading to an increased computational load. This can be overcome only by changing the hardware configuration of the scanner, e.g., using replicated camera arrays instead of a rotating platform. However, besides physical changes to the acquisition chamber, this approach requires considerable expenses for cameras, means of their interfacing and data collection unit(s). Therefore, the use of a turntable together with the proposed mole set merging scheme offers a trade-off between hardware cost/complexity, mapping precision and computational load.

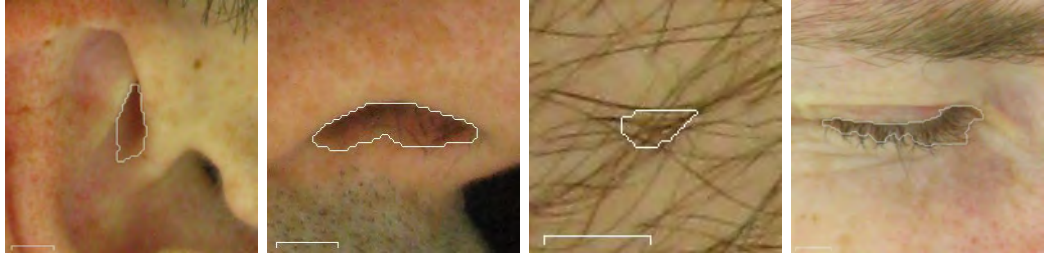


Figure 5.12: Examples of outliers, or false PSLs, present in a mole map. The contours denote rough segmentations provided by the MSER detector, and the scales correspond to 5 mm on the skin’s surface at a given view. Locations of the outliers *from left to right*: right ear, right nostril, abdominal area (body hair), and right eye.

5.2 Mole map validation

The output of the pipeline described above is a *mole map*, i.e. images of pigmented lesions linked with their approximate 3D locations on the patient’s body. The three-dimensional components of this map for the two patient’s poses are shown in Figs. 5.13a and b. The camera planes in the images denote turntable positions, and the coordinate systems refer to the global reference frame at the center of the turntable. The 3D points are triangulations of all the PSLs detected, which, besides nevi, freckles, lentigines and other lesions, also include outliers. Outliers comprise image blobs that represent maximally stable regions during the detection phase that are clearly unrelated to PSLs. For example, these can be MSER blobs detected on the ears, nose and even body hair (see Fig. 5.12).

5.2.1 The ground truth problem

Attempting the validation of the mole mapping pipeline raises the cornerstone question: *what is the ground truth?* This question seems a trivial one, however, a conclusive answer can be given only taking into account the goal of mole mapping. We stated our principal goal in the beginning of this document: the detection of changes in PSLs indicative of melanoma. It is known that not all changing lesions are equally important from the diagnostic point of view. Moreover, in practice, dermatologists performing a total-body skin examination look for “suspicious” lesions: those that have specific malignancy features related to shape and/or color. Depending on the patient, they may also consider looking only for an “ugly duckling”,⁴ paying less attention to the lesions that are unlikely to be or become malignant from their point of view.

⁴An “ugly duckling” is a PSL with significant morphological differences as compared to the rest of the patient’s skin lesions. This may be a sign of a developing malignancy.

5. RESULTS AND DISCUSSION

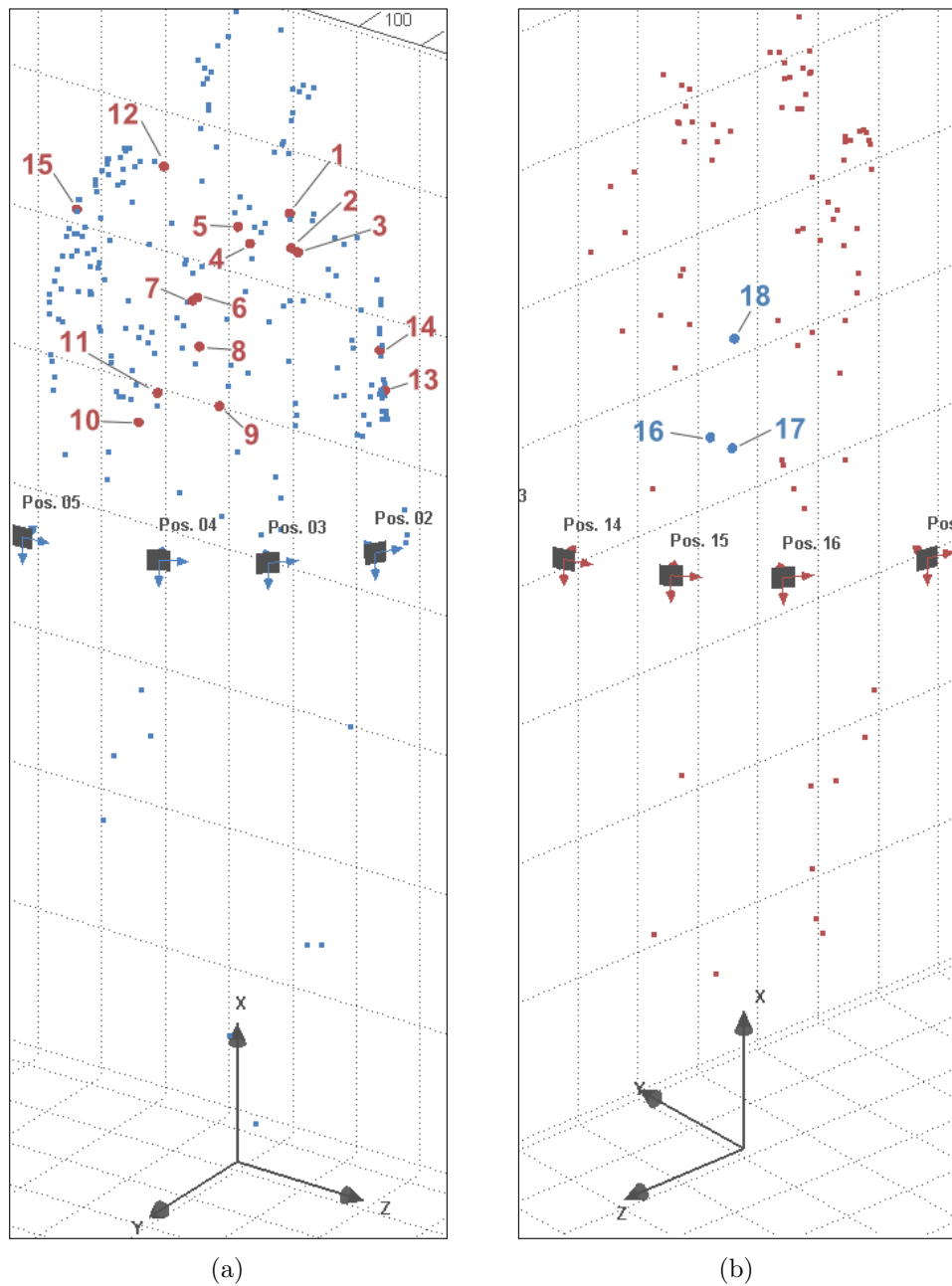


Figure 5.13: A complete PSL map of the reference patient. The lesions that have been undergoing dermoscopy follow-up during the last 11 years are highlighted and numbered (see Fig. 5.14 for their images). (a) Pose 1: patient facing the backrest column of the scanner. Lesions 1–12 are located on the patient's back in the scapular and paravertebral regions. Moles 13 and 14 are found on the right arm, while lesion 15 is on the left shoulder. (b) Pose 2: patient with back to the column. Lesions 16 and 17 are located in the right lumbar region of the abdominal area and mole 18 is located on the patient's chest.

Consequently, we are discussing a restriction on the total body skin examination to the lesions considered *relevant*. This is a rational approach which saves time in the presence of numerous nevi; however, the definition of relevance is rather subjective and can vary from physician to physician. Relevant lesions may also include different types of PSLs depending on the patient’s history and risk factors. For example, in some patients, a physician will bias the screening to dysplastic nevi, while in others, lentigines will be of interest too. As a result, lesions irrelevant from the point of view of a dermatologist are ignored during the examination, and their evolution over time is not closely followed.⁵ In most cases, these skipped lesions do not have any malignancy potential. However, a manual PSL screening influenced, in addition, by subjective criteria leaves room for human error.

From this point, we can see that there is no general unambiguous answer to the ground truth question. Nevertheless, at the current stage of the scanner’s development, we can specify the minimum results the mapping is expected to produce. In particular, an exploration map should contain all lesions considered relevant by dermatologists for a specific patient, as well as those satisfying some appearance criteria. Without additional filtering (e.g. based on machine learning), the appearance criteria are conditioned only by the scanner’s camera system and the skin-to-lesion contrast. The camera resolution restricts the size of observable PSLs, while low-contrast lesions are discarded to avoid cluttering the map. Having more than relevant lesions in the map reduces the risk of missing PSLs that can potentially lead to a malignancy.

Thus, in order to comprehensively evaluate the performance of the PSL mapping, we need to have the ground truth of the patient’s lesions which are considered relevant by several dermatologists. In clinical practice, such data collection requires combining both a manual TBSE procedure and an automated exploration using the scanner prototype. Therefore, the scanner was recently installed in the Melanoma Unit of the Hospital Clínic de Barcelona for clinical validation under the supervision of Dr. Josep Malvehy and Dr. Susanna Puig.

5.2.2 Preliminary evaluation

For evaluation of the algorithms’ performance in a laboratory setting, we used the total body examination history available for one of our volunteer patients. This history data

⁵In this respect, there is an important conceptual advantage with our scanner. If a lesion that was not detected previously is detected during the latest scan, it is possible to verify whether this is a result of its evolution over time or was simply missed before. By tracking only relevant lesions, as currently practiced in TBSE, this verification is impossible.

5. RESULTS AND DISCUSSION

included dermoscopy (MoleMaxTM) and clinical images of several PSLs undergoing regular monitoring over the last 11 years. During this period, the patient was examined by several dermatologists trained in dermoscopy, and the images were acquired by different technicians. The clinical photographs comprise only low-resolution macroscopic images of the patient in standardized poses (see Section 1.4.1.1), while the high-resolution dermoscopy images were used for the analysis and temporal monitoring of the lesions. Hence, the PSLs subject to dermoscopy follow-up were qualified as the relevant lesion ground truth for that patient.

We selected a total of 17 lesions in the areas visible by the scanner’s cameras⁶ and not completely occluded by body hair. The moles undergoing dermoscopy follow-up were found in the paravertebral and scapular regions, as well as on the right arm, left shoulder and chest (Fig. 5.13). As shown in Figs. 5.13 and 5.14, all these lesions were successfully mapped by the scanner. The side-by-side views of the clinical and corresponding dermoscopic images of the moles are shown in the latter figure. Although the level of detail offered by the images of different types is incomparable, the scanner’s photographs can be well used for the detection of changes in the lesions’ shape and color.

While the lesions in the clinical photographs have the same global orientation,⁷ their orientations in the dermoscopic images are arbitrary. We deliberately left them unaltered in order to demonstrate the difficulty of establishing lesion-to-image correspondences manually (see also Fig. 1.6 in Section 1.5). In addition, one of the lesions examined in the chest region (#18), heavily occluded by body hair, was mapped by the scanner as well. However, due to the hair occlusion, it cannot be used in automatic change detection.

The results of the preliminary evaluation do not give a definitive assessment of the mole mapping pipeline. Nevertheless, they provide valuable information that will help to anticipate and improve the performance of the algorithms in future clinical trials. Thus, the following conclusions of this validation can be highlighted:

- In a larger trial, we strive to achieve the same results regarding the sensitivity: in the test patient, 100% of the lesions considered relevant were mapped.
- The repeatability of mapping smaller/less salient lesions (freckles and lentigines) should be improved: on average, 7–10 PSLs mapped in one exploration were missed in other scans. In total, 208–222 lesions (the minimum and maximum

⁶The lesions found on the soles, the palms and the scalp were not taken into account.

⁷The vertical dimension of the images coincides with the vertical axis of the scanner.

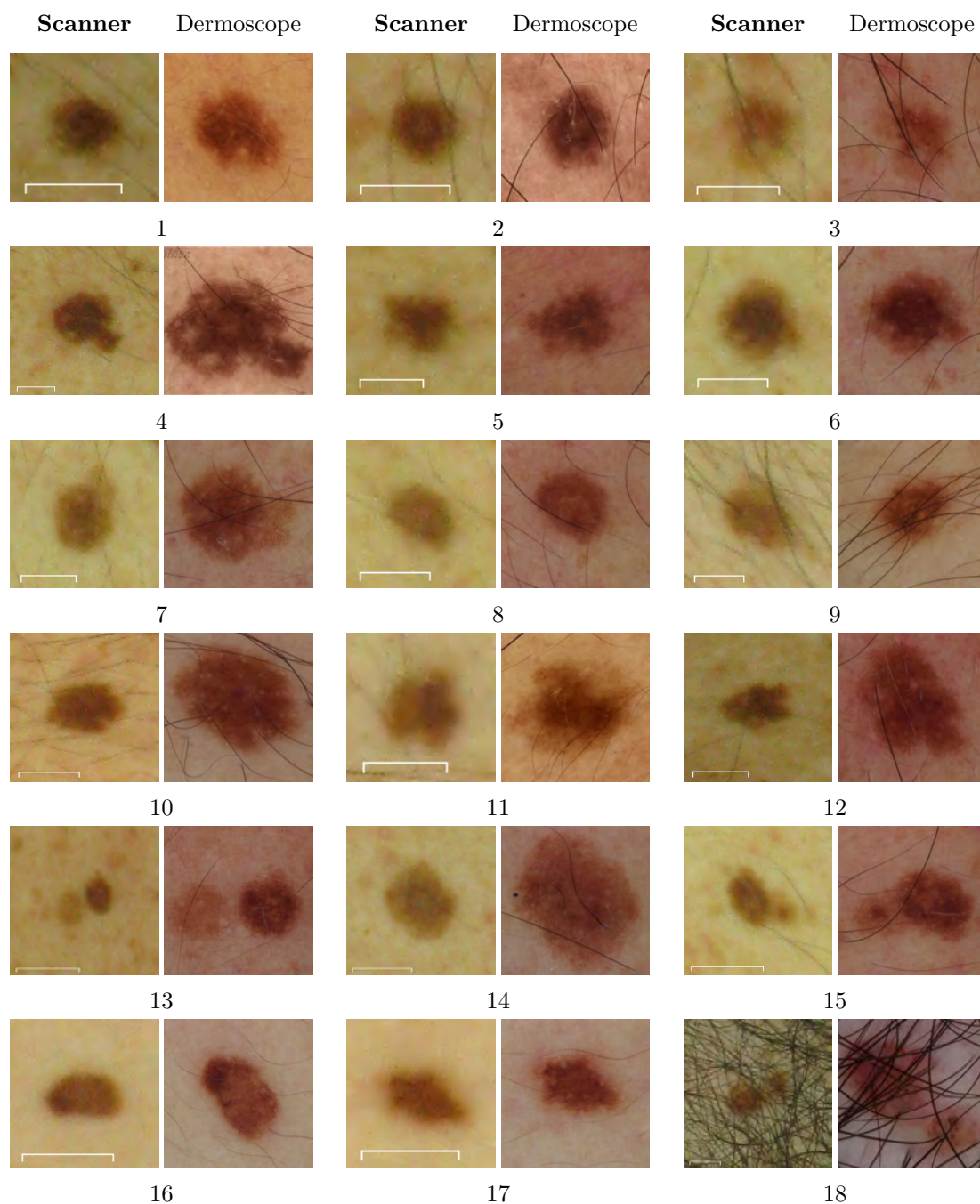


Figure 5.14: Clinical and dermoscopy images of regularly monitored PSLs of a reference patient acquired by the scanner and using MoleMax[™] (courtesy of Dr. Malvey), respectively. The locations of these lesions are highlighted in Fig. 5.13. The automatically selected views of each mole minimize its skew and maximize its image resolution (px/mm) (see Section 4.1.4.1). The scales in the images correspond to 5 mm on the skin at the moles' locations.

5. RESULTS AND DISCUSSION

mole counts across 3 explorations) were mapped for the test patient in pose 1, and 81–90 in pose 2. The PSLs marked as relevant were repeatedly mapped in all explorations. It must be noted though, that less salient lesions missed in one of the explorations will still be compared with their baseline images in the change detection pipeline (see the following Section).

- The MSER detection outliers and mole set merging artifacts should be eliminated from the map.

Overall, our approach to PSL mapping, even taking into account its current imperfections, demonstrated promising results. The scanner is able to create a permanent visual record of all the patient’s moles, mapping distinguishable PSLs with a diameter larger than 2 mm. In this way, change tracking is not limited only to the lesions considered relevant by the dermatologists.

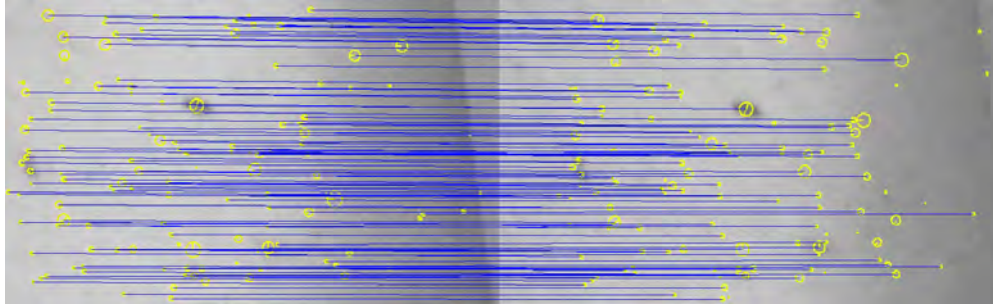
5.3 Inter-exploration operations

With two maps of a patient’s skin lesions created at different times, we can use the change detection pipeline to assess the evolution of each PSL (Section 4.2). To do this, we need to (1) determine corresponding lesions in the maps and (2) perform change detection in their aligned ROI images.

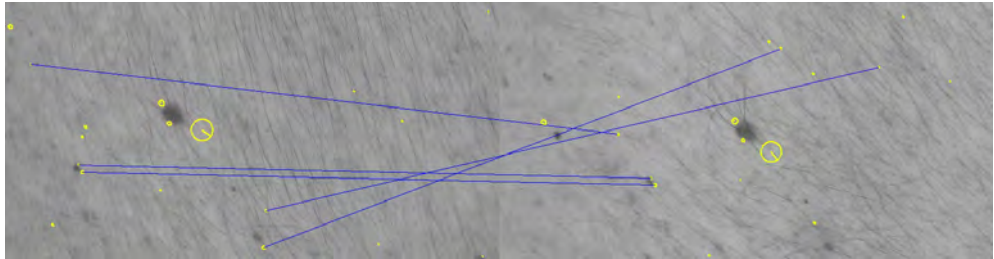
5.3.1 Lesion matching

In this work, we used a naive approach to inter-exploration lesion matching. Our main assumption (given that the scanning procedures were followed correctly) is that PSLs photographed during one exploration, E_1 , by camera C at position P , are very likely to be found in the same P - C view in another exploration, E_2 . This assumption holds true for most lesions, however, it may fail for those detected closer to image borders. The reason for this being slight differences in the patient’s position during image acquisition. It especially concerns PSLs located on the arms when the patient is in pose 1, because it is more difficult to ensure that they are in the same exact position in all the explorations.

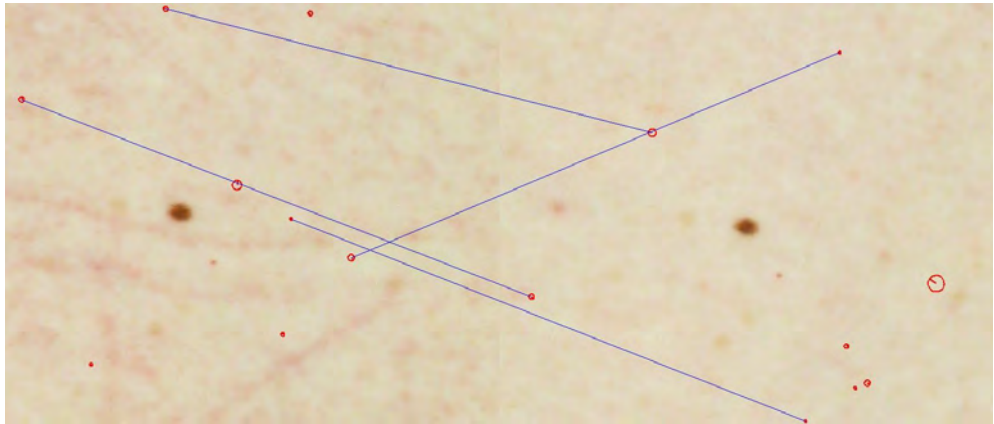
Nevertheless, when using the SIFT-based visual comparison of image ROIs (see Section 4.2.1), it is still possible to verify whether our assumption holds true for a particular lesion. A valid homography transformation between two ROIs, like the one modeling SIFT feature matches shown in Fig. 5.15a, projects the location of the mole mapped in E_1 to the image in E_2 . Our assumption fails if the projection is outside the



(a)



(b)



(c)

Figure 5.15: Inter-exploration lesion matching. SIFT feature correspondences in the images of the same lesions in different explorations after fitting a homography model using RANSAC. (a) Outliers removed, the homography model is correct. (b) Not enough inliers due to different body hair orientation. (c) No inliers because of pressure-induced skin marks in the left image (e.g. marks on the back after driving a car for some time).

image borders, however, the projection coordinates, together with the direction of the turntable's rotation, will point to the view in which this lesion is likely to be found.

The main drawback of the naive approach to PSL matching is that it is not always possible to establish the map index of the corresponding lesion in E_2 . Since a map index is determined based on the mole's MSER ellipse location, a PSL not detected in

5. RESULTS AND DISCUSSION

a particular image will be untraceable. On the other hand, this approach will succeed in performing change detection even though the lesion in E_1 is not mapped in E_2 because it will still be present in both images. Therefore, in order to produce stable map index matches as well as account for missing lesions, the naive approach can be combined with a more sophisticated technique, e.g. based on a non-rigid point cloud registration. This will be addressed in future work.

The estimation of a homography between two skin image patches can fail if the images have completely different gradient information. This will lead to a proportion of false feature correspondences that the RANSAC algorithm is unable to filter out. In our experiments, we have determined two situations causing such behavior:

1. Body hair in the image patches with different orientations, Fig. 5.15b.
2. Presence of pressure-induced skin marks in one of the images, Fig. 5.15c.

As the figures demonstrate, the RANSAC algorithm was not able to estimate a correct homography model, because the percentage of SIFT match outliers is too high. Consequently, as these results suggest, the scanning procedure should be limited to patients with no or little body hair, and any skin alteration that drastically changes its image gradient information should be avoided.

5.3.2 Change detection

After applying a homography to align the images and refine this alignment by means of normalized cross-correlation, we can obtain a difference image of the two skin images. Figs. 5.16a–d show image patches of moles that did not evolve between explorations. The respective change maps in Figs. 5.16a, b and d, nevertheless, contain artifacts (clusters of black pixels) that correspond to alignment inaccuracies, sensor noise and body hair influence. Such artifacts do not produce false change alerts as they are filtered out by thresholding the ratio of their total area to the union area of the two lesion segmentations (see Section 4.2.2).

Because our experiments were conducted using limited data, we modified some of the patients' lesions and added new moles using color markers. The newly appearing "lesions" are shown in Figs. 5.16e–f. The difference images masked by the coarse MSER segmentations indicate a 100% change. In other words, it can be automatically determined that the lesion was not there during the previous exploration. This demonstrates that the scanner is capable of early detection of small (less than 3 mm) new lesions.

Examples of the detection of artificial changes are shown in Figs. 5.16g–j. Real changes, in most cases, may not have as high a contrast between the skin and lesion

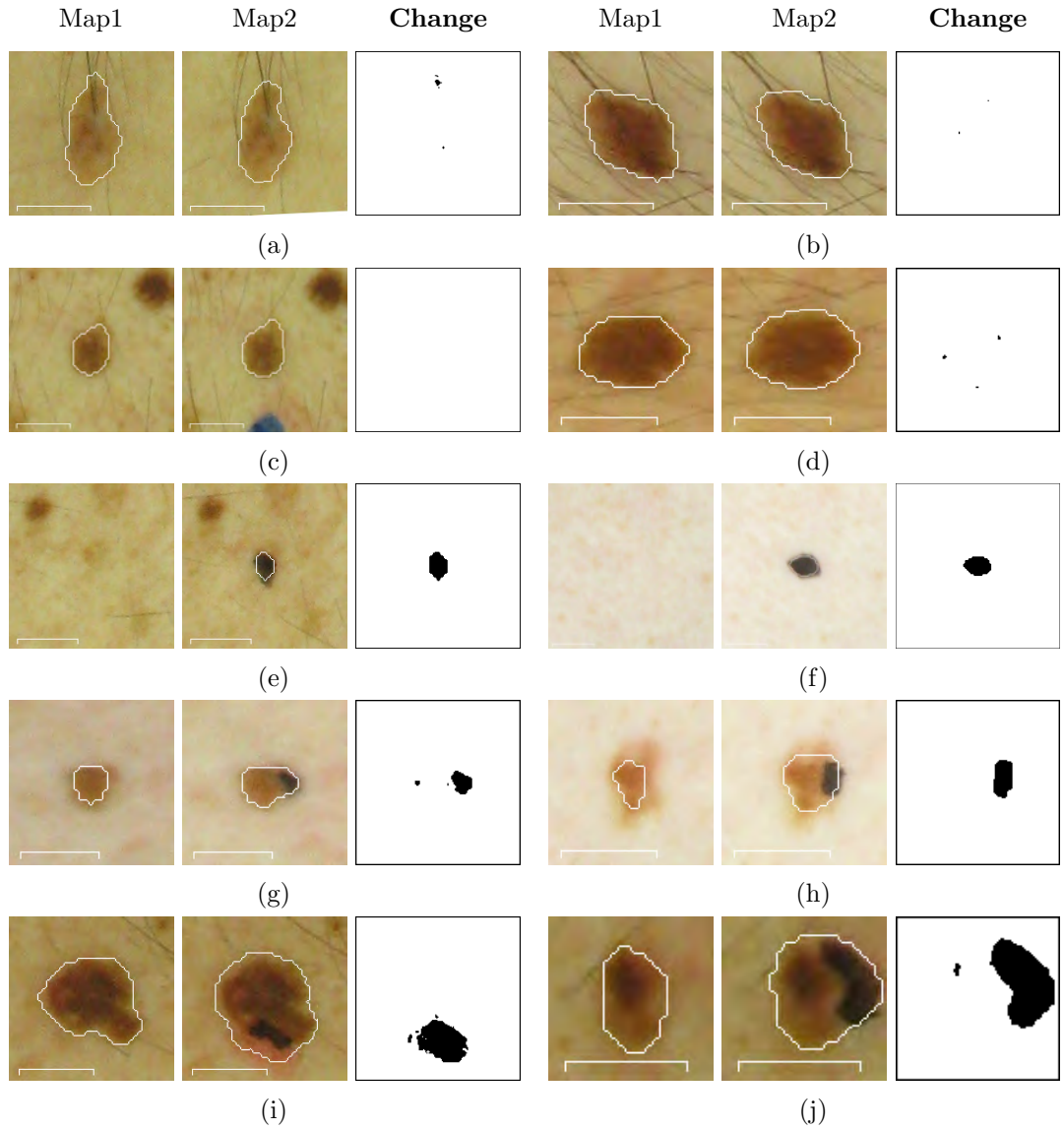


Figure 5.16: The detection of new and evolving (synthetic) skin lesions. In each subfigure, the images are ordered from left to right: lesion view in the 1st exploration, transformed view in the 2nd exploration and the change map. The scales correspond to 5 mm on the skin's surface at the lesions' location. (a)–(d) Lesions without any evolution. (e)–(f) Newly appeared artificial “moles”. (g)–(j) PSLs with changes added using black and red markers.

texture. Nevertheless, these approximations can give an idea of the scale at which the changes can be easily detected. In Fig. 5.16h, the segmentations of the lesion are fairly inaccurate, and can potentially lead to missed changes. Therefore, besides the global MSER detection/segmentation, it may be useful to apply additional algorithms for refining the border delineation.

5. RESULTS AND DISCUSSION

Due to the use of an HSV color space, subtle differences, such as the artificial red-denning in Fig. 5.16i, can be easily spotted. Of course, this can also produce false positive changes due to sensor noise or illumination inconsistencies caused by the camera-to-skin-surface angle. However, the actual influence of the noise on change detection can be fully analyzed after a much wider validation on real changing lesions. It must also be noted that the current approach does not take into account skin tan variations between images acquired in different seasons. In order to account for such differences, we will need to build an appropriate illumination model based on future exploration data.

Overall, Fig. 5.16 demonstrates the ability of the skin scanner to automatically detect new and evolving lesions between explorations, although, for now, just on synthetic examples. The initial experimental material, gathered during the validation of all the steps in the mapping and change detection pipelines, highlights both advantages and drawbacks of our approach, suggesting ways to improve the algorithms. This is further discussed in the next and concluding chapter of this thesis.

Chapter 6

Conclusions

Ever since the first description of melanoma as a disease entity in 1806 [8], science has been trying to find efficient ways to fight this dangerous malignancy. As a consequence, numerous important findings about the nature and features of this cancer have been made and have led to the elaboration of various methodologies to recognize melanoma as well as the creation of its core treatment philosophy: *excision as early as possible*.

Adhering to this philosophy, dermatologists seek reliable visual signs that would indicate an early melanoma in order to remove it safely and eliminate any chance of cancerous spreading. However, the appearance of pigmented skin lesions, the precursors of melanoma, can be exceptionally misleading and renders lesion feature interpretation a particularly difficult task whose outcome greatly depends on the professional experience of the physician. Moreover, the most advanced state-of-the-art artificial intelligence systems cannot as yet outperform human experts.

Nevertheless, there is an alternative way in which computer vision can significantly contribute to the timely detection of melanoma. A factor which is widely acknowledged to be indicative of a developing deadly malignancy is rapid evolution of or some change in pigmented lesions. This change may be hard to perceive with the naked eye, especially since the term “rapid” normally refers to a period of 3 to 6 months. Consequently, during a patient’s examination, physicians rely on baseline photography and an unaided visual search for lesions that could have evolved since the previous check-up. It is not difficult to imagine the amount of work and error risk involved when examining a patient with dozens of atypical moles exhibiting ambiguous features. Moreover, the recognition and localization of lesions depicted in baseline photographs can be extremely time-consuming.

Hence, it is clear that the automation of routine TBSE/TBSI procedures can save

6. CONCLUSIONS

time and resources, reduce patient morbidity, and minimize potential detection errors. For this reason, we have carefully reviewed the literature related to the application of computer vision to diagnosing melanoma. Our review showed that throughout the entire history of the field, change detection has not received due attention, and few attempts have been made to automate the multiple lesion analysis. This important finding gave us motivation to develop a tool for TBSE automation as well as attract more attention to the problem of automatic change detection in PSLs.

6.1 Summary of the thesis

We started our research by studying the intersection area of computer vision with the part of dermatology concerned with malignancies developing from pigmented skin lesions. The introduction chapter briefly presented the medical aspects of the field clarifying ambiguities in terminology and explaining in detail the motivation behind this work. In particular, it described the structure of the human skin and the main types of cells present in the cutis, giving basic information about benign PSLs that are known to be precursors of melanoma, and outlining the imaging techniques and diagnosis methodologies used to detect this deadly cancer. We highlighted the fact that a primordial role in detecting a developing melanoma is played by a total body skin examination, and that its automation has not received due attention.

Chapter 2 extended this study by an in-depth review of the literature addressing the computerized analysis of PSL images (micro- and macroscopic) aimed at diagnosing melanoma. We classified the existing literature according to the nature of publication (clinical or computer vision articles) differentiating between individual and multiple PSL image analysis. Relevant references were categorized, emphasizing the importance of the difference in content between dermoscopic and clinical images. Various approaches for implementing PSL computer-aided diagnosis systems and their standard workflow components were reviewed and summary tables provided. Based on the conclusions drawn from this review, we directed our work towards the development of a strategy aimed at the automation of TBSE/TBSI procedures.

In Chapter 3, we described a new total body skin scanning system designed and built in-house (briefly presented in [15] for the first time). This chapter dwells on the system's hardware including the imaging module, operation concept and the calibration procedure. The scanner allows for the acquisition of a series of overlapping cross-polarized high-resolution images covering 85-90% of the patient's skin surface. In order to process these images and use their content for change detection in multiple nevi, we

have developed a set of computer vision algorithms described in Chapter 4.

Instead of performing a complete reconstruction of the patient’s skin surface (this is practically possible), our strategy consisted of binding locations of individual PSLs with their images acquired by means of the scanner. Thus, after each exploration, the lesions are detected in the images, matched across stereo pairs at different positions of the turntable and grouped into sets. Merging these sets into a mole map creates a topological description of all visible PSLs on the patient’s body. Using the controlled environment of the acquisition chamber and following the scanning protocol, two such maps from different scans can be matched, and temporal changes in individual lesions detected. The results of a successful application of these algorithms to the real image sets are reported in Chapter 5.

6.2 Contributions

The following are the major contributions of this thesis:

- A set of algorithms used in conjunction with a total body skin scanner that automatically solve two important TBSE problems:
 - Lesion-to-image and image-to-lesion correspondence: localize the PSL on the patient’s body given its image, and vice versa.
 - Inter-exploration lesion correspondence: match an image of a PSL acquired during examination 1 to the image of the same lesion after examination 2.

As a result, the scanner is able to assist in routine TBSE procedures and automatically select lesions that require a closer analysis due to changes they have undergone since the baseline examination. It allows verification of the previous state of any PSL, and not just those considered relevant by a dermatologist during a previous examination. This is the first research work proposing a complete solution (software- and hardware-wise) for the problem of automatic change detection in multiple PSLs.

- An in-depth literature review spanning publications from over 20 years of research in the field of computerized analysis of PSLs. The review demonstrated a large discrepancy in the number of articles published on individual and multiple PSL image analysis and a scarcity of reported material on the automation of lesion change detection. Furthermore, we proposed an extended categorization of PSL

6. CONCLUSIONS

feature descriptors, associating them with the specific methods for diagnosing melanoma and separating images of the two modalities.

- A method for pattern assembly using several unique squares and one separator square: the “abacus encoding scheme”. The internal corners of the resulting pattern hold a unique signature conditioned by the four surrounding squares. The scheme was used to design the color-coded pattern for a one-shot external calibration of the scanner’s camera rig.

6.3 Limitations

Any device has its limitations, and the total body skin scanner presented is no exception. The nature of the algorithms and the hardware design establishes 2 main shortcomings:

- Body hair restriction. Due to the properties of the SIFT detector, which, in this case, relies heavily on the skin texture, patients undergoing the scanning procedure should have as little body hair as possible. Although the mole mapping pipeline will perform as expected even in the presence of thick hair, the inter-exploration mole matching may fail because of an alteration in their orientation.¹ Such an alteration results in a change of skin texture, which in turn leads to a significant dissimilarity of the SIFT points detected in the images from different explorations. Therefore, ideally, body hair should be completely removed before the examination.
- Unreachable body regions. The two poses assumed by the patient during the scanning procedure leave some areas unobserved: the soles of the feet, the palms of the arms, the inner surface of the arms, the scalp and the area behind the ears. For a complete TBSE, these areas should be photographed and analyzed separately.

6.4 Further work

The main directions for further work can be viewed in short-term and long-term perspectives. The short-term goals include:

¹This may happen when changing clothes, for example.

-
- ▶ Continuous validation of the scanner’s hardware and software in a real clinical setting. This stage is vital for discovering potential weak points in the approach, correcting exiting errors (“debugging”) and fine-tunning the parameters.
 - ▶ Various algorithm improvements: removal of the mole set merging artifacts, enhancement of the inter-exploration lesion matching (naive approach + point cloud registration) and refinement of rough MSER segmentations.
 - ▶ Merging the mole maps for the two poses. Some of the lesions mapped when the patient is in pose 1 will overlap with those acquired at pose 2, for example PSLs on the shoulders and cheeks. A unified representation of the map for the whole body will reduce unnecessary redundancy and facilitate data interpretation for physicians.
 - ▶ PSL classification. Apart from the nevi, interesting from the point of view of melanoma diagnosis, the output of the mole detection may contain other “blobs”. For example, lesions of similar appearance, such as freckles or acne, or even non-lesion spots, e.g. nostrils or ear convolutions, can be detected as PSLs. They produce noise in the output of the change detection pipeline as well as waste computational resources, and thus should be discarded in earlier stages. One possible way to do this is by applying a binary classifier to the detected blobs, which, based on certain features, can determine whether these blobs represent a PSL of interest or not. The research alone needed to obtain such a classifier forms some serious scientific work.

Among the long-term work directions we can highlight the following:

- Improve camera focusing. In the presented scanning system, the focusing in some images is clearer than in others. This is conditioned by the fact that the focus distance is fixed throughout the entire exploration, while the space between the body and the cameras varies. Consequently, the established depth of field of the cameras is not enough to account for the difference. This can be overcome by employing an external focusing aid (e.g. ultrasonic sensors) or using cameras/optics allowing for a more flexible tuning. In either case, simultaneous image acquisition by all the cameras must be preserved.
- Improve camera resolution. In order to perform a more minute analysis and catch the smallest change in a PSL, the image resolution should be increased (currently, the cameras acquire 12-megapixel images). As a side effect, this will increase the

6. CONCLUSIONS

amount of image data as well and affect the performance of the algorithms, so the data handling procedures must be changed accordingly.

- Change characterization. Given the higher-resolution images with improved focusing, we can work out strategies for detailed automatic change characterization. Since lesions change not only in size, but also in color and morphology, the scanning system may be used to better study the character of changes in malignant growths.

Appendix A

Methodology

A.1 Maximally Stable Extremal Regions

The notion of maximally stable extremal regions (MSER) was introduced by Matas et al. in [394]. The MSERs are sets of image elements (pixels), closed under the affine transformation of image coordinates and invariant to affine transformation of intensity.¹ In other words, these regions are salient image areas that can preserve their structure over a wide range of binarization thresholds.

The authors described MSERs informally in the following way: given a sequence of all possible intensity thresholds applied to an 8-bit gray-scale image, the resulting 255 binary images can be combined into a motion picture, where frame t corresponds to the image after binary thresholding at intensity level t . Some frames in this “movie” are shown in Fig. A.1. Playing back this frame sequence, the observer will see a completely white image at first, then, black regions will emerge, grow and join together, until the entire image changes its color to black. Consequently, it is possible to define stability criteria for these changing regions and detect the most salient ones, based on how stable they are over the applied thresholds.

In order to formally define and describe maximally stable extremal regions, it is essential to introduce the concepts of *regions*, their *outer boundaries* and *extremal regions* as used in [394]:

1. For an 8-bit grayscale image I and a 4-neighborhood pixel connectivity A , a region

¹In accordance with the affine photometric model, given N measured images of a static scene q , the following holds: $g_i = a_i q + b_i$, where g_i is the i -th measured image, and the gain (a_i) and offset (b_i) parameters can model global external illumination changes and camera parameters such as exposure rate, aperture size, and white balancing. The affine model is successful when photometric changes are small [401].

A. METHODOLOGY

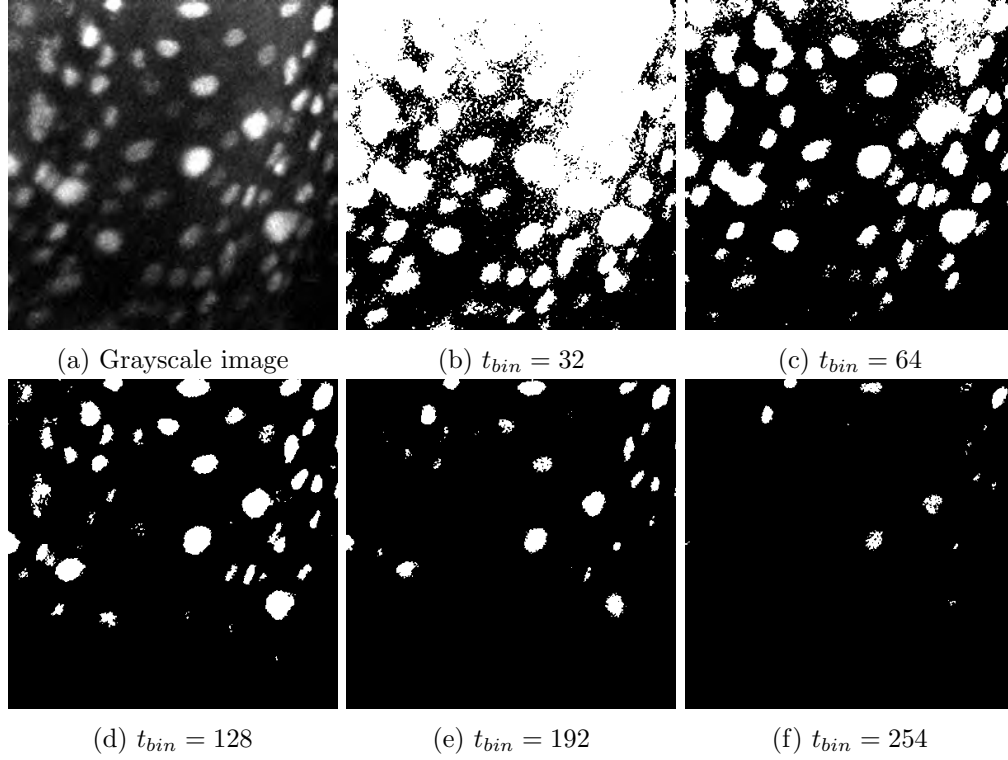


Figure A.1: Sample image of binarization using different intensity threshold values t_{bin} . The image shows cells in a 70-micrometer thick piece of vocal cord from a pig. Taken with a two-photon fluorescence microscope (Ben-Yakar Group, University of Texas at Austin).

Q is a group of adjacent image pixels, so that for two pixels $p, q \in Q$ there is a sequence of pixels $a_1, a_2, \dots, a_n \in Q$ so that $pAa_1, a_1Aa_2, \dots, a_nAq$.

2. The outer region boundary ∂Q is the set of pixels not belonging to Q that are adjacent to at least one pixel of Q .
3. A region Q is extremal if all pixels p in region Q and all pixels q on its boundary ∂Q satisfy the inequality $I(p) > I(q)$, yielding a maximum intensity region (or $I(p) < I(q)$ defining a minimum intensity region). In the informal explanation above, the set of all the connected components of all the frames in the movie is the set of all extremal regions in the image.

In this way, given a sequence of nested extremal regions $Q_1, \dots, Q_{i-1}, Q_i, \dots$, i.e. $Q_i \subset Q_{i+1}$, extremal region Q_{i^*} is maximally stable if and only if the function

$$f(i) = \frac{|Q_{i+\Delta} \setminus Q_{i-\Delta}|}{|Q_i|}, \quad (\text{A.1.1})$$

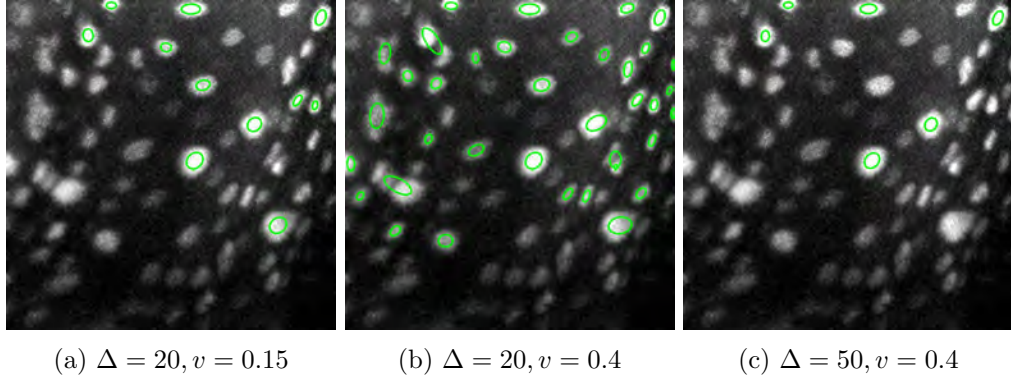


Figure A.2: Example of MSER detection with different parameters of relative (Δ) and absolute (v) stability scores.

has a local minimum at i^* . Operator \setminus denotes set-theoretic difference of two sets, while $|\cdot|$ is a set's cardinality (number of elements). Among several nested extremal regions, the maximally stable one is the one whose area is the largest in comparison with the area of the set-theoretic difference of its bounding (outer) and bounded (inner) sets. The nesting level of the outer and inner sets is controlled by the relative stability parameter, Δ . During MSER detection, it is also possible to parameterize the absolute stability score of f , known as maximum variation of the region. An example of a MSER detection results is shown in Fig. A.2.

Maximally stable extremal regions have a number of important properties which make them particularly interesting for PSL detection in the scanner:

- Invariance to affine transformation of image intensities. This means that the same skin area photographed at two different moments in time using the same camera orientation will produce the same MSERs (given that the skin's surface change is not radical).
- Covariance to continuous linear transformations in the image domain preserving pixel adjacency. Although the transformation between the stereo images in the scanner is not linear, the repeatability of the MSER detector is very good, especially for darker lesions with a well-marked border.
- Stability of the regions. Only areas virtually unchanged over a range of thresholds are selected, so unstable image artifacts such as thin body hair, light freckles, rashes or acne will be discarded.
- Multi-scale detection. It is possible to detect both smaller and larger lesions

A. METHODOLOGY

without specific multi-scale processing.

- Fast detection: the set of all extremal regions can be enumerated in $O(n \log \log n)$. The algorithm's performance is very important given the amount of images to be processed per exploration. The processing speed can be additionally improved by detecting MSERs in resized images.

In this project, we used the Matlab[®] implementation of the MSER algorithm from the VLFeat library [402].

A.2 Epipolar geometry

Epipolar geometry is the intrinsic projective geometry between two views of a scene [388]. It is defined by the intersection of the image planes with the family of planes passing through the line joining the camera centers (the baseline). Fig. A.3 describes the epipolar geometry in the context of a point correspondence search. A point \mathbf{X} in space is viewed at \mathbf{x} and \mathbf{x}' by the cameras with centers \mathbf{C} and \mathbf{C}' , respectively. The baseline of the cameras is the segment \mathbf{CC}' . The epipolar geometry in a generic camera view configuration, such as the one in Fig. A.3, is defined by the following elements:

- The *epipoles* \mathbf{e} and \mathbf{e}' . These are the points of intersection of the baseline with the camera planes. Equivalently, \mathbf{e} is the image of \mathbf{C}' in the left view, and \mathbf{e}' is the image of \mathbf{C} in the right view.
- An *epipolar plane* passing through the baseline \mathbf{CC}' . As shown in Fig. A.3, this plane also passes through the point in space \mathbf{X} , and its projections \mathbf{x} and \mathbf{x}' .
- *Epipolar lines* produced by the intersection of an epipolar plane with the image planes (in Fig. A.3, these are \mathbf{l} and \mathbf{l}'). All epipolar lines intersect at the epipole.

Thus, knowing the coordinates of one of the projections, \mathbf{x} , the coordinates of the other projection, \mathbf{x}' , can be found along line \mathbf{l}' . In other words, there is a projective mapping

$$\mathbf{x} \mapsto \mathbf{l}',$$

so that a point in one image corresponds to an epipolar line in the other image. This mapping is defined by the so called *fundamental matrix*, \mathbf{F} .

The definition of \mathbf{F} can be derived using the notion of planar homography. Considering that the point in space \mathbf{X} lies on plane π that does not pass through either of

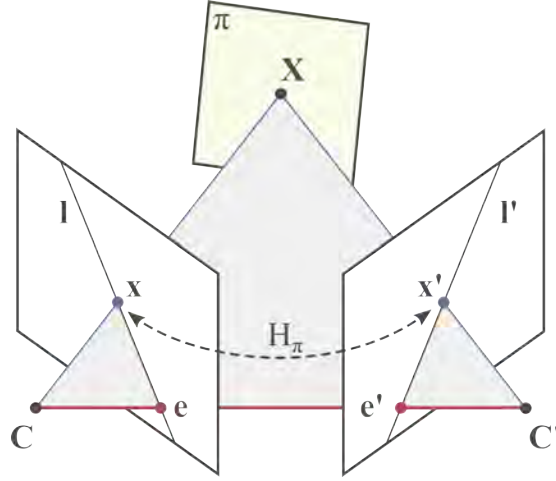


Figure A.3: Point correspondence and epipolar geometry. The two cameras are represented by their image planes and centers \mathbf{C} and \mathbf{C}' . The line connecting the camera centers is called the baseline. The baseline intersects the image planes at points \mathbf{e} and \mathbf{e}' , called epipoles, which, together with the point in space \mathbf{X} , its projections \mathbf{x} and \mathbf{x}' , and the camera centers, lie on the epipolar plane. The intersection of the epipolar plane with the image planes produces epipolar lines, \mathbf{l} and \mathbf{l}' . If \mathbf{X} lies on plane π that does not pass through either of the two camera centers, projections \mathbf{x} and \mathbf{x}' are related by a planar homography \mathbf{H}_π : $\mathbf{x}' = \mathbf{H}_\pi \mathbf{x}$.

the two camera centers (Fig. A.3), the projections \mathbf{x} and \mathbf{x}' will be related by a planar homography, \mathbf{H}_π :

$$\mathbf{x}' = \mathbf{H}_\pi \mathbf{x}.$$

Furthermore, the epipolar line \mathbf{l}' passing through \mathbf{x}' and the epipole \mathbf{e}' can be defined as a cross-product:

$$\mathbf{l}' = \mathbf{e}' \times \mathbf{x}' = \begin{bmatrix} 0 & -e_3 & e_2 \\ e_3 & 0 & -e_1 \\ -e_2 & e_1 & 0 \end{bmatrix} \begin{bmatrix} x'_1 \\ x'_2 \\ x'_3 \end{bmatrix} = [\mathbf{e}']_{\times} \mathbf{x}'.$$

Since $\mathbf{x}' = \mathbf{H}_\pi \mathbf{x}$, we have

$$\mathbf{l}' = [\mathbf{e}']_{\times} \mathbf{H}_\pi \mathbf{x} = \mathbf{F} \mathbf{x},$$

where $\mathbf{F} = [\mathbf{e}']_{\times} \mathbf{H}_\pi$ is the fundamental matrix. It is a rank 2 homogeneous matrix with 7 degrees of freedom. For the corresponding image points \mathbf{x} and \mathbf{x}' , $\mathbf{x}'^T \mathbf{F} \mathbf{x} = 0$, while for the epipoles: $\mathbf{F} \mathbf{e} = 0$ and $\mathbf{F}^T \mathbf{e}' = 0$.

For a stereo rig, calibrated both intrinsically and extrinsically, the fundamental matrix can be computed from the *essential matrix*. The essential matrix is the specialization of the fundamental matrix to the case of the normalized image coordinates:

A. METHODOLOGY

$\hat{\mathbf{x}} = \mathbf{K}^{-1}\mathbf{x}$, where \mathbf{K} is the intrinsic calibration matrix (see Eq. 3.3 in Section 3.3.1). With the effect of the known \mathbf{K} removed, the camera matrix $\mathbf{K}^{-1}\mathbf{P} = [\mathbf{R}|\mathbf{t}]$ is called a normalized camera matrix. Given two such matrices, $\mathbf{P} = [\mathbf{I}|\mathbf{0}]$ and $\mathbf{P}' = [\mathbf{R}|\mathbf{t}]$ with the world origin at the first camera, the essential matrix has the form (for proof, see [388]):

$$\mathbf{E} = [\mathbf{t}]_{\times}\mathbf{R} = \begin{bmatrix} 0 & -t_3 & t_2 \\ t_3 & 0 & -t_1 \\ -t_2 & t_1 & 0 \end{bmatrix} \begin{bmatrix} r_1 \\ r_2 \\ r_3 \end{bmatrix}.$$

Therefore, the defining equation for the essential matrix is

$$\hat{\mathbf{x}}'^T \mathbf{E} \hat{\mathbf{x}} = 0.$$

The fundamental matrix can be obtained from \mathbf{E} substituting for $\hat{\mathbf{x}}$ and $\hat{\mathbf{x}}'$:

$$\mathbf{x}'^T \mathbf{K}'^{-T} \mathbf{E} \mathbf{K}^{-1} \mathbf{x} = 0,$$

hence

$$\mathbf{F} = \mathbf{K}'^{-T} \mathbf{E} \mathbf{K}^{-1}.$$

A.3 Scale-Invariant Feature Transform

Scale-Invariant Feature Transform (SIFT) is an algorithm for the detection and description of interest points in gray level images, developed and patented by David Lowe [315]. It is widely used in computer vision for view-based feature matching and object recognition. The main advantage of SIFT points (features) is their invariance to image scale and rotation. This means that a salient point detected by SIFT in image \mathbf{I} will be detected at the same location in the resized and/or rotated version of \mathbf{I} , and will have the same or a very similar descriptor.

SIFT features are also robust against changes in a 3D viewpoint and illumination. These are especially important properties for the PSL matching scheme used in this work. In the scanner, the images may be acquired at different viewing angles and have variable illumination, depending on whether the body region viewed is farther from or closer to the lighting system. Chapter 5 of this thesis reported a successful application of SIFT in the lesion mapping pipeline, and below, we provide a brief description of this algorithm.

The detection of SIFT features in a grayscale image is performed using a cascade

filtering approach which includes scale-space extrema detection, accurate keypoint localization, post-filtering, and orientation assignment. Then, using the gradient information, the feature descriptor encodes a local image neighborhood at the location of the stable keypoints. In this explanation, all the steps leading to a SIFT feature extraction are joined in one sequence:

1. **Scale-space extrema detection.** In this step, the original image is represented as a multi-resolution image pyramid. Each level in this pyramid contains a stack of repeatedly smoothed images, called *scale space*. The scale-space representation is motivated by the basic observation that objects at different scales are composed of different structures. For example, a forest consists of individual trees, the trees have boughs, branches and leaves, etc. Hence, to discern structures within an object at a larger scale, we need to ignore smaller details. To do this, we can either stand farther away from the object, or observe it with squinted eyes. The more our eyelids are drawn together, the blurrier the object is going to appear, rendering fine details indistinguishable, but emphasizing coarser elements of its structure.

The scale-space representation imitates this approach allowing for the detection of fine and coarse structures of the object(s) in the scene. Thus, the scale space of an image is a collection of smoothed versions of this image, controlled by one parameter σ , that can be defined as the function

$$L(x, y, \sigma) = G(x, y, \sigma) * I(x, y), \quad (\text{A.3.1})$$

where G is a variable-scale Gaussian kernel, I is the input image, and $*$ is the convolution operator. The Gaussian kernel is defined as

$$G(x, y, \sigma) = \frac{1}{2\pi\sigma^2} e^{-\frac{x^2+y^2}{2\sigma^2}} \quad (\text{A.3.2})$$

with σ being the standard deviation of the Gaussian distribution. Fig. A.4 shows the scale-space representation of a tree drawing at different scales. The discrete size of the Gaussian filter applied to the image was set to $6\sigma \times 6\sigma$ pixels, since the pixels outside this range have a very low statistical significance. Notice, how at higher (coarser) scales it gets harder to distinguish individual branches of the tree.

To efficiently detect stable keypoint candidate locations, Lowe proposed [403] finding the scale space extrema in the difference-of-Gaussian (DoG) function. This function can be computed as the difference of the nearby scales of I separated by a constant

A. METHODOLOGY

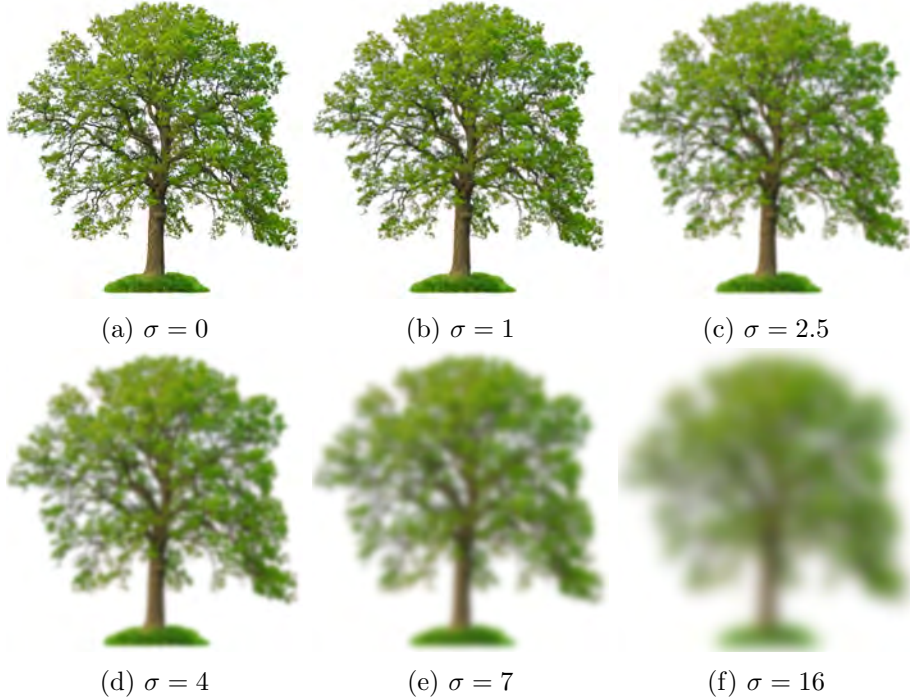


Figure A.4: Image scale-space representation: the drawing of a tree at different scales of Gaussian smoothing. The support of the Gaussian filter is $6\sigma \times 6\sigma$ pixels.

multiplicative factor k :

$$D(x, y, \sigma) = (G(x, y, k\sigma) - G(x, y, \sigma)) * I(x, y) = L(x, y, k\sigma) - L(x, y, \sigma). \quad (\text{A.3.3})$$

The DoG function was chosen because it is simple and efficient to compute (just an image difference) and, in addition, it provides a close approximation to the scale-normalized Laplacian of Gaussian $\sigma^2 \nabla^2 G$, whose maxima and minima produce the most stable image features [315]. Moreover, it allows filtering key points located along the edges and those with low contrast.

Furthermore, to create the image pyramid needed for scale-invariant² feature detection, the scale-space sampling is combined with the image downsampling (resizing). This effectively divides the scale space into *octaves* in which smoothed images with the same resolution are separated by a constant scale factor k (*scale sampling*). Fig. A.5 shows a graphical representation of octaves. The amount of prior smooth-

²The term “scale” may have different meanings depending on the context. In the scale-space representation of a signal/image, “scale” refers to the level of the signal’s detail: fine (lower) or coarse (higher) scale. However, when referring to an image, scale is the image’s size (resolution).

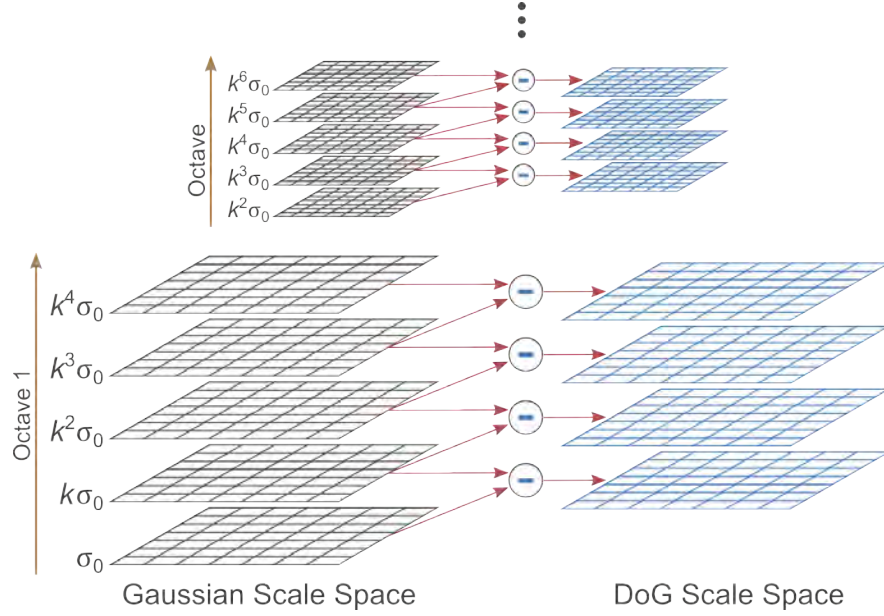


Figure A.5: The scale-space pyramid with $s = 2$ intervals and $s + 3$ images per octave. The octaves of the scale space are formed by repeatedly convolving the original image with Gaussians. The initial image of each subsequent octave is the down-sampled (halved) version of the last image in the previous octave. The subtraction of adjacent Gaussian images produces the difference-of-Gaussian images.

ing σ_0 , constant for the whole scale-space, defines the *space sampling* of the pyramid. The scale of an octave's initial image is two times smaller than the scale of its last image:

$$\sigma_{s+1}^o = 2\sigma_1^o,$$

where o represents the octave's index, and s is the integer number of intervals, so that $k = 2^{1/s}$. The initial image of each successive octave is the down-sampled (halved) version of the last image of the preceding octave:

$$\sigma_1^{o+1} = \sigma_{s+1}^o.$$

Adjacent image scales are subtracted to produce the difference-of-Gaussian images. Note that since the scale-space extrema are computed from the DoG function (as shown further), we must obtain $s + 3$ blurred images per octave to cover all its scales (see Fig. A.5).

To give an example, for $O = 3$ octaves divided into $s = 2$ intervals with the initial scale σ_0 , the Gaussian scale-space of a 200×200 image will contain the following image scales (see Fig. A.5 for the first two octaves):

A. METHODOLOGY

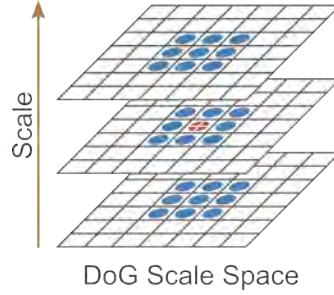


Figure A.6: Extrema detection in the difference-of-Gaussian images. The pixel of interest in a DoG image is compared to its 26 neighbors in the 3×3 region at the current and adjacent scales (above and below). A pixel is considered an extremum if it is larger or smaller than all of the 26 neighbors. Pixels belonging to the scales at the top and bottom of a DoG octave are not checked for extrema.

Octave 1 (200×200):	σ_0	$2^{\frac{1}{2}}\sigma_0$	$2\sigma_0$	$2^{\frac{3}{2}}\sigma_0$	$4\sigma_0$
Octave 2 (100×100):	$2\sigma_0$	$2^{\frac{3}{2}}\sigma_0$	$4\sigma_0$	$2^{\frac{5}{2}}\sigma_0$	$8\sigma_0$
Octave 3 (50×50):	$4\sigma_0$	$2^{\frac{5}{2}}\sigma_0$	$8\sigma_0$	$2^{\frac{7}{2}}\sigma_0$	$16\sigma_0$

2. Keypoint localization. To detect local extrema in the DoG images, each sample point (pixel) is compared to its 26 neighbors: 8 at the same image scale and 9 at the scales immediately above and below (see Fig. A.6). The point will be selected only if it is larger or smaller than all of its neighbors. The experiments conducted by Lowe in [315] showed that the highest repeatability of keypoint detection with respect to location and scale was achieved with prior smoothing $\sigma_0 = 1.6$ and $s = 3$ intervals per octave. Moreover, if the original image is doubled in size after smoothing with $\sigma = 0.5$, it increases the number of stable keypoints by a factor of almost 4.

Once the local extrema in the DoG images have been found, their locations are refined by using quadratic interpolation. For that purpose, the author used the Taylor expansion up to the quadratic terms to represent the DoG image:

$$D(\mathbf{x}_0 + \mathbf{h}) = D(\mathbf{x}_0) + \left(\frac{\partial D}{\partial \mathbf{x}} \right)^T \bigg|_{\mathbf{x}=\mathbf{x}_0} \cdot \mathbf{h} + \frac{1}{2} \mathbf{h}^T \cdot \frac{\partial^2 D}{\partial \mathbf{x}^2} \bigg|_{\mathbf{x}=\mathbf{x}_0} \cdot \mathbf{h}, \quad (\text{A.3.4})$$

where \mathbf{x}_0 is the candidate extremum point, $\mathbf{h} = (x, y, \sigma)^T$ is the offset from \mathbf{x}_0 to the precise location of the extremum, and

$$\frac{\partial D}{\partial \mathbf{x}} = \begin{bmatrix} \frac{\partial D}{\partial x} \\ \frac{\partial D}{\partial y} \\ \frac{\partial D}{\partial \sigma} \end{bmatrix} \quad \text{and} \quad \frac{\partial^2 D}{\partial \mathbf{x}^2} = \begin{bmatrix} D_{xx} & D_{xy} & D_{x\sigma} \\ D_{yx} & D_{yy} & D_{y\sigma} \\ D_{\sigma x} & D_{\sigma y} & D_{\sigma\sigma} \end{bmatrix}$$

are the first- and the second-order derivatives (Hessian matrix) of D at the candidate

point. The offset \mathbf{h} to the precise extremum point is found by taking the derivative of D (Eq. A.3.4) with respect to \mathbf{h} and setting it at zero:

$$\left. \frac{\partial D}{\partial \mathbf{x}} \right|_{\mathbf{x}=\mathbf{x}_0} + \left. \frac{\partial^2 D}{\partial \mathbf{x}^2} \right|_{\mathbf{x}=\mathbf{x}_0} \cdot \mathbf{h} = 0.$$

Hence,

$$\mathbf{h} = - \left(\left. \frac{\partial^2 D}{\partial \mathbf{x}^2} \right|_{\mathbf{x}=\mathbf{x}_0} \right)^{-1} \cdot \left. \frac{\partial D}{\partial \mathbf{x}} \right|_{\mathbf{x}=\mathbf{x}_0}. \quad (\text{A.3.5})$$

The derivative and the Hessian are approximated by neighboring pixel differences, and the resulting 3×3 linear system of equations can be solved with minimal cost. If the offset value \mathbf{h} is larger than 0.5 in any dimension, it means that the extremum lies closer to a different sample point, and the interpolation is performed there instead.

3. **Keypoint filtering.** The unstable extrema points (keypoints with low contrast) are rejected by thresholding the value of D at the interpolated location \mathbf{h} . The authors chose to discard all extrema with $|D(\mathbf{h})| < 0.03$ corresponding to the “peak threshold”. The value of $|D(\mathbf{h})|$ can be found by substituting equation A.3.5 into A.3.4:

$$D(\mathbf{h}) = D(\mathbf{x}_0) + \frac{1}{2} \left(\left. \frac{\partial D}{\partial \mathbf{x}} \right|_{\mathbf{x}=\mathbf{x}_0} \right)^T \cdot \mathbf{h}. \quad (\text{A.3.6})$$

Keypoints originating from edges are often represented by flat peaks in the DoG function, which makes them unstable in the presence of noise. These keypoints can be removed by evaluating the principal curvatures³ of D at the corresponding peak. The idea is that a poorly defined peak will have a large principal curvature across the edge, but a small one in the perpendicular direction. Therefore, we can discard peaks based on the ratio of the principal curvatures only.

This ratio can be obtained from Hessian matrix \mathbf{H} computed at the location and the scale of keypoint \mathbf{x} :

$$\mathbf{H}(\mathbf{x}) = \begin{bmatrix} D_{xx} & D_{xy} \\ D_{xy} & D_{yy} \end{bmatrix}. \quad (\text{A.3.7})$$

The eigenvalues of Hessian matrix $\mathbf{H}(\mathbf{x})$ are proportional to the principal curvatures of $D(\mathbf{x})$, but their explicit computation can be avoided by finding the trace and the

³The principal curvatures are the maximum and minimum normal curvatures of a regular surface at a given point. The normal curvature at a point is the amount of the curve’s curvature in the direction of the surface normal.

A. METHODOLOGY

determinant of $\mathbf{H}(\mathbf{x})$, respectively:

$$\text{Tr}(\mathbf{H}(\mathbf{x})) = D_{xx} + D_{yy} = e_1 + e_2,$$

$$\text{Det}(\mathbf{H}(\mathbf{x})) = D_{xx}D_{yy} - (D_{xy})^2 = e_1e_2.$$

Here, e_1 is the eigenvalue with the largest magnitude and e_2 is the smallest one. By representing the ratio between the eigenvalues as $e_1 = r \cdot e_2$, we can obtain an equation with only one unknown, r :

$$\frac{\text{Tr}(\mathbf{H}(\mathbf{x}))^2}{\text{Det}(\mathbf{H}(\mathbf{x}))} = \frac{(e_1 + e_2)^2}{e_1e_2} = \frac{(re_2 + e_2)^2}{re_2^2} = \frac{(r + 1)^2}{r}. \quad (\text{A.3.8})$$

Thus, to discard keypoints with a principal curvature ratio below some threshold, r , it is enough to check that

$$\frac{\text{Tr}(\mathbf{H}(\mathbf{x}))^2}{\text{Det}(\mathbf{H}(\mathbf{x}))} < \frac{(r + 1)^2}{r}.$$

The experiments conducted in [315] assumed an “edge threshold” $r = 10$.

4. **Keypoint orientation assignment.** The filtered keypoints can be invariant to rotation if they are represented relative to their orientation in the local neighborhood. This representation is done by means of a histogram of gradient orientations. In particular, using the scale of the keypoint of interest, we select the Gaussian smoothed image \mathbf{L} with the closest scale, σ_L . For each pixel in \mathbf{L} , the gradient magnitude $m(x, y)$ and orientation $\theta(x, y)$ are precomputed using the pixel differences:

$$m(x, y) = \sqrt{(\mathbf{L}(x + 1, y) - \mathbf{L}(x - 1, y))^2 + (\mathbf{L}(x, y + 1) - \mathbf{L}(x, y - 1))^2},$$

$$\theta(x, y) = \tan^{-1} \frac{\mathbf{L}(x, y + 1) - \mathbf{L}(x, y - 1)}{\mathbf{L}(x + 1, y) - \mathbf{L}(x - 1, y)}.$$

An orientation histogram is formed within a region around the keypoint of interest defined by a Gaussian-weighted circular window, G_L with a standard deviation $1.5 \cdot \sigma_L$. This histogram consists of 36 bins covering a 360° range of orientations. The pixels added to the histogram are weighted by their gradient magnitude and G_L .

Peaks of this orientation histogram correspond to dominant directions of the gradients in the neighborhood. The keypoint is assigned the orientation corresponding to the highest peak, as well as any other peak within 80% of the highest magnitude (up to 2 peaks in total). In this way, there can be several keypoints with the same

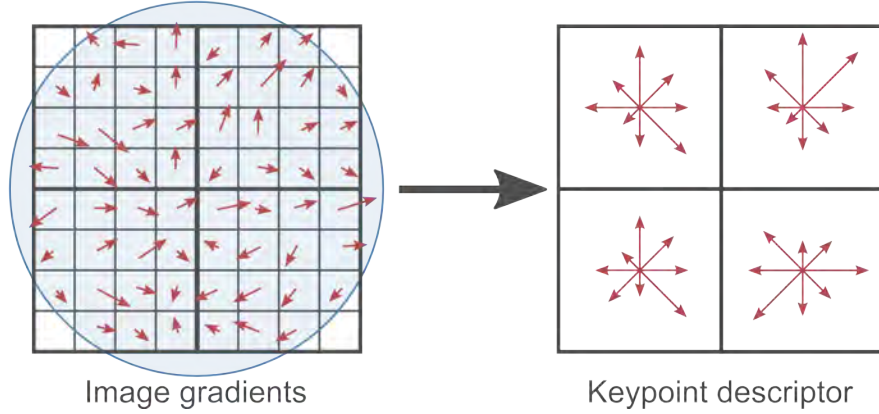


Figure A.7: Creation of a SIFT keypoint descriptor. First, the gradient magnitude and orientation are computed at each image sample point in a region around the keypoint location and weighted by a Gaussian window (blue circle). The computed samples are then accumulated into a 2×2 array of orientation histograms that summarize the contents over 4×4 neighborhoods (shown on the right). Each histogram consists of 8 bins, and the lengths of the arrows correspond to the sum of gradient magnitudes of all samples falling into that bin. In the experiments described in [315], the author used 4×4 descriptors computed from 16×16 sample regions.

location and scale but different orientations. This approach contributes significantly to the stability of feature matching.

5. **Local image description.** The keypoints acquired using the previous operations have an assigned image location, scale and orientation. In this step, SIFT creates a distinct encoding of the local image information around the points which makes the features robust against changes in 3D viewpoint and illumination. At first, orientations and magnitudes of the image gradient are sampled around the feature location in the blurred image of the Gaussian scale-space corresponding to the scale of the feature.⁴ In order to achieve orientation invariance, the coordinates of the descriptor and the gradient orientations are rotated relative to the keypoint's orientation. In Fig. A.7 (left), the gradients are denoted by small arrows: the longer the arrow, the larger the magnitude of the gradient. The magnitude of each gradient is weighted by means of a Gaussian function with $\sigma_d = \frac{1}{2}w_d$, where w_d is the width of the descriptor. The weighting window is centered on the descriptor as shown by the blue transparent circle in Fig. A.7. This window is used to avoid abrupt changes in the descriptor due to small shifts in the keypoint's location. In addition, it gives less importance to pixels farther from the center of the descriptor which are more susceptible to misregistration errors.

⁴The gradients were precomputed for all levels in the pyramid in the previous step.

A. METHODOLOGY

The descriptor window is divided into sub-windows which are then used to create gradient orientation histograms, as shown in Fig. A.7 (right). The lengths of the arrows correspond to the magnitudes of the histogram entries, and in this example, the 8-bin histograms are created over 4×4 sample neighborhoods. During the histogram creation, trilinear interpolation is used to distribute the gradient sample values into adjacent bins. This is done to avoid boundary problems caused by samples shifting smoothly from one histogram to another. Thus, each entry into the bin is multiplied by $1 - d$ for each dimension, where d is the distance of the sample from the central value of the bin as measured in units of the histogram bin spacing.

The final feature vector is formed by concatenating the values of all the orientation histogram bins (the lengths of the arrows). Fig. A.7 shows a 2×2 histogram array, while in his experiments the author used a 4×4 array of histograms with 8 orientation bins in each, yielding a 128-element feature vector. To make the SIFT features robust to affine changes in illumination, such as image contrast and brightness, the vector is normalized to unit length. However, the effects of non-linear illumination changes (e.g. camera saturation or uneven illumination of 3D surfaces with different orientations) can cause important changes in gradient magnitudes. In order to reduce this effect, the values of magnitudes in the unit vector are thresholded so that they are not greater than 0.2 (determined experimentally), and the vector is renormalized. After this operation, the distribution of gradient orientations has more importance in the feature vector than the magnitudes of large gradients. Fig. A.8 shows an example of SIFT features detected in a drawing of a tree. We used the implementation of SIFT provided by the VLFeat library [402]. The algorithm was run with the default parameters: $O = 3$ octaves in the Gaussian scale space, $s = 3$ intervals per octave, zero “peak threshold”, and “edge threshold” $r = 10$.

A.4 The RANSAC algorithm

RANSAC, or RANdom SAmple Consensus, is an algorithm introduced by Fischler and Bolles [316] for general parameter estimation from data with a large proportion of outliers. RANSAC is a re-sampling technique that partitions a data set into inliers and outliers. The inliers are the largest consensus set of the data that satisfies the model sought, while the outliers are the rest of the data.

Algorithm 7 summarizes the main steps in the RANSAC algorithm [388]. The sequence starts with the smallest possible subset of the input data (a sample) used to estimate the parameters of the model that describes it. Then, RANSAC extracts all



Figure A.8: Sample SIFT feature detection in a drawing of a tree. The different sizes of the descriptors correspond to features detected at different scales.

data points, S_i , that satisfy this model (the inliers) based on some distance function and a threshold, t . The algorithm continues by randomly selecting new samples until either the number of data points satisfying the model is sufficient ($|S_i| > T$), or the iteration limit, N , is reached. Thus, the goal is to find a set of model parameters that describe as many points of the data as possible.

For homography estimation, the RANSAC algorithm is applied to the putative set of SIFT feature correspondences in a stereo pair. It solves two tasks at the same time: filtering out incorrect feature correspondences and finding the parameters of the

Algorithm 7: The RANSAC robust estimation algorithm.

Data: Dataset S with outliers

Result: A model M robustly fit to the dataset

- 1 Randomly select a sample subset of s data points from S and use it to initialize the model M .
 - 2 Determine the set of data points S_i which are within a distance threshold t of the model. This set is the consensus set of the sample and defines the inliers of S .
 - 3 Check the number of inliers (the size of S_i). If it is greater than some threshold T , re-estimate M using all the points in S_i and terminate. If it is smaller than T , repeat steps 1–3;
 - 4 After N trials, the largest consensus subset S_i is selected, and the model is re-estimated using all the points in subset S_i .
-

A. METHODOLOGY

Algorithm 8: Adaptive algorithm for determining the number of RANSAC samples, N .

```

Data: Dataset  $S$ 
1  $N = \infty$  ;                                /* Number of samples */
2  $n = 0$  ;                                    /* Sample count */
3 while  $N > n$  do
4   Choose a sample of  $s$  points and count the number of inliers,  $|S_i|$ ;
5    $\epsilon = 1 - |S_i|/|S|$  ;                /* Probability that a data point is an outlier */
6   Compute  $N$  for  $p = 0.99$  (Eq.A.4.2);
7    $n = n + 1$ ;
8 end

```

homography matrix between the two images. Each sample used by RANSAC for this purpose is size $s = 4$, and the distance function is defined as the symmetric transfer error:

$$d_{transfer}^2 = d(\mathbf{x}, \mathbf{H}^{-1}\mathbf{x}')^2 + d(\mathbf{x}', \mathbf{H}\mathbf{x})^2, \quad (\text{A.4.1})$$

where $\mathbf{x} \leftrightarrow \mathbf{x}'$ are the point correspondences in the two images, \mathbf{H} is the estimated homography, and d returns the Euclidean distance between the points.

One of the key features of the RANSAC approach is that, instead of trying every possible sample for model estimation, it uses a limited number of randomly selected samples, N . This number is chosen high enough to ensure a probability (normally, $p = 0.99$) that at least one of the random samples of s points does not contain any outliers. If ι is the probability that any selected point is an inlier, $\epsilon = 1 - \iota$ defines the probability that it is an outlier. Thus, we need to select at least N samples, containing s points each, in order to obtain one that is free of outliers with a probability p :

$$(1 - \iota^s)^N = 1 - p,$$

hence,

$$N = \frac{\log(1 - p)}{\log(1 - (1 - \epsilon)^s)}. \quad (\text{A.4.2})$$

When ϵ is unknown, the number of samples can be set adaptively as the proportion of outliers determined from each consensus set, as described in Algorithm 8.

In our pipeline, we used the implementation of RANSAC for homography computation from [404], which does not employ the T threshold and relies only on the adaptive N . The value of the distance threshold, t , was set to 0.05.

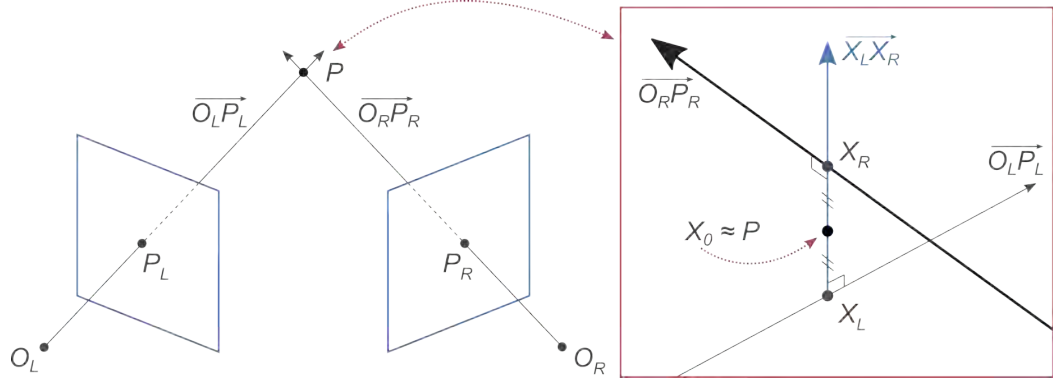


Figure A.9: Triangulation of a 3D point using its projections in stereo images. Rays $\overrightarrow{O_L P_L}$ and $\overrightarrow{O_R P_R}$ should intersect at point P , however, this is not true in most cases. The right part of the image is a zoomed-in area of the supposed intersection. Line $\overrightarrow{X_L X_R}$ is orthogonal to both rays and intersects them at points X_L and X_R . According to the “midpoint method”, point P can be approximated by the midpoint of the line segment $\overrightarrow{X_L X_R}$.

A.5 Triangulation⁵

A point P in the scene is projected onto the image planes π_L and π_R of the two cameras, producing points P_L and P_R , respectively (see the left part of Fig. A.9). Rays $\overrightarrow{O_L P_L}$ and $\overrightarrow{O_R P_R}$, starting at the cameras’ optical centers O_L and O_R and passing through P_L and P_R respectively, should intersect at point P . However, in reality, due to image noise, the rays will not actually intersect but will pass close to intersection point P , as shown on the right in Fig. A.9. In this case, the simplest solution would be to find a point of minimum distance from both rays, i.e. the midpoint, X_0 , of the line segment $\overrightarrow{X_L X_R}$ perpendicular to both $\overrightarrow{O_L P_L}$ and $\overrightarrow{O_R P_R}$.

In order to do this, we need to introduce the parametric representation of the line passing through points M_1 and M_2 :

$$\overrightarrow{M_1 M_2}(k) = M_1 + k(M_2 - M_1), \quad (\text{A.5.1})$$

where $k(M_2 - M_1)$ is the direction of the line and $k \in \mathbb{R}$ is a scalar parameter. This representation allows for the definition of any point on the line using the variable parameter k . Fig. A.10 demonstrates its geometrical meaning.

In this way, the parametric representations of rays $\overrightarrow{O_L P_L}$ and $\overrightarrow{O_R P_R}$ will be the following:

⁵This explanation was inspired by [405].

A. METHODOLOGY

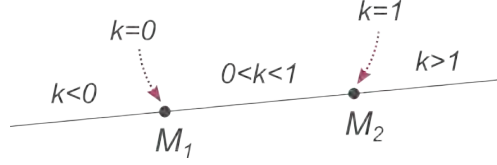


Figure A.10: Line parameterization according to Eq. A.5.1.

$$\overrightarrow{O_L P_L}(a) = O_L + a(P_L - O_L) = aP_L, \quad (\text{A.5.2})$$

$$\overrightarrow{O_R P_R}(b) = O_R^L + b(P_R^L - O_R^L) = \mathbf{t} + b\mathbf{R}^T P_R, \quad (\text{A.5.3})$$

where $a, b \in \mathbb{R}_0^+$ are the ray parameters. Since all calculations are made in the reference frame of the left camera (O_L is the origin), the resulting equation for the $\overrightarrow{O_R P_R}(b)$ ray is based on the following: $O_R^L = \mathbf{R}^T O_R + \mathbf{t} = \mathbf{t}$ and $P_R^L = \mathbf{R}^T P_R + \mathbf{t}$. \mathbf{R} and \mathbf{t} are the rotation matrix and the translation vector between the left and right cameras, respectively.

The endpoints X_L and X_R can be given as

$$X_L = a_0 P_L \quad \text{and} \quad X_R = \mathbf{t} + b_0 \mathbf{R}^T P_R, \quad (\text{A.5.4})$$

with a_0 and b_0 being the values of the parameters a and b corresponding to the intersection points of rays $\overrightarrow{O_L P_L}$ and $\overrightarrow{O_R P_R}$ with line $\overleftrightarrow{X_L X_R}$.

Then, the ray beginning at X_L and passing through X_R is parameterized by $c \in \mathbb{R}_0^+$:

$$\overrightarrow{X_L X_R}(c) = X_L + c(X_R - X_L) = a_0 P_L + c\mathbf{w}. \quad (\text{A.5.5})$$

X_0 , the midpoint of $\overleftrightarrow{X_L X_R}$, is computed for $c = 1/2$. Vector \mathbf{w} (the direction of $\overrightarrow{X_L X_R}$) orthogonal to both $\overrightarrow{O_L P_L}$ and $\overrightarrow{O_R P_R}$ is given by the cross-product:

$$\mathbf{w} = M_L \times M_R = (P_L - O_L) \times (P_R^L - O_R^L) = P_L \times \mathbf{R}^T P_R, \quad (\text{A.5.6})$$

since $P_R = \mathbf{R}(P_R^L - O_R^L)$.

Finally, point X_R lies on ray $\overrightarrow{X_L X_R}$ and can be computed for some $c = c_0$:

$$\overrightarrow{X_L X_R}(c_0) = X_R \quad (\text{A.5.7})$$

$$a_0 X_1 + c_0 \mathbf{w} = \mathbf{t} + b_0 \mathbf{R}^T P_R \quad (\text{A.5.8})$$

$$a_0 X_1 - b_0 \mathbf{R}^T P_R + c_0 (P_L \times \mathbf{R}^T P_R) = \mathbf{t}. \quad (\text{A.5.9})$$

After solving the system of equations A.5.9 for a_0 , b_0 and c_0 , points X_L and X_R can be easily found from equation A.5.4. With the points obtained, X_0 can be computed from the parameterized equation A.5.5 for $\overrightarrow{X_L X_R}$.

A. METHODOLOGY

References

- [1] H. Kaufman, *The melanoma book: a complete guide to prevention and treatment*, 1st ed. New York: Gotham Books, 2005. 2, 3, 5
- [2] S. Cade, “Malignant melanoma: Bradshaw Lecture delivered at the Royal College of Surgeons of England on 7th December 1960,” *Ann. R. Coll. Surg. Engl.*, vol. 28, pp. 331–6, 1961. 1, 17, 45, 71
- [3] J. A. McGrath and J. Uitto, “Anatomy and organization of human skin,” in *Rook’s Textbook of Dermatology*, T. Burns, S. Breathnach, N. Cox, and C. Griffiths, Eds. Oxford: Wiley-Blackwell, 2010, ch. 3, pp. 1–53. 2, 3
- [4] A. Jerant, J. Johnson, C. Sheridan, and T. Caffrey, “Early detection and treatment of skin cancer,” *Am. Fam. Physician*, vol. 62, no. 2, pp. 357–386, 2000. 3, 6
- [5] J. Newton Bishop, “Lentigos, melanocytic naevi and melanoma,” in *Rook’s Textbook of Dermatology*, T. Burns, S. Breathnach, N. Cox, and C. Griffiths, Eds. Oxford: Wiley-Blackwell, 2010, ch. 54, pp. 1–57. 5, 6
- [6] R. Friedman, D. Rigel, and A. Kopf, “Early detection of malignant melanoma: The role of physician examination and self-examination of the skin,” *CA-Cancer J. Clin.*, vol. 35, no. 3, pp. 130–151, 1985. 5, 7, 11
- [7] W. Norris, “Case of fungoid disease,” *Edinburgh Medical and Surgical Journal*, vol. 16, pp. 562–5, 1820. 5
- [8] J. P. Bennett and P. Hall, “Moles and melanoma: a history,” *Ann. R. Coll. Surg. Engl.*, vol. 76, no. 6, p. 373, 1994. 5, 131
- [9] S. Markovic, L. Erickson, R. Rao, R. McWilliams, L. Kottschade, E. Creagan *et al.*, “Malignant melanoma in the 21st century, part 1: epidemiology, risk factors, screening, prevention, and diagnosis,” *Mayo Clin. Proc.*, vol. 82, no. 3, pp. 364–380, 2007. 6, 7
- [10] American Cancer Society, “Cancer facts & figures 2013,” Atlanta: American Cancer Society, Tech. Rep., 2013. 6, 14
- [11] A. Breslow, “Thickness, cross-sectional areas and depth of invasion in the prognosis of cutaneous melanoma,” *Ann. Surg.*, vol. 172, no. 5, p. 902, 1970. 6, 7

REFERENCES

- [12] A. Marghoob, L. Swindle, C. Moricz, F. Sanchez Negron, B. Slue, A. Halpern, and A. Kopf, "Instruments and new technologies for the in vivo diagnosis of melanoma," *J. Am. Acad. Dermatol.*, vol. 49, no. 5, pp. 777–797, 2003. 7
- [13] A. Halpern, "Total body skin imaging as an aid to melanoma detection," *Semin. Cutan. Med. Surg.*, vol. 22, no. 1, pp. 2–8, 2003. 7, 8, 9, 43
- [14] D. Ratner, C. Thomas, and D. Bickers, "The uses of digital photography in dermatology," *J. Am. Acad. Dermatol.*, vol. 41, no. 5, pp. 749–756, 1999. 7
- [15] J. Quintana, "Computer vision techniques for early detection of skin cancer," Ph.D. dissertation, University of Girona, 2012. 7, 132
- [16] L. Smith and S. MacNeil, "State of the art in non-invasive imaging of cutaneous melanoma," *Skin Res. Tech.*, vol. 17, no. 3, pp. 257–269, 2011. 7
- [17] D. Rigel, J. Russak, and R. Friedman, "The evolution of melanoma diagnosis: 25 years beyond the ABCDs," *CA-Cancer J. Clin.*, vol. 60, no. 5, pp. 301–316, 2010. 7, 11
- [18] S. Wang and P. Hashemi, "Noninvasive imaging technologies in the diagnosis of melanoma," *Semin. Cutan. Med. Surg.*, vol. 29, no. 3, pp. 174–184, 2010. 7
- [19] A. Gadeliya Goodson and D. Grossman, "Strategies for early melanoma detection: Approaches to the patient with nevi," *J. Am. Acad. Dermatol.*, vol. 60, no. 5, pp. 719–735, 2009. 7
- [20] E. Psaty and A. Halpern, "Current and emerging technologies in melanoma diagnosis: the state of the art," *Clin. Dermatol.*, vol. 27, no. 1, pp. 35–45, 2009. 7
- [21] A. Esmaeili, A. Scope, A. C. Halpern, and A. A. Marghoob, "Imaging techniques for the in vivo diagnosis of melanoma," *Semin. Cutan. Med. Surg.*, vol. 27, no. 1, pp. 2–10, 2008. 7
- [22] J. Patel, S. Konda, O. Perez, S. Amini, G. Elgart, and B. Berman, "Newer technologies/techniques and tools in the diagnosis of melanoma," *Eur. J. Dermatol.*, vol. 18, no. 6, pp. 617–631, 2008. 7
- [23] G. Day and R. Barbour, "Automated melanoma diagnosis: where are we at?" *Skin Res. Tech.*, vol. 6, no. 1, pp. 1–5, 2000. 8, 37
- [24] A. Halpern, A. Marghoob, T. Bialoglow, W. Witmer, and W. Slue, "Standardized positioning of patients (poses) for whole body cutaneous photography," *J. Am. Acad. Dermatol.*, vol. 49, no. 4, pp. 593–598, 2003. 8
- [25] N. Feit, S. Dusza, and A. Marghoob, "Melanomas detected with the aid of total cutaneous photography," *Br. J. Dermatol.*, vol. 150, no. 4, pp. 706–714, 2004. 8, 45
- [26] M. Rademaker and A. Oakley, "Digital monitoring by whole body photography and sequential digital dermoscopy detects thinner melanomas," *J. Prim. Health Care*, vol. 2, no. 4, pp. 267–272, 2010. 8

REFERENCES

- [27] V. Terushkin, S. Oliveria, A. Marghoob, and A. Halpern, "Use of and beliefs about total body photography and dermatoscopy among us dermatology training programs: An update," *J. Am. Acad. Dermatol.*, vol. 62, no. 5, pp. 794–803, 2010. 9
- [28] A. W. Kopf, M. Elbaum, and N. Provost, "The use of dermoscopy and digital imaging in the diagnosis of cutaneous malignant melanoma," *Skin Res. Tech.*, vol. 3, no. 1, pp. 1–7, 1997. 9
- [29] S. W. Menzies, "Automated epiluminescence microscopy: Human vs machine in the diagnosis of melanoma," *Arch. Dermatol.*, vol. 135, no. 12, pp. 1538–40, 1999. 9
- [30] G. Pellacani and S. Seidenari, "Comparison between morphological parameters in pigmented skin lesion images acquired by means of epiluminescence surface microscopy and polarized-light videomicroscopy," *Clin. Dermatol.*, vol. 20, no. 3, pp. 222–227, 2002. 9, 10, 50
- [31] C. Benvenuto-Andrade, S. Dusza, A. Agero, M. Rajadhyaksha, A. Halpern, and A. Marghoob, "Differences between polarized light dermoscopy and immersion contact dermoscopy for the evaluation of skin lesions," *Arch. dermatol.*, vol. 143, no. 3, pp. 329–338, 2007. 10
- [32] S. Seidenari, G. Pellacani, and P. Pepe, "Digital videomicroscopy improves diagnostic accuracy for melanoma," *J. Am. Acad. Dermatol.*, vol. 39, no. 2, pp. 175–181, 1998. 10, 36, 38
- [33] X. Yuan, N. Situ, and G. Zouridakis, "A narrow band graph partitioning method for skin lesion segmentation," *Pattern Recogn.*, vol. 42, no. 6, pp. 1017–28, 2009. 10, 23
- [34] A. P. Dhawan, R. Gordon, and R. M. Rangayyan, "Nevoscopy: Three-dimensional computed tomography of nevi and melanomas in situ by transillumination," *IEEE T. Med. Imaging*, vol. 3, no. 2, pp. 54–61, 1984. 10, 17, 40
- [35] A. P. Dhawan, "Early detection of cutaneous malignant melanoma by three-dimensional nevoscopy," *Comput. Meth. Programs Biomed.*, vol. 21, no. 1, pp. 59–68, 1985. 10, 40
- [36] A. Dhawan, "Apparatus and method for skin lesion examination," US Patent 5.146.923, 1992. 10
- [37] J. Banky, J. Kelly, D. English, J. Yeatman, and J. Dowling, "Incidence of new and changed nevi and melanomas detected using baseline images and dermoscopy in patients at high risk for melanoma," *Arch. Dermatol.*, vol. 141, no. 8, pp. 998–1006, 2005. 10
- [38] N. Abbasi, H. Shaw, D. Rigel, R. Friedman, W. McCarthy, I. Osman *et al.*, "Early diagnosis of cutaneous melanoma: Revisiting the ABCD criteria," *J. Am. Med. Assoc.*, vol. 292, no. 22, pp. 2771–76, 2004. 11, 30, 45
- [39] R. Mackie and V. Doherty, "Seven-point checklist for melanoma," *Clin. Exp. Dermatol.*, vol. 16, no. 2, pp. 151–152, 1991. 11

REFERENCES

- [40] H. Kittler, H. Pehamberger, K. Wolff, and M. Binder, "Follow-up of melanocytic skin lesions with digital epiluminescence microscopy: Patterns of modifications observed in early melanoma, atypical nevi, and common nevi," *J. Am. Acad. Dermatol.*, vol. 43, no. 3, pp. 467–476, 2000. 11
- [41] S. Menzies, A. Gutenev, M. Avramidis, A. Batrac, and W. McCarthy, "Short-term digital surface microscopic monitoring of atypical or changing melanocytic lesions," *Arch. Dermatol.*, vol. 137, no. 12, pp. 1583–89, 2001. 11, 32, 35, 38
- [42] J. Malvehy, S. Puig, G. Argenziano, A. A. Marghoob, and H. P. Soyer, "Dermoscopy report: Proposal for standardization. Results of a consensus meeting of the International Dermoscopy Society," *J. Am. Acad. Dermatol.*, vol. 57, no. 1, pp. 84–95, 2007. 11, 12, 27, 28, 30, 44
- [43] G. Argenziano, H. Soyer, S. Chimenti, R. Talamini, R. Corona, F. Sera *et al.*, "Dermoscopy of pigmented skin lesions: Results of a consensus meeting via the Internet," *J. Am. Acad. Dermatol.*, vol. 48, no. 5, pp. 679–693, 2003. 12
- [44] G. Capdehourat, A. Corez, A. Bazzano, R. Alonso, and P. Musé, "Toward a combined tool to assist dermatologists in melanoma detection from dermoscopic images of pigmented skin lesions," *Pattern Recogn. Lett.*, vol. 32, no. 16, pp. 2187–2196, 2011. 12, 27, 36
- [45] G. Day and R. Barbour, "Automated skin lesion screening—a new approach," *Melanoma Res.*, vol. 11, no. 1, pp. 31–35, 2001. 12, 13, 14, 17, 22, 36
- [46] R. Marchesini, A. Bono, C. Bartoli, M. Lualdi, S. Tomatis, and N. Cascinelli, "Optical imaging and automated melanoma detection: questions and answers," *Melanoma Res.*, vol. 12, no. 3, pp. 279–286, 2002. 12, 37, 44
- [47] M. Vestergaard and S. Menzies, "Automated diagnostic instruments for cutaneous melanoma," *Semin. Cutan. Med. Surg.*, vol. 27, no. 1, pp. 32–36, 2008. 12, 37, 39
- [48] J. Fröhaupt, B. Leinweber, R. Fink-Puches, V. Ahlgrimm-Siess, E. Richtig, I. Wolf *et al.*, "Patient acceptance and diagnostic utility of automated digital image analysis of pigmented skin lesions," *J. Eur. Acad. Dermatol. Venereol.*, vol. 26, no. 3, pp. 368–372, 2011. 13, 44
- [49] S. Dreiseitl and M. Binder, "Do physicians value decision support? A look at the effect of decision support systems on physician opinion," *Artif. Intell. Med.*, vol. 33, no. 1, pp. 25–30, 2005. 14
- [50] R. S. Stern, "Prevalence of a history of skin cancer in 2007: Results of an incidence-based model," *Arch. Dermatol.*, vol. 146, no. 3, pp. 279–282, 2010. 14
- [51] A. C. Halpern, "The use of whole body photography in a pigmented lesion clinic," *Dermatol. Surg.*, vol. 26, no. 12, pp. 1175–80, 2000. 15

-
- [52] R. Drugge, C. Nguyen, L. Gliga, and E. Drugge, "Clinical pathway for melanoma detection using comprehensive cutaneous analysis with Melanoscan[®]," *Dermatol. Online J.*, vol. 16, no. 8, 2010. 15, 45
 - [53] W. V. Stoecker and R. H. Moss, "Editorial: digital imaging in dermatology," *Comput. Med. Imaging Graph.*, vol. 16, no. 3, pp. 145–150, 1992. 17, 42
 - [54] A. Green, N. Martin, G. McKenzie, J. Pfitzner, F. Quintarelli, B. Thomas *et al.*, "Computer image analysis of pigmented skin lesions," *Melanoma Res.*, vol. 1, no. 4, pp. 231–236, 1991. 17, 30, 36
 - [55] M. E. Celebi, W. V. Stoecker, and R. H. Moss, "Advances in skin cancer image analysis," *Comput. Med. Imaging Graph.*, vol. 35, no. 2, pp. 83–84, 2011. 17
 - [56] M. Celebi, H. Iyatomi, G. Schaefer, and W. Stoecker, "Lesion border detection in dermoscopy images," *Comput. Med. Imaging Graph.*, vol. 33, no. 2, pp. 148–153, 2009. 17, 20, 22, 24, 25
 - [57] V. Berenguer, D. Ruiz, and A. Soriano, "Application of Hidden Markov Models to melanoma diagnosis," in *Proc. Int. Symp. Distrib. Comput. and Artif. Intell.*, J. Corchado, S. Rodriguez, J. Llinas, and J. Molina, Eds., vol. 50. Berlin: Springer, 2009, pp. 357–365. 19, 20, 21, 28, 33, 36
 - [58] S. Skrøvseth, T. Schopf, K. Thon, M. Zortea, M. Geilhufe, K. Mollersen *et al.*, "A computer aided diagnostic system for malignant melanomas," in *Proc. Int. Symp. Applied Sciences in Biomed. and Comm. Tech. (ISABEL)*. Piscataway, NJ: IEEE Press, 2010, pp. 1–5. 19, 27, 28, 33
 - [59] T. Lee, V. Ng, R. Gallagher, A. Coldman, and D. McLean, "DullRazor[®]: A software approach to hair removal from images," *Comput. Biol. Med.*, vol. 27, no. 6, pp. 533–543, 1997. 20, 21
 - [60] M. G. Fleming, C. Steger, J. Zhang, J. Gao, A. B. Cognetta, Ilya Pollak, and C. R. Dyer, "Techniques for a structural analysis of dermoscopic imagery," *Comput. Med. Imaging Graph.*, vol. 22, no. 5, pp. 375–389, 1998. 20, 21, 22, 23, 27
 - [61] O. Debeir, C. Decaestecker, J. Pasteels, I. Salmon, R. Kiss, and P. Van Ham, "Computer-assisted analysis of epiluminescence microscopy images of pigmented skin lesions," *Cytometry*, vol. 37, no. 4, pp. 255–266, 1999. 20, 21, 23, 27
 - [62] D. H. Chung and G. Sapiro, "Segmenting skin lesions with partial-differential-equations-based image processing algorithms," *IEEE T. Med. Imaging*, vol. 19, no. 7, pp. 763–767, 2000. 20, 21, 23
 - [63] P. Schmid-Saugeon, J. Guilloid, and J. Thiran, "Towards a computer-aided diagnosis system for pigmented skin lesions," *Comput. Med. Imaging Graph.*, vol. 27, no. 1, pp. 65–78, 2003. 20, 21, 28

REFERENCES

- [64] H. Zhou, M. Chen, R. Gass, J. Rehg, L. Ferris, J. Ho, and L. Drogowski, “Feature-preserving artifact removal from dermoscopy images,” in *Proc. SPIE*, ser. Medical Imaging: Image Processing, J. M. Reinhardt and J. P. W. Pluim, Eds., vol. 6914(1B). San Diego, CA: SPIE, 2008. 20, 21
- [65] P. Wighton, T. Lee, and M. Atkins, “Dermoscopic hair disocclusion using inpainting,” in *Proc. SPIE*, ser. Medical Imaging: Image Processing, J. M. Reinhardt and J. P. W. Pluim, Eds., vol. 6914(27). San Diego, CA: SPIE, 2008. 20, 21
- [66] F.-Y. Xie, S.-Y. Qin, Z.-G. Jiang, and R.-S. Meng, “PDE-based unsupervised repair of hair-occluded information in dermoscopy images of melanoma,” *Comput. Med. Imaging Graph.*, vol. 33, no. 4, pp. 275–282, 2009. 20, 21
- [67] C. Barcelos and V. Pires, “An automatic based nonlinear diffusion equations scheme for skin lesion segmentation,” *Appl. Math. Comput.*, vol. 215, no. 1, pp. 251–261, 2009. 20, 21, 23
- [68] Q. Abbas, I. Fondón, and M. Rashid, “Unsupervised skin lesions border detection via two-dimensional image analysis,” *Comput. Meth. Programs Biomed.*, vol. 27, no. 1, pp. 65–78, 2010. 20, 21
- [69] K. Møllersen, H. Kirchesch, T. Schopf, and F. Godtliebsen, “Unsupervised segmentation for digital dermoscopic images,” *Skin Res. Tech.*, vol. 16, no. 4, pp. 401–407, 2010. 20
- [70] N. Nguyen, T. Lee, and M. Atkins, “Segmentation of light and dark hair in dermoscopic images: a hybrid approach using a universal kernel,” in *Proc. SPIE*, ser. Medical Imaging: Image Processing, B. M. Dawant and D. R. Haynor, Eds., vol. 7623(4N). San Diego, CA: SPIE, 2010. 20, 21
- [71] K. Kiani and A. R. Sharafat, “E-shaver: An improved DullRazor[®] for digitally removing dark and light-colored hairs in dermoscopic images,” *Comput. Biol. Med.*, vol. 41, no. 3, pp. 139–145, 2011. 20, 21
- [72] P. Wighton, T. Lee, H. Lui, D. McLean, and M. Atkins, “Generalizing common tasks in automated skin lesion diagnosis,” *IEEE T. Inf. Technol. B.*, vol. 4, pp. 622–629, 2011. 20, 21, 23, 27
- [73] Q. Abbas, M. Celebi, and I. Garcia, “Hair removal methods: A comparative study for dermoscopy images,” *Biomed. Signal Process. Contr.*, vol. 6, no. 4, pp. 395–404, 2011. 20, 21
- [74] Q. Abbas, M. E. Celebi, and I. F. García, “Skin tumor area extraction using an improved dynamic programming approach,” *Skin Res. Tech.*, vol. 18, no. 2, pp. 133–142, 2012. 20, 23
- [75] A. Afonso and M. Silveira, “Hair detection in dermoscopic images using percolation,” in *Proc. IEEE Ann. Int. Conf. Eng. Med. Biol. Soc. (EMBC)*, 2012, pp. 4378–4381. 20

REFERENCES

- [76] M. T. B. Toossi, H. R. Pourreza, H. Zare, M.-H. Sigari, P. Layegh, and A. Azimi, "An effective hair removal algorithm for dermoscopy images," *Skin Res. Tech.*, vol. 19, pp. 230–235, 2013. 20
- [77] A. Huang, S.-Y. Kwan, W.-Y. Chang, M.-Y. Liu, M.-H. Chi, and G.-S. Chen, "A robust hair segmentation and removal approach for clinical images of skin lesions," in *Proc. IEEE Ann. Int. Conf. Eng. Med. Biol. Soc. (EMBC)*, 2013, pp. 3315–3318. 20
- [78] Q. Abbas, I. García, and M. Rashid, "Automatic skin tumour border detection for digital dermoscopy using a new digital image analysis scheme," *Br. J. Biomed. Sci.*, vol. 67, no. 4, pp. 177–183, 2010. 20, 21
- [79] A. Gutenev, V. Skladnev, and D. Varvel, "Acquisition-time image quality control in digital dermatoscopy of skin lesions," *Comput. Med. Imaging Graph.*, vol. 25, no. 6, pp. 495–499, 2001. 20
- [80] E. Zagrouba and W. Barhoumi, "A preliminary approach for the automated recognition of malignant melanoma," *Image Anal. Stereol.*, vol. 23, no. 2, pp. 121–135, 2004. 20, 21, 30, 36
- [81] A. Chiem, A. Al-Jumaily, and R. Khushaba, "A novel hybrid system for skin lesion detection," in *Proc. Int. Conf. Intell. Sensors, Sensor Netw. and Inform.*, M. Palaniswami, S. Marusic, and Y. W. Law, Eds. Piscataway, NJ: IEEE Press, 2007, pp. 567–572. 20, 21, 28, 34, 36
- [82] M. Messadi, A. Bessaid, and A. Taleb-Ahmed, "Extraction of specific parameters for skin tumour classification," *J. Med. Eng. Tech.*, vol. 33, no. 4, pp. 288–295, 2009. 20, 28, 36
- [83] M. E. Celebi, H. A. Kingravi, B. Uddin, H. Iyatomi, Y. A. Aslandogan, W. V. Stoecker, and R. H. Moss, "A methodological approach to the classification of dermoscopy images," *Comput. Med. Imaging Graph.*, vol. 31, no. 6, pp. 362–373, 2007. 20, 26, 28, 36
- [84] A. Dhawan, B. D'Alessandro, S. Patwardhan, and N. Mullani, "Multispectral optical imaging of skin-lesions for detection of malignant melanomas," in *Proc. IEEE Ann. Int. Conf. Eng. Med. Biol. Soc. (EMBC)*. Piscataway, NJ: IEEE Press, 2009, pp. 5352–55. 20, 21
- [85] D. Ruiz, V. Berenguer, A. Soriano, and B. Sánchez, "A decision support system for the diagnosis of melanoma: A comparative approach," *Expert Syst. Appl.*, vol. 38, no. 12, pp. 217–23, 2011. 20, 21, 34, 36
- [86] J. Blackledge and D. Dubovitskiy, "Object detection and classification with applications to skin cancer screening," *ISAST T. Intelligent Systems*, vol. 1, pp. 34–45, 2008. 20, 28, 29, 31, 36
- [87] Y. Haeghen, J. Naeyaert, I. Lemahieu, and W. Philips, "An imaging system with calibrated color image acquisition for use in dermatology," *IEEE T. Med. Imaging*, vol. 19, no. 7, pp. 722–730, 2000. 20

REFERENCES

- [88] C. Grana, G. Pellacani, and S. Seidenari, “Practical color calibration for dermoscopy, applied to a digital epiluminescence microscope,” *Skin Res. Tech.*, vol. 11, no. 4, pp. 242–247, 2005. 20
- [89] H. Iyatomi, M. Celebi, G. Schaefer, and M. Tanaka, “Automated color calibration method for dermoscopy images,” *Comput. Med. Imaging Graph.*, vol. 35, no. 2, pp. 89–98, 2011. 20
- [90] J. Quintana, R. García, and L. Neumann, “A novel method for color correction in epiluminescence microscopy,” *Comput. Med. Imaging Graph.*, vol. 35, no. 7-8, pp. 646–652, 2011. 20, 21
- [91] P. Wighton, T. K. Lee, H. Lui, D. McLean, and M. S. Atkins, “Chromatic aberration correction: an enhancement to the calibration of low-cost digital dermoscopes,” *Skin Res. Tech.*, vol. 17, no. 3, pp. 339–347, 2011. 20, 21
- [92] J. Alcón, C. Ciuhu, W. ten Kate, A. Heinrich, N. Uzunbajakava, G. Krekels *et al.*, “Automatic imaging system with decision support for inspection of pigmented skin lesions and melanoma diagnosis,” *IEEE J. Sel. Topics in Signal Proc.*, vol. 3, no. 1, pp. 14–25, 2009. 20, 30, 31, 36
- [93] P. Cavalcanti and J. Scharcanski, “Automated prescreening of pigmented skin lesions using standard cameras,” *Comput. Med. Imaging Graph.*, vol. 35, pp. 481–491, 2011. 20, 26, 30, 36
- [94] K.-A. Norton, H. Iyatomi, M. E. Celebi, S. Ishizaki, M. Sawada, R. Suzaki, K. Kobayashi *et al.*, “Three-phase general border detection method for dermoscopy images using non-uniform illumination correction,” *Skin Res. Tech.*, vol. 18, pp. 290–300, 2012. 20
- [95] J. Glaister, R. Amelard, A. Wong, and D. Clausi, “Msim: Multistage illumination modeling of dermatological photographs for illumination-corrected skin lesion analysis,” *IEEE T. Biomed. Eng.*, vol. 60, no. 7, pp. 1873–83, July 2013. 20
- [96] D. Delgado, C. Butakoff, B. Ersbøll, and W. Stoecker, “Independent histogram pursuit for segmentation of skin lesions,” *IEEE T. Biomed. Eng.*, vol. 55, no. 1, pp. 157–161, 2008. 20, 22
- [97] M. Celebi, H. Iyatomi, and G. Schaefer, “Contrast enhancement in dermoscopy images by maximizing a histogram bimodality measure,” in *Proc. IEEE Int. Conf. Image Process. (ICIP)*. Piscataway, NJ: IEEE Press, 2009, pp. 2601–04. 20
- [98] G. Schaefer, M. I. Rajab, M. E. Celebi, and H. Iyatomi, “Colour and contrast enhancement for improved skin lesion segmentation,” *Comput. Med. Imaging Graph.*, vol. 35, no. 2, pp. 99–104, 2011. 20
- [99] Q. Abbas, I. F. Garcia, M. Emre Celebi, W. Ahmad, and Q. Mushtaq, “A perceptually oriented method for contrast enhancement and segmentation of dermoscopy images,” *Skin Res. Tech.*, vol. 19, no. 1, pp. e490–e497, 2013. 20

REFERENCES

- [100] Q. Abbas, I. F. Garcia, M. Emre Celebi, and W. Ahmad, "A feature-preserving hair removal algorithm for dermoscopy images," *Skin Res. Tech.*, vol. 19, pp. e27–e36, 2013. 21
- [101] E. Claridge and A. Orun, "Modelling of edge profiles in pigmented skin lesions," in *Proc. Med. Image Understand. Anal. (MIUA)*, A. Houston and R. Zwigelaar, Eds. Portsmouth, UK: BMVA, 2002, pp. 53–55. 22
- [102] J. Guilloid, P. Schmid-Saugeon, D. Guggisberg, J. Cerottini, R. Braun, J. Krischer *et al.*, "Validation of segmentation techniques for digital dermoscopy," *Skin Res. Tech.*, vol. 8, no. 4, pp. 240–249, 2002. 22, 24
- [103] H. Iyatomi, H. Oka, M. Saito, A. Miyake, M. Kimoto, J. Yamagami *et al.*, "Quantitative assessment of tumour extraction from dermoscopy images and evaluation of computer-based extraction methods for an automatic melanoma diagnostic system," *Melanoma Res.*, vol. 16, no. 2, pp. 183–190, 2006. 22, 24
- [104] L. Xu, M. Jackowski, A. Goshtasby, D. Roseman, S. Bines, C. Yu *et al.*, "Segmentation of skin cancer images," *Image Vis. Comput.*, vol. 17, no. 1, pp. 65–74, 1999. 22, 23
- [105] H. Zhou, M. Chen, R. Gass, L. Ferris, L. Drogowski, and J. Rehg, "Spatially constrained segmentation of dermoscopy images," in *Proc. IEEE Int. Symp. Biomed. Imag.: From Nano to Macro*. Piscataway, NJ: IEEE Press, 2008, pp. 800–803. 22, 24
- [106] S. Umbaugh, R. Moss, and W. Stoecker, "Automatic color segmentation of images with application to detection of variegated coloring in skin tumors," *IEEE Eng. Med. Biol.*, vol. 8, no. 4, pp. 43–50, 1989. 22, 29, 31
- [107] S. E. Umbaugh, R. H. Moss, and W. V. Stoecker, "An automatic color segmentation algorithm with application to identification of skin tumor borders," *Comput. Med. Imaging Graph.*, vol. 16, no. 3, pp. 227–235, 1992. 22
- [108] S. Umbaugh, R. Moss, W. Stoecker, and G. Hance, "Automatic color segmentation algorithms with application to skin tumor feature identification," *IEEE Eng. Med. Biol.*, vol. 12, no. 3, pp. 75–82, 1993. 22
- [109] J. Golston, R. Moss, and W. Stoecker, "Boundary detection in skin tumor images: An overall approach and a radial search algorithm," *Pattern Recogn.*, vol. 23, no. 11, pp. 1235–47, 1990. 22
- [110] A. P. Dhawan and A. Sicsu, "Segmentation of images of skin lesions using color and texture information of surface pigmentation," *Comput. Med. Imaging Graph.*, vol. 16, no. 3, pp. 163–177, 1992. 23
- [111] Z. Zhang, W. Stoecker, and R. Moss, "Border detection on digitized skin tumor images," *IEEE T. Med. Imaging*, vol. 19, no. 11, pp. 1128–1143, 2000. 23

REFERENCES

- [112] W. Denton, A. Duller, and P. Fish, "Boundary detection for skin lesions: an edge focusing algorithm," in *Proc. Int. Conf. Image Process. and its Appl.*, no. 410. IEE, 1995, pp. 399–403. 23
- [113] J. Tang, "A multi-direction GVF snake for the segmentation of skin cancer images," *Pattern Recogn.*, vol. 42, no. 6, pp. 1172–79, 2009. 23
- [114] D. Gutkiewicz-Krusin, M. Elbaum, P. Szwaykowski, and A. Kopf, "Can early malignant melanoma be differentiated from atypical melanocytic nevus by in vivo techniques?" *Skin Res. Tech.*, vol. 3, no. 1, pp. 15–22, 1997. 23, 28
- [115] M. Rajab, M. Woolfson, and S. Morgan, "Application of region-based segmentation and neural network edge detection to skin lesions," *Comput. Med. Imaging Graph.*, vol. 28, no. 1-2, pp. 61–68, 2004. 23
- [116] M. E. Yüksel and M. Borlu, "Accurate segmentation of dermoscopic images by image thresholding based on type-2 fuzzy logic," *IEEE T. Fuzzy. Syst.*, vol. 17, pp. 976–982, August 2009. 23
- [117] M. E. Celebi, H. Iyatomi, G. Schaefer, and W. V. Stoecker, "Approximate lesion localization in dermoscopy images," *Skin Res. Tech.*, vol. 15, no. 3, pp. 314–322, 2009. 23
- [118] M. Celebi, S. Hwang, H. Iyatomi, and G. Schaefer, "Robust border detection in dermoscopy images using threshold fusion," in *Proc. IEEE Int. Conf. Image Process. (ICIP)*. Piscataway, NJ: IEEE Press, 2010, pp. 2541–44. 23
- [119] E. M. Celebi, Q. Wen, S. Hwang, H. Iyatomi, and G. Schaefer, "Lesion border detection in dermoscopy images using ensembles of thresholding methods," *Skin Res. Tech.*, vol. 19, no. 1, pp. e252–e258, 2013. 23
- [120] R. Garnavi, M. Aldeen, M. Celebi, G. Varigos, and S. Finch, "Border detection in dermoscopy images using hybrid thresholding on optimized color channels," *Comput. Med. Imaging Graph.*, vol. 35, no. 2, pp. 105–115, 2011. 23
- [121] Q. Abbas, I. F. Garcia, M. Emre Celebi, W. Ahmad, and Q. Mushtaq, "Unified approach for lesion border detection based on mixture modeling and local entropy thresholding," *Skin Res. Tech.*, vol. 19, no. 3, pp. 314–319, 2013. 23
- [122] F. Peruch, F. Bogo, M. Bonazza, V.-M. Cappelleri, and E. Peserico, "Simpler, faster, more accurate melanocytic lesion segmentation through meds," *IEEE T. Biomed. Eng.*, vol. 61, no. 2, pp. 557–565, 2014. 23
- [123] P. Schmid, "Segmentation of digitized dermatoscopic images by two-dimensional color clustering," *IEEE T. Med. Imaging*, vol. 18, no. 2, pp. 164–171, 1999. 23, 24
- [124] H. Zhou, G. Schaefer, A. Sadka, and M. Celebi, "Anisotropic mean shift based fuzzy c-means segmentation of dermoscopy images," *IEEE J. Sel. Topics in Signal Proc.*, vol. 3, no. 1, pp. 26–34, 2009. 23

REFERENCES

- [125] M. Mete, S. Kockara, and K. Aydin, "Fast density-based lesion detection in dermoscopy images," *Comput. Med. Imaging Graph.*, vol. 35, no. 2, pp. 128–136, 2011. 23
- [126] Z. Liu, J. Sun, M. Smith, L. Smith, and R. Warr, "Unsupervised sub-segmentation for pigmented skin lesions," *Skin Res. Tech.*, vol. 18, no. 2, pp. 77–87, 2012. 23
- [127] T. Donadey, C. Serruys, A. Giron, G. Aitken, J. Vignali, R. Triller, and B. Fertl, "Boundary detection of black skin tumors using an adaptive radial-based approach," in *Proc. SPIE*, ser. Medical Imaging: Image Processing, K. M. Hanson, Ed., vol. 3979. San Diego, CA: SPIE, 2000, pp. 810–816. 23
- [128] G. Schaefer, M. Rajab, M. Celebi, and H. Iyatomi, "Skin lesion segmentation using co-operative neural network edge detection and colour normalisation," in *Proc. Int. Conf. Inform. Tech. and Appl. in Biomed. (ITAB)*. Piscataway, NJ: IEEE Press, 2009, pp. 1–4. 23
- [129] X. Yuan, N. Situ, and G. Zouridakis, "Automatic segmentation of skin lesion images using evolution strategies," *Biomed. Signal Process. Contr.*, vol. 3, no. 3, pp. 220–228, 2008. 23
- [130] P. Wighton, T. Lee, G. Mori, H. Lui, D. McLean, and M. Atkins, "Conditional random fields and supervised learning in automated skin lesion diagnosis," *Int. J. Biomed. Imag.*, vol. 2011, 10 pages, 2011. 23
- [131] M. Zortea, S. O. Skrovseth, T. Schopf, H. Kirchesch, and F. Godtliessen. (2011) Automatic segmentation of dermoscopic images by iterative classification. Article ID 972648. [Online]. Available: <http://dx.doi.org/10.1155/2011/972648> 23
- [132] H. Zhou, G. Schaefer, M. E. Celebi, F. Lin, and T. Liu, "Gradient vector flow with mean shift for skin lesion segmentation," *Comput. Med. Imaging Graph.*, vol. 35, no. 2, pp. 121–127, 2011. 23
- [133] G. Hance, S. Umbaugh, R. Moss, and W. Stoecker, "Unsupervised color image segmentation: with application to skin tumor borders," *IEEE Eng. Med. Biol.*, vol. 15, no. 1, pp. 104–111, 1996. 24
- [134] R. Melli, C. Grana, and R. Cucchiara, "Comparison of color clustering algorithms for segmentation of dermatological images," in *Proc. SPIE*, vol. 6144, 2006, pp. 1–9. 24
- [135] M. Silveira, J. Nascimento, J. Marques, A. Marçal, T. Mendonça, S. Yamauchi *et al.*, "Comparison of segmentation methods for melanoma diagnosis in dermoscopy images," *IEEE J. Sel. Topics in Signal Proc.*, vol. 3, no. 1, pp. 35–45, 2009. 24
- [136] M. Celebi, H. Kingravi, H. Iyatomi, J. Lee, Y. Aslandogan, W. Stoecker *et al.*, "Fast and accurate border detection in dermoscopy images using statistical region merging," in *Proc. SPIE*, ser. Medical Imaging: Image Processing, J. P. W. Pluim and J. M. Reinhardt, Eds., vol. 6512(3V). San Diego, CA: SPIE, 2007. 24

REFERENCES

- [137] M. Celebi, H. Kingravi, H. Iyatomi, Y. Aslandogan, W. Stoecker, R. Moss *et al.*, “Border detection in dermoscopy images using statistical region merging,” *Skin Res. Tech.*, vol. 14, no. 3, pp. 347–353, 2008. 24
- [138] B. Erkol, R. Moss, R. Joe Stanley, W. Stoecker, and E. Hvatum, “Automatic lesion boundary detection in dermoscopy images using gradient vector flow snakes,” *Skin Res. Tech.*, vol. 11, no. 1, pp. 17–26, 2005. 24
- [139] M. Celebi, Y. Aslandogan, W. Stoecker, H. Iyatomi, H. Oka, and X. Chen, “Unsupervised border detection in dermoscopy images,” *Skin Res. Tech.*, vol. 13, no. 4, pp. 454–462, 2007. 24
- [140] H. Zhou, J. Rehg, and M. Chen, “Exemplar-based segmentation of pigmented skin lesions from dermoscopy images,” in *Proc. IEEE Int. Symp. Biomed. Imag.: From Nano to Macro*. Piscataway, NJ: IEEE Press, 2010, pp. 225–228. 24
- [141] P. M. Ferreira, T. Mendonça, and P. Rocha, “A wide spread of algorithms for automatic segmentation of dermoscopic images,” in *Pattern Recognition and Image Analysis*, ser. Lecture Notes in Computer Science, J. Sanches, L. Micó, and J. Cardoso, Eds. Springer Berlin Heidelberg, 2013, vol. 7887, pp. 592–599. 24
- [142] M. Celebi, G. Schaefer, H. Iyatomi, W. Stoecker, J. Malters, and J. Grichnik, “An improved objective evaluation measure for border detection in dermoscopy images,” *Skin Res. Tech.*, vol. 15, no. 4, pp. 444–450, 2009. 24, 25
- [143] R. Garnavi, M. Aldeen, and M. Celebi, “Weighted performance index for objective evaluation of border detection methods in dermoscopy images,” *Skin Res. Tech.*, vol. 17, no. 1, pp. 35–44, 2011. 24, 25
- [144] T. Mendonca, P. M. Ferreira, J. S. Marques, A. R. Marcal, and J. Rozeira, “PH² - a dermoscopic image database for research and benchmarking,” in *Proc. IEEE Ann. Int. Conf. Eng. Med. Biol. Soc. (EMBC)*, 2013, pp. 5437–40. 25, 44
- [145] S. Umbaugh, Y.-S. Wei, and M. Zuke, “Feature extraction in image analysis. A program for facilitating data reduction in medical image classification,” *IEEE Eng. Med. Biol.*, vol. 16, no. 4, pp. 62–73, 1997. 25
- [146] E. Zagrouba and W. Barhoumi, “An accelerated system for melanoma diagnosis based on subset feature selection,” *J. Comput. Inform. Tech.*, vol. 13, no. 1, pp. 69–82, 2005. 25, 30, 37
- [147] R. Rohrer, H. Ganster, A. Pinz, and M. Binder, “Feature selection in melanoma recognition,” in *Proc. Int. Conf. Pattern Recogn. (ICPR)*, vol. 2. Los Alamitos, CA: IEEE Computer Society Press, 1998, pp. 1668–70. 26
- [148] M. Celebi and Y. Aslandogan, “Content-based image retrieval incorporating models of human perception,” in *Proc. Int. Conf. Inform. Tech.: Coding and Computing (ITCC)*, vol. 2. Los Alamitos, CA: IEEE Computer Society Press, 2004, pp. 241–245. 26, 30, 39

-
- [149] Y. Chang, R. J. Stanley, R. H. Moss, and W. Van Stoecker, "A systematic heuristic approach for feature selection for melanoma discrimination using clinical images," *Skin Res. Tech.*, vol. 11, no. 3, pp. 165–178, 2005. 26, 30
- [150] N. Situ, X. Yuan, T. Wadhawan, and G. Zouridakis, "Computer-aided skin cancer screening: feature selection or feature combination," in *Proc. IEEE Int. Conf. Image Process. (ICIP)*. Piscataway, NJ: IEEE Press, 2010, pp. 273–276. 26
- [151] I. Maglogiannis and C. Doukas, "Overview of advanced computer vision systems for skin lesions characterization," *IEEE T. Inf. Technol. B.*, vol. 13, no. 5, pp. 721–733, 2009. 26, 29, 31, 34, 37
- [152] T. Tanaka, S. Torii, I. Kabuta, K. Shimizu, M. Tanaka, and H. Oka, "Pattern classification of nevus with texture analysis," in *Proc. IEEE Ann. Int. Conf. Eng. Med. Biol. Soc. (EMBC)*, vol. 1. Piscataway, NJ: IEEE Press, 2004, pp. 1459–62. 27
- [153] C. Serrano and B. Acha, "Pattern analysis of dermoscopic images based on Markov random fields," *Pattern Recogn.*, vol. 42, no. 6, pp. 1052–57, 2009. 27
- [154] A. Sáez, C. Serrano, and B. Acha, "Model-based classification methods of global patterns in dermoscopic images," *IEEE T. Med. Imaging*, vol. 33, no. 5, pp. 1137–1147, May 2014. 27
- [155] Q. Abbas, M. Emre Celebi, and I. Fondón, "Computer-aided pattern classification system for dermoscopy images," *Skin Res. Tech.*, vol. 18, pp. 278–289, 2012. 27, 36
- [156] A. G. Isasi, B. G. Zapirain, and A. M. Zorrilla, "Melanomas non-invasive diagnosis application based on the ABCD rule and pattern recognition image processing algorithms," *Comput. Biol. Med.*, vol. 41, no. 9, pp. 742–755, 2011. 27
- [157] C. Mendoza, C. Serrano, and B. Acha, "Scale invariant descriptors in pattern analysis of melanocytic lesions," in *Proc. IEEE Int. Conf. Image Process. (ICIP)*. Piscataway, NJ: IEEE Press, 2009, pp. 4193–96. 27
- [158] S. Fischer, P. Schmid, and J. Guillo, "Analysis of skin lesions with pigmented networks," in *Proc. IEEE Int. Conf. Image Process. (ICIP)*, vol. 1. Piscataway, NJ: IEEE Press, 1996, pp. 323–326. 27
- [159] M. G. Fleming, C. Steger, A. B. Cognetta, and J. Zhang, "Analysis of the network pattern in dermatoscopic images," *Skin Res. Tech.*, vol. 5, no. 1, pp. 42–48, 1999. 27
- [160] B. Caputo, V. Panichelli, and G. Gigante, "Toward a quantitative analysis of skin lesion images," *Stud. Health Tech. Informat.*, vol. 90, pp. 509–513, 2002. 27
- [161] M. Anantha, R. Moss, and W. Stoecker, "Detection of pigment network in dermatoscopy images using texture analysis," *Comput. Med. Imaging Graph.*, vol. 28, no. 5, pp. 225–234, 2004. 27

REFERENCES

- [162] C. Grana, R. Cucchiara, G. Pellacani, and S. Seidenari, "Line detection and texture characterization of network patterns," in *Proc. Int. Conf. Pattern Recogn. (ICPR)*, vol. 2. Los Alamitos, CA: IEEE Computer Society Press, 2006, pp. 275–278. 27
- [163] B. Shrestha, J. Bishop, K. Kam, X. Chen, R. H. Moss, W. V. Stoecker *et al.*, "Detection of atypical texture features in early malignant melanoma," *Skin Res. Tech.*, vol. 16, no. 1, pp. 60–65, 2010. 27, 28
- [164] M. Sadeghi, M. Razmara, T. Lee, and M. Atkins, "A novel method for detection of pigment network in dermoscopic images using graphs," *Comput. Med. Imaging Graph.*, vol. 35, no. 2, pp. 137–143, 2011. 27
- [165] C. Barata, J. Marques, and J. Rozeira, "A system for the detection of pigment network in dermoscopy images using directional filters," *IEEE T. Biomed. Eng.*, vol. 59, no. 10, pp. 2744–54, 2012. 27
- [166] G. Betta, G. Di Leo, G. Fabbrocini, A. Paolillo, and M. Scalvenzi, "Automated application of the "7-point checklist" diagnosis method for skin lesions: Estimation of chromatic and shape parameters," in *Proc. IEEE Conf. Instrum. and Meas. Tech. (IMTC)*, vol. 22(2). Piscataway, NJ: IEEE Press, 2005, pp. 1818–22. 27
- [167] G. Betta, G. Di Leo, G. Fabbrocini, A. Paolillo, and P. Sommella, "Dermoscopic image-analysis system: estimation of atypical pigment network and atypical vascular pattern," in *Proc. IEEE Int. Work. Med. Meas. and Appl.* Los Alamitos, CA: IEEE Computer Society Press, 2006, pp. 63–67. 27
- [168] G. Di Leo, C. Liguori, A. Paolillo, and P. Sommella, "An improved procedure for the automatic detection of dermoscopic structures in digital ELM images of skin lesions," in *Proc. IEEE Conf. Virtual Environ., Hum.-Comput. Interf. and Meas. Syst.* Piscataway, NJ: IEEE Press, 2008, pp. 190–194. 27
- [169] S. Yoshino, T. Tanaka, M. Tanaka, and H. Oka, "Application of morphology for detection of dots in tumor," in *Proc. SICE Ann. Conf.*, vol. 1. Piscataway, NJ: IEEE Press, 2004, pp. 591–594. 27
- [170] H. Mirzaalian, T. K. Lee, and G. Hamarneh, "Learning features for streak detection in dermoscopic color images using localized radial flux of principal intensity curvature," in *Proc. IEEE Work. Math. Meth. in Biomed. Image Anal. (MMBIA)*. IEEE, 2012, pp. 97–101. 27
- [171] M. Sadeghi, T. Lee, D. McLean, H. Lui, and M. Atkins, "Detection and analysis of irregular streaks in dermoscopic images of skin lesions," *IEEE T. Med. Imaging*, vol. 32, no. 5, pp. 849–861, 2013. 27
- [172] G. Fabbrocini, G. Betta, G. Di Leo, C. Liguori, A. Paolillo, A. Pietrosanto *et al.*, "Epi-luminescence image processing for melanocytic skin lesion diagnosis based on 7-point

REFERENCES

- check-list: A preliminary discussion on three parameters,” *Open Dermatol. J.*, vol. 4, pp. 110–115, 2010. 27
- [173] M. Celebi, H. Kingravi, Y. Aslandogan, and W. Stoecker, “Detection of blue-white veil areas in dermoscopy images using machine learning techniques,” in *Proc. SPIE*, ser. Medical Imaging: Image Processing, J. M. Reinhardt and J. P. W. Pluim, Eds., vol. 6144(5T). San Diego, CA: SPIE, 2006. 27
- [174] M. E. Celebi, H. Iyatomi, W. V. Stoecker, R. H. Moss, H. S. Rabinovitz, G. Argenziano, and H. P. Soyer, “Automatic detection of blue-white veil and related structures in dermoscopy images,” *Comput. Med. Imaging Graph.*, vol. 32, no. 8, pp. 670–677, 2008. 27, 28, 29, 31, 36
- [175] A. Madooei, M. S. Drew, M. Sadeghi, and M. S. Atkins, “Automatic detection of blue-white veil by discrete colour matching in dermoscopy images,” in *Proc. Int. Conf. Med. Image Comput. and Comput. Assist. Interv. (MICCAI)*, 2013. 27
- [176] M. Lingala, R. J. Stanley, R. K. Rader, J. Hagerty, H. S. Rabinovitz, M. Oliviero, I. Choudhry, and W. V. Stoecker, “Fuzzy logic color detection: Blue areas in melanoma dermoscopy images,” *Comput. Med. Imaging Graph.*, 2014. 27, 28
- [177] G. Di Leo, G. Fabbrocini, C. Liguori, A. Pietrosanto, and M. Scлавenzi, “ELM image processing for melanocytic skin lesion diagnosis based on 7-point checklist: a preliminary discussion,” in *Proc. Int. Symp. Meas. for Res. and Ind. Appl.*, E. Kayafas and V. Loumos, Eds. Budapest, Hungary: IMEKO, 2004, pp. 474–479. 27
- [178] G. Di Leo, G. Fabbrocini, A. Paolillo, O. Rescigno, and P. Sommella, “Towards an automatic diagnosis system for skin lesions: Estimation of blue-whitish veil and regression structures,” in *Proc. Int. Multi-Conf. Systems, Signals and Devices*. Piscataway, NJ: IEEE Press, 2009, pp. 1–6. 27
- [179] W. Stoecker, M. Wronkiewicz, R. Chowdhury, R. Stanley, J. Xu, A. Bangert *et al.*, “Detection of granularity in dermoscopy images of malignant melanoma using color and texture features,” *Comput. Med. Imaging Graph.*, vol. 35, no. 2, pp. 144–147, 2011. 27
- [180] J. Garcia Arroyo, B. Zapirain, and A. Mendez Zorrilla, “Blue-white veil and dark-red patch of pigment pattern recognition in dermoscopic images using machine-learning techniques,” in *Proc. IEEE Int. Symp. Signal Process. and Inform. Tech. (ISSPIT)*, 2011, pp. 196–201. 27
- [181] A. Dalal, R. Moss, R. Stanley, W. Stoecker, K. Gupta, D. Calcara *et al.*, “Concentric decile segmentation of white and hypopigmented areas in dermoscopy images of skin lesions allows discrimination of malignant melanoma,” *Comput. Med. Imaging Graph.*, vol. 35, no. 2, pp. 148–154, 2011. 27, 36
- [182] A. Murali, W. Stoecker, and R. Moss, “Detection of solid pigment in dermatoscopy images using texture analysis,” *Skin Res. Tech.*, vol. 6, no. 4, pp. 193–198, 2000. 27

REFERENCES

- [183] W. V. Stoecker, K. Gupta, R. J. Stanley, R. H. Moss, and B. Shrestha, "Detection of asymmetric blotches (asymmetric structureless areas) in dermoscopy images of malignant melanoma using relative color," *Skin Res. Tech.*, vol. 11, no. 3, pp. 179–184, 2005. 27
- [184] V. Madasu and B. Lovell, "Blotch detection in pigmented skin lesions using fuzzy co-clustering and texture segmentation," in *Digital Image Comput.: Tech. Appl. (DICTA)*. IEEE Computer Society, 2009, pp. 25–31. 27
- [185] G. Pellacani, C. Grana, R. Cucchiara, and S. Seidenari, "Automated extraction and description of dark areas in surface microscopy melanocytic lesion images." *Dermatology*, vol. 208, no. 1, pp. 21–26, 2004. 27, 28
- [186] A. Khan, K. Gupta, R. Stanley, W. V. Stoecker, R. H. Moss, G. Argenziano, H. P. Soyer, H. S. Rabinovitz, and A. B. Cognetta, "Fuzzy logic techniques for blotch feature evaluation in dermoscopy images," *Comput. Med. Imaging Graph.*, vol. 33, no. 1, pp. 50–57, 2009. 27
- [187] H. Iyatomi, K. Norton, M. Celebi, G. Schaefer, M. Tanaka, and K. Ogawa, "Classification of melanocytic skin lesions from non-melanocytic lesions," in *Proc. IEEE Ann. Int. Conf. Eng. Med. Biol. Soc. (EMBC)*. Piscataway, NJ: IEEE Press, 2010, pp. 5407–10. 26, 28, 36
- [188] G. Pellacani, C. Grana, and S. Seidenari, "Automated description of colours in polarized-light surface microscopy images of melanocytic lesions," *Melanoma Res.*, vol. 14, no. 2, pp. 125–130, 2004. 28
- [189] S. Seidenari, G. Pellacani, and C. Grana, "Colors in atypical nevi: a computer description reproducing clinical assessment," *Skin Res. Tech.*, vol. 11, no. 1, pp. 36–41, 2005. 28
- [190] G. Pellacani, C. Grana, and S. Seidenari, "Algorithmic reproduction of asymmetry and border cut-off parameters according to the ABCD rule for dermoscopy," *J. Eur. Acad. Dermatol. Venereol.*, vol. 20, no. 10, pp. 1214–19, 2006. 28
- [191] S. Seidenari, G. Pellacani, and C. Grana, "Asymmetry in dermoscopic melanocytic lesion images: a computer description based on colour distribution," *Acta Derm. Venereol.*, vol. 85, no. 2, pp. 123–128, 2006. 28
- [192] M. Binder, H. Kittler, A. Seeber, A. Steiner, H. Pehamberger, and K. Wolff, "Epiluminescence microscopy-based classification of pigmented skin lesions using computerized image analysis and an artificial neural network," *Melanoma Res.*, vol. 8, no. 3, pp. 261–266, 1998. 28, 36
- [193] P. Kahofer, R. Hofmann-Wellenhof, and J. Smolle, "Tissue counter analysis of dermatoscopic images of melanocytic skin tumours: preliminary findings," *Melanoma Res.*, vol. 12, no. 1, pp. 71–75, 2002. 28, 36

-
- [194] A. Gerger, R. Pompl, and J. Smolle, “Automated epiluminescence microscopy–tissue counter analysis using CART and 1-NN in the diagnosis of melanoma,” *Skin Res. Tech.*, vol. 9, no. 2, pp. 105–110, 2003. 28, 36
- [195] K. Hoffmann, T. Gambichler, A. Rick, M. Kreutz, M. Anschuetz, T. Grünendick *et al.*, “Diagnostic and neural analysis of skin cancer (DANAOS). A multicentre study for collection and computer-aided analysis of data from pigmented skin lesions using digital dermoscopy,” *Br. J. Dermatol.*, vol. 149, no. 4, pp. 801–809, 2003. 28, 36, 38
- [196] A. Sboner, P. Bauer, G. Zumiani, C. Eccher, E. Blanzieri, S. Forti, and M. Cristofolini, “Clinical validation of an automated system for supporting the early diagnosis of melanoma,” *Skin Res. Tech.*, vol. 10, no. 3, pp. 184–192, 2004. 28, 36, 38
- [197] T. Fikrle and K. Pizinger, “Digital computer analysis of dermatoscopical images of 260 melanocytic skin lesions; perimeter/area ratio for the differentiation between malignant melanomas and melanocytic nevi,” *J. Eur. Acad. Dermatol. Venereol.*, vol. 21, no. 1, pp. 48–55, 2007. 28, 36, 38
- [198] K. Clawson, P. Morrow, B. Scotney, D. McKenna, and O. Dolan, “Computerised skin lesion surface analysis for pigment asymmetry quantification,” in *Proc. Int. Conf. Mach. Vis. and Image Process.* Los Alamitos, CA: IEEE Computer Society Press, 2007, pp. 75–82. 28
- [199] M. Kreutz, M. Anschütz, T. Grünendick, A. Rick, S. Gehlen, and K. Hoffmann, “Automated diagnosis of skin cancer using digital image processing and mixture-of-experts,” *Biomed. Tech.*, vol. 46, pp. 376–377, 2001. 28, 36
- [200] A. Sboner, C. Eccher, E. Blanzieri, P. Bauer, M. Cristofolini, G. Zumiani, and S. Forti, “A multiple classifier system for early melanoma diagnosis,” *Artif. Intell. Med.*, vol. 27, no. 1, pp. 29–44, 2003. 28, 36, 38
- [201] S. Tasoulis, C. Doukas, I. Maglogiannis, and V. Plagianakos, “Classification of dermatological images using advanced clustering techniques,” in *Proc. IEEE Ann. Int. Conf. Eng. Med. Biol. Soc. (EMBC)*. Piscataway, NJ: IEEE Press, 2010, pp. 6721–24. 28, 36, 37
- [202] G. Surówka, “Symbolic learning supporting early diagnosis of melanoma,” in *Proc. IEEE Ann. Int. Conf. Eng. Med. Biol. Soc. (EMBC)*. Piscataway, NJ: IEEE Press, 2010, pp. 4104–07. 28, 36
- [203] G. Schaefer, B. Krawczyk, M. Celebi, and H. Iyatomi, “Melanoma classification using dermoscopy imaging and ensemble learning,” in *Proc. Asian Conf. Pattern Recogn. (ACPR)*, Nov 2013, pp. 386–390. 28, 36
- [204] H. Ganster, M. Gelautz, A. Pinz, M. Binder, H. Pehamberger, M. Bammer, and J. Krocza, “Initial results of automated melanoma recognition,” in *Proc. Scand. Conf. on Image*

REFERENCES

- Anal.*, G. Borgefors, Ed. River Edge, NJ: World Scientific Publishing Co., Inc., 1995, pp. 343–353. 28, 36
- [205] M. Hintz-Madsen, L. Hansen, J. Larsen, and K. Drzewiecki, “A probabilistic neural network framework for detection of malignant melanoma,” in *Artif. neural netw. in cancer diagn., prognosis and patient manag.*, R. N. G. Naguib and G. V. Sherbet, Eds. Boca Raton, FL: CRC Press, 2001, vol. 1, pp. 141–183. 28
- [206] H. Ganster, P. Pinz, R. Rohrer, E. Wildling, M. Binder, and H. Kittler, “Automated melanoma recognition,” *IEEE T. Med. Imaging*, vol. 20, no. 3, pp. 233–239, 2001. 28, 36
- [207] I. Maglogiannis, E. Zafropoulos, and C. Kyranoudis, “Intelligent segmentation and classification of pigmented skin lesions in dermatological images,” in *Proc. Hellenic Conf. AI*, ser. LNCS, G. Antoniou, G. Potamias, C. Spyropoulos, and D. Plexousakis, Eds. Berlin: Springer, 2006, pp. 214–223. 28, 36
- [208] M. Ogorzałek, G. Surówka, L. Nowak, and C. Merkwirth, “Computational intelligence and image processing methods for applications in skin cancer diagnosis,” in *Biomed. Eng. Syst. and Tech.*, ser. CCIS, A. Fred, J. Filipe, and H. Gamboa, Eds., vol. 52. Berlin: Springer, 2010, pp. 3–20. 28, 36
- [209] S. Seidenari, G. Pellacani, and C. Grana, “Early detection of melanoma by image analysis,” in *Bioengineering of the skin: Skin Imaging and Analysis*, K. Wilhelm, P. Elsner, E. Berardesca, and H. Maibach, Eds. New York, NY: Informa HealthCare, 2006, vol. 31, ch. 22, pp. 305–311. 28
- [210] P. Schmid-Saugeon, “Symmetry axis computation for almost-symmetrical and asymmetrical objects: Application to pigmented skin lesions,” *Med. Image Anal.*, vol. 4, no. 3, pp. 269–282, 2000. 28
- [211] K. Clawson, P. Morrow, B. Scotney, D. McKenna, and O. Dolan, “Determination of optimal axes for skin lesion asymmetry quantification,” in *Proc. IEEE Int. Conf. Image Process. (ICIP)*, vol. 2. Piscataway, NJ: IEEE Press, 2007, pp. II–453–456. 28
- [212] Z. Liu, L. Smith, J. Sun, M. Smith, and R. Warr, “Biological indexes based reflectional asymmetry for classifying cutaneous lesions,” in *Proc. Int. Conf. Med. Image Comput. and Comput. Assist. Interv. (MICCAI)*, ser. LNCS, G. Fichtinger, A. Martel, and T. Peters, Eds., vol. 6893. Berlin: Springer, 2011, pp. 124–132. 28
- [213] S. Seidenari, G. Pellacani, and C. Grana, “Pigment distribution in melanocytic lesion images: a digital parameter to be employed for computer-aided diagnosis,” *Skin Res. Tech.*, vol. 11, no. 4, pp. 236–241, 2005. 28
- [214] H. Iyatomi, H. Oka, M. Celebi, K. Ogawa, G. Argenziano, H. Soyer, H. Koga, T. Saida, K. Ohara, and M. Tanaka, “Computer-based classification of dermoscopy images of melanocytic lesions on acral volar skin,” *J. Invest. Dermatol.*, vol. 128, no. 8, pp. 2049–54, 2008. 28

-
- [215] S. Gilmore, R. Hofmann-Wellenhof, and H. Soyer, "A support vector machine for decision support in melanoma recognition," *Exp. Dermatol.*, vol. 19, no. 9, pp. 830–835, 2010. 28, 36
- [216] H. Iyatomi, H. Oka, M. Celebi, M. Tanaka, and K. Ogawa, "Parameterization of dermoscopic findings for the internet-based melanoma screening system," in *Proc. IEEE Symp. Computat. Intell. in Image and Signal Process.* Piscataway, NJ: IEEE Press, 2007, pp. 189–193. 28
- [217] H. Iyatomi, H. Oka, M. Celebi, M. Hashimoto, M. Hagiwara, M. Tanaka, and K. Ogawa, "An improved internet-based melanoma screening system with dermatologist-like tumor area extraction algorithm," *Comput. Med. Imaging Graph.*, vol. 32, no. 7, pp. 566–579, 2008. 28, 36, 37
- [218] H. Iyatomi, "Computer-based diagnosis of pigmented skin lesions," in *New developments in biomedical engineering*, D. Campolo, Ed. Vukovar, Croatia: InTech, 2010, pp. 183–200. 28
- [219] A. Piantanelli, P. Maponi, L. Scalise, S. Serresi, A. Cialabrini, and A. Basso, "Fractal characterisation of boundary irregularity in skin pigmented lesions," *Med. Biol. Eng. Comput.*, vol. 43, pp. 436–442, 2005. 28
- [220] G. R. Day, "How blurry is that border? An investigation into algorithmic reproduction of skin lesion border cut-off," *Comput. Med. Imaging Graph.*, vol. 24, no. 2, pp. 69–72, 2000. 28
- [221] C. Grana, G. Pellacani, R. Cucchiara, and S. Seidenari, "A new algorithm for border description of polarized light surface microscopic images of pigmented skin lesions," *IEEE T. Med. Imaging*, vol. 22, no. 8, pp. 959–964, 2003. 28
- [222] K. Clawson, P. Morrow, B. Scotney, J. McKenna, and O. Dolan, "Analysis of pigmented skin lesion border irregularity using the harmonic wavelet transform," in *Proc. Int. Conf. Mach. Vis. and Image Process.* Los Alamitos, CA: IEEE Computer Society Press, 2009, pp. 18–23. 28
- [223] K. Przystalski, L. Nowak, M. Ogorzalek, and G. Surowka, "Semantic analysis of skin lesions using radial basis function neural networks," in *Proc. Conf. Hum. Syst. Interact. (HSI)*, T. Pardela and B. Wilamowski, Eds. Piscataway, NJ: IEEE Press, 2010, pp. 128–132. 28
- [224] M. Ruela, C. Barata, and J. Marques, "What is the role of color symmetry in the detection of melanomas?" in *Proc. Int. Symp. Visual Computing (ISVC)*, ser. LNCS, G. Bebis, R. Boyle, B. Parvin, D. Koracin, B. Li, F. Porikli, V. Zordan, J. Klosowski, S. Coquillart, X. Luo, M. Chen, and D. Gotz, Eds. Springer Berlin Heidelberg, 2013, vol. 8033, pp. 1–10. 28

REFERENCES

- [225] G. Capdehourat, A. Corez, A. Bazzano, and P. Musé, “Pigmented skin lesions classification using dermatoscopic images,” in *Progress in Pattern Recogn., Image Anal., Comput. Vis., and Appl.*, E. Bayro-Corrochano and J.-O. Eklundh, Eds. Berlin: Springer, 2009, pp. 537–544. 28, 36
- [226] N. Situ, T. Wadhawan, X. Yuan, and G. Zouridakis, “Modeling spatial relation in skin lesion images by the graph walk kernel,” in *Proc. IEEE Ann. Int. Conf. Eng. Med. Biol. Soc. (EMBC)*. Piscataway, NJ: IEEE Press, 2010, pp. 6130–33. 28, 29, 36
- [227] L. Ballerini, X. Li, R. Fisher, and J. Rees, “A query-by-example content-based image retrieval system of non-melanoma skin lesions,” in *Medical Content-Based Retrieval for Clinical Decision Support*, ser. LNCS, B. Caputo, H. Müller, T. Syeda-Mahmood, J. Duncan, F. Wang, and J. Kalpathy-Cramer, Eds., vol. 5853. Berlin: Springer, 2010, pp. 31–38. 28, 39
- [228] C. Barata, M. Ruela, M. Francisco, T. Mendonça, and J. Marques, “Two systems for the detection of melanomas in dermoscopy images using texture and color features,” *IEEE Syst. J.*, pp. 1–15, 2013. 28, 29, 36
- [229] M. Rahman and P. Bhattacharya, “An integrated and interactive decision support system for automated melanoma recognition of dermoscopic images,” *Comput. Med. Imaging Graph.*, vol. 34, no. 6, pp. 479–486, 2010. 28, 32, 36, 39
- [230] R. J. Stanley, W. V. Stoecker, and R. H. Moss, “A relative color approach to color discrimination for malignant melanoma detection in dermoscopy images,” *Skin Res. Tech.*, vol. 13, no. 1, pp. 62–72, 2007. 28
- [231] S. Seidenari, G. Pellacani, and C. Grana, “Computer description of colours in dermoscopic melanocytic lesion images reproducing clinical assessment,” *Br. J. Dermatol.*, vol. 149, no. 3, pp. 523–529, 2003. 28
- [232] H. Motoyama, T. Tanaka, M. Tanaka, and H. Oka, “Feature of malignant melanoma based on color information,” in *Proc. SICE Ann. Conf.*, vol. 1. Piscataway, NJ: IEEE Press, 2004, pp. 230–233. 28
- [233] R. Stanley, W. V. Stoecker, R. H. Moss, H. S. Rabinovitz, A. B. Cagnetta, G. Argenziano, and H. Peter Soyer, “A basis function feature-based approach for skin lesion discrimination in dermatology dermoscopy images,” *Skin Res. Tech.*, vol. 14, no. 4, pp. 425–435, 2008. 28
- [234] E. La Torre, B. Caputo, and T. Tommasi, “Learning methods for melanoma recognition,” *Int. J. Imag. Syst. Tech.*, vol. 20, no. 4, pp. 316–322, 2010. 28, 34, 36
- [235] R. Walvick, K. Patel, S. Patwardhan, and A. Dhawan, “Classification of melanoma using wavelet-transform-based optimal feature set,” in *Proc. SPIE*, ser. Medical Imaging: Image Processing, J. M. Fitzpatrick and M. Sonka, Eds., vol. 5370. San Diego, CA: SPIE, 2004, pp. 944–951. 28, 36

-
- [236] S. Patwardhan, A. Dhawan, and P. Relue, "Classification of melanoma using tree structured wavelet transforms," *Comput. Meth. Programs Biomed.*, vol. 72, no. 3, pp. 223–239, 2003. 28, 36
 - [237] S. V. Patwardhan, S. Dai, and A. P. Dhawan, "Multi-spectral image analysis and classification of melanoma using fuzzy membership based partitions," *Comput. Med. Imaging Graph.*, vol. 29, no. 4, pp. 287–296, 2005. 28, 36
 - [238] G. Surówka, C. Merkwirth, E. Zabinska-Plazak, and A. Graca, "Wavelet based classification of skin lesion images," *Bio-Algorithms and Med-Systems*, vol. 2, no. 4, pp. 43–50, 2006. 28, 36
 - [239] G. Surówka and K. Grzesiak-Kopec, "Different learning paradigms for the classification of melanoid skin lesions using wavelets," in *Proc. IEEE Ann. Int. Conf. Eng. Med. Biol. Soc. (EMBC)*. Piscataway, NJ: IEEE Press, 2007, pp. 3136–39. 28, 34, 36
 - [240] G. Surówka, "Supervised learning of melanocytic skin lesion images," in *Proc. Conf. Hum. Syst. Interact. (HSI)*, L. Piatek, Ed. Piscataway, NJ: IEEE Press, 2008, pp. 121–125. 28, 34, 36
 - [241] —, "Inductive learning of skin lesion images for early diagnosis of melanoma," in *Proc. IEEE World Cong. Computat. Intell. (WCCI)*. Piscataway, NJ: IEEE press, 2008, pp. 2623–27. 28, 36
 - [242] N. Situ, X. Yuan, J. Chen, and G. Zouridakis, "Malignant melanoma detection by Bag-of-Features classification," in *Proc. IEEE Ann. Int. Conf. Eng. Med. Biol. Soc. (EMBC)*. Piscataway, NJ: IEEE Press, 2008, pp. 3110–13. 28, 29, 34, 36
 - [243] R. Braun, H. Rabinovitz, M. Oliviero, A. Kopf, and J. Saurat, "Dermoscopy of pigmented skin lesions," *J. Am. Acad. Dermatol.*, vol. 52, no. 1, pp. 109–121, 2005. 28
 - [244] J. Kontinen, J. Rönig, and R. MacKie, "Texture features in the classification of melanocytic lesions," in *Image Analysis and Processing*, ser. LNCS, A. Del Bimbo, Ed. Berlin: Springer, 1997, vol. 1311, pp. 453–460. 29, 36
 - [245] M. Zortea, S. Skrøvseth, and F. Godtliebsen, "Automatic learning of spatial patterns for diagnosis of skin lesions," in *Proc. IEEE Ann. Int. Conf. Eng. Med. Biol. Soc. (EMBC)*. Piscataway, NJ: IEEE Press, 2010, pp. 5601–04. 29, 36
 - [246] X. Yuan, Z. Yang, G. Zouridakis, and N. Mullani, "SVM-based texture classification and application to early melanoma detection," in *Proc. IEEE Ann. Int. Conf. Eng. Med. Biol. Soc. (EMBC)*. Piscataway, NJ: IEEE Press, 2006, pp. 4775–78. 29, 36
 - [247] I. Stanganelli, A. Brucale, L. Calori, R. Gori, A. Lovato, S. Magi *et al.*, "Computer-aided diagnosis of melanocytic lesions," *Anticancer Res.*, vol. 25, pp. 4577–82, 2005. 27, 29, 36
 - [248] M. d'Amico, M. Ferri, and I. Stanganelli, "Qualitative asymmetry measure for melanoma detection," in *Proc. IEEE Int. Symp. Biomed. Imag.: From Nano to Macro*. Piscataway, NJ: IEEE Press, 2004, pp. 1155–58. 27, 29

REFERENCES

- [249] F. Massimo and S. Ignazio. (2010) Size functions for the morphological analysis of melanocytic lesions. Article ID 621357. [Online]. Available: <http://dx.doi.org/10.1155/2010/621357> 27, 29, 36
- [250] H. Zhou, M. Chen, and J. Rehg, “Dermoscopic interest point detector and descriptor,” in *Proc. IEEE Int. Symp. Biomed. Imag.: From Nano to Macro*. Piscataway, NJ: IEEE Press, 2009, pp. 1318–21. 27, 29
- [251] E. Claridge, P. Hall, M. Keefe, and J. Allen, “Shape analysis for classification of malignant melanoma,” *J. Biomed. Eng.*, vol. 14, no. 3, pp. 229–234, 1992. 29, 30, 31
- [252] A. G. Manousaki, A. G. Manios, E. I. Tsompanaki, J. G. Panayiotides, D. D. Tsiftsis, A. K. Kostaki, and A. D. Tosca, “A simple digital image processing system to aid in melanoma diagnosis in an everyday melanocytic skin lesion unit. A preliminary report,” *Int. J. Dermatol.*, vol. 45, no. 4, pp. 402–410, 2006. 30, 31
- [253] W. V. Stoecker, W. W. Li, and R. H. Moss, “Automatic detection of asymmetry in skin tumors,” *Comput. Med. Imaging Graph.*, vol. 16, no. 3, pp. 191–197, 1992. 30
- [254] K. Cheung, “Image processing for skin cancer detection: Malignant melanoma recognition,” Master’s thesis, Graduate Dept. of Electrical and Computer Engineering, University of Toronto, 1997. 30
- [255] B. Kusumoputro and A. Ariyanto, “Neural network diagnosis of malignant skin cancers using principal component analysis as a preprocessor,” in *Proc. IEEE World Cong. Computat. Intell. (WCCI)*, vol. 1. Piscataway, NJ: IEEE Press, 1998, pp. 310–315. 30
- [256] Z. She, Y. Liu, and A. Damatoa, “Combination of features from skin pattern and ABCD analysis for lesion classification,” *Skin Res. Tech.*, vol. 13, no. 1, pp. 25–33, 2007. 30, 31, 32
- [257] F. Ercal, A. Chawla, W. Stoecker, H. Lee, and R. Moss, “Neural network diagnosis of malignant melanoma from color images,” *IEEE T. Biomed. Eng.*, vol. 41, no. 9, pp. 837–845, 1994. 30, 36
- [258] A. Kjoelen, M. Thompson, S. Umbaugh, R. Moss, and W. Stoecker, “Performance of AI methods in detecting melanoma,” *IEEE Eng. Med. Biol.*, vol. 14, no. 4, pp. 411–416, 1995. 30, 36
- [259] Z. Zhang, R. Moss, and W. Stoecker, “Neural networks skin tumor diagnostic system,” in *Proc. Int. Conf. Neural Netw. and Signal Process.*, vol. 1. Piscataway, NJ: IEEE Press, 2003, pp. 191–192. 30, 36
- [260] I. Maglogiannis and E. Zafropoulos, “Characterization of digital medical images utilizing support vector machines,” *BMC Med. Informat. Decis. Making*, vol. 4, no. 4, 2004. 30, 34, 36

REFERENCES

- [261] M. Metz, J. Curnow, W. Groch, E. Ifeachor, and P. Kersey, "Classifying pigmented skin lesions utilizing non-parametric and artificial intelligence techniques," in *Proc. Comput. Intell. in Med. and Health.*, 2005. 30, 36
- [262] A. Kjoelen, S. Umbaugh, R. Moss, and W. Stoecker, "Artificial intelligence applied to detection of melanoma," in *Proc. IEEE Ann. Int. Conf. Eng. Med. Biol. Soc. (EMBC)*. NY: IEEE Press, 1993, pp. 602–603. 30, 36
- [263] S. Chung and Q. Wang, "Content-based retrieval and data mining of a skin cancer image database," in *Proc. Int. Conf. Inform. Tech.: Coding and Computing*. Los Alamitos, CA: IEEE Computer Society Press, 2001, pp. 611–615. 30, 31, 39
- [264] I. Maglogiannis, S. Pavlopoulos, and D. Koutsouris, "An integrated computer supported acquisition, handling, and characterization system for pigmented skin lesions in dermatological images," *IEEE T. Inf. Technol. B.*, vol. 9, no. 1, pp. 86–98, 2005. 30, 34, 36
- [265] K. Taouil, Z. Chtourou, and N. B. Romdhane, "A robust system for melanoma diagnosis using heterogeneous image databases," *J. Biomed. Sci. Eng.*, vol. 3, no. 6, pp. 576–583, 2010. 30, 36
- [266] J. Christensen, M. Soerensen, Z. Linghui, S. Chen, and M. Jensen, "Pre-diagnostic digital imaging prediction model to discriminate between malignant melanoma and benign pigmented skin lesion," *Skin Res. Tech.*, vol. 16, no. 1, pp. 98–108, 2010. 30, 31
- [267] A. Parolin, E. Herzer, and C. Jung, "Semi-automated diagnosis of melanoma through the analysis of dermatological images," in *Proc. Conf. Graphics, Patterns and Images (SIBGRAPI)*. Los Alamitos, CA: IEEE Computer Society Press, 2010, pp. 71–78. 30, 36
- [268] V. Ng and D. Cheung, "Measuring asymmetries of skin lesions," in *Proc. IEEE Int. Conf. Syst., Man, and Cybernetics (SMC)*, vol. 5. Piscataway, NJ: IEEE Press, 1997, pp. 4211–16. 30
- [269] V. T. Ng, B. Y. Fung, and T. K. Lee, "Determining the asymmetry of skin lesion with fuzzy borders," *Comput. Biol. Med.*, vol. 35, no. 2, pp. 103–120, 2005. 30
- [270] N. Cascinelli, M. Ferrario, R. Bufalino, S. Zurrida, V. Galimberti, L. Mascheroni *et al.*, "Results obtained by using a computerized image analysis system designed as an aid to diagnosis of cutaneous melanoma," *Melanoma Res.*, vol. 2, no. 3, pp. 163–170, 1992. 30, 31
- [271] A. Green, N. Martin, J. Pfitzner, M. O'Rourke, and N. Knight, "Computer image analysis in the diagnosis of melanoma," *J. Am. Acad. Dermatol.*, vol. 31, no. 6, pp. 958–964, 1994. 30, 36
- [272] B. Farina, C. Bartoli, A. Bono, A. Colombo, M. Lualdi, G. Tragni, and R. Marchesini, "Multispectral imaging approach in the diagnosis of cutaneous melanoma: potentiality and limits," *Phys. Med. Biol.*, vol. 45, pp. 1243–54, 2000. 30, 31, 36

REFERENCES

- [273] S. Tomatis, A. Bono, C. Bartoli, M. Carrara, M. Lualdi, G. Tragni, and R. Marchesini, “Automated melanoma detection: multispectral imaging and neural network approach for classification,” *Med. Phys.*, vol. 30, pp. 212–221, 2003. 30, 31, 36
- [274] S. Tomatis, M. Carrara, A. Bono, C. Bartoli, M. Lualdi, G. Tragni *et al.*, “Automated melanoma detection with a novel multispectral imaging system: results of a prospective study,” *Phys. Med. Biol.*, vol. 50, pp. 1675–87, 2005. 30, 31, 36, 38
- [275] J. E. Golston, W. V. Stoecker, R. H. Moss, and I. P. S. Dhillon, “Automatic detection of irregular borders in melanoma and other skin tumors,” *Comput. Med. Imaging Graph.*, vol. 16, no. 3, pp. 199–203, 1992. 30
- [276] T.-B. Holmström, “A survey and evaluation of features for the diagnosis of malignant melanoma,” Master’s thesis, Umea University, Computing Science Dept., 2005. 30
- [277] Y. I. Cheng, R. Swamisai, S. E. Umbaugh, R. H. Moss, W. V. Stoecker, S. Teegala, and S. K. Srinivasan, “Skin lesion classification using relative color features,” *Skin Res. Tech.*, vol. 14, no. 1, pp. 53–64, 2008. 30, 34, 36
- [278] M. Larabi, N. Richard, and C. Fernandez-Maloigne, “Using combination of color, texture and shape features for image retrieval in melanomas databases,” in *Proc. SPIE*, ser. Internet imaging III, G. B. Beretta and R. Schettini, Eds., vol. 4672. San Jose, CA: SPIE, 2002, pp. 147–156. 30, 31, 39
- [279] V. Ng and T. Lee, “Measuring border irregularities of skin lesions using fractal dimensions,” in *Proc. SPIE*, ser. Electronic Imaging and Multimedia Systems, C.-S. Li, R. L. Stevenson, and L. Zhou, Eds., vol. 2898. San Diego, CA: SPIE, 1996, pp. 64–71. 30
- [280] E. Claridge, J. Smith, and P. Hall, “Evaluation of border irregularity in pigmented skin lesions against a consensus of expert clinicians,” in *Proc. Med. Image Understand. Anal. (MIUA)*, E. Berry, D. Hogg, K. Mardia, and M. Smith, Eds. Leeds, UK: BMVA, 1998, pp. 85–88. 30
- [281] A. G. Manousaki, A. G. Manios, E. I. Tsompanaki, and A. D. Tosca, “Use of color texture in determining the nature of melanocytic skin lesions—a qualitative and quantitative approach,” *Comput. Biol. Med.*, vol. 36, no. 4, pp. 419–427, 2006. 30
- [282] S. Carbonetto and S. Lew, “Characterization of border structure using fractal dimension in melanomas,” in *Proc. IEEE Ann. Int. Conf. Eng. Med. Biol. Soc. (EMBC)*. Piscataway, NJ: IEEE Press, 2010, pp. 4088–91. 30, 36
- [283] T. Lee, D. McLean, and M. Stella Atkins, “Irregularity index: a new border irregularity measure for cutaneous melanocytic lesions,” *Med. Image Anal.*, vol. 7, no. 1, pp. 47–64, 2003. 30
- [284] T. Lee and E. Claridge, “Predictive power of irregular border shapes for malignant melanomas,” *Skin Res. Tech.*, vol. 11, no. 1, pp. 1–8, 2005. 30

REFERENCES

- [285] T. Lee, M. Atkins, R. Gallagher, C. MacAulay, A. Coldman, and D. McLean, "Describing the structural shape of melanocytic lesions," in *Proc. SPIE*, ser. Medical Imaging: Image Processing, K. M. Hanson, Ed., vol. 3661. San Diego, CA: SPIE, 1999, pp. 1170–79. 30
- [286] B. Aribisala and E. Claridge, "A border irregularity measure using a modified conditional entropy method as a malignant melanoma predictor," in *Image Analysis and Recognition*, ser. LNCS, M. Kamel and A. Campilho, Eds. Berlin: Springer, 2005, vol. 3656, pp. 914–921. 30
- [287] —, "A border irregularity measure using Hidden Markov Models as a malignant melanoma predictor," in *Proc. Int. Conf. Biomed. Eng.*, Innsbruck, Austria, 2005. 30
- [288] L. Ma, B. Qin, W. Xu, and L. Zhu, "Multi-scale descriptors for contour irregularity of skin lesion using wavelet decomposition," in *Proc. Int. Conf. Biomed. Eng. Informat. (BMEI)*, vol. 1. Piscataway, NJ: IEEE Press, 2010, pp. 414–418. 30
- [289] Y. Zhou, M. Smith, L. Smith, and R. Warr, "A new method describing border irregularity of pigmented lesions," *Skin Res. Tech.*, vol. 16, no. 1, pp. 66–76, 2010. 30, 34, 36
- [290] A. Durg, W. Stoecker, J. Cookson, S. Umbaugh, and R. Moss, "Identification of variegated coloring in skin tumors: neural network vs. rule-based induction methods," *IEEE Eng. Med. Biol.*, vol. 12, no. 3, pp. 71–74, 98, 1993. 30
- [291] K. Tabatabaie and A. Esteki, "Independent component analysis as an effective tool for automated diagnosis of melanoma," in *Proc. Cairo Int. Biomed. Eng. Conf.* Piscataway, NJ: IEEE Press, 2008, pp. 1–4. 30, 31
- [292] M. Landau, H. Matz, E. Tur, M. Dvir, and S. Brenner, "Computerized system to enhance the clinical diagnosis of pigmented cutaneous malignancies," *Int. J. Dermatol.*, vol. 38, no. 6, pp. 443–446, 1999. 30, 36
- [293] S. Umbaugh, R. Moss, and W. Stoecker, "Applying artificial intelligence to the identification of variegated coloring in skin tumors," *IEEE Eng. Med. Biol.*, vol. 10, no. 4, pp. 57–62, 1991. 30
- [294] R. J. Stanley, R. H. Moss, W. V. Stoecker, and C. Aggarwal, "A fuzzy-based histogram analysis technique for skin lesion discrimination in dermatology clinical images," *Comput. Med. Imaging Graph.*, vol. 27, no. 5, pp. 387–396, 2003. 30, 36
- [295] J. Chen, R. J. Stanley, R. H. Moss, and W. Van Stoecker, "Colour analysis of skin lesion regions for melanoma discrimination in clinical images," *Skin Res. Tech.*, vol. 9, no. 2, pp. 94–104, 2003. 30
- [296] Y. Faziloglu, R. J. Stanley, R. H. Moss, W. Van Stoecker, and R. P. McLean, "Colour histogram analysis for melanoma discrimination in clinical images," *Skin Res. Tech.*, vol. 9, no. 2, pp. 147–156, 2003. 30

REFERENCES

- [297] E. Claridge, S. Cotton, P. Hall, and M. Moncrieff, “From colour to tissue histology: Physics based interpretation of images of pigmented skin lesions,” in *Proc. Int. Conf. Med. Image Comput. and Comput. Assist. Interv. (MICCAI)*, ser. LNCS, T. Dohi and R. Kikinis, Eds., vol. 2488. Berlin: Springer, 2003, pp. 730–738. 30, 38
- [298] M. Carrara, A. Bono, C. Bartoli, A. Colombo, M. Lualdi, D. Moglia *et al.*, “Multispectral imaging and artificial neural network: mimicking the management decision of the clinician facing pigmented skin lesions,” *Phys. Med. Biol.*, vol. 52, pp. 2599–2613, 2007. 31, 38
- [299] A. J. Round, A. W. G. Duller, and P. J. Fish, “Lesion classification using skin patterning,” *Skin Res. Tech.*, vol. 6, no. 4, pp. 183–192, 2000. 31, 32
- [300] Z. She and P. Fish, “Analysis of skin line pattern for lesion classification,” *Skin Res. Tech.*, vol. 9, no. 1, pp. 73–80, 2003. 31, 32
- [301] Y. Liu and Z. She, “Skin pattern analysis for lesion classification using skin line intensity,” in *Proc. Med. Image Understand. Anal. (MIUA)*, M. Mirmehdi, Ed. Bristol, UK: BMVA, 2005, pp. 207–210. 31, 32
- [302] Z. She and P. S. Excell, “Skin pattern analysis for lesion classification using local isotropy,” *Skin Res. Tech.*, vol. 17, no. 2, pp. 206–212, 2011. 31, 32
- [303] —, “Lesion classification using 3D skin surface tilt orientation,” *Skin Res. Tech.*, vol. 19, no. 1, pp. e305–e311, 2013. 31
- [304] S. V. Deshabhoina, S. E. Umbaugh, W. V. Stoecker, R. H. Moss, and S. K. Srinivasan, “Melanoma and seborrheic keratosis differentiation using texture features,” *Skin Res. Tech.*, vol. 9, no. 4, pp. 348–356, 2003. 31, 36
- [305] W. V. Stoecker, C.-S. Chiang, and R. H. Moss, “Texture in skin images: Comparison of three methods to determine smoothness,” *Comput. Med. Imaging Graph.*, vol. 16, no. 3, pp. 179–190, 1992. 31
- [306] M. Chaudhry, R. Ashraf, M. Jafri, and M. Akbar, “Computer aided diagnosis of skin carcinomas based on textural characteristics,” in *Proc. Int. Conf. Mach. Vis. (ICMV)*. Piscataway, NJ: IEEE Press, 2007, pp. 125–128. 31, 36
- [307] A. Jukić, I. Kopriva, and A. Cichocki, “Noninvasive diagnosis of melanoma with tensor decomposition-based feature extraction from clinical color image,” *Biomed. Signal Process. Contr.*, vol. 8, no. 6, pp. 755–763, 2013. 31
- [308] N. Situ, T. Wadhawan, R. Hu, K. Lancaster, X. Yuan, and G. Zouridakis, “Evaluating sampling strategies of dermoscopic interest points,” in *Proc. IEEE Int. Symp. Biomed. Imag.: From Nano to Macro*, 2011, pp. 109–112. 32
- [309] C. Barata, J. S. Marques, and T. Mendonça, “Bag-of-features classification model for the diagnose of melanoma in dermoscopy images using color and texture descriptors,” in *Proc. Int. Conf. Image Anal. and Recogn. (ICIAR)*. Springer, 2013, pp. 547–555. 32

-
- [310] R. Popa and D. Aiordachioaie, “Genetic recognition of changes in melanocytic lesions,” in *Proc. Int. Symp. Autom. Control and Comput. Sci. (SACCS)*, Iasi, Romania, 2004. 33
 - [311] M. Geilhufe, S. O. Skrøvseth, and F. Godtliebsen, “Digital monitoring of changes in skin lesions,” in *Proc. IADIS Int. Conf. e-Health*, 2010, pp. 229–233. 33
 - [312] I. Maglogiannis, “Automated segmentation and registration of dermatological images,” *J. Math. Model. Algorithms*, vol. 2, no. 3, pp. 277–294, 2003. 33
 - [313] S. Pavlopoulos, “New hybrid stochastic-deterministic technique for fast registration of dermatological images,” *Med. Biol. Eng. Comput.*, vol. 42, no. 6, pp. 777–786, 2004. 33
 - [314] C. Anagnostopoulos, D. Vergados, and P. Mintzias, “Image registration of follow-up examinations in digital dermoscopy,” in *Proc. IEEE Int. Conf. Bioinform. Bioeng. (BIBE)*, Nov 2013, pp. 1–4. 33
 - [315] D. G. Lowe, “Distinctive image features from scale-invariant keypoints,” *Int. J. Comput. Vision*, vol. 60, no. 2, pp. 91–110, 2004. 33, 76, 142, 144, 146, 148, 149
 - [316] M. A. Fischler and R. C. Bolles, “Random sample consensus: a paradigm for model fitting with applications to image analysis and automated cartography,” *Communications of the ACM*, vol. 24, no. 6, pp. 381–395, 1981. 33, 76, 150
 - [317] D. Furusho and H. Iyatomi, “Registration and color calibration for dermoscopy images in time-course analysis,” in *Proc. SPIE*, ser. Medical Imaging. International Society for Optics and Photonics, 2014, p. 90353B. 33
 - [318] S. Dreiseitl, L. Ohno-Machado, H. Kittler, S. Vinterbo, H. Billhardt, and M. Binder, “A comparison of machine learning methods for the diagnosis of pigmented skin lesions,” *J. Biomed. Informat.*, vol. 34, no. 1, pp. 28–36, 2001. 34, 35, 36, 38
 - [319] R. Bostock, E. Claridge, A. Harget, and P. Hall, “Towards a neural network based system for skin cancer diagnosis,” in *Proc. Int. Conf. Artif. Neural Netw.*, 1993, pp. 215–219. 36
 - [320] M. Hintz-Madsen, L. K. Hansen, J. Larsen, E. Olesen, and K. T. Drzewiecki, “Detection of malignant melanoma using neural classifiers,” in *Proc. Int. Conf. Eng. Appl. Neural Netw.*, A. B. Bulsari, S. Kallio, and D. Tsapsinos, Eds. London, UK: Syst. Eng. Assoc., 1996, pp. 395–398. 36
 - [321] G. Castiello, G. Castellano, and A. Fanelli, “Neuro-fuzzy analysis of dermatological images,” in *Proc. IEEE Int. Joint Conf. Neural Netw.*, vol. 4. Piscataway, NJ: IEEE Press, 2004, pp. 3247–52. 36
 - [322] M. Binder, A. Steiner, M. Schwarz, S. Knollmayer, K. Wolff, and H. Pehamberger, “Application of an artificial neural network in epiluminescence microscopy pattern analysis of pigmented skin lesions: a pilot study,” *Br. J. Dermatol.*, vol. 130, no. 4, pp. 460–465, 1994. 36

REFERENCES

- [323] P. Bauer, P. Cristofolini, S. Boi, M. Burroni, G. Dell'Eva, R. Micciolo, and M. Cristofolini, "Digital epiluminescence microscopy: usefulness in the differential diagnosis of cutaneous pigmentary lesions. A statistical comparison between visual and computer inspection," *Melanoma Res.*, vol. 10, no. 4, pp. 345–349, 2000. 36, 37, 38
- [324] M. Binder, H. Kittler, S. Dreiseitl, H. Ganster, K. Wolff, and H. Pehamberger, "Computer-aided epiluminescence microscopy of pigmented skin lesions: the value of clinical data for the classification process," *Melanoma Res.*, vol. 10, no. 6, pp. 556–561, 2000. 36
- [325] P. Rubegni, G. Cevenini, M. Burroni, R. Perotti, G. Dell'Eva, P. Sbrano *et al.*, "Automated diagnosis of pigmented skin lesions," *Int. J. Cancer*, vol. 101, no. 6, pp. 576–580, 2002. 36, 38
- [326] D. Piccolo, A. Ferrari, K. Peris, R. Daidone, B. Ruggeri, and S. Chimenti, "Dermoscopic diagnosis by a trained clinician vs. a clinician with minimal dermoscopy training vs. computer-aided diagnosis of 341 pigmented skin lesions: a comparative study," *Br. J. Dermatol.*, vol. 147, no. 3, pp. 481–486, 2002. 36, 37, 38, 39
- [327] P. Rubegni, M. Burroni, G. Cevenini, R. Perotti, G. Dell'Eva, P. Barbini, M. Fimiani, and L. Andreassi, "Digital dermoscopy analysis and artificial neural network for the differentiation of clinically atypical pigmented skin lesions: a retrospective study," *J. Invest. Dermatol.*, vol. 119, no. 2, pp. 471–474, 2002. 36, 38
- [328] M. Barzegari, H. Ghaninezhad, P. Mansoori, A. Taheri, Z. Naraghi, and M. Asgari, "Computer-aided dermoscopy for diagnosis of melanoma," *BMC Dermatol.*, vol. 5, no. 8, 2005. 36, 38
- [329] U. Wollina, M. Burroni, R. Torricelli, S. Gilardi, G. Dell'Eva, C. Helm, and W. Bardey, "Digital dermoscopy in clinical practise: a three-centre analysis," *Skin Res. Tech.*, vol. 13, no. 2, pp. 133–142, 2007. 36, 38
- [330] J. C. Boldrick, C. J. Layton, J. Nguyen, and S. M. Swetter, "Evaluation of digital dermoscopy in a pigmented lesion clinic: Clinician versus computer assessment of malignancy risk," *J. Am. Acad. Dermatol.*, vol. 56, no. 3, pp. 417–421, 2007. 36, 38
- [331] S. Dreiseitl, M. Binder, K. Hable, and H. Kittler, "Computer versus human diagnosis of melanoma: evaluation of the feasibility of an automated diagnostic system in a prospective clinical trial," *Melanoma Res.*, vol. 19, no. 3, pp. 180–184, 2009. 36, 38
- [332] B. Salah, M. Alshraideh, R. Beidas, and F. Hayajneh, "Skin cancer recognition by using a neuro-fuzzy system," *Cancer Informatics*, vol. 10, pp. 1–11, 2011. 36
- [333] G. Di Leo, A. Paolillo, P. Sommella, G. Fabbrocini, and O. Rescigno, "A software tool for the diagnosis of melanomas," in *Proc. IEEE Conf. Instrum. and Meas. Tech. (IMTC)*. Piscataway, NJ: IEEE Press, 2010, pp. 886–891. 36

REFERENCES

-
- [334] M. Burroni, R. Corona, G. Dell'Eva, F. Sera, R. Bono, P. Puddu *et al.*, "Melanoma computer-aided diagnosis," *Clin. Canc. Res.*, vol. 10, no. 6, pp. 1881–86, 2004. 36, 38
 - [335] S. Seidenari, G. Pellacani, and A. Giannetti, "Digital videomicroscopy and image analysis with automatic classification for detection of thin melanomas," *Melanoma Res.*, vol. 9, no. 2, pp. 163–171, 1999. 36, 38
 - [336] L. Andreassi, R. Perotti, P. Rubegni, M. Burroni, G. Cevenini, M. Biagioli *et al.*, "Digital dermoscopy analysis for the differentiation of atypical nevi and early melanoma: a new quantitative semiology," *Arch. Dermatol.*, vol. 135, no. 12, pp. 1459–65, 1999. 36, 38
 - [337] J. Smolle, "Computer recognition of skin structures using discriminant and cluster analysis," *Skin Res. Tech.*, vol. 6, no. 2, pp. 58–63, 2000. 36
 - [338] P. Rubegni, A. Ferrari, G. Cevenini, D. Piccolo, M. Burroni, R. Perotti *et al.*, "Differentiation between pigmented Spitz naevus and melanoma by digital dermoscopy and stepwise logistic discriminant analysis," *Melanoma Res.*, vol. 11, no. 1, pp. 37–44, 2001. 36, 38
 - [339] P. Rubegni, G. Cevenini, M. Burroni, G. Dell'Eva, P. Sbanò, A. Cuccia, and L. Andreassi, "Digital dermoscopy analysis of atypical pigmented skin lesions: a stepwise logistic discriminant analysis approach," *Skin Res. Tech.*, vol. 8, no. 4, pp. 276–281, 2002. 36, 38
 - [340] M. Burroni, P. Sbanò, G. Cevenini, M. Risulo, G. Dell'Eva, P. Barbini, C. Miracco, M. Fimiani, L. Andreassi, and P. Rubegni, "Dysplastic naevus vs. in situ melanoma: digital dermoscopy analysis," *Br. J. Dermatol.*, vol. 152, no. 4, pp. 679–684, 2005. 35, 36, 38, 39
 - [341] M. Cristofolini, P. Bauer, S. Boi, P. Cristofolini, R. Micciolo, and M. C. Sicher, "Diagnosis of cutaneous melanoma: accuracy of a computerized image analysis system (Skin View)," *Skin Res. Tech.*, vol. 3, no. 1, pp. 23–27, 1997. 36
 - [342] A. Blum, H. Luedtke, U. Ellwanger, R. Schwabe, G. Rassner, and C. Garbe, "Digital image analysis for diagnosis of cutaneous melanoma. Development of a highly effective computer algorithm based on analysis of 837 melanocytic lesions," *Br. J. Dermatol.*, vol. 151, no. 5, pp. 1029–38, 2004. 36, 37
 - [343] A. Tenenhaus, A. Nkengne, J. Horn, C. Serruys, A. Giron, and B. Fertil, "Detection of melanoma from dermoscopic images of naevi acquired under uncontrolled conditions," *Skin Res. Tech.*, vol. 16, no. 1, pp. 85–97, 2010. 36
 - [344] S. Merler, C. Furlanello, B. Larcher, and A. Sboner, "Tuning cost-sensitive boosting and its application to melanoma diagnosis," in *Multiple Classifier Systems*, ser. LNCS. Berlin: Springer, 2001, vol. 2096, pp. 32–42. 36
 - [345] W. V. Stoecker, R. H. Moss, F. Ercal, and S. E. Umbaugh, "Nondermatoscopic digital imaging of pigmented lesions," *Skin Res. Tech.*, vol. 1, no. 1, pp. 7–16, 1995. 37

REFERENCES

- [346] P. Hall, E. Claridge, and J. Smith, "Computer screening for early detection of melanoma—is there a future?" *Br. J. Dermatol.*, vol. 132, no. 3, pp. 325–338, 1995. 37
- [347] B. Rosado, S. Menzies, A. Harbauer, H. Pehamberger, K. Wolff, M. Binder, and H. Kittler, "Accuracy of computer diagnosis of melanoma: a quantitative meta-analysis." *Arch. Dermatol.*, vol. 139, no. 3, pp. 361–367, 2003. 37
- [348] A. Blum, I. Zalaudek, and G. Argenziano, "Digital image analysis for diagnosis of skin tumors," *Semin. Cutan. Med. Surg.*, vol. 27, no. 1, pp. 11–15, 2008. 37
- [349] S. Rajpara, A. Botello, J. Townend, and A. Ormerod, "Systematic review of dermoscopy and digital dermoscopy/artificial intelligence for the diagnosis of melanoma," *Br. J. Dermatol.*, vol. 161, no. 3, pp. 591–604, 2009. 37
- [350] A. Perrinaud, O. Gaide, L. French, J. Saurat, A. Marghoob, and R. Braun, "Can automated dermoscopy image analysis instruments provide added benefit for the dermatologist? A study comparing the results of three systems," *Br. J. Dermatol.*, vol. 157, no. 5, pp. 926–933, 2007. 38, 39
- [351] G. Pellacani, M. Martini, and S. Seidenari, "Digital videomicroscopy with image analysis and automatic classification as an aid for diagnosis of spitz nevus," *Skin Res. Tech.*, vol. 5, no. 4, pp. 266–272, 1999. 38
- [352] M. Burroni, U. Wollina, R. Torricelli, S. Gilardi, G. Dell'Eva, C. Helm *et al.*, "Impact of digital dermoscopy analysis on the decision to follow up or to excise a pigmented skin lesion: a multicentre study," *Skin Res. Tech.*, vol. 17, pp. 451–460, 2011. 38
- [353] M. J. Jamora, B. D. Wainwright, S. A. Meehan, and J.-C. Bystryrn, "Improved identification of potentially dangerous pigmented skin lesions by computerized image analysis," *Arch. Dermatol.*, vol. 139, no. 2, pp. 195–198, 2003. 38
- [354] M. Elbaum, A. Kopf, H. Rabinovitz, R. Langley, H. Kamino, M. Mihm *et al.*, "Automatic differentiation of melanoma from melanocytic nevi with multispectral digital dermoscopy: A feasibility study," *J. Am. Acad. Dermatol.*, vol. 44, no. 2, pp. 207–218, 2001. 38
- [355] G. Monheit, A. Cognetta, L. Ferris, H. Rabinovitz, K. Gross, M. Martini *et al.*, "The performance of MelaFind: A prospective multicenter study," *Arch. Dermatol.*, vol. 147, no. 2, pp. 188–194, 2011. 38, 39
- [356] A. Blum, R. Hofmann-Wellenhof, H. Luedtke, U. Ellwanger, A. Steins, S. Roehm *et al.*, "Value of the clinical history for different users of dermoscopy compared with results of digital image analysis," *J. Eur. Acad. Dermatol. Venereol.*, vol. 18, no. 6, pp. 665–669, 2004. 38
- [357] M. Moncrieff, S. Cotton, E. Claridge, and P. Hall, "Spectrophotometric intracutaneous analysis: a new technique for imaging pigmented skin lesions," *Br. J. Dermatol.*, vol. 146, no. 3, pp. 448–457, 2002. 38, 39

REFERENCES

-
- [358] H. Tehrani, J. Walls, G. Price, S. Cotton, E. Sassoon, and P. Hall, "A novel imaging technique as an adjunct to the in vivo diagnosis of nonmelanoma skin cancer," *Br. J. Dermatol.*, vol. 155, no. 6, pp. 1177–83, 2006. 38
 - [359] S. Menzies, L. Bischof, H. Talbot, A. Gutenev, M. Avramidis, L. Wong *et al.*, "The performance of SolarScan: an automated dermoscopy image analysis instrument for the diagnosis of primary melanoma." *Arch. Dermatol.*, vol. 141, no. 11, pp. 1388–97, 2005. 38
 - [360] P. Rubegni, M. Burroni, G. Dell'Eva, and L. Andreassi, "Digital dermoscopy analysis for automated diagnosis of pigmented skin lesions," *Clin. Dermatol.*, vol. 20, no. 3, pp. 309–312, 2002. 39
 - [361] A. Baldi, R. Murace, E. Dragonetti, M. Manganaro, O. Guerra, S. Bizzi, and L. Galli, "Definition of an automated content-based image retrieval (CBIR) system for the comparison of dermoscopic images of pigmented skin lesions," *Biomed. Eng. Online*, vol. 8, no. 1, pp. 18–28, 2009. 39
 - [362] P. Kini and A. P. Dhawan, "Three-dimensional imaging and reconstruction of skin lesions," *Comput. Med. Imaging Graph.*, vol. 16, no. 3, pp. 153–161, 1992. 40
 - [363] S. McDonagh, R. Fisher, and J. Rees, "Using 3D information for classification of non-melanoma skin lesions," in *Proc. Med. Image Understand. Anal. (MIUA)*, S. McKenna and J. Hoey, Eds., vol. 1. Dundee, UK: BMVA, 2008, pp. 164–168. 40
 - [364] L. Smith, M. Smith, A. Farooq, J. Sun, Y. Ding, and R. Warr, "Machine vision 3D skin texture analysis for detection of melanoma," *Sensor Review*, vol. 31, no. 2, pp. 111–119, 2011. 40
 - [365] Y. Zhou, M. Smith, L. Smith, and R. Warr, "Using 3D differential forms to characterize a pigmented lesion in vivo," *Skin Res. Tech.*, vol. 16, no. 1, pp. 77–84, 2010. 40
 - [366] Y. Zhou, M. Smith, L. Smith, A. Farooq, and R. Warr, "Enhanced 3D curvature pattern and melanoma diagnosis," *Comput. Med. Imaging Graph.*, vol. 35, no. 2, pp. 155–165, 2011. 40
 - [367] H. Voigt and R. Claßen, "Topodermatographic image analysis for melanoma screening and the quantitative assessment of tumor dimension parameters of the skin," *Cancer*, vol. 75, no. 4, pp. 981–988, 1995. 40
 - [368] D. A. Perednia, R. G. White, and R. A. Schowengerdt, "Localization of cutaneous lesions in digital images," *Comput. Biomed. Res.*, vol. 22, no. 4, pp. 374–392, 1989. 41
 - [369] R. G. White, D. A. Perednia, and R. A. Schowengerdt, "Automated feature detection in digital images of skin," *Comput. Meth. Programs Biomed.*, vol. 34, no. 1, pp. 41–60, 1991. 41

REFERENCES

- [370] D. P. Filiberti, P. Bellutta, P. Ngan, and D. A. Perednia, "Efficient segmentation of large-area skin images: an overview of image processing," *Skin Res. Tech.*, vol. 1, no. 4, pp. 200–208, 1995. 41
- [371] D. Filiberti, J. Gaines, P. Bellutta, P. Ngan, and D. Perednia, "Efficient segmentation of large-area skin images: a statistical evaluation," *Skin Res. Tech.*, vol. 3, no. 1, pp. 28–35, 1997. 41
- [372] S. Taeg, W. Freeman, and H. Tsao, "A reliable skin mole localization scheme," in *Proc. IEEE Int. Conf. Comput. Vis. (ICCV)*. Piscataway, NJ: IEEE Press, 2007, pp. 1–8. 41
- [373] T. Lee, M. Atkins, M. King, S. Lau, and D. McLean, "Counting moles automatically from back images," *IEEE T. Med. Imaging*, vol. 52, no. 11, pp. 1966–69, 2005. 41
- [374] J. Pierrard and T. Vetter, "Skin detail analysis for face recognition," in *Proc. IEEE Conf. Comput. Vis. Pattern Recogn. (CVPR)*. Los Alamitos, CA: IEEE Computer Society Press, 2007, pp. 1–8. 41
- [375] D. Perednia and R. White, "Automatic registration of multiple skin lesions by use of point pattern matching," *Comput. Med. Imaging Graph.*, vol. 16, no. 3, pp. 205–216, 1992. 41
- [376] R. G. White and D. A. Perednia, "Automatic derivation of initial match points for paired digital images of skin," *Comput. Med. Imaging Graph.*, vol. 16, no. 3, pp. 217–225, 1992. 41
- [377] J. Roning and M. Riech, "Registration of nevi in successive skin images for early detection of melanoma," in *Proc. Int. Conf. Pattern Recogn. (ICPR)*, vol. 1. Piscataway, NJ: IEEE Press, 1998, pp. 352–357. 41
- [378] B. McGregor, "Automatic registration of images of pigmented skin lesions," *Pattern Recogn.*, vol. 31, no. 6, pp. 805–817, 1998. 41
- [379] H. Huang and P. Bergstresser, "A new hybrid technique for dermatological image registration," in *Proc. IEEE Int. Conf. Bioinformat. Bioeng. (BIBE)*. Piscataway, NJ: IEEE Press, 2007, pp. 1163–1167. 42
- [380] H. Mirzaalian, G. Hamarneh, and T. Lee, "A graph-based approach to skin mole matching incorporating template-normalized coordinates," in *Proc. IEEE Conf. Comput. Vis. and Pattern Recogn. (CVPR)*. Los Alamitos, CA: IEEE Computer Society Press, 2009, pp. 2152–59. 42
- [381] H. Mirzaalian, T. K. Lee, and G. Hamarneh, "Uncertainty-based feature learning for skin lesion matching using a high order MRF optimization framework," in *Proc. Int. Conf. Med. Image Comput. and Comput. Assist. Interv. (MICCAI)*. Springer, 2012, pp. 98–105. 42
- [382] B. Negin, E. Riedel, S. Oliveria, M. Berwick, D. Coit, and M. Brady, "Symptoms and signs of primary melanoma," *Cancer*, vol. 98, no. 2, pp. 344–348, 2003. 45

REFERENCES

-
- [383] N. Apuzzo, “Recent advances in 3D full body scanning with applications to fashion and apparel,” in *Optical 3-D Measurement Techniques IX*, A. Gruen and H. Kahmen, Eds., 2009. 45
 - [384] F. Remondino, “Human body reconstruction from image sequences,” in *Pattern Recogn.*, ser. LNCS. Springer, 2002, pp. 50–57. 45
 - [385] D. L. DiLaura, K. W. Houser, R. G. Mistrick, and G. R. Steffy, Eds., *The lighting handbook*, 10th ed. Illuminating Engineering Society of North America, 2011. 51
 - [386] Scientific Committee on Emerging and Newly Identified Health Risks (SCENIHR), “Health effects of artificial light,” European Commission, Tech. Rep., 2012. 51
 - [387] I. Zalaudek, H. Kittler, A. Marghoob, A. Balato, A. Blum, S. Dalle, G. Ferrara, R. Fink-Puches, C. Giorgio, R. Hofmann-Wellenhof, J. Malvehy, E. Moscarella, S. Puig, M. Scalvenzi, L. Thomas, and G. Argenziano, “Time required for a complete skin examination with and without dermoscopy: A prospective, randomized multicenter study,” *Archives of Dermatology*, vol. 144, no. 4, pp. 509–513, 2008. 53
 - [388] R. Hartley and A. Zisserman, *Multiple View Geometry in Computer Vision*. Cambridge University Press, 2003. 54, 58, 78, 86, 140, 142, 150
 - [389] J. Salvi, X. Armangué, and J. Batlle, “A comparative review of camera calibrating methods with accuracy evaluation,” *Pattern Recogn.*, vol. 35, no. 7, pp. 1617–1635, 2002. 54
 - [390] J.-Y. Bouguet. (2010, July) Camera calibration toolbox for matlab. [Online]. Available: http://www.vision.caltech.edu/bouguetj/calib_doc/ 54, 56, 57
 - [391] C. Harris and M. Stephens, “A combined corner and edge detector,” in *Alvey vision conf.*, vol. 15. Manchester, UK, 1988, p. 50. 65
 - [392] R. Smith, “An overview of the tesseract OCR engine,” in *Int. Conf. Document Anal. Recogn.*, vol. 2, 2007, pp. 629–633. 66
 - [393] N. Otsu, “A threshold selection method from gray-level histograms,” *Automatica*, vol. 11, no. 285-296, pp. 23–27, 1975. 66
 - [394] J. Matas, O. Chum, M. Urban, and T. Pajdla, “Robust wide baseline stereo from maximally stable extremal regions,” in *Br. Mach. Vis. Conf. (BMVC)*, vol. 1, 2002, pp. 384–393. 72, 137
 - [395] V. Vezhnevets, V. Sazonov, and A. Andreeva, “A survey on pixel-based skin color detection techniques,” in *Proc. Graphicon*, vol. 3. Moscow, Russia, 2003, pp. 85–92. 73
 - [396] E. Trucco and A. Verri, *Introductory techniques for 3-D computer vision*. Prentice Hall Englewood Cliffs, 1998, vol. 93. 78
 - [397] R. Hartley and P. Sturm, “Triangulation,” in *Computer Analysis of Images and Patterns*, ser. LNCS, V. Hlaváč and R. Šára, Eds. Springer Berlin Heidelberg, 1995, vol. 970, pp. 190–197. 78

REFERENCES

- [398] J. Lewis, “Fast normalized cross-correlation,” in *Vision interface*, vol. 10, no. 1, 1995, pp. 120–123. 96
- [399] B. Washington, *The Booker T. Washington Papers: 1903-4*, L. Harlan and R. Smock, Eds. University of Illinois Press, 1977. 103
- [400] C. Poynton, *Digital Video and HDTV: Algorithms and Interfaces*. USA: Morgan Kaufmann Publishers, 2003. 107
- [401] R. Lukac, Ed., *Computational Photography: Methods and Applications*. CRC Press, 2010. 137
- [402] A. Vedaldi and B. Fulkerson. (2008) VLFeat: An open and portable library of computer vision algorithms. [Online]. Available: <http://www.vlfeat.org/> 140, 150
- [403] D. G. Lowe, “Object recognition from local scale-invariant features,” in *Proc. IEEE Int. Conf. Comput. Vis. (ICCV)*, vol. 2. Ieee, 1999, pp. 1150–1157. 143
- [404] P. Kovesi. (2006) MATLAB and octave functions for computer vision and image processing. [Online]. Available: <http://www.csse.uwa.edu.au/~pk/research/matlabfns/> 152
- [405] G. Bebis. Lecture notes on stereo reconstruction. University of Nevada, Computer Vision Department. [Online]. Available: <http://www.cse.unr.edu/~bebis/CS791E/Notes/StereoReconstruction.pdf> 153